AIX-MARSEILLE UNIVERSITE
TECHNISCHE UNIVERSITÄT MÜNCHEN
Ecole doctorale Physique et Sciences de la Matière
UFR Sciences
Centre Interdisciplinaire de Nanosciences de Marseille / UMR 7325

Thèse présentée pour obtenir le grade universitaire de docteur

Discipline : Physique et sciences de la matière
Spécialité : Matière Condensée et Nanosciences

Tony LELAIDIER

Organic semiconductor characterisation by scanning tunnelling microscopy and optical spectroscopy

Soutenue le JJ/MM/AAAA devant le jury :

M. Vincent REPAIN	MQP	Université Paris Diderot	Rapporteur
M. Eric LE MOAL	ISMO	Université Paris Sud	Rapporteur
M. Johannes BARTH	TUM-PH	Technische Universität München	Examinateur
M. Moritz SOKOLOWSKI	PTC	Universität Bonn	Examinateur
M. Ulrich HEIZ	TUM-PC	Technische Universität München	Co-directeur de thèse
M. Conrad BECKER	CINaM	Aix-Marseille Université	Directeur de thèse

Technische Universität München

Lehrstuhl für Physikalische Chemie

Organic semiconductor characterisation by scanning tunnelling microscopy and optical spectroscopy

Tony Lelaidier

Vollständiger Adbruck der von der Fakultät für Chemie der Technische Universität München zur Erlangung des akademischen Grades eines

Doktors der Naturwissenschaften

genehmigten Dissertation.

Vorsitzender: Univ.-Prof. Dr. Johannes BARTH
Prüfer der dissertation:

1. Univ.-Prof. Dr. Vincent REPAIN
2. Dr. Eric LE MOAL
3. Univ.-Prof. Dr. Moritz SOKOLOWSKI
4. Univ.-Prof. Dr. Ulrich HEIZ
5. Univ.-Prof. Dr. Conrad BECKER

Die Dissertation wurde am bei der Technischen Universität München eingereicht und durch die Fakultät für Chemie am angenommen.

Cette oeuvre est mise à disposition selon les termes de la Licence Creative Commons Attribution - Pas d'Utilisation Commerciale - Pas de Modification 3.0 France.

Résumé

Les semi-conducteurs organiques sont des matériaux très prometteurs dans le cadre d'applications dans le domaine de l'électronique moléculaire. L'intérêt pour ces matériaux provient de la possibilité de modifier leur propriétés optiques, électroniques et d'auto-assemblages par l'ajout de groupements fonctionnels. Toutefois, une profonde connaissance des processus de croissance et d'auto-assemblage est requis dans le cadre de ces applications, particulièrement due au fait que les propriétés de ces matériaux sont fortement reliées à ce degré d'organisation.

Dans le cadre de cette thèse, le 5,14-dihydro-5,7,12,14-tetraazapentacene (DHTAP) et le 1,4-Di-n-octyloxy-2,5-bis(pyren-1-ylethenyl)benzene (bis-pyrène), deux composés synthétisés au département IMMF du CINaM (Centre Interdisciplinaire de Nanosciences de Marseille) ont été étudiés. Les propriétés électroniques et d'auto-assemblages ont été étudiées par microscopie à effet tunnel (STM), sous ultra-vide à basse température. Les propriétés optiques ont été étudiées par spectroscopie en cavité résonnante (CRD), également sous ultra-vide.

Ces matériaux, en plus de présenter des propriétés de semi-conducteur en couches minces, ont été fonctionnalisés afin de permettre la croissance de structures hautement organisées. La molécule de DHTAP présente des groupements N-H en positions 5 et 14 ainsi que des atomes d'azote en positions 7 et 12, qui, en plus de conférer à cette molécule une bonne stabilité dans les conditions ambiantes, lui permet également d'établir des liaisons hydrogènes avec les molécules voisines. La molécule de bis-pyrène possède deux chaines d'octyles, en positions 1 et 4, qui, outre le fait d'augmenter la solubilité du composé en solution et d'être la longueur optimale pour la formation de monocristaux, permet l'interaction de ces molécules lorsqu'elles sont déposées sur une surface par des interactions de type van der Waals.

La croissance du DHTAP a été étudiée sur des métaux nobles de nature et d'orientation cristallographique différentes (Au(111), Au(110) et Ag(110)). La croissance du bis-pyrène a été étudiée sur Au(111). Dans chaque cas, les conditions de température idéales pour la formation d'une première couche organisée ont été déterminées. En effet, cette température joue un rôle très important durant les premières étapes de la croissance du film moléculaire, et peut conduire à la formation de différentes structures moléculaires ou encore à une reconstruction de la surface cristalline.

Les différentes étapes de la formation de la première mono-couche ont été caractérisées pour chaque système. Le rôle, la nature ainsi que l'évolution de l'influence des différentes interactions (molécule-substrat et molécule-molécule) ont été étudiés. Dans la plupart des cas, la première partie de la croissance

est principalement due aux interactions molécule-substrat. L'augmentation de la densité moléculaire conduit à une augmentation de l'influence des interactions intermoléculaires. Au-delà d'une certaine densité ces interactions intermoléculaires prévalent sur les interactions molécule-substrat, une réorganisation moléculaire est observée et la suite de la croissance est principalement assurée par ces interactions intermoléculaires.

Différents modèles sont proposés pour les structures auto-organisées observées en première couche et la densité moléculaire de ces films ont été déterminées. Ces modèles présentent une commensuration entre le substrat et le film moléculaire, excepté dans le cas du DHTAP/Au(111). La formation de la seconde couche moléculaire a également été étudiée et la croissance de structures organisées a été observée pour DHTAP/Au(111) et bis-pyrène/Au(111).

Les propriétés optiques du bis-pyrène déposé sur du verre borosilicate ont été étudiées par CRD en fonction de la densité moléculaire et de la température. L'évolution des propriétés optiques en fonction de la densité moléculaire combinée aux informations obtenues par STM ont permit d'associer ces modifications aux interactions des moments dipolaires de transition des molécules de la première et de la seconde couche. Ces études ont également permis de déterminer que le mode de croissance du bis-pyrene sur du verre borosilicate est une croissance en ilot (Volmer-Weber) par opposition au modes de croissance observés pour le bis-pyrène et pour le DHTAP sur métaux noble, qui est soit une croissance en couche par couche (Frank-van der Merwe), soit une croissance de type Stransky-Krastanov (couche complète puis formation d'ilots). Des études complémentaires (spectroscopie par effet tunnel) concernant les propriétés électroniques du bis-pyrène ont permit de déterminer un gap électronique de 2.85 eV, en très bon accord avec la transition optique principale de la molécule observée a 434 nm (2.86 eV) par CRD.

Finalement, la possibilité d'induire des modifications chimiques de la molécule de DHTAP, intégrée dans une couche auto-assemblée, en utilisant le courant tunnel du STM a été observée. Il s'avère que la molécule de DHTAP intégrée en première couche peut subir une double déshydrogénation pour conduire à la formation d'un composé identifié comme étant le 5,7,12,14-tetraazapentacene (TAP). En seconde couche, la formation de deux radicaux, en plus du TAP, a été observé. La formation de ces composés, qui intervient seulement en seconde couche, nous laisse penser que ces radicaux ne sont pas stables en première couche, dû à un couplage différent avec le substrat métallique. La molécule de TAP présente un certain intérêt du fait qu'elle n'est pas synthétisable pas les méthodes conventionnelles de chimie organique, en revanche, nous avons montré qu'il est possible de synthétiser cette molécule par déshydrogénation du 5,14-DHTAP en utilisant le courant tunnel inélastique.

Mots clés : microscopie à effet tunnel, spectroscopie en cavité résonnante, ultra vide, semi-conducteur organique, couche mince, auto-assemblage, déshy-

drogénation par courant tunnel.

Abstract

Organic semiconductors are very promising materials for applications in the field of organic electronics. The interest for these materials arises from the possibility of tuning their optical, electronic and self-assembling properties. However, a deeper understanding of the growth and self-assembling processes is needed for these applications, especially due to the fact that the properties of these materials will be strongly related to this organisational order.

In the framework of this thesis, the 5,14-dihydro-5,7,12,14-tetraazapentacene (DHTAP) and the 1,4-Di-n-octyloxy-2,5-bis(pyren-1-ylethenyl)benzene (bis-pyrene), two molecular compounds synthesized by the IMMF department in the CINaM laboratory, have been studied. Electronic and self-assembling properties have been studied by low temperature scanning tunnelling microscopy (STM) under ultrahigh vacuum conditions. Optical properties have been studied by cavity ring-down (CRD) spectroscopy, also under ultrahigh vacuum conditions.

These materials, which have semiconducting properties in thin films, have been functionalized to allow the growth of well-ordered structures. The DHTAP molecule possesses N-H groups in positions 5 and 14 and nitrogen atoms in positions 7 and 12. In addition to the fact that they improve stability under ambient conditions, they allow for the establishment of hydrogen bonds between neighbouring molecules. On the other hand, the bis-pyrene molecule possess two octyl chains, in positions 1 and 4. Besides the fact of the increasing solubility in solvent and the fact that it is the optimal length for the formation of single crystals, these alkyl chains allow interactions of van der Waals type between neighbouring molecules deposited on a surface.

The growth of DHTAP has been studied on Au(111), Au(110), and Ag(110). The growth of bis-pyrene has been studied on Au(111). In each case, the optimal temperature conditions for the formation of a well-ordered first monolayer have been determined. This temperature plays indeed a very important role during the first steps of growth of molecular films and can lead to the formation of different molecular structures or to the reconstruction of the crystalline surface.

The different steps of the formation of the first monolayer have been characterised for each system. The role, the nature and the evolution of the influence of molecule-substrate and intermolecular interactions have been studied. Generally, the first part of growth is mainly guided by molecule-substrate interactions. The increase of the molecular density leads to an increase of the influence of intermolecular interactions. Above a certain density, intermolecular interactions become more important than molecule-substrate interactions. A molecular reorganization is observed and the following steps of the growth are guided mostly by intermolecular interactions.

Models are proposed for the different self-organized structures observed in the

first molecular layer and the molecular densities of these films have been determined. These models show a commensuration between the substrate and the molecular structures, with the exception of DHTAP/Au(111). The formation of second monolayers has also been studied, and the formation of well-ordered second monolayer has been observed for DHTAP/Au(111) and bis-pyrene/Au(111).

The optical properties of bis-pyrene deposited on borosilicate glass have been studied by cavity ring-down spectroscopy as a function of molecular density and temperature. The evolution of the optical properties as a function of the coverage combined with information obtained from STM allow us to identify these modifications as interactions between transition dipole moments of molecules in the first and in the second layer. These investigations allow us to also determine that the growth mode of bis-pyrene on borosilicate glass is an island growth mode (Volmer-Weber), instead of the growth mode observed for bis-pyrene or DHTAP on noble metal surfaces, which is either a layer-by-layer growth mode (Frank-van der Merwe), or a Stansky-Krastanov growth mode (complete layer followed by islands formations). Complementary studies, performed by the means of scanning tunnelling spectroscopy, concerning the electronic properties of the bis-pyrene molecules allowed us to determine a HOMO-LUMO gap of 2.85 eV, in very good agreement with the optical transition of the molecule observed at 434 nm (2.86 eV) by the means of CRD.

Finally, the possibility to induce chemical modification of DHTAP molecules embedded in an ordered monolayer using the tunnelling current of the STM has been studied. It appears that the molecule embedded in the first ML can be doubly dehydrogenated which leads to the formation of a compound identified as 5,7,12,14-tetraazapentacene (TAP). In the second layer, the formation of two radicals in addition to the TAP has been observed. The formation of these radicals which takes place only in the second monolayer, suggests that they are unstable in the first monolayer due to stronger coupling between these compounds and the metallic substrate. The TAP molecule is interesting because that it cannot be synthesized using common organic chemical methods. However, we showed that it is possible to synthesize this molecule through dehydrogenation of a single 5,14-DHTAP using the tunnelling current.

Keywords : scanning tunnelling microscopy, cavity ring-down spectroscopy, ultrahigh vacuum, organic semiconductor, thin film, self-assembly, dehydrogenation induced by STM.

Acknowledgements

I would like to thank in the first place the professor Conrad Becker as well as the professor Ueli Heiz who gave me the opportunity to do my PhD in collaboration between Aix-Marseille Université and the Technische Universität München. This gave to me the opportunity to confront myself to the world of the scientific research in an international environment during these years.

I also would like to thank the research director Claude Henry, former director of the "Centre Interdisciplinaire de Nanosciences de Marseille", and the professor Frédéric Fagès, actual director of the CINaM, to have welcomed me in the laboratory to do my PhD.

I would like to thank Thomas Léoni, lecturer at the CINAM laboratory, with whom I had the pleasure to work during all my PhD. Thanks you for all these interesting discussions concerning the scanning tunnelling technique.

I would also like to thank Aras Kartouzian, researcher at the Technische Universität München, to have welcomed me in the team "surface spectroscopy" and for all the interesting discussions concerning the cavity ring-down and the second harmonic generation spectroscopy techniques.

I would like to thank Olivier Siri, research director at the CINaM laboratory, in the department IMMF, for providing the DHTAP molecules and the interesting discussions concerning their properties.

I also would like to thank Anthony D'Aléo, researcher at the CINaM in the department IMMF, for providing the bis-pyrene molecules and the helpful discussions concerning their properties.

I would like to thank Alain Ranguis, engineer at the CINaM laboratory for all the advices and explanations about ultra high vacuum technique, and concerning the preparation of the surface prior to STM investigations.

I also would like to thank Laurence Masson, professor at the CINaM, for providing the Ag(110) single crystal, which allowed us to investigate the growth properties of DHTAP on this metal.

I would like to thank the professor Peter Zeppenfeld for the interesting discussions concerning our LEED results which have led to a full understanding of these.

I also would like to thank Tobias Lünskens and Alexander von Weber, PhD students at the Technische Universität München, with whom I had the pleasure to work on the optical characterisation of my compounds, and also on the studies of optical properties of other organic compounds and metallic clusters.

I also would like to thank Anthony Thomas, PhD student at the CINaM, for our discussions concerning the experiments performed on the dehydrogenation of the DHTAP during my stays in Munich, and also concerning the growth of this compound on other substrates (Cu, thin oxide film...).

I would like to thank again Conrad Becker for his professional guidance, our interesting scientific discussions of the experimental results.

I would like to thank Eloi Perdereau, as well as Urs Moosmuller and Alma Esteban for the proof reading of the manuscript.

Finally, I would like to deeply thank all my family and particularly my parents, Eric and Christelle Lelaidier, who supported me all along these years.

Contents

Résumé 9

Abstract 12

Acknowledgements 14

List of Figures 17

List of Tables 19

Introduction 23

1 Experimentals techniques and materials 25
1.1 Scanning tunnelling microscopy 25
1.1.1 Introduction 25
1.1.2 Theory of Scanning Tunneling Microscopy 28
1.1.3 Overview of the experimental setup 38
1.2 Surface Cavity Ring-Down Spectroscopy 44
1.2.1 Introduction 44
1.2.2 Theory of cavity ring-down spectroscopy 46
1.2.3 Experimental setup 48
1.3 The organic compounds 54
1.3.1 5,14-Dihydro-5.7.12.14-tetraazapentacene 54
1.3.2 1,4-Di-n-octyloxy-2,5-bis(pyren-1-ylethenyl)benzene 55
1.4 The surfaces 58
1.4.1 Au(111) 58
1.4.2 Au(110) 59
1.4.3 Ag(110) 60
1.4.4 Borosilicate glass 61

2 Characterisation of DHTAP 63
2.1 Growth of DHTAP on noble metal surfaces: nucleation and initial steps of growth 63
2.1.1 DHTAP/Au(111) 63
2.1.2 DHTAP/Au(110) 68
2.1.3 DHTAP/Ag(110) 72
2.1.4 Discussion 76
2.2 Growth of DHTAP on noble metal surfaces: submonolayer coverage 79
2.2.1 DHATP/Au(111) 79
2.2.2 DHATP/Au(110) 83

2.2.3 DHATP/Ag(110) 88
2.2.4 Discussion 91
2.3 DHTAP on noble metal surfaces: above the monolayer 93
2.3.1 DHATP/Au(111) 93
2.3.2 DHATP/Au(110) 99
2.3.3 DHATP/Ag(110) 106
2.3.4 Discussion 109
2.4 Conclusion of the DHTAP growth 112

3 Characterisation of bis-pyrene 115
3.1 Growth of bis-pyrene on Au(111) 115
3.1.1 Overall growth behaviour 115
3.1.2 Structure of the ordered bis-pyrene domains 122
3.1.3 Discussion 129
3.2 Optical properties of bis-pyrene 133
3.2.1 UV-Vis measurements of bis-pyrene 133
3.2.2 S-CRDS of bis-pyrene deposited at LT 134
3.2.3 S-CRDS of bis-pyrene deposited at RT 136
3.2.4 Discussion 136
3.3 Conclusion and outlook 139

4 DHTAP/Au(111): chemical modifications induced by STM 143
4.1 Modifications induced in the first monolayer 143
4.1.1 STM/STS results 143
4.1.2 Discussion 147
4.2 Modifications induced in the second monolayer 149
4.2.1 STM observations 149
4.2.2 DFT calculations and discussion 151
4.2.3 Electronic properties of azapentacenes in the second monolayer 157
4.3 Conclusions and outlook 160

5 Conclusion 163

Bibliography 167

ANNEXES: List of publications 181
A Article 1: Growth of Si ultrathin films on silver surfaces: Evidence of an Ag(110) reconstruction induced by Si. 181
B Article 2: Highly Ordered Molecular Films on Au(111): The N-Heteroacene Approach. 181
C Article 3: Optical and morphological properties of thin films of bis-pyrenyl π-conjugated molecules. 181

List of Figures

1.1 STM: basic scheme 26
1.2 Unidimensional potential step 28
1.3 Unidimensional potential barrier 31
1.4 Influence of the bias voltage on the Fermi level alignment 33
1.5 Schematic STM tip in Tersoff Hamann Theory 35
1.6 Scanning tunnelling spectroscopy principle 36
1.7 STS: the lock in technique 38
1.8 Photography of the STM lab 39
1.9 Tip preparation scheme 41
1.10 E-beam heater: principle and calibration curve 42
1.11 Cavity ring-down spectroscopy in transmission mode 45
1.12 Cavity ring-down: principle and theory 46
1.13 S-CRDS: exponential decay 47
1.14 Experimental setup of s-CRD spectroscopy 49
1.15 Quartz micro-balance: determination of the molecular density 50
1.16 S-CRDS: data correction process 52
1.17 DHTAP: Chemical Structure 54
1.18 Synthesis of DHTAPs 55
1.19 Bis-pyrene: chemical structure 56
1.20 Au(111) surface 58
1.21 Au(110) surface 60
1.22 Ag(110) surface 61

2.1 DHTAP/Au(111): determination of the deposition rate 64
2.2 DHTAP/Au(111): influence of the temperature 65
2.3 DHTAP/Au(111): nucleation and first molecular structure 66
2.4 DHTAP/Au(111): molecular diffusion 67
2.5 DHTAP/Au(110): strong molecular diffusion at submonolayer coverage 69
2.6 DHTAP/Au(110): diffusion and orientation at low submonolayer coverage 70
2.7 DHTAP/Au(110) at low submonolayer coverage: adsorption site 71
2.8 DHTAP/Ag(110): influence of the temperature 73
2.9 SI/Ag(110) and DHTAP/Si/Ag(110): determination of the molecular adsorption site 75
2.10 DHTAP/Au(111): Submonolayer growth 80
2.11 Monte Carlos modelling: growth of DHTAP/Au(111) 81
2.12 Monte Carlos modelling: configuration of DHTAP/Au(111) 83
2.13 DHTAP/Au(110): submonolayer regime 85
2.14 DHTAP/Au(110): influence the temperature 87

2.15 DHTAP/Ag(110): submonolayer regime, medium coverage 89
2.16 DHTAP/Ag(110): submonolayer regime, high coverage 90
2.17 DHTAP/Au(111): monolayer regime 93
2.18 DHTAP/Au(111): R- and L-domains 94
2.19 DHTAP/Au(111): LEED patterns 95
2.20 DHTAP/Au(111): head to tail configuration and model 97
2.21 DHTAP/Au(111): Stranski-Krastanov transition 99
2.22 DHTAP/Au(110): monolayer regime 100
2.23 DHTAP/Au(110): model 102
2.24 DHTAP/Au(110): mirror domains 104
2.25 DHTAP/Au(110): defect 105
2.26 DHTAP/Ag(110): monolayer regime at low temperature 106
2.27 DHTAP/Ag(110): monolayer regime at room temperature 107
2.28 DHTAP/Ag(110): model 108

3.1 Bis-pyrene/Au(111): submonolayer growth: formation of wires 115
3.2 Bis-pyrene/Au(111): submonolayer growth: formation of 2D domains 117
3.3 Bis-pyrene/Au(111): monolayer regime 119
3.4 Bis-pyrene/Au(111): submonolayer regime, detailed structure 120
3.5 Bis-pyrene/Au(111): α unit cell structure and model 123
3.6 Bis-pyrene/Au(111): β unit cell structure and model 125
3.7 Bis-pyrene/Au(111): γ unit cell structure and model 126
3.8 Bis-pyrene/Au(111): δ unit cell structure and model 128
3.9 Bis-pyrene: conformation consideration 131
3.10 UV-Vis spectroscopy of bis-pyrene 133
3.11 S-CRDS spectra of bis-pyrene: LT deposition 135
3.12 S-CRDS spectra of bis-pyrene: loss per pass at 434 nm as a function of the molecular density 135
3.13 S-CRDS spectra of bis-pyrene: RT deposition 137
3.14 Schematic growth of bis-pyrene on Au(111) and BK7 138
3.15 Scanning tunnelling spectroscopy of bis-pyrene on Au(111) 139

4.1 DHTAP/Au(111): STS of molecules embedded in the first monolayer 144
4.2 DHTAP/Au(111): STS induced chemical modification 145
4.3 Induced chemical modification: reproducible process 146
4.4 DFT calculation: HOMO and LUMO of DHTAP, THTAP and TAP 148
4.5 DHTAP/Au(111): modifications induced in the second monolayer using STS 150
4.6 DFT calculation and STM image: identification of the compounds and summary 152
4.7 STM image of TrHTAP 153
4.8 Comparison between DFT and STM 154
4.9 Formation of MHTAP: preferential dehydrogenation 155

4.10 Influence of the bias voltage for imaging TAP and MHTAP 158
4.11 STS of the second monolayer 159
4.12 Synthesis of TAP 160
4.13 Synthesis of TAP, MHTAP and TrHTAP 161

List of Tables

1.1 Highly reflective mirrors characteristics 51

2.1 DHTAP/Au(110): molecular orientations at submonolayer coverage 86
2.2 Self-assembled domains of DHTAP on noble metal surface: summary 110

3.1 Bis-pyrene/Au(111): ordered layers and molecular wire properties 129

Introduction

Today, organic semiconductors play a very important role in the field of nanotechnology, especially in organic electronics where these materials are promising candidates to replace inorganic semiconductors. The properties of organic semiconductor thin films are very interesting, especially with respect to the possibility of tuning the optical, electronic and self-assembling properties of these materials by incorporating new molecular blocks or functionalities. These materials also present interesting mechanical flexibility compared to inorganic semiconductors, promising a wide range of applications. The low cost of fabrication of these materials and the conception of devices can be very attractive if the use of clean-room, ultrahigh vacuum conditions or expensive substrate are no longer required.

Self-assembled monolayers of functionalized molecules play a key role in the current and future development of organic materials with tailored optical and electrical properties. These two classes of materials are very promising for applications as optical memories, solar cells, biological fluorescent probes, or organic transistors. However, a deeper understanding of the interaction between the molecules and the surfaces is needed, especially for applications in electronic components. Moreover, the properties of devices depend strongly on the degree of organization of the semiconducting layers, because a better organization results in improved device performance.

It is known that the growth of highly-ordered structures depends on the combination of various factors. Furthermore, the self-assembling properties of molecules are strongly related to the chemical composition, thus the synthesis of compounds with particular functional blocks can be realized in order to improve the self-assembling properties of these compounds. For example, the incorporation of donor and acceptor moieties of hydrogen bonds in a molecular compound (O-H$\cdots$O, N-H$\cdots$N...) or the incorporation of alkyl chains can be used to guide the growth process of self-assembled monolayers.

Another important point is the substrate. The nature of the substrate (metal, semiconductor or oxide) will also be of prime importance depending on the application. The growth behaviour of identical compounds may be completely different depending on the substrate nature. On crystalline surfaces, growth processes also depend strongly on the crystal orientation and generally lead to the formation of different structures.

Finally, the kinetics of the growth process on a given surface depend mainly on two parameters: the temperature and the flux. After a precise adjustment of these parameters, the growth process can lead to the formation of well-ordered structures. The early stages of the growth process, i.e. from the nucleation to the formation of the first monolayer, are also a crucial step because this layer will be

used as a template for the growth of subsequent layers.

The scanning tunnelling microscope (STM) developed at the beginning of the 80's by Binning and Rohrer is a powerful tool for the investigation of structure of surfaces at the atomic scale.[1] This scanning probe technique uses the quantum mechanical tunnelling effect, induced by applying a voltage between two electrodes (in our case the sample and the tip) separated by some Angstroms. The working principle is rather simple: the tip is moved over the surface using piezo-electric actuators, allowing a precise control of the tip position in three directions, to obtain topographic information of the surface. The exponential dependence of the tunnelling current with the surface-tip distance allows to achieve resolution in the order of a few picometers in the direction normal to the surface plane. Combined with a lateral resolution of the order of the Angstrom, this allows STM to 'image' surfaces at the atomic scale and in real space. Consequently, this technique can be used to monitor the growth and study the self-assembling properties of adsorbates deposited on various surfaces.

However, due to the fact that STM is a technique measuring a current, the substrate has to be a metal or a semiconductor. Thin oxide layers grown on metallic substrates can also be used. Indeed, the thinness of these layers allows the establishment of the tunnelling current. Moreover, the scanning tunnelling technique can also be used as a spectroscopic tool to investigate the electronic properties of these substrates, and adsorbates deposited on these substrates. That makes STM one of the most versatile tools for surface sciences investigations.

The study of the optical properties of these adsorbates is also interesting. However, the sensitivity of conventional techniques, such as UV-Vis spectroscopy, is not sufficient to investigate the optical properties of very small quantities of materials. Surface cavity ring-down (CRD) spectroscopy is a very powerful spectroscopic technique allowing the detection of traces of materials. The working principle is rather simple: a light pulse is guided to and trapped into an optical cavity constituted of two highly reflective mirrors. The sample of interest is localized inside the optical cavity, in the optical path of the light pulse. At each reflection of the light pulse on the highly reflective mirror, a small portion of the light leaks off the cavity and the time dependence behaviour of the signal is recorded. The high sensitivity of this technique is due to the extremely long path length of the light inside the cavity and to the fact that the sample is probed thousands of times. Furthermore, with this spectroscopic technique, the absorption is determined by the time behaviour of the signal for a single laser pulse and is consequently independent of laser power fluctuations.

In this thesis the characterisation of the growth process, the optical, and electronic properties of two organic semiconductor has been performed under ultrahigh vacuum conditions by low temperature scanning tunnelling microscopy and by surface cavity ring-down spectroscopy. These compounds are synthesized in the department "Ingénierie Moléculaire et Matériaux Fonctionnels" (IMMF) at the laboratory "Centre Interdisciplinaire de Nanoscience de Marseille" (CINaM).

The characterisation of the growth processes and the electronic properties by the means of STM has been performed at the CINaM laboratory, in the department "Nanomatériaux et Réactivité" (NMR). The optical properties characterisation by the means of CRD spectroscopy has been carried out at the Technische Universität München, at the chair of Physical Chemistry.

1. Experimentals techniques and materials

The aim of this chapter is to present the two main characterisation techniques used during this thesis, scanning tunnelling microscopy and cavity ring-down spectroscopy, the different organic compounds studied and the surfaces used as substrates.

1.1. Scanning tunnelling microscopy

In this section we will introduce the technique of scanning tunnelling microscopy, the tunnelling effect, the theory of scanning tunnelling microscopy, and finally we give an overview of the experimental setup used during this thesis.

1.1.1. Introduction

The forefather of the STM is the topographiner, developed by Young, Ward, and Scire[2] at the beginning of the 70's. It is a surface sensitive technique that uses field emission rather than a tunnelling current. The resolution was limited to 3 nm in the vertical and 400 nm in the horizontal direction due to the weak distance dependence of the field emission current. At the beginning of the 80's, Binnig et al. showed that vacuum tunnelling between two metallic electrodes with externally controllable tunnel distance is technically feasible.[3] From these observations they decided to develop the STM and use the exponential dependence of the tunnelling current to create a new tool to investigate metal surfaces. A few months later they published the first STM measurements performed on Au(110) and $CaIrSn_4$(110) surfaces where atomic steps are resolved.[1,4] Binnig et al. published in 1983 another article where they extend the previous observations to Si(111) and GaAs(111) surfaces.[5] Furthermore they reported the possibility to perform scanning tunnelling spectroscopy to determine work functions at the atomic scale. In 1986, they received the Nobel Price for the observation of the 7 x 7 reconstruction of Si(111) in real space.[6,7]

After the establishment of the theory by Thersoff and Hamann[8,9] and during the following years STM has been widely used in various environments (ambient conditions, liquid, ultrahigh vacuum) for the characterisation of metal surfaces at the atomic scale with different crystalline orientation such as Au(111)[10,11,12,13] for example and various semiconductor surfaces.[14,15] STM studies of surfaces have been extended to ultrathin oxide layers grown on metallic substrates.[16] In addition to the broad scope of applications of oxide layers in new technolo-

gies, these well-ordered surface can be used as a template for the growth of nanostructures.[17] Moreover, these surfaces can be useful for the investigation of the properties of adsorbed compounds in a weakly perturbed state due to the large gap of the oxide layer.[18,19]

STM can also be used to investigate various properties of organic or inorganic adsorbates deposited on the previously mentioned surfaces. In 1990 the possibility of single-atom manipulation was demonstrated by Eigler and Schweizer[20] by writing the "IBM" company logo with Xe atoms on a Ni(110) surface. In 1995 Meyer et al showed the possibility to manipulate CO molecules deposited on Cu(211).[21] More recently the possibility to induce chemical changes, such as tautomerisation[22,23] or dehydrogenation,[22,24,25,26] using inelastic electron tunnelling on isolated molecules adsorbed on surfaces has been investigated.

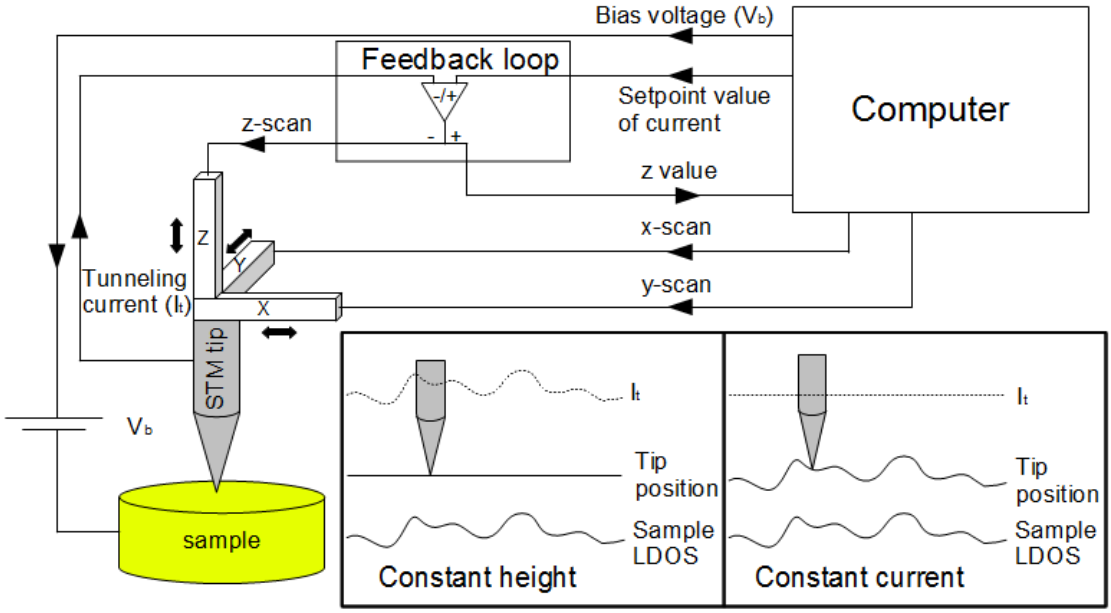

Figure 1.1.: Basic scheme for a STM operating in constant current mode. Piezos X and Y are used to move the tip in the surface plane, piezo Z is used to control the tip-sample distance. Insert: Illustration of the tunnelling current and the tip position measured in constant height or constant current mode.

The working principle of the STM is rather simple, as illustrated in figure 1.1. This is a basic scheme integrating the most important features of an STM working in constant current mode. A metallic atomically sharp tip, generally made of W or PtIr alloy, is mounted onto piezoelectric translators (X,Y,Z). Piezoelectric materials have the property to elongate or retract if they are subject to an electric potential. Piezos X and Y are used to move the tip over the surface plane (x, y) and the piezo Z is used to control the tip-surface distance z. The tip is brought very close the surface (3-5 Å) and a bias voltage V_b applied between the sample

and the tip allows electrons to tunnel from the sample to the tip or vice-versa, depending on the sign of the bias voltage applied to the sample. This leads to the emergence of a tunnelling current, generally in the range of a few pA to a few nA, depending on the tip-surface distance and the value of the applied bias voltage.

It is possible to perform two kinds of STM measurements: constant height measurements or constant current measurements. Principles are displayed schematically in bottom right corner of figure 1.1. The name generally used for constant height measurements can lead to confusion, because the distance between the surface and the tip is not constant due to the atomic corrugation. In fact the constant height is related to the tip position on the z axis which does not change during the scanning process, by opposition to the constant current mode. In the case of the constant height mode measurement, the result is a measurement of the tunnelling current as a function of the (x, y) position. This constant height mode has the advantage that pictures are obtained very quickly compared to measurements performed in constant current mode. On the other hand, the disadvantage is that the surface has to be flat at the atomic scale in order to not damage the STM tip. During this thesis, all measurements were performed in constant current mode. In this case it is the height displacement of the tip (along the z direction) which is measured. A value is fixed for the tunnelling current (generally in the pA range) and is maintained constant during the scanning process through the action of a feedback loop. After a measurement at the first point the tip is moved to the second point and the feedback loop adjusts the tip height in order to correspond to the current setpoint. This height is automatically adjusted by applying a voltage on the Z piezo until the current setpoint and the tunnelling current measured are equal. When this value is reached, the z position is recorded and the tip is moved to the next point. The exponential dependence of the tunnelling current on the sample-tip distance leads to a resolution of the order of the picometer in the vertical direction and the Angstrom in the horizontal direction, giving the possibility to image surfaces with atomic resolution.

In the case of the work realized in this thesis, the STM has been used essentially at liquid nitrogen (LN_2) temperature (77 K) to characterise the growth and self-assembling properties of physically adsorbed organic material on metal surfaces, from very low coverage up to the formation of several monolayers. Moreover, the influence of the substrate temperature, which is a critical parameter for the growth of ordered structures, has been investigated. Scanning tunnelling spectroscopy has been used to characterise electronic properties of adsorbed organic compounds. Finally we also look at the possibility to use the STM tip and the tunnelling electron to induce chemical modifications of single molecules embedded in a complete highly-ordered layer.

1.1.2. Theory of Scanning Tunneling Microscopy

1.1.2.1. Unidimensional potential step and barrier: a quantum mechanic point of view

In quantum mechanics a particle is described as a wave function. This will lead to different properties concerning the reflection and transmission of the particle compared to the classical case. In this part we will introduce the mathematical description of a quantum particle interacting with a potential step and a potential barrier.

1.1.2.2. Unidimensional potential step

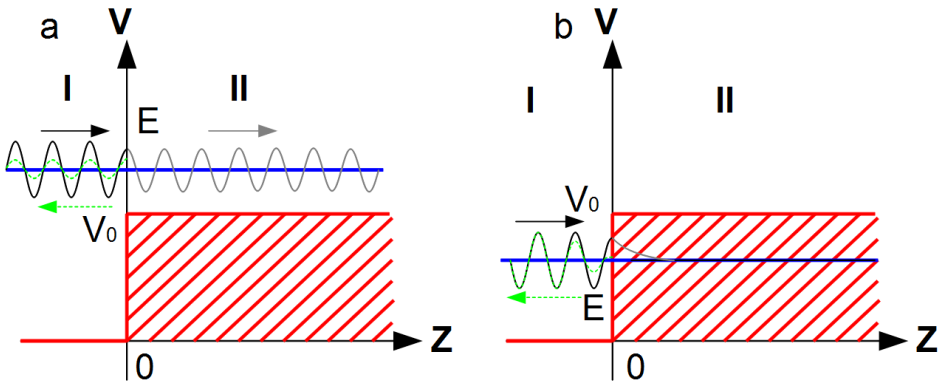

Figure 1.2.: Schematic representation of a potential step. Two cases are considered: a) Finite potential with V_0 < E. b) Finite potential with V_0 > E. Coloured arrows indicate the direction of propagation of the wave functions.

Considering a particle with an energy E described by a wave function Ψ, and a potential $V(z)$ independent of the time defined by:

$$V(z) = \begin{cases} 0 & \text{if } z < 0 \\ V_0 & \text{if } z \geq 0 \end{cases} \tag{1.1}$$

The unidimensional time independent Shrödinger equation for a wave function is given by:

$$H\Psi(z) = \left[-\frac{\hbar^2}{2m}\frac{d^2}{dz^2} + V(z) \right] \Psi(z) = E\Psi(z) \tag{1.2}$$

With H being the Hamiltonian of the system, $\hbar = \frac{h}{2\pi}$ the reduced Plank constant, m the mass of the particle, $V(z)$ the height of the potential step, E the energy of the particle, and $\Psi(z)$ the particle wave function.

Let's first consider the case where $E > V_0$, as depicted in figure 1.2.a. Using the general solution of the time independent Shrödinger equation, a superposition

of forward ($e^{ik_x z}$) and backward ($e^{-ik_x z}$) waves, the following equation system can be obtained:

$$\begin{cases} \Psi_I(z) = Ae^{ik_I z} + Be^{-ik_I z} \\ \Psi_{II}(z) = Ce^{ik_{II} z} + De^{-ik_{II} z} \end{cases} \tag{1.3}$$

k_I and k_{II} are the wave vectors in regions I and II respectively. Their values can be calculated using equation 1.2 and equation 1.3:

$$\begin{cases} k_I = \sqrt{\frac{2mE}{\hbar^2}} \\ k_{II} = \sqrt{\frac{2m(E-V_0)}{\hbar^2}} \end{cases} \tag{1.4}$$

We assume the particle comes from $-\infty$ and that it cannot be reflected at $+\infty$. Consequently D=0 and equation 1.3 can be rewritten:

$$\begin{cases} \Psi_I(z) = Ae^{ik_I z} + Be^{-ik_I z} \\ \Psi_{II}(z) = Ce^{ik_{II} z} \end{cases} \tag{1.5}$$

Moreover, Ψ_I, Ψ_{II} and their derivatives must be continuous at $z = 0$, consequently:

$$\begin{cases} \Psi_I(z=0) = \Psi_{II}(z=0) \Longrightarrow A + B = C \\ \frac{d\Psi_I(z=0)}{dz} = \frac{d\Psi_{II}(z=0)}{dz} \Longrightarrow ik_I A - ik_I B = ik_{II} C \end{cases} \tag{1.6}$$

From the previous equations, it is possible to estimate ratios B/A and C/A, calculate the reflection coefficient ($R = \frac{|B|^2}{|A|^2}$) and estimate the transmission coefficient (T) due to the fact that $R + T = 1$:

$$\begin{cases} \frac{B}{A} = \frac{k_I - k_{II}}{k_I + k_{II}} \\ \frac{C}{A} = \frac{2k_I}{k_I + k_{II}} \\ R = \frac{(k_I - k_{II})^2}{(k_I + k_{II})^2} \\ T = \frac{4k_I k_{II}}{(k_I + k_{II})^2} \end{cases} \tag{1.7}$$

These results concerning reflection and transmission coefficients are surprising compared to classical mechanics: when a classical particle has an energy $E > V_0$ the transmission coefficient is 1. In the case of quantum mechanics, the transmission coefficient is not 1 and a particle with an energy $E > V_0$ can be reflected depending on the value of the wave vectors (i.e. of the difference $E - V_0$) .

Let's now consider the case where $E < V_0$ (figure 1.2.b). In this case the general solutions of the Shrödinger equation are:

$$\begin{cases} \Psi_I(z) = Ae^{ik_I z} + Be^{-ik_I z} \\ \Psi_{II}(z) = Ce^{-k'_{II} z} \end{cases} \tag{1.8}$$

Values of wave vectors k_I and k'_{II} can be calculated using eq. 1.2 and eq. 1.8:

$$\begin{cases} k_I = \sqrt{\frac{2mE}{\hbar^2}} \\ k'_{II} = \sqrt{\frac{2m(V_0-E)}{\hbar^2}} \end{cases} \tag{1.9}$$

From the conditions of continuous functions and derivatives at $z = 0$, the following equation system can be obtained:

$$\begin{cases} \Psi_I(z=0) = \Psi_{II}(z=0) \Longrightarrow A + B = C \\ \frac{d\Psi_I(z=0)}{dz} = \frac{d\Psi_{II}(z=0)}{dz} \Longrightarrow ik_I A - ik_I B = k_{II} C \end{cases} \tag{1.10}$$

From these equations, it is possible to calculate ratios B/A and C/A and the reflection and transmission coefficients:

$$\begin{cases} \frac{B}{A} = \frac{k_I - ik_{II}}{k_I + ik_{II}} \\ \frac{C}{A} = \frac{2k_I}{k_I + ik_{II}} \\ R = \frac{|B|^2}{|A|^2} = 1 \\ T = 0 \end{cases} \tag{1.11}$$

In this case there the transmission is zero and the particle will be reflected. However, it is possible to find the particle inside the potential step, where it is classically forbidden. This can be demonstrated by calculation of the density probability as a function of the unit length:

$$|\Psi_{II}(z)|^2 = C^2 e^{-2\sqrt{\frac{2m(V_0-E)}{\hbar^2}}z} \tag{1.12}$$

This probability is non-zero and consequently the particle can be found in the region II. This equation also displays the exponential dependence of the presence probability with the distance z.

1.1.2.3. Unidimensional potential barrier: the tunnelling effect

The figure 1.3 schematically displays a particle of energy E passing through a potential barrier with a constant height V_0 and a width of z_0. In this case three regions (labelled I, II and III) are available for the particle. Assuming the particle comes from $-\infty$ and that it cannot be reflected at $+\infty$, this particle is described by the following wave functions which are solutions of the time independent Shrödinger equation (eq. 1.2)

$$\begin{cases} \Psi_I(z) = Ae^{ik_I z} + Be^{-ik_I z} \\ \Psi_{II}(z) = Ce^{ik_{II} z} + De^{-ik_{II} z} \\ \Psi_{III}(z) = Ee^{ik_{III} z} \end{cases} \tag{1.13}$$

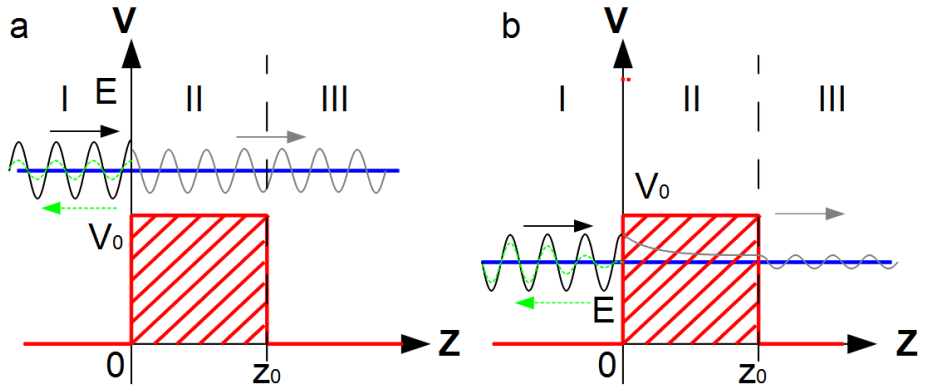

Figure 1.3.: Schematic representation of a potential barrier. Two cases are considered. a) Finite potential with V_0 < E. b) Finite potential with V_0 > E. Coloured arrows indicate the direction of propagation of the wave functions.

From these equations it is possible to calculate wave vectors for each region using the time independent Shrödinger equation (eq.1.2). Two cases are observed depending on the energy of the particle: In the first case (figure 1.3.a), $E > V_0$, values for wave vectors are:

$$\begin{cases} k_I = \sqrt{\frac{2mE}{\hbar^2}} \\ k_{II} = \sqrt{\frac{2m(E-V_0)}{\hbar^2}} \\ k_{III} = \sqrt{\frac{2mE}{\hbar^2}} = k_I \end{cases} \tag{1.14}$$

After the determination of the different constants B, C, D, and E as a function of A, by using the conditions of continuous functions and derivatives at the boundaries ($z = 0$ and $z = z_0$), reflection ($R = |B|^2/|A|^2$), and transmission coefficients ($T = |E|^2|A|^2$) can be calculated:

$$\begin{cases} R = \frac{|B|^2}{|A|^2} = \frac{(k_I^2-k_{II}^2)^2 sin^2(k_{II}z_0)}{4k_I^2k_{II}^2+(k_I^2-k_{II}^2)^2 sin^2(k_{II}z_0)} \\ T = \frac{4k_I^2k_{II}^2}{4k_I^2k_{II}^2+(k_I^2-k_{II}^2)^2 sin^2(k_{II}z_0)} \end{cases} \tag{1.15}$$

Once again it appears that in quantum mechanics a particle with an energy higher than the potential barrier height has a non-zero probability to be reflected, by opposition to the classical case.

Now if we consider the energy of the particle lower than the potential barrier height ($E < V_0$), wave functions solutions of the Shrödinger equation for

different regions are:

$$\begin{cases} \Psi_I(z) = Ae^{ik_I z} + Be^{-ik_I z} \\ \Psi_{II}(z) = Ce^{-k'_{II} z} + De^{k'_{II} z} \\ \Psi_{III}(z) = Ee^{ik_I z} \end{cases} \tag{1.16}$$

and the associated wave vectors are:

$$\begin{cases} k_I = \sqrt{\frac{2mE}{\hbar^2}} \\ k'_{II} = \sqrt{\frac{2m(V_0 - E)}{\hbar^2}} \\ k_{III} = \sqrt{\frac{2mE}{\hbar^2}} = k_I \end{cases} \tag{1.17}$$

Once again by using the conditions at the boundary it is possible to calculate reflection ($R = |B|^2/|A|^2$) and transmission ($T = |E|^2/|A|^2$) coefficients:

$$\begin{cases} R = \frac{(k_I^2 + k'^2_{II}) sinh(k'_{II} z_0)}{(k_I + k'_{II}) sinh^2(k'_{II} z_0) + 4k_I^2 k'^2_{II}} \\ \\ T = \frac{4k_I^2 k'^2_{II}}{(k_I + k'_{II}) sinh^2(k'_{II} z_0) + 4k_I^2 k'^2_{II}} \end{cases} \tag{1.18}$$

Unlike classical expectation, a particle with a total energy lower than the potential barrier height has a non-zero probability of tunnelling through this barrier. This is the principle used in scanning tunnelling microscopy.

1.1.2.4. Tunnelling effect: influence of the bias voltage

The tunnelling effect is the property for a quantum particle to cross a potential barrier even if its energy is lower than the energy required to overcome this barrier. In classical physics the particle can cross the potential barrier if its energy is higher than the energy of the potential barrier. In the other case the particle cannot cross the barrier, because the position inside the barrier is forbidden. It is different from the quantum point of view where the particle is described as a wave function $\psi(z)$. If we consider an electron with an energy E and a mass m_e moving through a barrier of constant height U, the wave function inside the barrier can be written:

$$\psi(z) = \psi(0) e^{-\frac{\sqrt{2m_e(U-E)}}{\hbar} z}$$

This equation displays the fact that the wave function is non-zero inside the barrier. Consequently the particle has a non-zero probability to cross the potential barrier and this probability can be written as follows:

$$P = |\psi(0)|^2 e^{-2\frac{\sqrt{2m_e(U-E)}}{\hbar} z}$$

This equation clearly displays the exponential dependence of the transmission probability as a function of the potential barrier width. In our case the particle is an electron and the potential barrier is the vacuum. If we now consider two electrodes (which are the tip and the sample in the case of STM) close enough to allow the overlap of the wave function, Fermi levels of both electrodes will be aligned if no potential is applied. The work function, W, is a property of the surface material depending on the nature of the metal, but also of the crystalline orientation of the surface and the presence of contamination. The work function is defined by the difference $W = -e\phi - E_F$, where $-e$ is the charge of an electron, ϕ is the electric potential in the vacuum nearby the surface, and E_F is the Fermi level (electrochemical potential of electrons) inside the material. In this configuration, with an alignment of the Fermi levels of both metal, it is not possible to generate a tunnelling current between the electrodes without applying a bias voltage between the electrodes. In the figure 1.4 a representation of the influence of the bias voltage on the Fermi level alignment in shown.

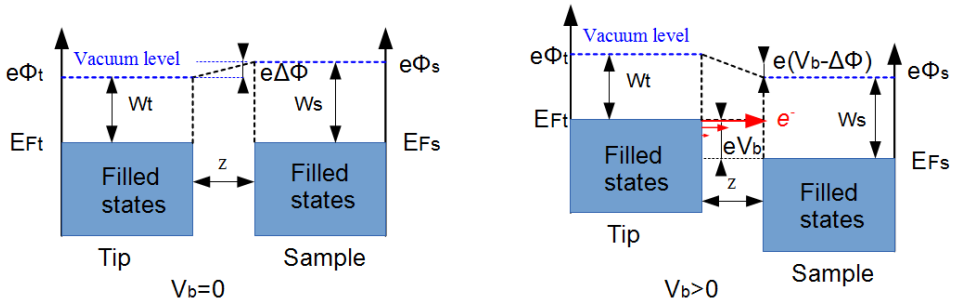

Figure 1.4.: Influence of the bias voltage on the Fermi level alignment. Right: U_b=O, Fermi levels of tip and sample are aligned. Left: U_b=V>0 is applied to the sample, Fermi levels are switched by an energy eV_b.

If a positive bias voltage is applied to the sample, Fermi levels will be shifted by en energy eV_b and the electron from the filled states of the tip can tunnel into the empty states of the sample. Electrons that tunnel from the tip to the substrate are mainly electrons from the Fermi level, with an energy eV_b, as underlined by the red arrows in figure 1.4. We will return to this point in the section concerning the scanning tunnelling spectroscopy technique. Inversely, applying a negative bias voltage to the sample will shift the Fermi levels of the metals by an energy $-eV_b$ and lead to a tunnelling current from the filled states of the surface to the empty states of the tip.

1.1.2.5. Scanning tunnelling microscopy: Tersoff and Hamann theory

Shortly after the development of the STM by Binnig and Rohrer, Tersoff and Hamann developed the theory of scanning tunnelling microscopy.[8] A theory is

presented for vacuum tunnelling between a real surface and a model probe with a locally spherical tip. The tunnelling current is found to be proportional to the local density of state (LDOS) of the surface at the position of the tip and the effective lateral resolution is related to the tip radius R and the vacuum gap distance d approximately as $[(2\kappa^{-1})(R+d)]^{1/2}$. The starting point of the theory is the tunnelling current given at the first order in Bardeen's formalism[27] by:

$$I_t = \frac{2\pi e}{\hbar} \sum_{\mu,\nu} f(E_\mu)[1 - f(E_\nu + eV)]|M_{\mu\nu}|^2 \delta(E_\mu - E_\nu)$$

Where $f(E)$ is the Fermi function, e is the charge of one electron, V is the applied voltage bias, $|M_{\mu,\nu}|$ is the tunnelling matrix between the states ψ_μ of the probe and ψ_ν of the surface, and E_μ is the energy of the state ψ_μ in the absence of tunnelling. Using the limit of small voltage and low temperature, the tunnelling current can be rewritten:

$$I_t = \frac{2\pi}{\hbar} e^2 V \sum_{\mu,\nu} |M_{\mu\nu}|^2 \delta(E_\nu - E_F)\delta(E_\mu - E_F)$$

Where E_F is the Fermi level. If we consider the limit where the tip is replaced by a point probe (leading to the maximum possible resolution) and if the tip wave functions are arbitrarily localized, the matrix elements are simply proportional to the amplitude of ψ_ν at the position $\vec{r_0}$ of the probe. The previous expression can then be reduced to

$$I_t \propto \sum_{\nu} |\psi_\nu(\vec{r_0})|^2 \delta(E_\nu - E_F)$$

The quantity on the right-hand side is the surface LDOS at E_F, i.e., the charge density from the states at E_F. Thus the tunnelling current is proportional to the LDOS at the position of the point probe and the scanning tunnelling microscope image represents a contour map of constant surface LDOS.

In order to resolve exactly the tunnelling current, it is mandatory to evaluate $M_{\mu\nu}$. Tersoff and Hamann showed that it is possible to calculate $M_{\mu\nu}$ starting from Bardeen's[27] expression and using a general expression for surface wave functions in the region of negligible potential:

$$M_{\mu\nu} = \frac{\hbar^2}{2m} \int d\vec{S} \cdot (\psi_\mu^* \vec{\nabla} \psi_\nu - \psi_\nu \vec{\nabla} \psi_\mu^*)$$

The wave function of the tip, due to the unknown geometry of the tip, is modelled as a locally spherical potential with a center located at $\vec{r_0}$ and a local radius of curvature R, as illustrated in the figure 1.5.

This leads to the following expression for the tunnelling current:

$$I_t = 32\pi^3\hbar^{-1}e^2V\varphi^2D_t(E_F)R^2k^{-4}e^{2kR}\sum_{\nu}|\psi_\nu(\vec{r}_0)|^2\delta(E_\nu - E_F)$$

Where D_t is the density of state per unit volume of the probe tip.

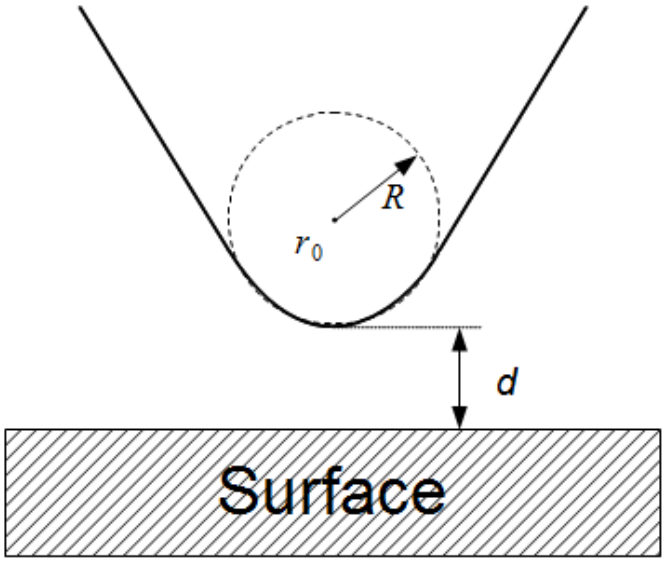

Figure 1.5.: Model used to approximate the wave function in Tersoff Hamann theory. The center of the tip is localized at r_0 with an assumed spherical geometry. R is the radius of curvature and d the distance between sample and tip.

Tersoff and Hamann also showed that the effective lateral resolution is related to the tip radius R and the vacuum gap distance d as $[2\kappa^{-1}(R+d)]^{1/2}$. If $R >> d$ the resolution is determined by the tip radius but remains inferior to R due to the prefactor $2\kappa^{-1}$. For $R << d$ (case of the ideal tip terminated by a single atom) the resolution is limited by d and by the smallest tunnelling resistance (current) that can be experimentally detected.

This theory has been applied in the case of the Au(110) surface[8,9] and is in very good agreement with the experimental STM measurements performed by Binnig et al. on this surface.[1,5] Furthermore they also consider tunnelling to a semiconductor surface, and apply the theory to GaAs(110) surface.[9] In this case valence and conduction band have very different charge distributions and the LDOS measured (STM image) will not reflect the topography of the substrate, by opposition to the LDOS measured in the case of Au(110). This has been demonstrated for the first time on this surface in 1987 by Feenstra et al.[14]

1.1.2.6. Scanning tunnelling spectroscopy

Scanning tunnelling spectroscopy (STS) is used to obtain information concerning the electronic structure of the sample at the position of the tip. The tip is positioned at the desired place and the feedback loop is deactivated to keep the sample-tip distance constant. A bias voltage range is ramped stepwise from one setpoint value to another one (generally few volts in the positive and negative range). The averaging time within one step influences the resolution of the spectra. The most basic scanning tunnelling spectroscopic measurement consists of the local measurement of the tunnelling current as a function of the bias voltage: $I_t(V_b)$.

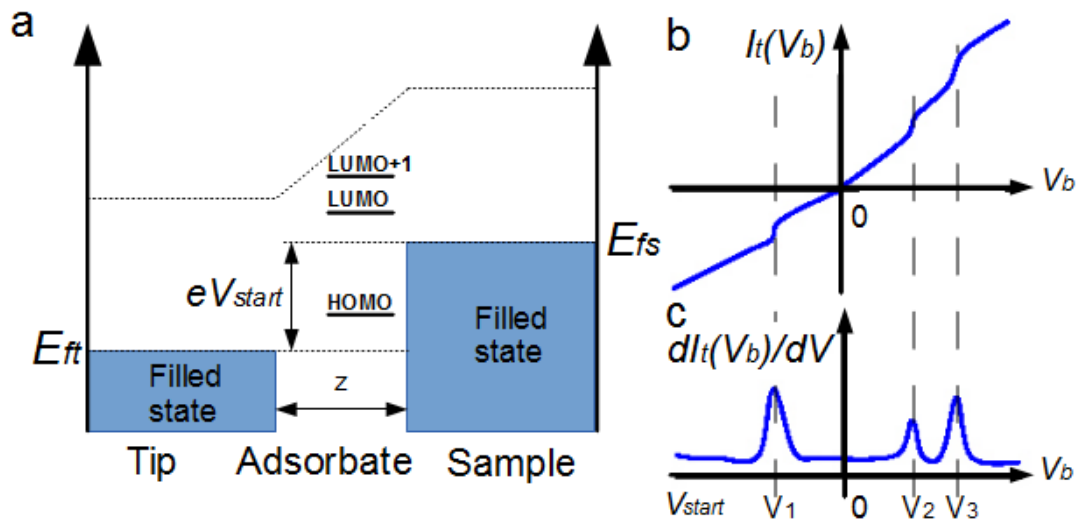

Figure 1.6.: a) Schematic representation of energy levels of a compound adsorbed on a metallic surface. A bias voltage is applied between the tip an the sample. b) Typical $I_t(V_b)$ measurement. c) Calculated differential conductivity: $dI_t(V_b)/dV$. The observed peaks correspond to the discrete energy levels of the adsorbate.

The figure 1.6 illustrates the STS principle. We consider that a compound with discrete energy levels (indicated as HOMO for highest occupied molecular orbital, LUMO for lowest unoccupied molecular orbital and LUMO+1) is adsorbed on a metallic surface (for more clarity, tip and sample density of states and work functions are considered constant in this example). At the bias voltage V_{start}<0, electrons from the filled states of the surface can tunnel to the empty states of the tip. As mentioned before most parts of these tunnelling electron arrive from the Fermi level of the sample and have an energy of eV_{start}. In the range V_{start}-V_1, the $I_t(V_b)$ curve varies linearly with the bias voltage (due to the considered constant density of states of the tip and the surface).

At $V_b = V_1$, the maximum energy of the tunnelling electron is eV_1 which is the energy level of the HOMO. Consequently at $V_b > V_1$ (V_b and V_1 are negatives) this tunnelling channel cannot be used anymore, because the electron energy is too low. This leads to an important decrease of the tunnelling current, as shown in the figure 1.6.b.

In the range V_1-0V, no discrete adsorbate energy levels are available for electron injection, but electrons at the Fermi level can tunnel from the filled state of the sample to the empty state of the tip. Consequently the tunnelling current will increase linearly, as in the range V_{start}/V_1. At V_b=0, filled states of both sample and tip are aligned and consequently the tunnelling current is zero. The behaviour is similar in the range V_b>0: the tunnelling current increases linearly with the bias voltage until the energy of the tunnelling electron is equal to eV_2 (resp. eV_3), where the tunnelling electron at the Fermi level of the tip can tunnel into the LUMO (resp. LUMO+1) of the adsorbate, leading to a more important increase of tunnelling current at this value. The $dI_t(V_b)/dV$ curve (differential conductivity), which corresponds to the LDOS of the sample, can be obtained from the $I_t(V_b)$ curve by numerical differentiation (see figure 1.6.c). From this differential conductivity we can obtain information concerning the HOMO-LUMO gap in the case of semiconductor or other information concerning, for example, surface states in the case of metal.

A second scanning tunnelling spectroscopy technique consists of the direct measurement of the differential conductivity. This technique involves the use of a lock-in amplifier in order to modulated the voltage bias with a high frequency (1kHz) and record directly the $d(I_t(V_b))/dV$ variation. This method leads to a better resolution and a better signal to noise ratio compared to the calculation from the $I_t(V_b)$. A small modulation at high frequency ($V_0 \sin(\omega t)$) is applied to the bias voltage leading to a sinusoidal response of the tunnelling current. Moreover, the amplitude of the modulated tunnelling current is sensitive to the slope of the curve at each point. Figure 1.7 shows a schematic representation of how the convolution of the applied sinusoidal signal and the tunnelling current can be used to detect the changes in the $I_t(V_b)$ characteristics.

To illustrate this principle we start from a simplified expression for the tunnelling current:

$$I_t(V_b + V_0 sin(\omega t)) \propto \int_0^{eV_b + eV_0 sin(\omega t)} \rho_s(E) dE.$$

Due to the small amplitude of the modulation ($V_b >> V_0$), the tunnelling current can be expended as a Taylor serie as such:

$$I_t(V_b + V_0 sin(\omega t)) \propto I_t(V_b) + \rho_s(eV_b) eV_0 sin(\omega t) + \frac{1}{2} \frac{d\rho_s(eV_b)}{dV} e^2 V_0^2 sin^2(\omega t) + ...$$

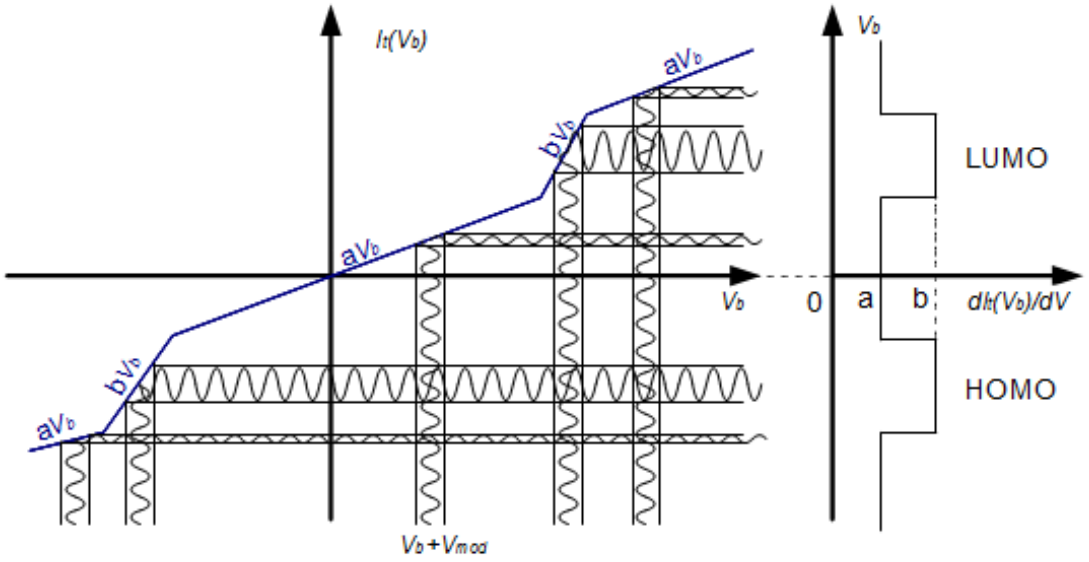

Figure 1.7.: Schematic representation of the influence of the of variation of the tunnelling current on the amplitude of the modulated signal.

It appears clearly that the first harmonic is proportional to $dI_t(V_b)/dV$ and the second harmonic to $d^2I_t(V_b)/dV^2$. These harmonic frequencies can be extracted by the means of a lock-in amplifier and allows a direct measurement of the LDOS. From a practical point of view, the measured tunnelling current is noised due to mechanical vibrations of the system and intrinsic sources. This signal is amplified then multiplied by a reference signal with the same frequency as the modulation (ω) and with a known phase shift. At the output, only one of the component depends on the phase difference between the noise and reference signal and this component is proportional to the first harmonic. Comparing phases of both signals, the lock-in extracts this component which contains noise essentially of high frequencies. Finally a low pass filter allows to remove an important part of this noise. The signal to noise ratio is directly dependant on the integration time of the lock-in amplifier: higher the acquisition time of a spectrum better the signal to noise ratio.

1.1.3. Overview of the experimental setup

The aim of this subsection is to give an overview of the experimental setup. All STM experiments presented in this thesis were performed under ultrahigh vacuum (UHV) conditions using a commercial low-temperature STM (Omicron). The experimental setup (see figure 1.8) is composed of a preparation chamber, an analysis chamber and a transfer chamber, allowing the introduction of new

Figure 1.8.: Photography of the STM lab.

tips or samples in the preparation chamber without breaking the UHV conditions in the chamber. A transfer rod is used to move new tips and samples from the transfer chamber to the preparation chamber where these tips and samples can be fixed onto a manipulator. This manipulator is used to move the sample from the preparation chamber to the analysis chamber which is equipped with several instruments that will be detailed later in this subsection. Inside the analysis chamber, tips and samples are transferred by the means of a wobble stick into the microscope, or are placed on a carousel for storage.

1.1.3.1. The preparation chamber

The preparation chamber is maintained at a pressure of 10^{-10} mbar in order to avoid any contamination of the substrate. This vacuum is ensured by an ion pump, and can be boosted by the use of a titanium sublimator. It is also equipped with a mass spectrometer, a LEED, a sputter gun, four gas lines (Ar, CO, H, N) equipped with leak valves, and a commercial organic material effusion cell (Kentax, TCE-BSC). The advantage of this type of evaporation cell is that it provides an excellent reproducibility in terms of evaporation temperatures and thus fluxes of evaporated materials. This largely facilitates the repetitive preparation of equivalent layers. Moreover, this evaporation source contains three individual evaporation cells allowing to store several compounds, but also allows a simultaneous deposition of two or three compounds. This chamber is used for the sample preparation (surface cleaning and molecular deposition) and also for the LEED experiments.

1.1.3.2. The manipulator

The manipulator, used to move the sample between the preparation chamber and the analysis chamber, is equipped with an electron beam sample heater and can be cooled down by liquid nitrogen (Omicron sample heater and cooling upgrade). It allows to move the sample inside the preparation chamber to perform the surface preparation and the LEED measurement. The cooling system allows to cool down the sample to a temperature of 130 K during the preparation process to deposit compounds on a cold surface. The highest obtainable temperature by heating the sample is 1300 K. Temperature is monitored by the means of a thermocouple in contact with the molybdenum plate on witch the crystal is fixed.

1.1.3.3. The analysis chamber

The analysis chamber is isolated from the preparation chamber by a gate-valve. The pressure in this chamber is maintained in the range of 10^{-11} mbar by the use of an ion pump and a titanium sublimator. This chamber includes a cryostat allowing to cool down the sample and the STM tip at the liquid nitrogen temperature or even at liquid helium temperature. The outer cryostat is cooled with liquid nitrogen and the inner cryostat can be cooled with liquid nitrogen or liquid helium, resulting in tip/sample temperatures of 77 K or 4 K, respectively. The analysis chamber is also equipped with a carousel allowing the storage of tips and samples. A wobble stick is used to move samples and tips between the manipulator, the carousel, and the microscope. A CCD camera is located in front of one of the windows allowing a more precise view of the STM for the manual approach of the tip over the sample.

1.1.3.4. Tip preparation

Metallic tips used for STM experiments are prepared by electrochemical etching.[28,29] A schematic representation is shown in figure 1.9.

A tungsten wire of 100 μm is fixed on the tip holder and cut to a length of 4 mm. This wire is then placed in a solution of NaOH (5 mol/L) with the axis normal to the solution surface plane, in order to obtain a tip of 1.5 mm length. A dc voltage is applied between the tungsten wire and a metallic electrode placed in the solution to perform the electrochemical etching. The chemical reaction is the following:

$$W(s) + 2OH^- + 2H_2O \longrightarrow WO_4^{2-} + 3H_2(g)$$

The chemical etching is particularly strong at the meniscus formed at the interface metal-solution-air especially due to convection movements in this region.

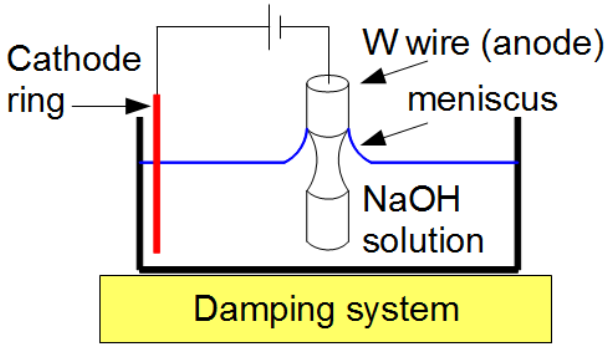

Figure 1.9.: Scheme of preparation device for STM tips.

After a few minutes, the immersed part drops of. At his point the voltage is automatically stopped to avoid further etching. The tip is then carefully cleaned in ethanol and distilled water. The shape of the tip and the apex are controlled using a binocular microscope (a more precise control has occasionally been performed using scanning electron microscopy). Before being used to perform STM measurements, the tip has to be cleaned under UHV conditions by field effect emission to remove oxide layers from the tip apex.

1.1.3.5. Surface preparation

Before each STM experiment the sample is prepared in several steps. Generally two cycles of ion sputtering / annealing are performed before the molecular deposition. The following paragraphs detail these steps which take place in the preparation chamber (the sample is localized on the manipulator).

Ion sputtering: This step is necessary to clean the substrate from impurities localized on the surface and the remaining compounds of previous experiments. In order to carry out the sputtering process, the sample is moved under the sputter gun, and a partial pressure of 1.10^{-6} mbar of argon is introduced in the preparation chamber. Electrons are emitted from a tungsten wire by thermionic emission and are accelerated and focused to ionize the Ar gas inside the gun. The emission current used during the sputtering process is 12 mA. Argon ions are then accelerated to the surface with an energy of 1.5 keV. The resulting sputter current on the sample is in the μA range.

The duration of the ion sputtering process can vary depending on the material and the cleanliness of the surface, but is generally close to 30 min. After that, impurities of the surface have been removed but the surface show a strong roughness. The next step is to smoothen this crystalline surface.

Annealing: The annealing step consists in heating the crystal to increase the mobility of surface atoms and induce a smoothening of the surface and the formation of large terraces atomically flat. To perform this step, we use an electron beam sample heater powered by a power supply which operates in the following way: to reach the desired temperature, a high voltage (U_s=650 V) is applied between the sample and the filament of the e-beam heater. The filament emits electrons via thermionic emission which are accelerated toward the backside of the molybdenum plate, on which the crystal is fixed (see the scheme of figure 1.10.a).

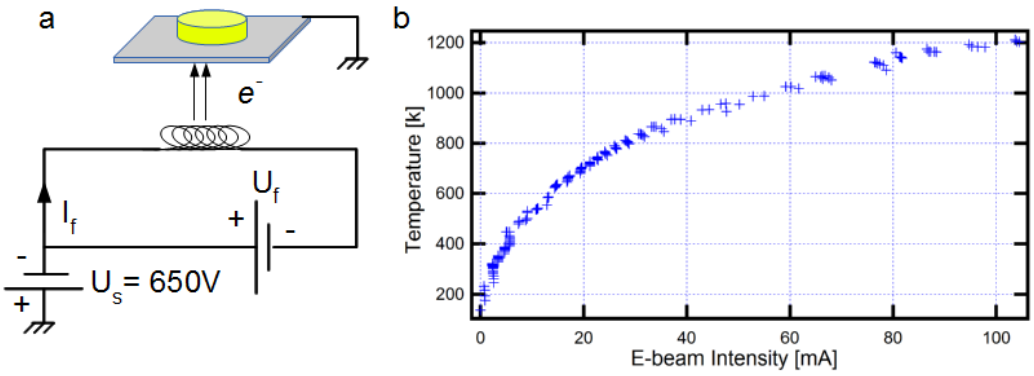

Figure 1.10.: a) Simplified scheme of the E-Beam heater. b) Calibration curve: temperature as a function of the e-beam intensity.

The e-beam intensity has been measured as a function of the power applied to the filament, and the surface temperature as a function of the e-beam intensity. The temperature has been characterised with the cooling system turned on. The temperature is measured by a thermocouple in contact with the molybdenum plate. This calibration curve is depicted in figure 1.10.b. The temperature evolves as a function of the e-beam intensity following a power law:

$$T = 232 I_E^{0.3627} \Longleftrightarrow I_E = \left(\frac{T}{232}\right)^{2.757}$$

From this calibration curve, it is easy to obtain the desired substrate temperature. The annealing temperature is a very important parameter: different annealing temperatures can lead to different kind of reconstruction or to the segregation of impurities to the surface. The duration of the annealing process is generally 20 min, but can be longer in case of a longer sputtering process. After this annealing step, the surface is clean and shows large atomically flat areas on which it is possible to deposit compounds and carry out STM investigations.

Molecular deposition: The sample is moved in front of the evaporation cell at a distance of 200 mm. The crystal surface plane is oriented perpendicularly to the axis of the evaporation in order to obtain a uniform deposition. The crystal temperature is set to the desired value thanks to the heating or cooling system. During the molecular deposition, we use substrate temperatures in the range from 170 K to room temperature (RT), in order to investigate the influence of these temperatures on the growth process. The molecules which are in the form of a powder, are placed in a quartz crucible surrounded by a tungsten filament. Prior to deposition, the evaporation cell is flashed at 10 K higher than the desired evaporation temperature of the compounds during 1 min to remove volatile impurities. Then the temperature is reduced to the desired value for evaporation. The deposition duration depends on the coverage we are interested in and can vary from one minute to more than one hour. As soon as the deposition process is finished, the sample is introduced in the analysis chamber. It is then necessary to wait a few hours for the thermalization of the sample in the STM in order to avoid thermal drift effects during STM imaging.

1.2. Surface Cavity Ring-Down Spectroscopy

The aim of this section is to introduce the technique of cavity ring-down spectroscopy, present the theory, give an overview of the experimental setup, and finally, introduce the data treatment process. This technique is also known as cavity ring-down laser absorption spectroscopy (CRLAS).

1.2.1. Introduction

Cavity ring-down (CRD) spectroscopy is a very sensitive direct absorption technique in which the rate of absorption rather than the magnitude of the absorption of a light pulse confined in an optical cavity is measured.[30] A CRD measurement consists in recording the decay time as a function of the laser wavelength to acquire an absorption spectrum. The principle of this technique is to trap a light pulse inside a closed optical cavity constituted of two highly reflective mirrors. At each reflection of the light pulse on the highly reflective mirror a very small portion of the light (of the order of 0.005%, depending of the mirror reflectivity to the corresponding wavelength) leaks out of the cavity and is detected by a photomultiplier tube. The very high sensitivity of the CRD spectroscopy is caused by the extremely long path length (up to several kilometers) of the light inside the cavity and to the fact that the sample is probed thousands of times. Furthermore, with this spectroscopic technique, the absorption is determined using the time behaviour of the signal and consequently is independent of the laser power fluctuations. The first CRDs experiment were published in 1988 by O'Keefe and Deacon.[31] They demonstrated the sensitivity of this technique by measuring several bands of the very weak forbidden b Σ^{-}_{g} - X Σ^{-}_{g} transition in gaseous molecular oxygen. Since then, it has been shown that CRD spectroscopy is a powerful technique used for the characterisation of various species (molecules, metal clusters...) in gas-phase,[32,33] in liquid phase,[34,35,36] or for materials deposited on solid substrate such as C60,[37] oxazine and malachite green dyes,[38] di- and trichloroethylene,[39] rhodamine 110,[40], and gold[41,42] and silver[43] clusters.

In the later case, when CRD is applied to a solid sample, the technique is known as surface cavity ring-down spectroscopy (s-CRDS). The introduction of a solid sample will consequently increase the optical losses due to reflection and scattering which will lead to a decrease of the sensitivity compared to gas phase measurements. For s-CRD performed in transmission mode, the sample is placed inside the cavity and the light passes through the sample. In order to reduce the optical losses induced by reflection, two configurations can be used and are schematically shown in figure 1.11.

- The sample can be placed with its plane perpendicular to the axis of propagation of the light pulse. This configuration allows that the reflected light remains on the optical axis of the cavity.

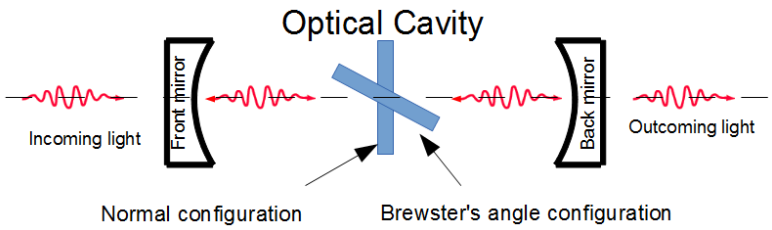

Figure 1.11.: Cavity ring-down spectroscopy in transmission mode: two configurations for the substrate can be used: Brewster's angle configuration or normal configuration. The optical axis is indicated by the black dashed line.

- The sample can be placed at the Brewster's angle to the optical axis. It is known that in this Brewster's angle configuration, the reflection of p-polarized light does not take place which will lead to a decrease in optical losses. The Brewster's angle can be determined using Snell's law:

$$\theta_B = tan^{-1}\left(\frac{n_2}{n_1}\right)$$

With θ_B being the Brewster's angle and n_1 and n_2 being the refractive index of the vacuum and the substrate respectively. It is this configuration that has been used for measurements performed in this thesis.

Moreover the substrate has to fulfil some important conditions in order to reduce the optical losses. First of all it has to be transparent in the wavelength range investigated. Secondly both faces constituting the sample have to be highly plane parallel. This is a condition to maintain the reflected light in the optical cavity in the case of measurement performed at normal incidence angle. This is also a condition for not having a partial reflection of the light at one of the interfaces in the case of measurements performed at Brewster's angle. However this dependence concerning the parallelism of the two surfaces is less critical in the case of Brewster's angle configuration than in the case of the normal configuration.

Moreover, as it has already been mentioned, the surface has to be of high optical quality which means that the roughness has to be as low as possible to avoid scattered light.

Another important condition for Brewster's angle configuration is that the substrate material should not possess birefringence in order to not rotate the polarisation of the light. This would lead to a partial reflection of the light out of the cavity by the substrate during the next passages. In this case, only materials showing a cubic structure (isotrope) or an amorphous structure (no long term crystalline order) may be employed.

1.2.2. Theory of cavity ring-down spectroscopy

The principle of CRD spectroscopy is very simple and consists, as mentioned above, in the measurement of the portion of light leaking out of an optical cavity, constituted of two highly reflective mirrors. This is illustrated in figure 1.12 for an empty cavity.

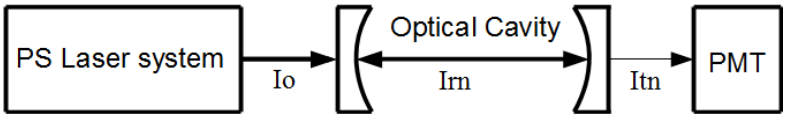

Figure 1.12.: Cavity ring-down spectroscopy principle: a light pulse is trapped in an optical cavity constituted of two highly reflective mirrors. The light leaving the cavity is detected by a photomultiplier.

Considering an initial light pulse with an intensity I_0 before entering in the optical cavity. The intensity of the beam inside the cavity, I_{rn}, depends on the mirrors reflectivity (R, considered identical for both mirrors) and on the number n of round-trips of the pulse inside the cavity. The intensity of the transmitted beam (I_{tn}) also depends on the number of round-trips and the reflectivity of the mirror. Before the first round-trip (n=0), if we consider a reflectivity R for both mirrors, the intensities can be written as:

$$I_{r0} = I_0(1-R)$$

$$I_{t0} = I_0(1-R)^2$$

After the first round-trip (n=1) the intensities can be expressed as:

$$I_{r1} = I_0(1-R)R^2$$

$$I_{t1} = I_0(1-R)^2R^2$$

And more generally, after n round-trips:

$$I_{rn} = I_0(1-R)R^{2n}$$

$$I_{tn} = I_0(1-R)^2R^{2n} = I_0(1-R)^2e^{2nln(R)}$$

The time necessary for one round-trip (t_{rt}) directly depends on the length of the cavity (d) as:

$$t_{rt} = \frac{2d}{c}$$

With c the speed of light, and the number of round-trips (n) can be simply ex-

pressed as a function of time:

$$n = \frac{t}{t_{rt}}$$

In the figure 1.13.a is shown a simple scheme displaying the exponential decay of the light intensity leaving the cavity as a function of the number of round-trips. Using the previous relations, it is possible to give a general expression for

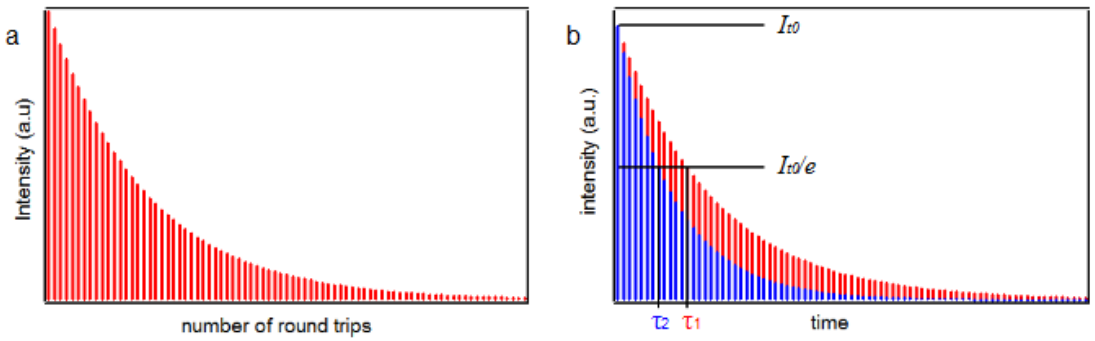

Figure 1.13.: a) Exponential decay of the light intensity leaving the optical cavity as a function of the number of round-trips. b) Evolution of the ring-down time before (red) and after (blue) an increase of the optical losses.

the intensity of the transmitted beam as a function of the time and the cavity length:

$$I_{tn}(t) = I_0(1-R)^2 e^{\frac{ct}{d}ln(R)}$$

The ring-down time, τ, is defined as the time necessary to reduce the initial intensity of the transmitted pulse by a factor of e:

$$I_{tn}(t=\tau) = \frac{I_{t0}}{e}$$

$$=> \tau = -\frac{d}{cln(R)} = \frac{d}{c(1-R)}$$

This ring-down time is the characteristic that we measure during a s-CRD experiment. The optical loss (L) is defined as the normalized intensity difference during a time δt, and it can be expressed as follows:

$$L(\delta t) = \frac{I_{tn}(t) - I_{tn}(t+\delta t)}{I_{tn}(t)}$$

It is necessary to point out that the optical loss does not evolve linearly with the time. In the case of the empty cavity, the intensity remains constant between two reflections and decreases due the non perfect reflection of the mirrors. Consequently, if we consider $\delta t = d/c$, the time between two reflection processes, the

optical loss can be expressed as:

$$L(\delta t = d/c) = 1 - e^{lnR} = 1 - R$$

Consequently the ring-down time τ can be expressed as a function of the optical loss and inversely:

$$\tau = \frac{d}{cL} \Leftrightarrow L = \frac{d}{c\tau}$$

In the case of the empty cavity as mentioned above, the losses are due only to the mirror characteristics. If a sample is introduced inside the cavity, the optical losses will increase due to the scattering and the absorption of the sample. The light intensity will decrease faster than in the case of the empty cavity and consequently, that will lead to a decrease of the ring-down time:

$$L_{total} = L_{cav} + L_{sub} \rightarrow \tau_{total} = \frac{d}{c(L_{cav} + L_{sub})}$$

The figure 1.13.b shows the influence of an increase in the total optical losses on the ring-down time. The optical losses due to the substrate can be calculated from the previous relation:

$$L_{sub} = \frac{d}{c}(\frac{1}{\tau_{total}} - \frac{1}{\tau_{sub}})$$

with τ_{sub} being the ring-down time determined in the case of the empty cavity and τ_{total} being the ring-down time determined for the system substrate+cavity. Using the same method, it is possible to calculate losses induced by adsorbates (metallic clusters, organic compounds...) deposited on the substrate.

1.2.3. Experimental setup

The laser system (EKSPLA) delivers pulses of p-polarized light at a frequency of 20 Hz and a pulse duration of 30 ps. A grey filter is used to reduce the intensity of light pulses in order to not saturate the photomultiplier tube. Several mirrors are used to adjust the beam height and bring the light pulses in the analysis chamber where different optical cavities can be built without breaking the vacuum of the chamber. The light pulses enter and leave the analysis chamber through two CaF_2 windows. All measurements are performed at Brewster's angle configuration in order to reduce the optical losses induced by reflection. Finally, the light pulses are guided toward a lens and focus on the photomultiplier tube (Hamamatsu H7732–10) connected to an oscilloscope (Lecroy Waverunner 6051). An overview of the experimental setup is depicted in figure 1.14.

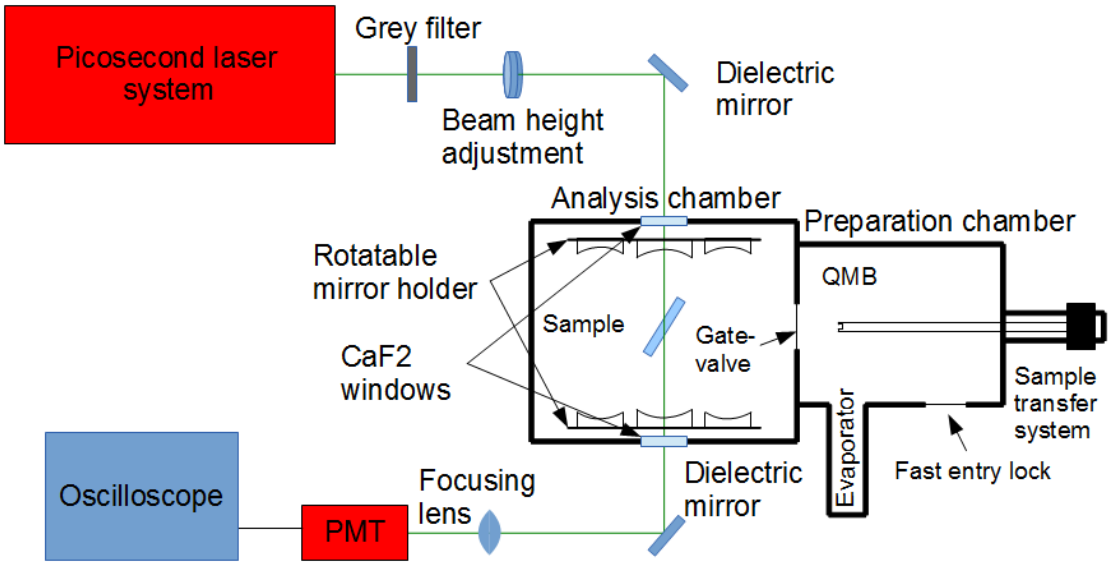

Figure 1.14.: Overview of the experimental setup used for surface cavity ring-down spectroscopy.

1.2.3.1. Preparation chamber

The preparation chamber is constituted of a fast entry lock, a sample transfer system, an evaporator with three evaporation cells, and a quartz micro-balance. The base pressure of the chamber is in the low 10^{-8} mbar. The fast entry lock allows the insertion of a new sample for each experiment without breaking the vacuum inside the analysis chamber. Prior to insertion, the sample is carefully cleaned with spectroscopic grade acetone. The molecular deposition is performed in this chamber after a sputtering process which takes place inside the analysis chamber. Organic compounds are evaporated from a boron-nitrate crucible heated by a tungsten wire surrounding the crucible. A quartz micro-balance allows to determine the molecular density deposited on the substrate using the Sauerbrey equation:

$$\Delta f = -\frac{2f_0^2}{A\sqrt{\rho_q \mu_q}}\Delta m$$

with Δf being the frequency change (Hz), f_0 the resonant frequency (Hz), A the piezoelectrical active crystal area (cm^2), ρ_q the density of quartz ($g.cm^{-3}$), μ_q the shear modulus of quartz ($g.cm^{-1}.s^{-2}$), and Δm the mass change (g). The frequency change is recorded before and after the deposition to ensure that the deposition rate is constant. During the deposition on the substrate, the quartz micro-balance is removed and the sample is placed at the same position in order to have a similar molecular flux deposited on the surface and on the quartz of the micro-balance. This explain the constant resonant frequency observed in

the center of the figure 1.15. On each side, the slope of the line is determined by a linear fit as shown in the same figure. From the value of the fit and the duration of deposition it is possible to calculate the mass variation Δm. Finally, it is possible to relate the mass variation to the molecular density deposited using the mass of a single molecule.

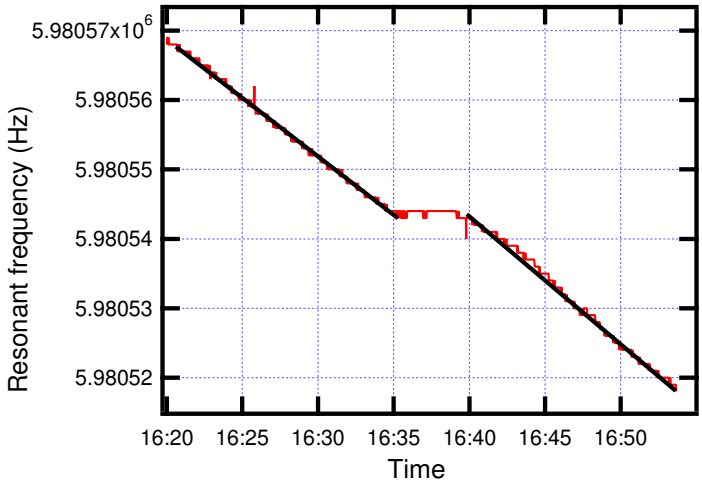

Figure 1.15.: Typical measurement recorded by QMB: the slope of the curve is linear and constant before and after the deposition and allows the determination of the molecular density deposited on the substrate.

1.2.3.2. Analysis chamber

The analysis chamber is constituted of a cryogenic manipulator, a sputter gun, gas lines (Ar^+, O_2...), and two rotatable mirror holders. The base pressure is in the low 10^{-10} mbar range. The manipulator allows us to move the sample in the three directions and adjust the angle of the sample for the various operations taking place in the analysis chamber (transfer, sputtering, measurement...). A cooling system allows us to cool down the substrate to 120 K and a heating system can be used to control the temperature of the substrate in the range of 120 K - RT or above. The temperature is measured by the means of a thermocouple in contact with the substrate. A sputter gun is used to clean the glass substrate by Ar^+ sputtering before the deposition and measurements. The two rotatable mirror holders have been specifically developed[44,45] in order to investigate the optical properties of adsorbates under ultrahigh vacuum conditions by surface cavity ring-down spectroscopy. One of the main issues was related to the fact that highly reflective mirrors are operational only on a small wavelength range (few tens of nanometres). The investigation over the entire visible (and infrared)

range can only be performed using different mirror pairs. These different cavities have to be built inside the analysis chamber without breaking the vacuum to avoid the sample contamination. Using rotatable mirror holders, it is possible to insert ten different sets of highly reflective mirrors (pairs of two) and consequently use ten different cavities to cover the desired range. During this thesis, we used five different mirror sets to cover the visible range. The wavelength ranges in which these mirror sets (named as a function of the highly reflective wavelength) can be used are summarized in table 1.1.

Mirror	430 nm	500 nm	532 nm	610 nm	680 nm
Highly reflective range	420-480	460-550	510-590	570-680	640-770

Table 1.1.: Highly reflective mirrors characteristics used during this thesis.

Note that an overlapping region of several tens of nanometres is present in successive mirror sets allowing for a comparison of the data measured by different cavities in the same range. Moreover, measurements at the edge of the mirror sets ranges are less accurate due to the lower reflectivity of mirrors at these wavelengths. This effect is clearly displayed in measurements presented in figure 1.16.a and 1.16.b where optical losses increase abruptly at the edges of the different wavelength ranges covered by these mirrors.

Due to the fact that the reflectivity of the mirrors depends on the wavelength, the intensity of the light leaking out of the optical cavity will also strongly depend on the wavelength. Consequently the sensitivity of the photomultiplier has to be adjusted in order to avoid saturation and achieve a maximum resolution for each wavelength. This is done by adjusting the voltage applied to the detector, which has been determined prior to experiments for each wavelength and each set of mirrors. Data acquisition and scanning of the laser are fully automated by a LabVIEW program. A final data treatment takes place using a custom procedure in IgorPro. For a better signal to noise ratio, 100 ring-down times are recorded and averaged for each wavelength.

1.2.3.3. Data treatment process

The CRD data obtained have to be corrected in order to obtain the information concerning the surface or the compounds adsorbed on the surface. In the first place, CRD spectra are recorded for each set of highly reflective mirrors for the empty cavity, as shown in figure 1.16.a. In this case, five spectra have been recorded for five sets of mirrors, allowing investigations over the complete visible range. The lack of data in the wavelength range from 680 to 740 nm is due to

fact that the laser cannot be used in this range because of the signal-idler cross-over of the used OPG laser system. We can see in the figure 1.16.a that all mirror sets show the same behaviour: losses are very low (generally in the range 150-500 ppm, depending on the quality of the mirror set) over a range of 50 nm and increase abruptly at each edge of the range.

The spectra shown in the figure 1.16.b have been measured after the insertion of the bare, acetone cleaned, and Ar^+ sputtered BK7 sample inside the optical cavity. The measured losses are the combination of the losses previously measured for the empty cavity and the losses newly induced by the substrate. In order to obtain the information concerning the absorption resulting only from the substrate, we subtract the losses of the empty cavity (due only to the non-perfect reflectivity of the mirrors) from the losses measured for the substrate and cavity.

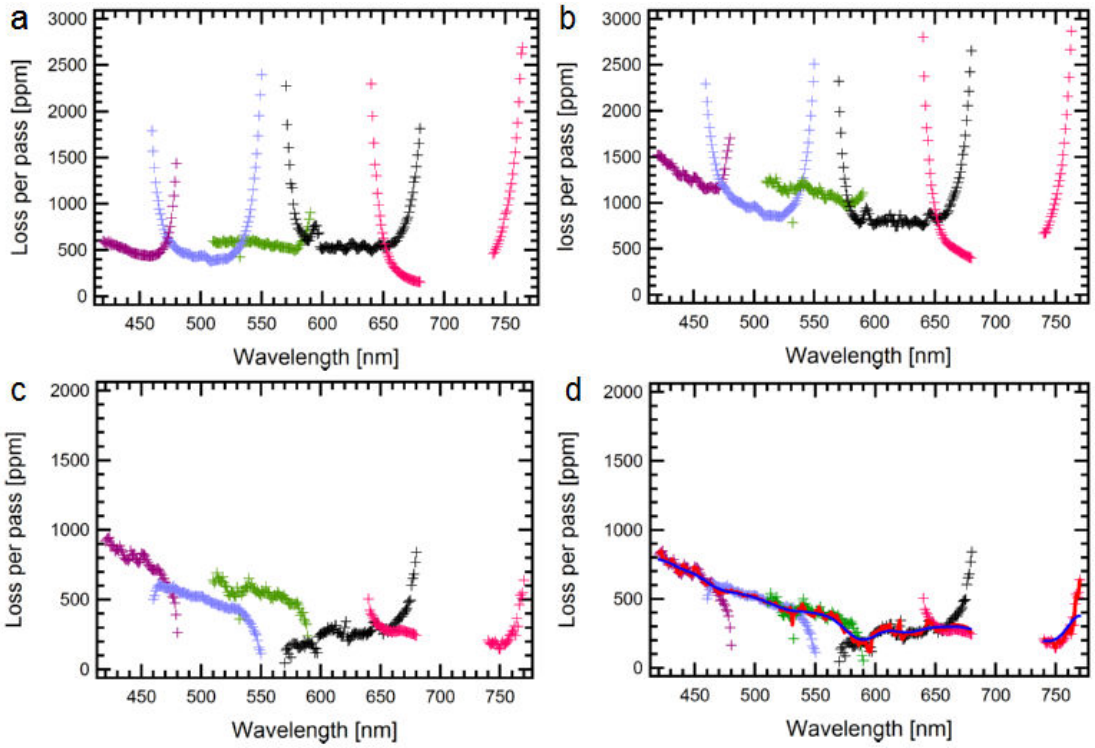

Figure 1.16.: CRDS spectra recorded for: a) Empty cavities, b) Cavities and glass substrate, c) Determination of the losses due to the substrate. d) Adjustment and fitting.

The resulting spectra are shown in figure 1.16.c. We can observe that the losses due to the substrate are in the range 200-900 ppm. Losses are more pronounced for shorter wavelengths in agreement with the strong wavelength dependence of the Rayleigh scattering (λ^{-4}). However, this spectrum remains

noisy, especially at the edges of the wavelength ranges covered by the mirrors. This can be attributed to the combination of a "low" value of the reflectivity of the mirrors at these wavelengths and to slightly different alignments of the cavity between both measurements recorded in the case of a and b. Moreover, after a closer analysis of spectra recorded in the range 510-590 nm (green spectra), we observed a relatively strong increase in the losses recorded by this set of mirrors compared to the losses recorded by other sets of mirrors. This can also be attributed to a slight misalignment of the cavity. It can be arbitrarily corrected to homogenize the losses recorded by adjacent sets of mirrors.

This is shown in figure 1.16.d, where the green spectrum (510-590 nm) has been shifted by -150 ppm, and the purple spectrum (420-480 nm) by -80 ppm. The next step is to precisely determinate the losses at the overlapping regions. This has been done using the following formula:

$$L_i = L_{ia}\frac{n+1-i}{n+1} + L_{ib}\frac{i}{n+1}$$

With L_i the calculated loss, L_{ia} (resp. L_{ib}) the loss measured at the overlap by the mirror covering the higher energy range (resp. the lower energy range), n the total number of points in the overlap, and i, ia and ib stand for the point number (ranging from 1 to n).

During the s-CRD experiments performed in this thesis, we did generally not record spectra for the empty cavities because it is not necessary for the data treatment. However, we have to record spectra for the system glass + cavity for each experiment before depositing organic compounds. After the molecular deposition, the spectra are recorded over the visible range and can be corrected for the losses due to the substrate and the cavities using the same principle described before. These data treatments have been used for s-CRD results presented in the following parts.

1.3. The organic compounds

1.3.1. 5,14-Dihydro-5.7.12.14-tetraazapentacene

The chemical structure of 5,14-Dihydro-5,7,12,14-tetraazapentacene (DHTAP, $C_{18}N_4H_{12}$) is displayed in figure 1.17. This compound has been synthesized in the CINaM[46,47] in the department of "Ingénierie Moléculaire et Matériaux Fonctionnels" (IMMF).

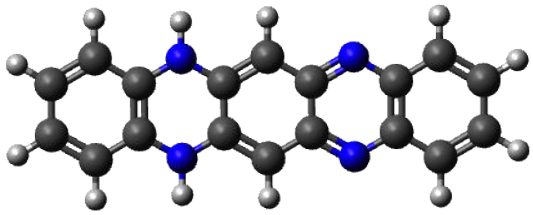

Figure 1.17.: Chemical structure of 5,14-Dihydro-5,7,12,14-tetraazapentacene. Note the symmetry breaking due to the presence of hydrogen on nitrogen 5 and 14.

The molecular backbone, very similar to pentacene, contains 4 nitrogen atoms in positions 5, 7, 12 and 14. Two of these nitrogens (5 and 14) are bonded to hydrogen atoms. This induces a break in the symmetry of the molecule along the small molecular axis, compared to pentacene. However, the symmetry remains along the long axis of the molecular backbone. This is an important point and we will return to it in the following chapters. Moreover, it has been shown that the incorporation of nitrogen atoms in heteroacenes leads to the modification of the electronic structure and molecular packing.[48,49,50,51]

Another difference to pentacene is that this molecule is not fully conjugated due to the N-H groups. One of the most interesting properties of DHTAP is the possibility to establish H-bonds with neighbouring DHTAP molecules. This is possible due to the presence of two N-H groups which are potentially donors of hydrogen bonds, and two N=C moieties potentially acceptors of hydrogen bonds. The fact that DHTAP molecules may form H-bond with neighbouring molecules could be used during the growth process to lead to the formation of well-ordered thin film stabilized by intermolecular interactions.

Another interesting property due to the incorporation of nitrogen in molecular backbone is the high stability under ambient conditions in devices.[52,53] The mobilities, on/off ratios and threshold voltages of amorphous organic thin film transistors based on tetraazapentaenes has been investigated by Ma et al.[50] in air. A charge carrier mobility of 1x10^{-2} cm^2 V^{-1} s^{-1} has been achieved in the case of the 5,14-DHTAP, erroneously reported as 5,12-DHTAP.[46] This relatively low value for the mobility can be attributed to the amorphous structure of the film.

Indeed, previous works clearly indicate that semiconductor thin films maximize their electrical conductivity when π-orbital are accessible for charge injection and hopping between neighbouring molecules by orbital overlap. This unique characteristic is partially lost in amorphous or polycrystalline films, in which molecular disorder effectively reduces the mobility of the charge carriers.

Improving carriers mobility in organic films is thus intimately related to molecular orientation and long-range order in the films.[54] These properties make DHTAP a very promising candidate for applications in the field of organic electronics if well-ordered thin films could be produced.

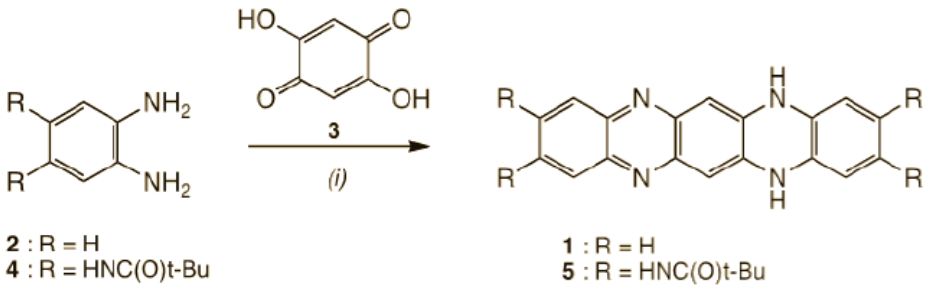

Figure 1.18.: Synthesis of DHTAPs: *(i)* $PhCO_2H$, 300° C, 2 min.

Synthesis The synthesis of DHTAPs is generally accomplished by the condensation of o-phenylenediamines and 2,5-dihydroxybenzoquinone in presence of different Bronsted acids[50,46] except for Miao et al.[49] who described a solvent and acid-free preparation. However, all these syntheses require long reaction times (several hours) at high temperatures, which limits the ability to introduce sensitive groups. The group of O. Siri has been able to considerably accelerate the synthesis by using benzoic acid as catalyst in a solvent-free reaction because this solid acid allows for higher temperature conditions (up to 300° C) and therefore activation of the reaction, which is completed in only 2 min.[47] Thus, the condensation of 2 and 3 in presence of excess $PhCO_2H$ at 300° C (heated with a heat gun) gives 1 that could be easily isolated by filtration with 80% yield (1.18). Interestingly, this extremely short time reaction allowed for the use of diaminobenzene precursor bearing amide functions (4)[55] that could react similarly with 3 affording 5 in 60% yield. The current protocol appeared to be unsuccessful in the absence of benzoic acid.

1.3.2. 1,4-Di-n-octyloxy-2,5-bis(pyren-1-ylethenyl)benzene

The chemical structure of 1,4-di-n-octylony-2,5-bis(pyren-1-ylethenyl)benzene (bis-pyrene, $C_{58}O_2H_{58}$) is depicted in figure 1.19. The molecular backbone is

constituted of two pyrene moieties connected to a central phenyl ring by a trans ethylenic bond. The all trans-configuration has been confirmed by H-NMR. In addition to this π-conjugated system, two octyloxy chains are connected to the central phenyl ring. Incorporation of pyrene into conjugated oligomers results in highly conjugated structures with unique photophysical properties.[56,57]

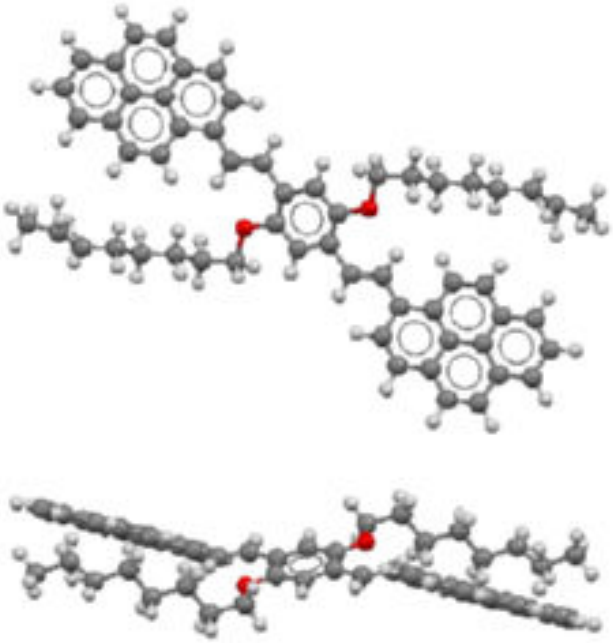

Figure 1.19.: Schematic representation of the bulk structure of the bis-pyrene molecule. The structure was deduced from X-ray diffraction measurements.

Moreover, pyrene and its derivatives are prone to experience π-staking in solid state and solution[58,59] which is a critical parameter for efficient charge hopping within the solid state material. Investigations on the optical and semiconducting properties of vacuum evaporated thin film of two pyrene-modified oligothiophenes[60] have shown strikingly low hole mobility compared to the distyryl analogues under identical conditions.[61] It was observed that bispyrene-terminated bithiophene compounds form highly disordered crystalline thin films, which could account for the low field effect mobility. Moreover, by analogy with the trans-1-styrylnaphtalene,[62] bis-pyrenyl compounds were believed to have a less planar geometry than their distyryl analogues, which could also hamper efficient π-stacking in the solid state. The oligo-phenylene-vinylene bridge, used as a central aromatic bridge, was introduced as a spacer unit between the pyrene moieties in order to provide efficient intramolecular electronic delocalisation along the conjugated backbone, better than in the case of oligo-phenylene-

ethynylene.[63] Furthermore, the 2,5-disubstituted-1,4-phenylene unit can be substituted with a large variety of functional groups in order to further endow these systems with improved solubility[64] or directed self-assembling properties.[65]

The crystalline structure of such compounds clearly shows that the most favorable length of the octyloxy chain is the half-length of the π-conjugated system. Longer chains (e.g. $C_{16}H_{33}$) induce disorder in the solid and thus monocrystals cannot be isolated. In the solid state, the dihedral angle between the two planes formed by pyrenes and the central phenyl ring is 175.4°, that is, both units are close to planarity, in agreement with the calculated angle in the case of the pyrene-oligo(phenylene vinylene)-2,2-bipyridine.[63] Introduction of phenylene ethynylene[56] spacer unit leads to a more pronounced dihedral angle compare to the phenylene-vinylene analogue. These results motivated us to investigate thin films of the symmetric compound 1,4-di-n-octyloxy-2,5-bis(pyren-1-ylethenyl)benzene, that contains the vinylene-phenylene group bridging two pyrene rings, which possesses a large π-conjugated system, an electronic gap of 2.9 eV and which is a p-semiconductor in thin film.

Synthesis The bis-pyrenyl compound bis-pyrene was synthesized in the group of F. Fagès in a one step Witting reaction. To a suspension of the bis(triphenylphosphonium) derivative of 1,4-bis(bromomethyl)2,5-bis(n-octyloxy)benzene16 (1.00 g, 1 mmol) in freshly distilled THF (20 m), 95% NaH (0.10 g, 4 mmol) was added portionwise at room temperature. A solution of the commercially available pyrene-1-carbaldehyde (0.46 g, 2 mmol) in THF (10 mL) was added. The reaction mixture was heated overnight at 30° C, then cooled down to room temperature prior to solvent evaporation. The residue was dissolved in dichloromethane. The organic layer was washed with water and then dried over Na_2SO_4. The solvent was removed under vacuum and the crude product was subjected to column chromatography (silica gel) eluting with dichloromethane then crystallized from a mixture of dichloromethane-methanol. Compound bis-pyrene was obtained (0.47 g, 60% yield) as an orange solide. The all trans-configuration was confirmed by ^{1}H NMR

1.4. The surfaces

Most part of the STM experiments in this thesis have been performed on gold. Gold is an interesting material to study molecular compounds because it possesses a well-known surface, which is chemically inert, allowing to study compounds in a weakly perturbed state. Furthermore in the case of potential applications in the field of organic electronics, electrodes are often made of gold. A deep understanding of the interaction between the molecules and the surface is thus very important. Consequently we decided to use a gold surface and also study the influence of the crystalline structure of the surface, using two different orientations: Au(111) and Au(110). We also had the occasion to investigate the growth properties on Ag(110). Concerning the characterisation of the optical properties, the most interesting substrate is a thin amorphous glass plate (BK7, VWR International) that we used to perform s-CRDS measurement. The aim of this section is to describe these different surfaces.

1.4.1. Au(111)

Most part of STM experiments have been performed on a gold monocrystal oriented (111) purchased from Mateck. This surface presents a particular reconstruction of its surface first atomic layer known as the herringbone reconstruction. Typical STM images are depicted in figure 1.20.

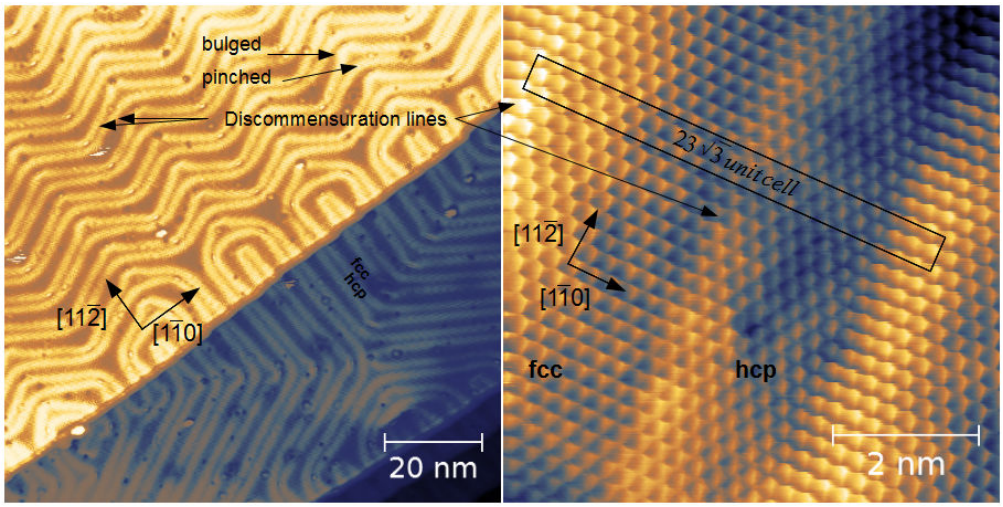

Figure 1.20.: STM picture of Au(111) surface. a) 100 nm x 100 nm; U_b=1 V; I_t=50 pA. Herringbone structure of Au(111). b) 6.7 nm x 6.7 nm; U_b=60 mV; I_t=1 nA. Atomic resolution of Au(111) surface and the $23x\sqrt{3}$ unit cell are shown.

The large scale image in figure 1.20.a displays two highly-oriented monoatomic

steps running in the $[1\bar{1}0]$ direction and the typical herringbone structure of the reconstructed Au(111) surface. These highly-oriented steps, running in the $[1\bar{1}0]$ direction, can be used to determine the crystallographic orientation of the crystal even if no atomic resolution is obtained. The reconstruction of the Au(111) surface is due to the fact that the atomic density of the first layer is more important than the atomic density of the bulk. This higher atomic density of the first atomic layer leads to a more compact layer with reduced interatomic distance. In the case of Au(111), the observation of 23 gold surface atoms on 22 bulk lattice sites leads to a compression of 4.55% in the $[1\bar{1}0]$ direction. The interatomic distance in the bulk is 2.88 Å, consequently the interatomic distance of the atoms constituting the first layer is 2.75 Å. Furthermore, this mismatch leads to stacking faults between atoms of the first and second layer of Au(111). It is known that the bulk structure is face-centered cubic (fcc), but due to the compression the surface shows an alternance of fcc and hexagonal closed-packed (hcp) domains, depending on the kind of stacking (ABA or ABC) of the atom of the first layer. These fcc and hcp domains are separated by discommensuration lines which show an apparent height of 20 pm and appear brighter in the STM image 1.20.a. These discommensuration lines reflect the three-fold symmetry of the Au(111) and show rotation angles of 120°. We can also observe that the width of fcc and hcp domains, measured along the $[1\bar{1}0]$ direction and delimited by the discommensuration lines, are different: fcc domains are larger than hcp domains. These observations can be confirmed in the STM image obtained with atomic resolution and are depicted in figure 1.20.b. The $23\text{x}\sqrt{3}$ unit cell of Au(111) is also shown in this figure.

1.4.2. Au(110)

In order to study the influence of the crystallographic orientation of the surface on the molecular growth, we decided to perform complementary measurements on Au(110). Schematic pictures displaying the different reconstructions of this surface are shown in figure 1.21.a, .b, .c, and a STM image of the (1x2) reconstruction is shown in 1.21.d. In the figure 1.21.a we can observe the schematic structure of the unreconstructed (1x1) surface. The interatomic distance are 2.88 Å and 4.08 Å along $[1\bar{1}0]$ and $[001]$ respectively. This surface is generally not stable and reconstructs during preparation to form the (1x2) structure[66] displayed in figure 1.21.b. In this case every second gold row running along the $[1\bar{1}0]$ direction is missing. Consequently the interatomic distance in the first layer along the $[001]$ direction is now 8.16 Å, but the distance along $[1\bar{1}0]$ remains 2.88 Å.

Under particular preparation conditions (or due to the presence of impurities) another reconstructed surface can be observed and is schematically displayed in figure 1.21.c. This structure is a (1x3) reconstruction.[67] By analogy with the previous structure, this one is constituted of missing rows, with two rows missing

on three, compared to the unreconstructed structure. Consequently, the distance along $[001]$ between two atomic rows running along $[1\bar{1}0]$ is now 12.24 Å. The interatomic distance along $[1\bar{1}0]$ remains the same as in the case of the unreconstructed and the (1x2) structure: 2.88 Å. The STM image depicted in figure 1.21.d shows the (1x2) reconstruction structure with resolution on atomic rows. Unfortunately, the resolution is not good enough to distinguish individual gold atoms constituting these rows. However, it appears clearly from this STM images that the monoatomic steps are rough perpendicular to the $[1\bar{1}0]$ direction.

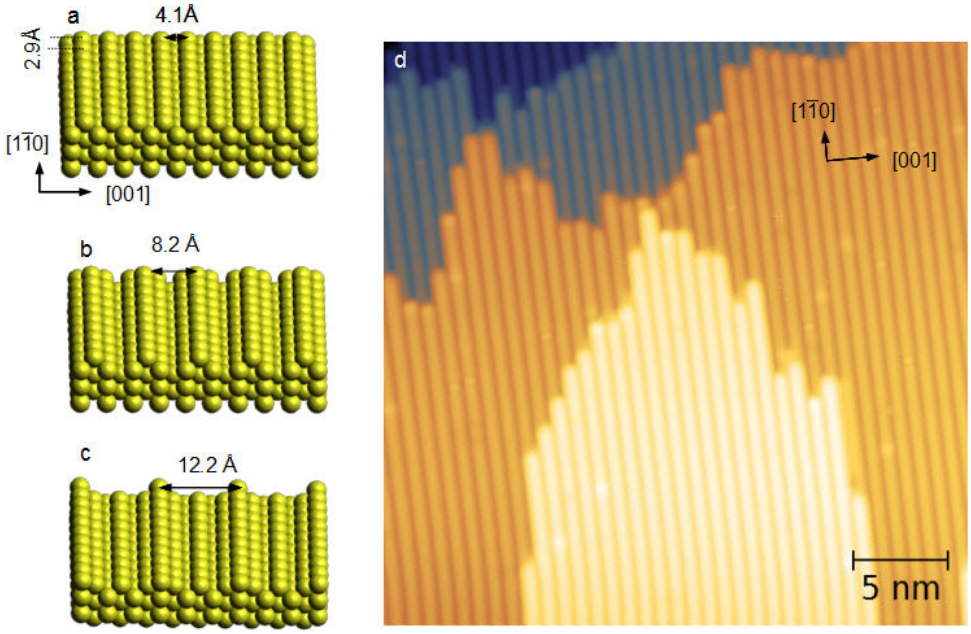

Figure 1.21.: Schematic representation of the different reconstructions of Au(110). a) Unreconstructed surface: (1x1); b) (1x2) reconstruction; c) (1x3) reconstruction. Crystallographic orientation and interatomic distances are indicated. d) Typical STM picture of bare Au(110) showing the (1x2) reconstruction. I_t=10 pA; U_b=0.05 V.

1.4.3. Ag(110)

The third substrate we used for the STM investigation is an Ag(110) surface. In figure 1.22 a schematic representation of the unreconstructed Ag(110) surface and a STM image obtained with atomic resolution are shown :

Contrary to Au(110) the unreconstructed surface is stable, and the (1x1) surface layer shows close-packed rows formed by surface atoms aligned along the $[1\bar{1}0]$ direction. On this surface, as in the case of Au(110), a reduced number of

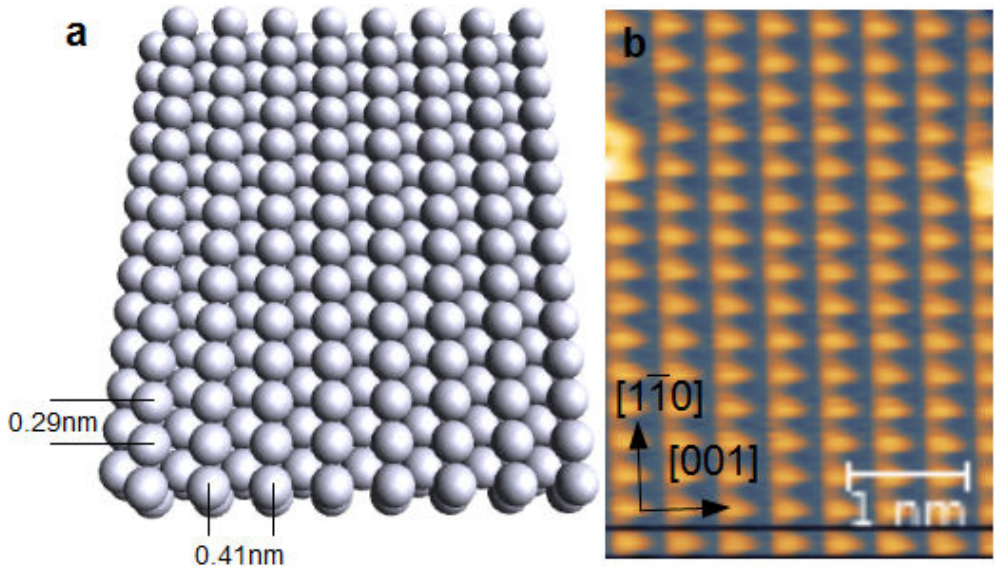

Figure 1.22.: Schematic representation of the unreconstructed Ag(110) surface. b) STM image (I_t=50 nA; U_b=1 V) of Ag(110) with atomic resolution.

molecular domain orientations should be observed compared to the (111) surface, due to the anisotropy of the (110) surface.[68] The interatomic distances are 2.89 Å and 4.09 Å along the $[1\bar{1}0]$ direction and $[001]$ respectively.

1.4.4. Borosilicate glass

In order to study the optical properties of the above-mentioned compounds by s-CRD we needed a suitable substrate to deposit the material. The sensitivity of the technique depends directly on the overall photon loss, which has to be as low as possible. A substrate with very low optical losses has to be chosen and particular conditions concerning the geometry have to be fulfilled. In previous work it has been found that the most suitable substrate for s-CRDS[69] is the BK7 amorphous borosilicate glass substrate.

The most important point, which is obvious because we are working in transmission mode, is to use a substrate transparent in the wavelength range investigated. In the case of BK7, the transparent range is 360-1700 nm and allows the characterisation over the entire visible range and the near infrared. The transparency windows for other substrates appear to be wider, but in the case of an amorphous glass substrate for example, the optical losses are about 500 ppm higher.

Moreover, CRS is a very sensitive technique allowing the detection of trace of materials. Potential substrates for s-CRS as yttria stabilized zirconia were investigated and trace of impurities of Nd were observed, leading to the appearance

of peaks in the optical spectrum, and an important increase of the optical losses. The effect of Ar^+ sputtering has also been investigated and it appears that this process can remove impurities or deposited material causing very low damage to the surface[69] (very little increase of the optical losses after sputtering).

The bulk structure of the sample is also an important parameter and has to be amorphous or possess a cubic structure to avoid birefringence, which would lead to an increase of the optical losses due to the rotation of the light polarization. Another point to take into account is that mechanical stress can lead to birefringence, consequently the substrate has to be fixed as gently as possible.

The roughness of the surface has also been investigated[70] and is an important point because it leads to scattering and consequently and increase of the optical losses. AFM measurements performed under ambient conditions on BK7 showed that the surface is smooth, which is the reason for the small scattering losses observed for this substrate. A RMS roughness of 0.56 nm has been found in the litterature.[71]

Finally, this substrate presents also interesting properties to be used for a nonlinear spectroscopic technique integrated into the system: the surface second harmonic generation (s-SHG) spectroscopy. For s-SHG spectroscopy the most important point is to use a substrate with centrosymmetric crystalline structure, which will not lead to the generation of second harmonic from the bulk. In the case of BK7, the structure is amorphous and the averaged randomly distributed contributions of each unit to the electric potential leads to a centrosymmetric potential. Unfortunately, technical issues encountered during this thesis prevented us from obtaining conclusive results with this technique.

2. Characterisation of DHTAP

2.1. Growth of DHTAP on noble metal surfaces: nucleation and initial steps of growth

In the framework of this thesis, most of the STM experiments have been performed at LN_2 temperature (both sample and tip). The temperature of the substrate during the deposition process has been controlled as explained in the previous chapter. It is known from literature[72] that the two main factors which control the growth process are the temperature of the substrate and the molecular flux.

In our case, the molecular flux is determined by the distance between the evaporation cell and the sample, and the temperature applied to evaporate the compound. We have always used identical conditions concerning the sample position and the temperature of evaporation leading to an identical flux for all deposition.

The remaining variable is the temperature of the substrate during the deposition. Its influence, which plays a very important role during all the steps of the growth process, will be investigated on three different surfaces: Au(111), Au(110) and Ag(110).

2.1.1. DHTAP/Au(111)

Prior to the study of the initial steps of the growth process, the formation of the first molecular structures, and the influence of the temperature during deposition, we would like to describe the procedure we used to determine the deposition rate.

Each deposition was performed with the same conditions of temperature and sample-evaporation cell distance in order to have a constant flux for each deposition process. Then, we determined the molecular densities for different deposition times by counting the number of molecules on a well defined area, until the formation of complete monolayer (ML).

The graph depicted in figure 2.1 shows the variation of the molecular density as a function of the deposition time. A linear fit, shown in red in the graph, allows us to determine a deposition rate of 4.14 ± 0.32 molecules per 100 nm^2 per minute. Using this deposition rate it was possible to reproducibly prepare molecular layers of predefined molecular density.

The molecular density of the complete monolayer has been determined from the unit cell parameters of the well-ordered first monolayer (111 molecules per 100 nm^2, see section 2.3.1). The combination of these information (measured

molecular density, deposition time and molecular density of the monolayer) allows us to determine a deposition rate in equivalents of monolayer with a resulting value of 0.037±0.003 ML/min.

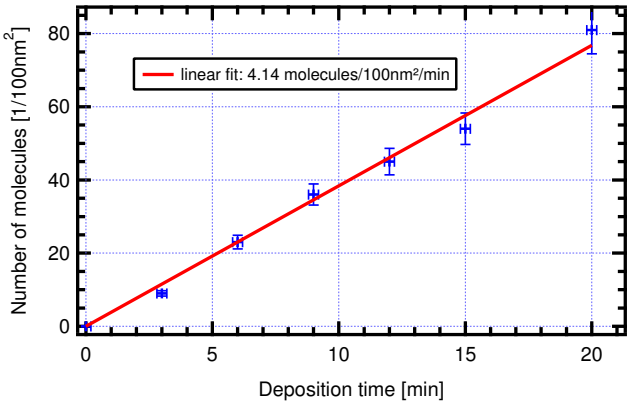

Figure 2.1.: Graph showing the evolution of the density of molecules adsorbed on the Au(111) surface as a function of the deposition time. A linear variation is observed, as expected, and permits us to determine a deposition rate of 4.14 molecules/100nm^2/min.

In figure 2.2 three STM images of 0.11 ML of DHTAP deposited on Au(111) at different substrate temperatures are shown. In figure 2.2.a the substrate temperature during deposition was 170 K. We can observe that molecules form one dimensional wires of about ten molecules that cross the herringbone structure of the Au(111) reconstruction. Measurements of the apparent height, length and width are in very good agreement with the value for pentacene molecules found in the literature,[73,74] and let us think that the molecules adsorb flat on the substrate, i.e. with their molecular planes parallel to the surface. This configuration is usually observed for planar polyacene molecules[75,76] or more generally for planar π-conjugated molecules adsorbing on noble metal substrates.[77,78]

A typical measurement allowing the determination of apparent height and intermolecular distance is shown in figure 2.2.d. The profile corresponds to the grey line in the STM image 2.2.a. The intermolecular distance, measured from center to center is 0.85±0.05 nm, and the apparent height is 165±25 pm. The smooth variations of the apparent height are due to the corrugation of the reconstructed Au(111) surface: we can see in the STM image that the molecular wire crosses a discommensuration line. Molecular wires are preferentially oriented along the $[1\bar{1}0]$ direction, which in addition to the intermolecular distance suggests a commensuration between the substrate and the molecular wire: the intermolecular distance is equal to three times the interatomic distance in the $[1\bar{1}0]$ direction (2.88 Å). Moreover, this suggests attractive intermolecular interactions between neighbouring molecules.

For a substrate temperature of 250 K during deposition (figure 2.2.b), a faster diffusion of DHTAP molecules, along with a higher thermal energy allows them to reach different metastable positions. At this temperature, the most stable structure are small linear aggregates of three or four DHTAP molecules which grow exclusively on the fcc domains of Au(111). These linear aggregates are assembled in a particular manner that leads to the formation of molecular wires, which perfectly follow the herringbone reconstruction.

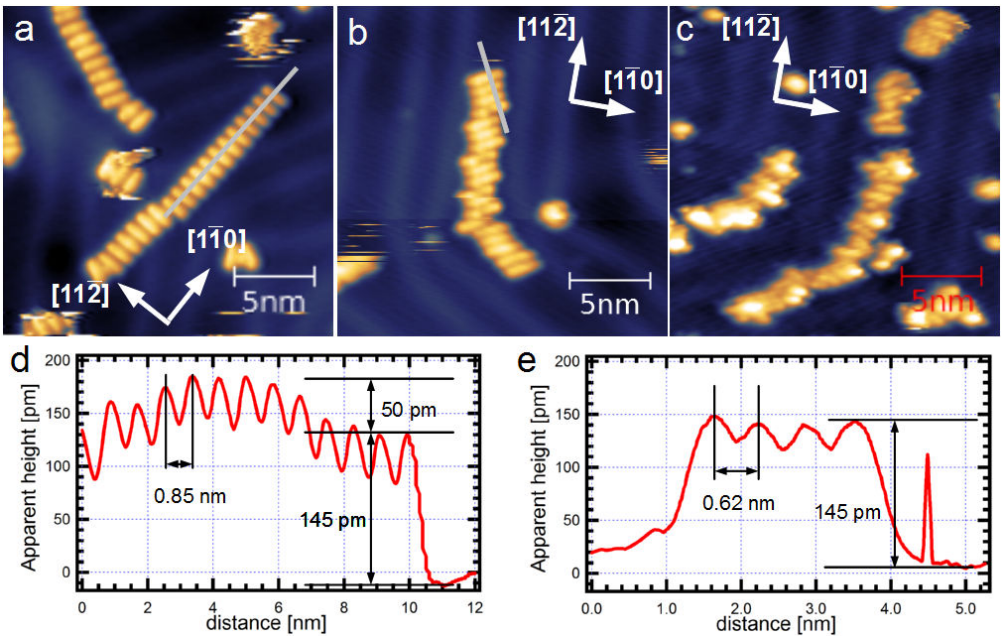

Figure 2.2.: STM images of 0.11 ML of DHTAP deposited on Au(111) at different temperatures resulting in three different adsorption structures. a) T=170 K; U_b=0.66 V; I_t=50 pA. b) T=250 K; U_b=0.73 V;I_t=20 pA. c) T=300 K; U_b=0.05 V; I_t=20 pA. d) Line profile measured along the molecular wire in STM image .a (grey line) along the $[1\bar{1}0]$ direction. e) Line profile measured along the molecular aggregate in STM image .b (grey line).

Measurements of the apparent height (150±15 pm) and full width at half maximum (FWMH) (1.8±0.1 nm) are similar to those obtained previously, for a deposition temperature of 170 K, but the intermolecular distance between molecules constituting these linear aggregates is reduced to 0.62±0.05 nm. Apparent height and intermolecular distance are deduced from STM profiles, a typical profile is shown in figure 2.2.e. These measurements are still in agreement with a molecular compound adsorbed with its molecular plane parallel to the surface plane.

The figure 2.2.c shows a STM image of a deposition performed at room temperature (RT). In this case the molecular diffusion and the thermal energy of

DHTAP molecules lead to the formation of amorphous molecular aggregates. Some molecules do not adsorb in a flat lying configuration on the surface and apparent heights above 260 pm have been observed. However, the influence of intermolecular interactions is still observed through the formation of molecular aggregates, and the influence of the molecule-substrate interactions through the fact that these are localized on particular regions: the fcc domains of the reconstructed Au(111) surface.

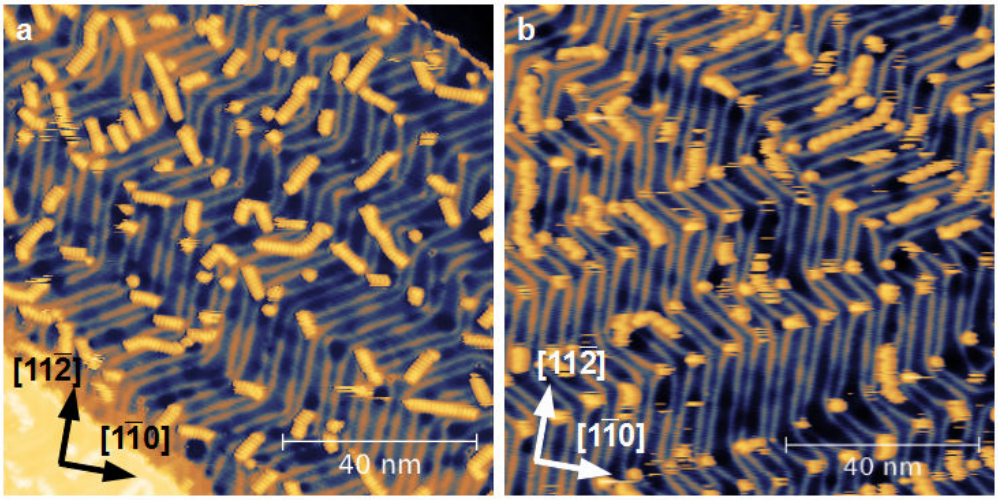

Figure 2.3.: STM images of 0.11 ML of DHTAP deposited on Au(111) a) T=170 K; U_b=0.7 V; I_t=100 pA. b) T=250 K; U_b=-0.73 V; I_t=20 pA.

Figure 2.3 shows two larger STM images recorded for DHTAP deposited at 170 K (2.3.a) and 250 K(2.3.b). At 250 K, it appears clearly that the nucleation of DHTAP takes place preferentially at the elbows of the reconstructed Au(111) surface and molecular wires grow mostly on the fcc domains. It is known from literature that elbows of the reconstructed Au(111) surface are particularly active nucleation centers for various metallic deposits, such as Fe,[79] Ni[80,81] or Mo,[82] or organic materials such as C_60,[83] 1-nitronaphthalene[84] and iron or manganese phthalocyanine.[85,86] The preferential growth observed on the fcc domains has also been observed in the case of iron phthalocyanine[85,87] and perylene[88] deposited on Au(111).

The figure 2.3.a shows that the formation of wires occurs, but these wires do not follow the herringbone structure of the substrate as in the case of depositions performed at 250 K. But interestingly most part of the elbows are decorated by molecular wires. This observation suggests that even at this temperature the nucleation takes place at the elbows, but the formation of the molecular structure after the nucleation process is different, due to the lower lower diffusion and the lower thermal energy of the molecules at 170 K. At this temperature, molecules are not able to reach their equilibrium structure, but are trapped in a

kinetically limited state stabilized by intermolecular and molecule-substrate interactions. From these observations it becomes obvious that the most favourable temperature for the growth of self-organized DHTAP layer on Au(111) is around 250 K.

We can also observe in the STM images 2.3.a and 2.3.b (and also in STM image 2.2.a and 2.2.b) the presence of bright stripes along the x direction. These stripes could result from the diffusion of molecules on the surface and/or from adsorption and desorption of a molecular compound on the surface and on the tip during the scan process. That could be the reason why the STM image 2.3.b appears so noisy.

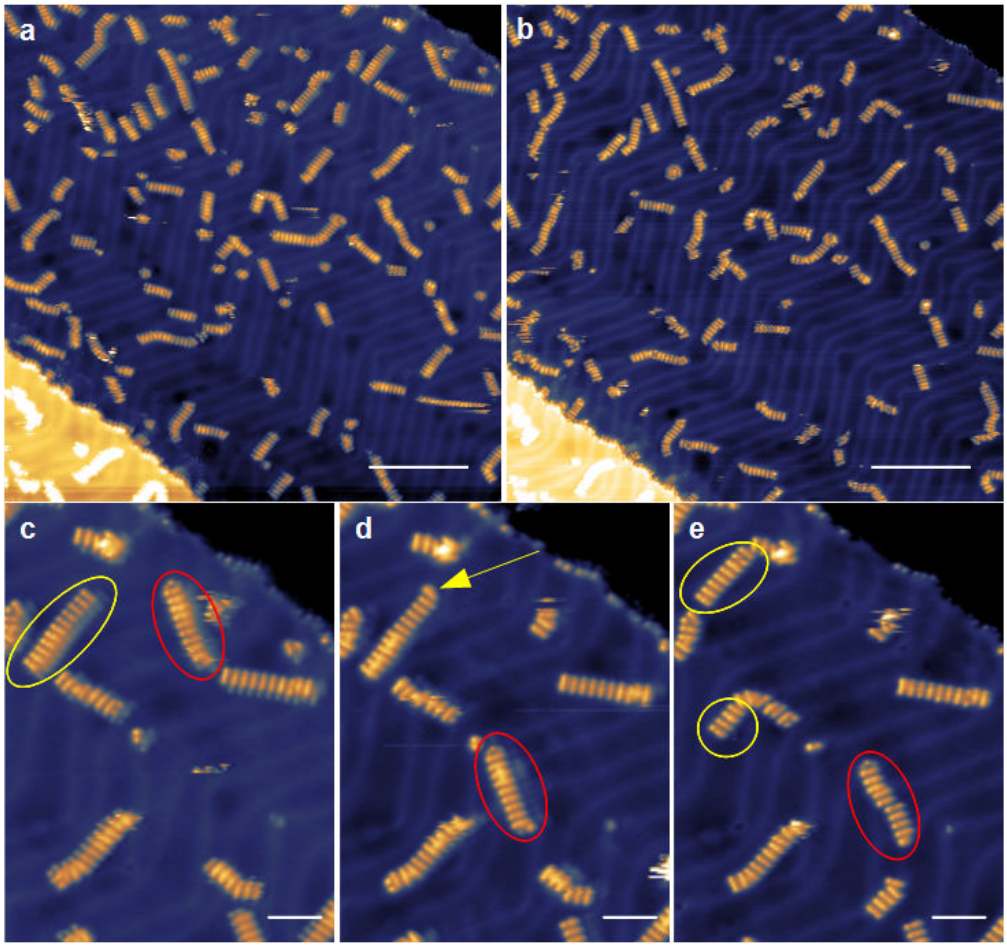

Figure 2.4.: STM images of 0.11 ML of DHTAP deposited on Au(111) at T=170 K (U_b=0.7 V; I_t=100 pA). a) and b) Scale bar: 20 nm. c), d) and e) Scale bar: 5 nm.

This molecular diffusion, which takes place even at LN_2 temperature, is clearly confirmed in figure 2.4, where successive STM images recorded at the same po-

sition are displayed. Important modifications are observed between the STM image 2.4.a and the STM image 2.4.b, which have been recorded after 10 scans on the same area (90 min between the first and the last scan). A slight decrease of the molecular density (3.1%) is observed, but the most important modifications arise from diffusion of single molecules, or DHTAP aggregates.

This is underlined in the following STM images recorded at smaller scale. In STM image 2.4.c, the DHTAP wire surrounded by a yellow circle is constituted of 11 DHTAP molecules. In the following STM picture, another DHTAP molecule, indicated by the yellow arrow, has diffused and is interacting with this wire, constituted now of 12 DHTAP molecules. Another example is the molecular wire surrounded by a red circle in the STM picture 2.4.c, constituted of 9 DHTAP molecules. It can be seen in the following STM pictures (2.4.d and 2.4.e) that this aggregate diffuses on the surface and remains constituted of 9 molecules. Furthermore, it can be observed that the other wire, constituted of 12 molecules in the figure 2.4.d (yellow arrow), has been split into two molecular wires of 8 and 4 DHTAP molecules, indicated by yellow circles in the STM image 2.4.e. This clearly indicates that molecular diffusion and diffusion of DHTAP aggregates takes places even at 77K.

2.1.2. DHTAP/Au(110)

In order to investigate the influence of the crystalline structure of the surface on the nucleation, growth process and the molecular self-assembly we decided to use a gold substrate with a different orientation.

During the investigation of DHTAP on Au(110) at very low coverage, the first STM images obtained appear very noisy due to the diffusion of DHTAP certainly influenced by the tip during the scan process, as underlined in the case of DHTAP/Au(111). From the STM picture 2.5.a it is clear that a preferential diffusion of DHTAP takes place in the $[1\bar{1}0]$ direction because the noise observed is confined between two atomic rows of gold, running in the $[1\bar{1}0]$ direction (see STM profile in figure 2.5.d. The molecule/surface bond is modified during scanning which can leads to different bonding geometries and adsorption sites. This preferential diffusion can be explained by the anisotropy of the Au(110) surface.

However, after several scans on the same area molecules reach a stable position on the Au(110) surface. This is shown in figure 2.5.b. This STM image has been recorded after several scans performed at smaller scales on areas indicated by white dashed squares. In these regions the resolution allows us to distinguish clearly the orientation of DHTAP molecules and, furthermore, we are still able to see the gold atomic rows running in the $[1\bar{1}0]$ direction. Outside these areas, the STM image appears noisy, due to molecular diffusion along the $[1\bar{1}0]$ direction.

From the deposition time of 5 min and the molecular flux determined in the previous subsection (4.14 molecules/100 nm^2/min), we can calculate an expected molecular density of 20.7 molecules/100 nm^2. It is not possible to de-

termine the molecular density precisely on STM images where the molecular diffusion occurs, however, it can be determined by counting the molecules adsorbed at stable positions after several scans, as in the case of the image shown in figure 2.5.b. In these cases, the molecular density is 21.1 molecules per 100 nm^2, which is in very good agreement with the expected molecular density, suggesting that no molecules are removed from the area during the scanning process.

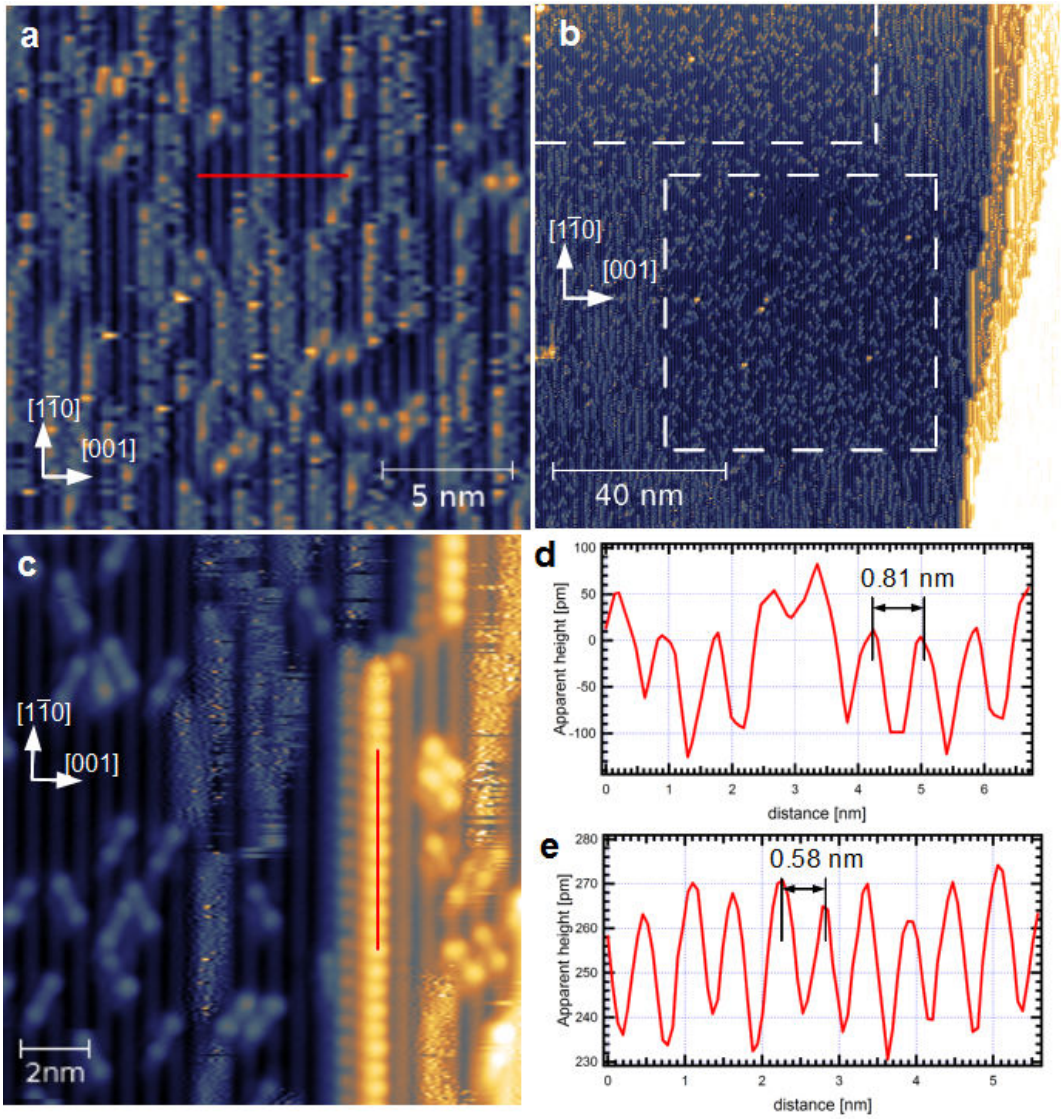

Figure 2.5.: STM images of DHTAP on Au(110) deposited at 210 K during 5 min. V_b=0.55 V; I_t=120 pA). a) 20 nm x 20 nm. b) 120 nm x 120 nm, dashed squares indicate areas previously scanned. c) STM picture (14.5 nm x 16 nm) showing the 1D structure observed at highly-oriented steps. d) STM profile recorded in a) (red line). e) STM profile recorded in c) (red line).

Another information can be extracted from the image 2.5.b: self-organization takes place at highly-oriented step edges running along the $[1\bar{1}0]$ close packed direction. This is confirmed by the STM image depicted in figure 2.5.c. DHTAP molecules form an unidimensional structure with a periodicity of 0.58±0.05 nm (see profile in 2.5.e), suggesting a commensuration between the substrate (2 x a$[1\bar{1}0]$=0.576 nm) and the molecular structure.

STM images recorded at smaller scale, which are displayed in figure 2.6.a and 2.6.b illustrate more precisely the diffusion phenomenon. The STM picture 2.6.a has been obtained by scanning line by line from the bottom to the top. The image 2.6.b has been recorded just after the image 2.6.a and is scanned from the top to the bottom.

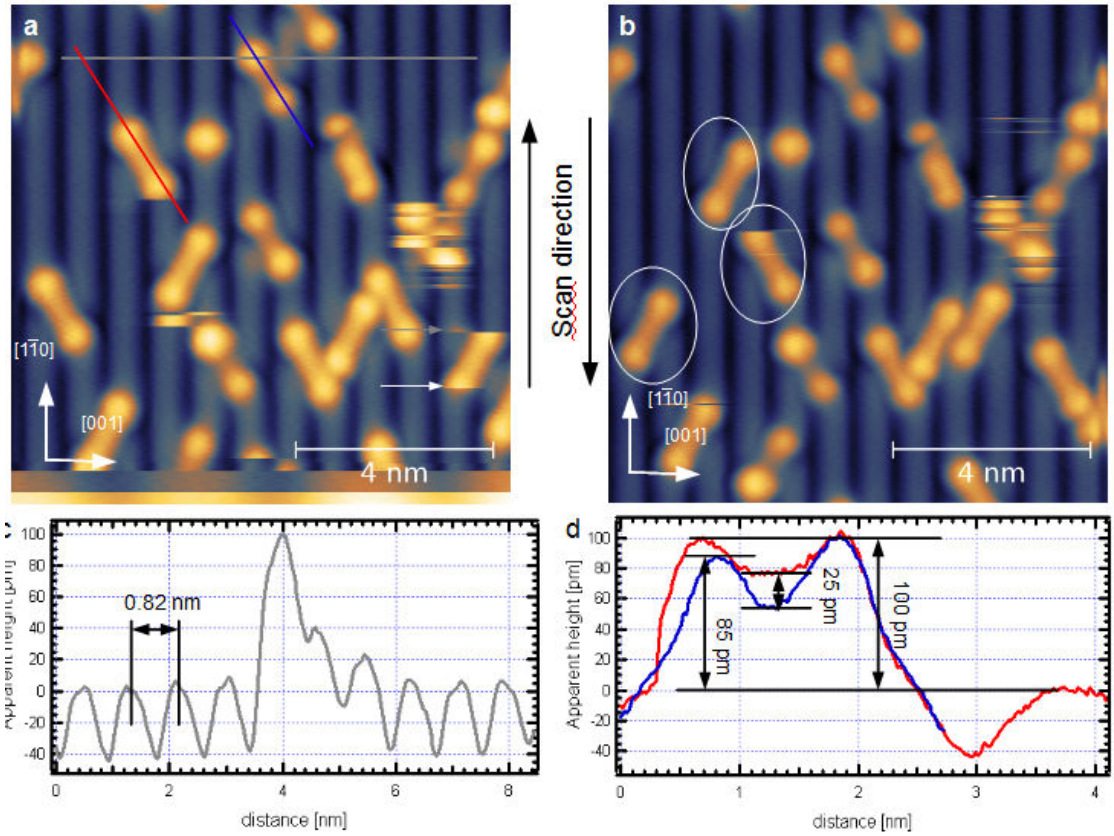

Figure 2.6.: STM images (10 nm x 10 nm; V_b=0.6 V; I_t=10 pA) of 0.19 ML of DHTAP deposited at 210 K on Au(110). a) Scanned line by line from the bottom to the top. Arrows indicate a change in the molecular orientation. b) STM image obtains just after the image a), scanned from the top to the bottom. Encircled molecules have different orientation with respect to the image a). c) and d) STM profiles recorded in STM image a).

The resolution of the STM image allows us to observe gold atomic rows run-

ning in the $[1\bar{1}0]$ direction. An inter-row distance of 0.82±0.05 nm is determined (see profile in figure 2.6.c) in very good agreement with the distance expected for the (1x2) reconstruction. In the image 2.6.a we can see on the right-hand side, indicated by a white arrow, that the molecule is not imaged completely: the lower part seems to be cut. This is due to a rotation of the DHTAP molecule. This rotation is observed a second time, indicated by the grey arrow. The same process is observed for other molecules which show different orientations between both images (some of these molecules are surrounded by a white circle in figure 2.6.b).

These two STM images obtained with high resolution allow us to determine two preferential orientations for the molecule which are very similar. The angle between the long molecular axis and the $[1\bar{1}0]$ direction of the Au(110) surface is $\pm 30 \pm 3^{\circ}$ in both cases but molecules appear differently in the STM images. One lies flat on the surface, this is deduced from the fact that the two bright lobes of the molecule show the same apparent height (100 pm). The other one shows an apparent height difference of 15 pm between these two brighter lobes suggesting a configuration with the long molecular axis tilted with respect to the surface plane. Another difference is observed in the center of the DHTAP molecule, where the apparent height is reduced by 25 pm. (see profiles in figure 2.6.d). Moreover, a difference is recorded for the FWMH: 1.62±0.1 nm for the tilted DHTAP and 1.81±0.1 nm in the case of the flat lying adsorption. However, it appears that the tilted absorption configuration is more stable than the other: no rotation or modification of the position has been observed for these molecules after several STM images recorded at the same position.

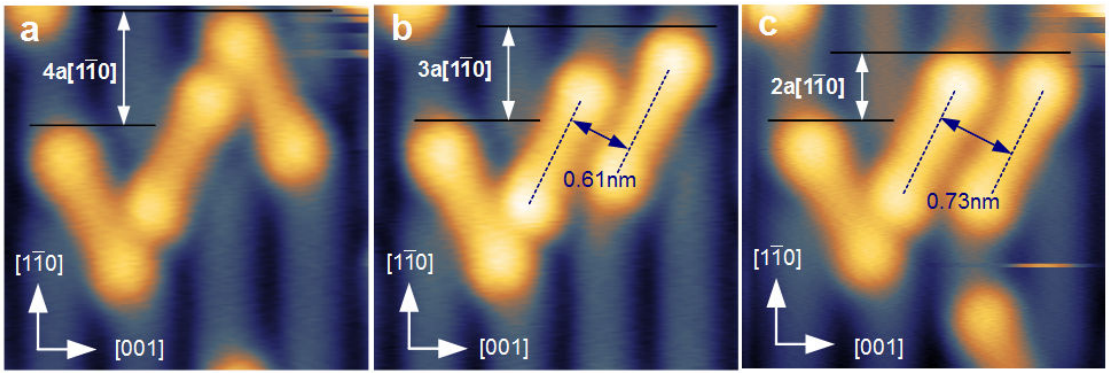

Figure 2.7.: Successive STM images (3.5 nm x 3.5 nm; V_b=0.6 V; I_t=10 pA) of 0.19 ML of DHTAP deposited at 210 K on Au(110).

Figure 2.7 shows three successive STM images recorded at the same position. The previous observations are confirmed: DHTAP molecules can rotate from one position to a mirrored position with respect to the $[1\bar{1}0]$ direction, and a diffusion of the DHTAP molecule can take place along this direction. The resolution allows

us to determine that between the STM image a and b, the molecule not only rotates, but has also been shifted along the $[1\bar{1}0]$ direction by one gold interatomic distance. The STM image 2.7.c confirms this last observation: the same DHTAP molecule is again shifted by one interatomic distance along the $[1\bar{1}0]$ direction.

A closer analysis of these STM images lets us determine that the center of the molecule is above the missing gold row of the (1x2) reconstruction. Unfortunately, the resolution is not sufficient along the $[1\bar{1}0]$ direction to observe individual Au atoms, and consequently it is not possible to determine with accuracy the position of the molecule along this direction. However, measurements done concerning the relative position of the molecule diffusing on the substrate suggest adsorption sites equivalent for each molecule in this configuration. The difference between intermolecular distances is mainly due to a geometric effect of the underlying substrate and is the signature of a strong influence of molecule-substrate interactions.

2.1.3. DHTAP/Ag(110)

During this thesis we had the opportunity to collaborate on the investigation of another system (not developed in this manuscript) concerning the growth of silicon nanoribbons on Ag(110).[89] It was the occasion to compare the results already observed in the case of DHTAP/Au(110) to those for DHTAP on Ag(110).

The influence of the substrate temperature at the early stage of molecular growth has been investigated in the case of DHTAP deposited on Ag(110). At very low coverage, the substrate temperature plays a role for the formation of particular molecular structures. STM pictures of DHTAP deposited on Ag(110) at 180 K and RT are displayed in figure 2.8.

The STM image presented in figure 2.8.a has been recorded after the deposition of 0.1 ML of DHTAP on this surface at 180 K. In this case DHTAP molecules are oriented with the long molecular axis along the $[1\bar{1}0]$ direction. Moreover, the DHTAP molecules form molecular wires running along the $[001]$ direction. The intermolecular distance (0.82 nm = 2 x a[001]), see STM profile in figure 2.8.c, clearly indicates a commensuration between the wire and substrate. Interestingly this distance correspond roughly to the distance found for DHTAP/Au(111) at 170 K. The apparent height (115 pm) and FWHM (1.8 nm) strongly suggest that DHTAP adsorbs on the surface with its molecular plane parallel to the surface plane.

In the second STM image (figure 2.8.b), recorded for a similar coverage (0.11 ML) we can observe that DHTAP molecules deposited at RT are mostly oriented with their long molecular axis along the $[1\bar{1}0]$ direction. However, some molecules can be observed with their long molecular axis forming a slight angle with the $[1\bar{1}0]$ direction. Intermolecular distance measurements (see STM profile in figure 2.8.d) do not suggest a commensuration between the molecular aggregates and the substrate. No ordered molecular structure has been observed on

terraces.

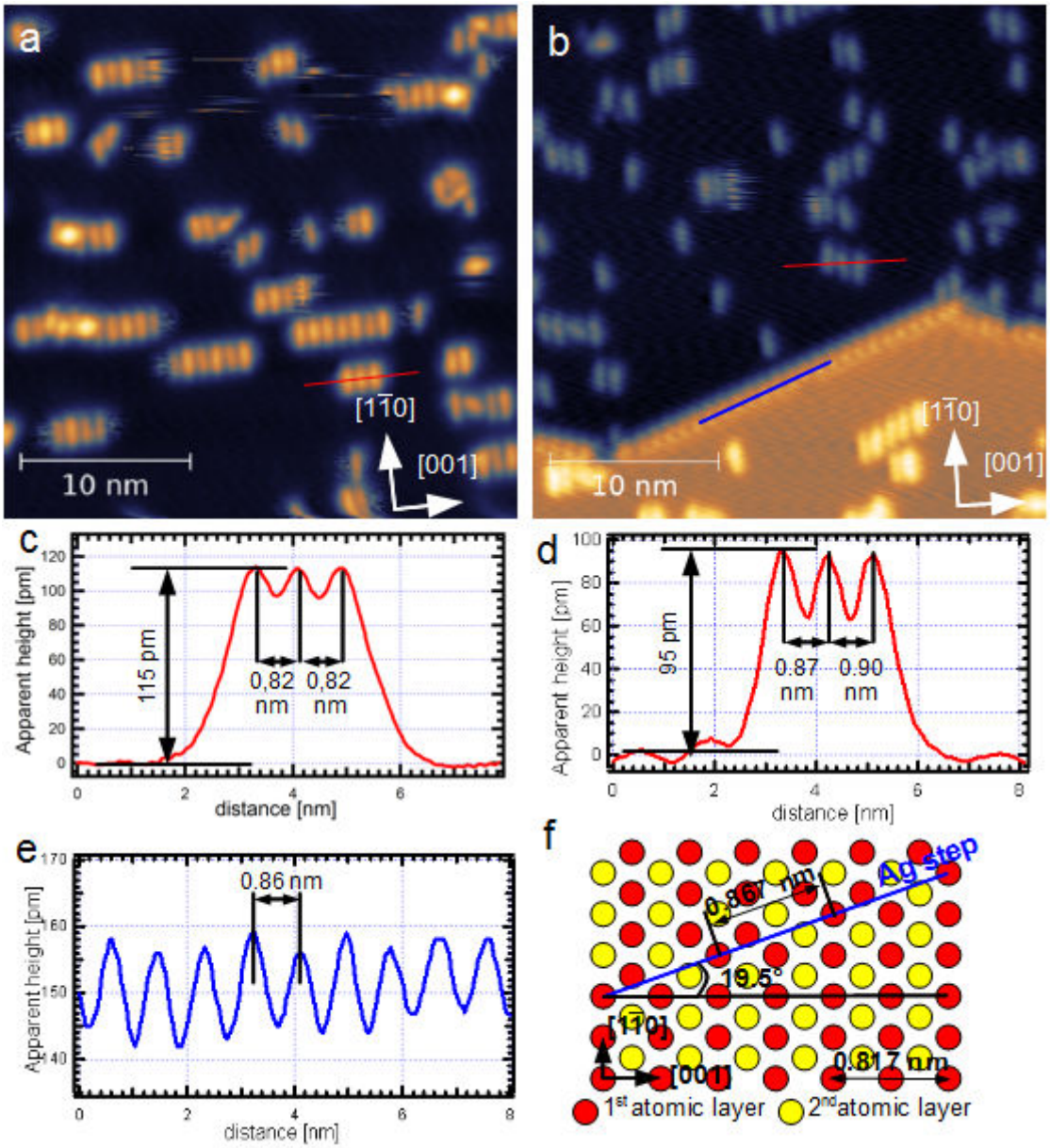

Figure 2.8.: a) STM image (U_b=0.95 V; I_t=40 pA) of 0.10 ML of DHTAP deposited on Ag(110) at 180 K. b) STM image (U_b=0.2 V; I_t=80 pA) of 0.11 ML of DHTAP deposited on Ag(110) at RT. c) STM profile measured in figure a) (red line). d) and e) STM profiles measured in figure b) (red line and blue line respectively). f) Schematic representation of the Ag step.

Densely packed atomic steps displayed in the lower part of the STM image are completely covered with DHTAP molecules as in the case of Au(110). The

angle between this step and the $[001]$ direction is $20\pm5^\circ$ and intermolecular distance measured along this direction is 0.86 nm (see profile 2.8.e). Comparing these measurements to the atomic structure of the silver surface suggests that this molecular assembly is commensurate with the substrate. A schematic representation of the atomic step is given in figure 2.8.f. The fact that these steps are completely covered with DHTAP clearly indicates a strong diffusion of DHTAP during the deposition process.

In this particular case, only the deposition performed at low temperature leads to the formation of ordered wires in contrast to deposition performed at RT. However, the commensuration observed between wires and substrate, along the $[1\bar{1}0]$ direction, suggests a strong influence of molecule-substrate interactions for deposition performed at 180 K.

Unfortunately, the resolution of the most part of STM images obtained during the investigation of DHTAP/Ag(110) is not sufficient to assign the exact adsorption site. But we observed at low coverage and preferentially at low temperature, that DHTAP molecule adsorbs with a particular orientation: the long molecular axis parallel to the $[1\bar{1}0]$ direction, and the molecular plane parallel to the surface plane.

During the investigation of Si nanoribbons on Ag(110), we also decided to deposit DHTAP on top of this surface to study the properties of DHTAP adsorbed on an inorganic semiconductor. Results obtained where not conclusive but the combination of two STM images presented below (figure 2.9.a and 2.9.b) allows us to determine unambiguously the position of an isolated DHTAP molecule on Ag(110).

The first STM image 2.9.a has been obtained for the system Si/Ag(110). The high resolution achieved in the upper part of the STM picture allows us to distinguish the silver atoms of the unreconstructed Ag(110) surface. We assume that this high resolution is due to the adsorption of silicon atom(s) on the tip apex. The resolution in the lower part of the STM image is not as good as the resolution in the upper part, however, it is possible to distinguish the Ag atomic rows running in the $[1\bar{1}0]$ direction. On the left part of this STM picture Si nanoribbons are localized (two doubles and one simple). A clear commensuration is observed between the crystallographic direction of the substrate and the protrusions of the Si nanoribbons.

The second STM image (2.9.b) has been recorded after the evaporation of DHTAP molecules on top of Ag(110) partially covered with Si nanoribbons. The deposition of DHTAP has been performed on a substrate at room temperature. From the deposition time, it is possible to estimate a molecular density of 49.7 molecules per 100 nm^2. Note that the molecular density observed on this picture is lower than the molecular density expected, but this image was in fact obtained at one location where molecular density on Si nanoribbons is lower than on other images recorded at larger scale. This allows for a better resolution of the dots structure. We can see that DHTAP molecules adsorb on Si nanorribons with

various orientations.

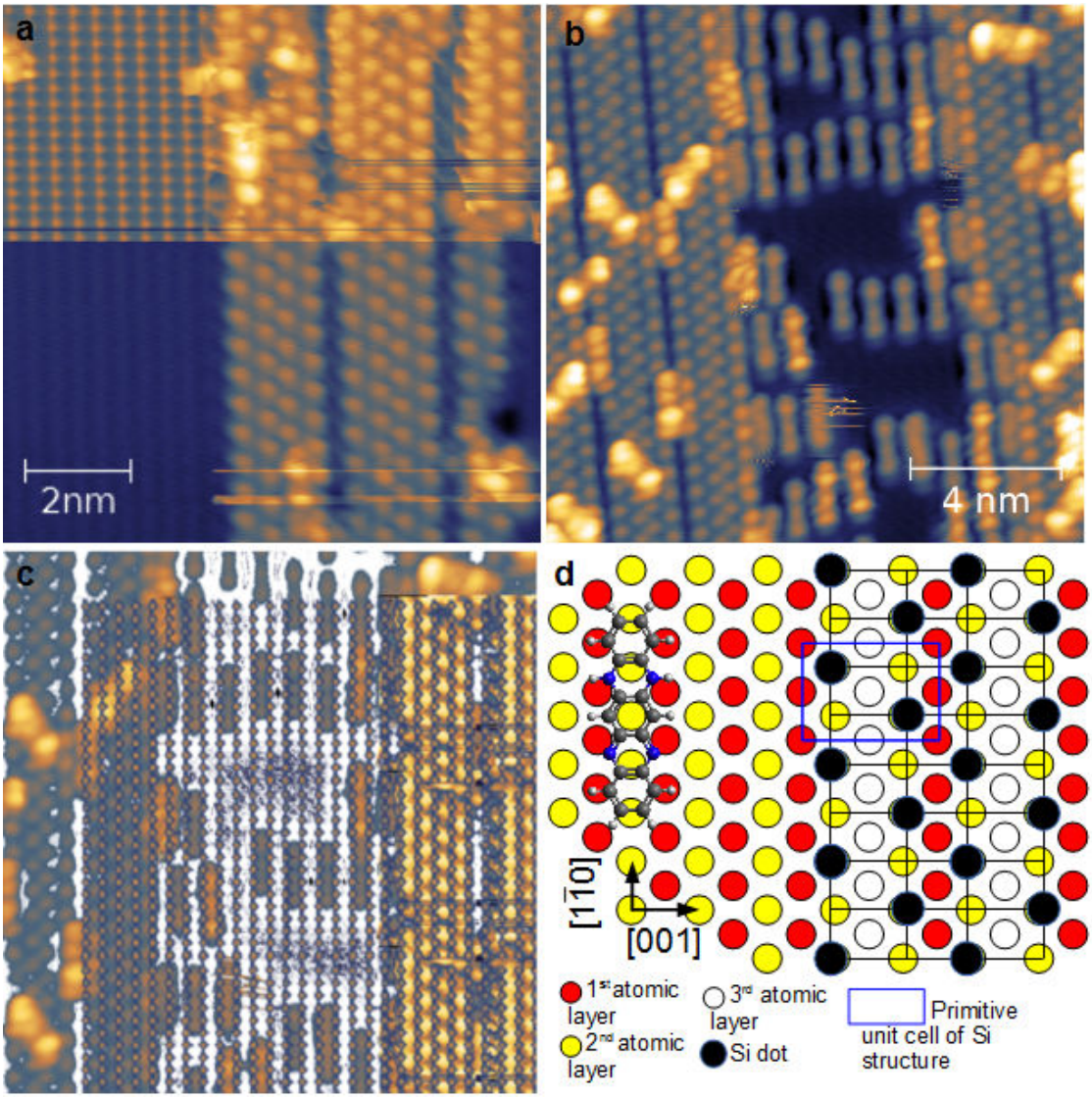

Figure 2.9.: a) STM image of Si nanoribbons grown on Ag(110) (U_b=100 mV, I_t=50 nA). Ag atoms are resolved on the upper left part of the STM image. b) STM image (U_b=2.34 V, I_t=30 pA) of DHTAP evaporated onto a Ag(110) at RT, partially covered with Si nanoribbons. c) Superposition of both STM images after correction of the drift d) Structure model showing the exact adsorption side of the DHTAP molecule on the bare Ag(110) area.

On the silver surface, molecules adsorb according the two configurations previously observed for depositions performed at RT. The long molecular axis is aligned with the $[1\bar{1}0]$ direction or show a small angle with this direction. Interestingly, the DHTAP molecules whose molecular axis is tilted from the $[1\bar{1}0]$ di-

rection are imaged with resolution of the molecular orbital at this voltage (2.34 eV).This is in good agreement with the increase of the apparent height from 100 to 150 pm between these molecule with different adsorption geometry.

The image depicted in figure 2.9.c is a superposition of the atomic Ag lattice and the Si nanoribbons, observed in the upper part of the STM image in 2.9.a, and the STM image shown in 2.9.b. For better clarity, the nanoribbon showing several defects in the STM image 2.9.a has been removed and the atomic lattice has been extended to determine its relative position with respect to the Si protrusions. The superposition of this atomic lattice on the second STM image, using the relative position of Ag atoms with respect to the Si dots allows us to determine unambiguously the adsorption site of individual DHTAP molecules. It turns out that all DHTAP molecules show equivalent adsorption sites, i.e. the center of a DHTAP molecule is localized between densely packed Ag rows. For better clarity, a schematic representation of the relative orientation between DHTAP molecule (long molecular axis parallel to the $[1\bar{1}0]$ direction), Si dots, and the Ag substrate is depicted in figure 2.9.d. It clearly shows the the center of the DHTAP molecule is located above an Ag atom of the second layer.

It has to be mentioned that the STM images depicted in figure 2.9.a and 2.9.b show a slight drift which can be observed through the angle between the $[1\bar{1}0]$ and the $[001]$ direction which is slightly different from 90°. Consequently these STM images have to be corrected from these drifts prior to being superposed. In these cases the drift effects are constant over the complete picture and can be corrected easily. This essential step can be done by adjusting the angle between the $[1\bar{1}0]$ and the $[001]$ direction to 90°, using the atomic lattice and/or the Si nanoribbon. Finally, these images can be rescaled if necessary, according the value known for the Ag(110) surface lattice and the commensurate Si dot structures.

2.1.4. Discussion

The initial steps of the growth of DHTAP and influence of the substrate temperature during deposition have been investigated on Au(111), Au(110) and Ag(110).

We observe on Au(111) that depositions performed at 170 K lead to the formation of commensurate molecular wires aligned with the close packed directions of the substrate. DHTAP molecules adsorb with their molecular planes parallel to the surface plane and show preferential side by side interaction. When DHTAP is deposited at 250 K, molecular wires are formed at the elbows of the reconstructed Au(111), which are known to be efficient nucleation centers, and are observed exclusively on fcc domains. Wires formed in this condition are not commensurate with the substrate and a strong decrease of the intermolecular distance is observed compared to deposition performed at 170 K. Depositing DHTAP at RT leads to the formation of disordered aggregates, where some

molecules are observed to adsorb on the substrate with their molecular plan tilted from the surface plane. However, the formation of these amorphous structure is observed exclusively on fcc domains, as in the case of deposition performed at 250 K. The formation of these different structures can be explained considering the kinetics of the growth process. Indeed, the structure observed after deposition performed at a temperature of 170 K are metastable structures, strongly influenced by molecule-substrate interactions. At 250 K the energy of the system (molecular wire/substrate) is more important and allows the formation of another kind of wire that cannot be formed at lower temperature.

On Au(110), we observe that DHTAP molecules show an anisotropic diffusion behaviour on the surface, preferentially along the $[1\bar{1}0]$ direction. This diffusion is certainly influenced by the STM tip during the scanning process. Molecules are immobilized by repeated cycle of scanning on the same area. STM images allow us to observe two preferential orientations for DHTAP on Au(110) at this low coverage: in both cases the long molecular axis is oriented with the same angle with respect to the $[1\bar{1}0]$ direction: $\pm 30^{\circ}$. The difference is related to the angle between the molecular plane and the surface plane: in the first case and for the most part of observed DHTAP molecules at these coverages, molecular and surface plane are parallel and the molecule lies on the surface in a flat lying configuration. In this case the center of the molecular backbone in located in bridge position between two gold rows running in the $[1\bar{1}0]$ direction. In the second case, the molecule lies on the surface with a tilted angle. It seems that this tilted configuration is more stable, indeed, no diffusion of the molecule adopting this configuration has been observed. We also observe that the formation of commensurate 1D structure takes place at highly-oriented steps running in the $[1\bar{1}0]$ direction.

On Ag(110), the deposition of DHTAP on a substrate at low temperature (180 K) leads to the formation of molecular wires which are commensurate along the $[001]$ direction. Interestingly, the formation of commensurate wires was also observed in the case of deposition performed at 170 K on Au(111). On Ag(110), DHTAP molecule lies flat on the surface, and the long molecular axis is aligned with the $[1\bar{1}0]$ direction. Deposited at RT, DHTAP molecules adopt different orientations: long molecular axis aligned with the $[1\bar{1}0]$ direction, or showing a slight angle ($\pm 3^{\circ}$) are predominant. However, no organized structure formation takes place on terraces under these conditions of temperature and coverage. However, the formation of a commensurate structure has been observed on densely packed monoatomic steps, as in the case of Au(110). Finally, the adsorption site of the DHTAP molecules has been determined at the atomic scale and it appears that the center of the molecular backbone is localized on top of an Ag atom of the second atomic layer.

In the case of DHTAP deposited on Au(111), the observations concerning the influence of the temperature let us think that 250 K is the best temperature to use for the growth process to obtain well-ordered structure. Consequently, we

will use this temperature for the following depositions. The temperature effect on Au(110) and Ag(110) which does not seem to be as critical as in the case of DHTAP on Au(111) for these coverages will still be investigated during the following step of growth.

2.2. Growth of DHTAP on noble metal surfaces: submonolayer coverage

In this section the growth of DHTAP deposited on Au(111), Au(110) and Ag(110) up to coverages close to the monolayer density will be presented. Particular attention will be paid on molecule-substrate and molecule-molecule interactions which play a very important role in the growth process. Results observed in the case of the growth performed on Au(111) are in very good agreement with modelling performed for this system and will be discussed.

2.2.1. DHATP/Au(111)

2.2.1.1. STM investigation

The figure 2.10.a shows a STM image of 0.21 ML of DHTAP deposited at 250 K. We can see that after a nucleation at the elbows and the appearance of molecular wires on fcc domains, the growth of these structures continue preferentially on the fcc domains. This preferential growth of molecular structures on fcc domains, already observed for various molecular compounds as phtalocyanine[85,87] and perylene,[88] indicates that DHTAP is more stable on fcc regions than on hcp regions.

Figure 2.10.b has been obtained for a coverage of 0.32 ML. In this case, fcc domains are saturated and the molecular wires growth takes place on the hcp domains. For a coverage of 0.45 ML (fig 2.10.c) the growth continues on the hcp domains which are now close to saturation. In the figure 2.10.d we can see that, for a coverage of 0.58 ML, fcc and hcp domains are saturated and observe the appearance of molecular wires which are not strictly following the herringbone structure of the substrate.

The following figure (2.10.e) displays a coverage of 0.75 ML. In this case the molecular wires do not follow the herringbone structure anymore. This indicates that between 0.58 ML and 0.75 ML a phase transition occurs.

As mentioned before, the growth process is governed by the competition between two kinds of interactions: intermolecular interactions and molecule-substrate interactions. In our case, during the first part of the growth, i.e. for coverages from 0.11 ML to 0.58 ML, the growth process is mainly governed by the molecule-substrate interactions. This leads to the nucleation at specific locations of the substrate and the preferential growth occurs in accordance with the fcc domains of the substrate, which act as a template. Increasing the coverage leads to an increase of the molecular density and consequently an increase of the intermolecular interactions contribution. This contribution of the intermolecular interactions becomes more important than the molecule-substrate interactions contribution for a coverage between 0.58 ML and 0.75 ML leading to a phase transition.

Finally the last STM image depicted in figure 2.10.f has been recorded for 0.93 ML of DHTAP. We can observe that molecular wires previously observed at 0.75 ML form now highly-ordered 2D domains with particular orientations. We can also note that domain boundaries follow the elbows of the reconstructed Au(111) surface.

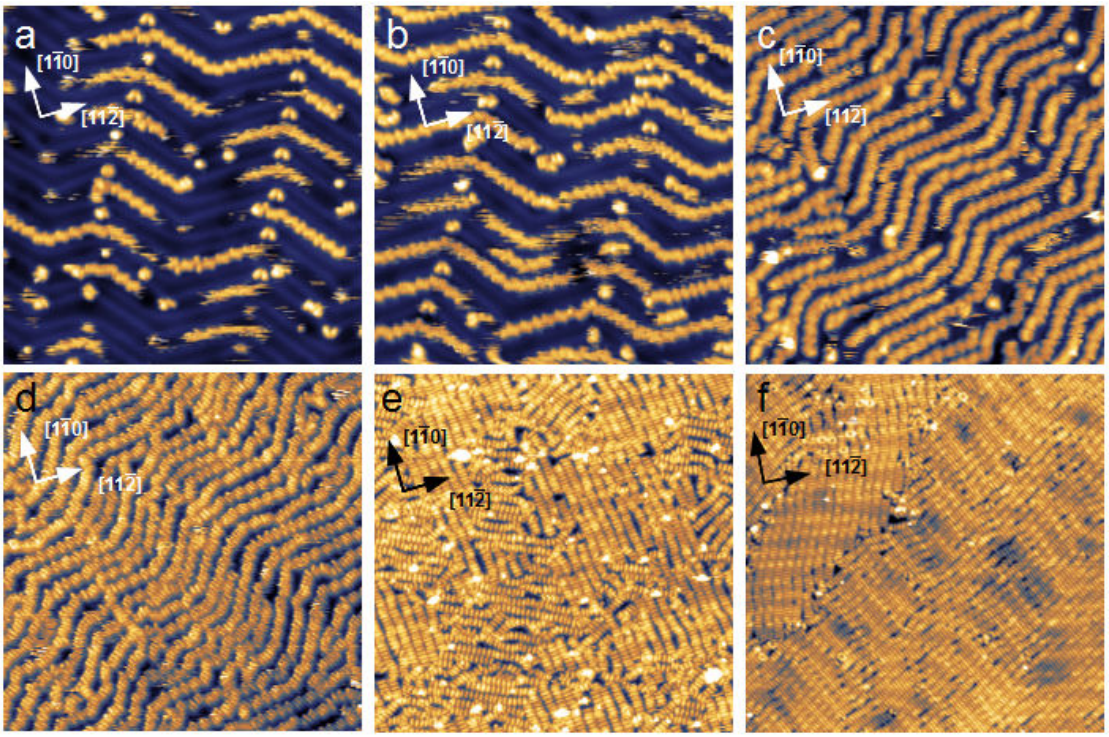

Figure 2.10.: STM images of DHTAP deposited on Au(111) at T=250 K. Size: 60 nm x 60 nm. a) 0.21 ML; U_b=-1 V; I_t=20 pA. b) 0.32 ML; U_b=-1.5 V; I_t=50 pA. c) 0.45 ML; U_b=-1 V; I_t=100 pA. d) 0.62 ML. U_b=-0.2 V; I_t=50 pA. e) 0.75 ML; U_b=0.49 V; I_t=30 pA. f) 0.93 ML; U_b=1 V; I_t=40 pA.

During the growth process of the first monolayer at 250 K, the intermolecular distance measured from center to center in molecular aggregates remains identical, 0.61$\pm$0.03 nm, even after the molecular reorganization observed between 0.58 ML and 0.75 ML.

The structure of these domains will be treated in details in section 2.3.1. An interesting point is that even at this coverage very close to the monolayer density, no DHTAP molecules have been observed on top of the first layer suggesting strongly that the growth mode of DHTAP on Au(111) is not a Volmer-Weber growth mode under these conditions i.e. the molecules are wetting the substrate.

2.2.1.2. Modelling of the growth

A collaboration with T. Roussel[90] from the "Institut de Ciènca de Material de Barcelona" has permitted us to investigate the surface effect of the gold reconstruction on DHTAP self-assembly using modelling. The self-assembly is simulated within a two-dimensional Grand-Canonical Monte-Carlos (GCMC) approach recently reported.[91] It allows performing atomistic simulations of thousands of organic molecules self-assembling on large crystalline surfaces independently of their number of atoms, starting from the bare substrate.

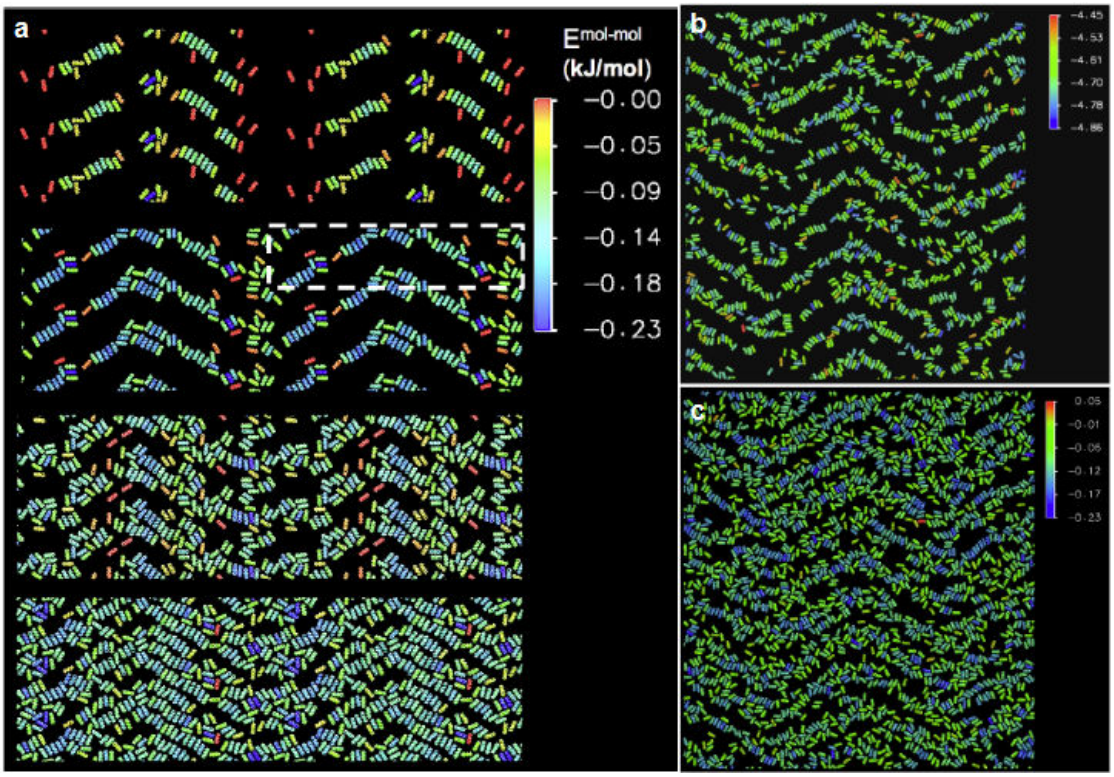

Figure 2.11.: Configuration snapshot of GCMC computations at different molecular densities and different simulation box sizes. a) Simulation box: one unit cell of the simulated Au(111) substrate (white dashed line) duplicated six times for better visualization. Four different molecular densities are considered. The coloured scale represents the intermolecular potential energy (kJ/mol). b) and c) Simulation box size: (2x10) unit cell of the simulated Au(111) substrate, coloured scale corresponds to molecule-substrate potential energy in the case of b) and to the intermolecular potential energy in the case of c).[90]

Snapshots of the configurations obtained by GCMC simulation are displayed in figure 2.11.a for different coverages which are, from top to bottom, 0.14 ML, 0.26 ML, 0.43 ML and 0.57 ML. The simulation has been done for one unit cell of

simulated Au(111) (represented by the white dashed line) and has been duplicated six times for a better visualisation. The formation of molecular aggregates at the elbows of the reconstructed surface, and of molecular structures preferentially on fcc domains are observed at the lower coverage simulated. DHTAP molecules constituting these structures show preferential side by side interactions. At higher molecular density, the formation of wires leads to the completion of fcc domains and the growth takes place on hcp domains and leads to the formation of new molecular wires on these regions. Similar results are obtained using a supercell of (2x10) unit cells of the simulated surface as shown in figure 2.11.b and 2.11.c. These computations have been performed with respectively 1200 and 2017 molecules, which correspond to coverages of 0.24 and 0.41 ML.

The simulations show that the intermolecular potential became stronger with the molecular density (see the coloured energy scale in figure 2.11.a), and the molecule-substrate potential became weaker with the molecular density (not shown). These potential energies strongly depend on the position of the DHTAP molecule on the surface and its surroundings: DHTAP molecules embedded in molecular wires show lower intermolecular potential energy compared to molecules localized at the end of the wires, or isolated molecules. The same remark can be done concerning the molecule-substrate potential energy, which is different depending on the position of the molecule on the surface. This is shown in figure 2.11.b, where the coloured energy scale stands for molecule-substrate potential energy. We can note in this case that DHTAP molecules showing the lowest energy are generally localized close to the elbow of the reconstructed surface, which are known to be efficient nucleation center.

These simulations are in very good agreement with the preferential growth observed at low coverages by the means of STM on Au(111). Moreover this is in agreement and illustrates the increase of the influence of the intermolecular interaction and the decrease of the influence of the molecule-substrate interactions with the coverage, found by the STM investigations.

Finally, these computations allow us to have access to the molecular orientation adopted by molecules. Figure 2.12 shows the molecular orientations (represented by an arrow) for one configuration snapshot. It appears clearly that molecules constituting ordered molecular wires are very often in a head to tail configuration, suggesting that intermolecular hydrogen bonds are responsible for the establishment and formation of molecular wires. This interesting information couldn't be obtained from the STM measurements at these coverages. We will come back to this below.

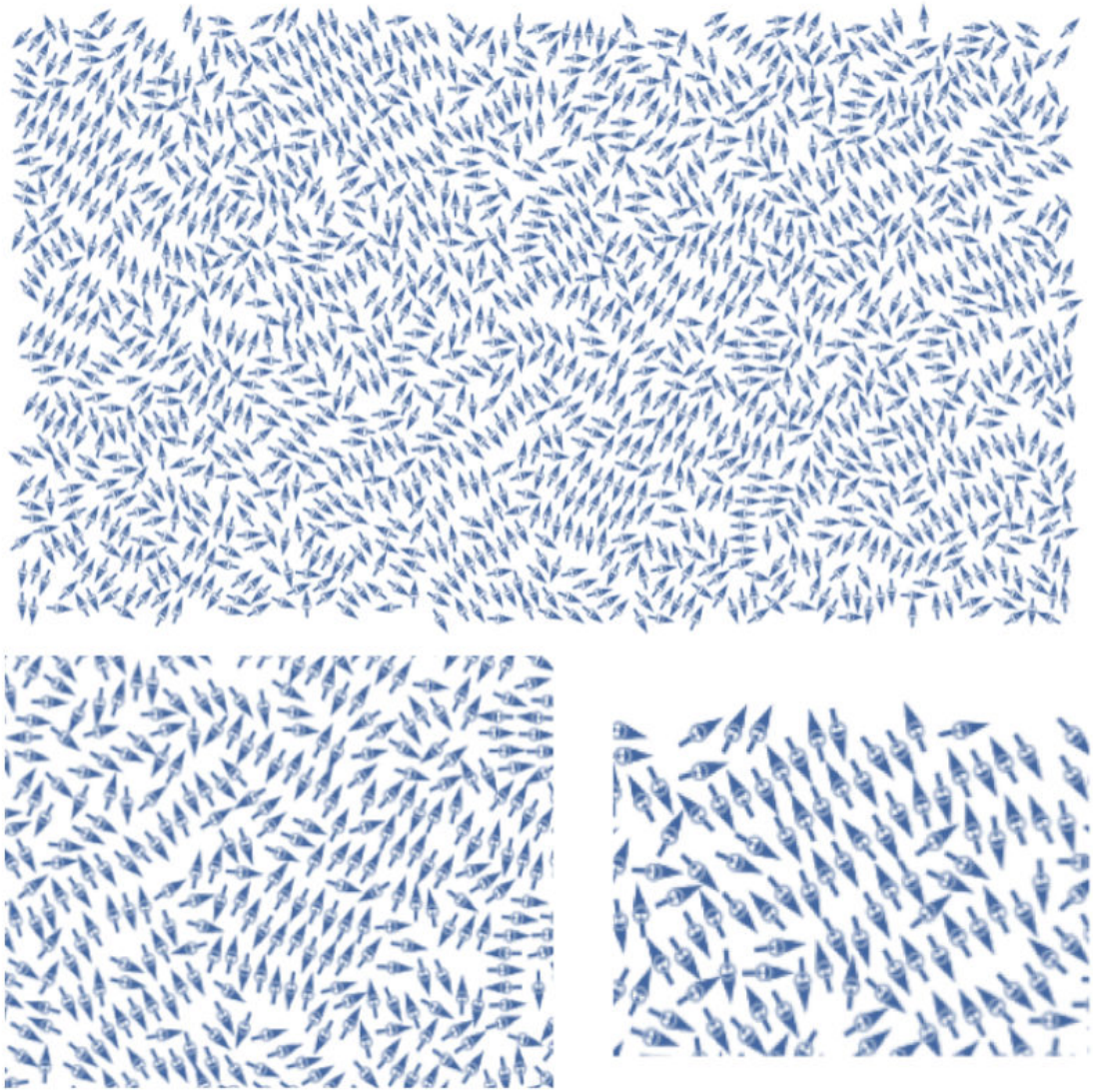

Figure 2.12.: Molecular orientations are represented by arrows for a configuration snapshot then zoomed.[90]

2.2.2. DHATP/Au(110)

The STM images in figure 2.13 have been recorded at different coverages for DHTAP deposited on Au(110) at 210 K, in order to investigate the influence of the coverage on the growth process. The molecular diffusion remains important in the $[1\bar{1}0]$ direction, as it has already been observed at lower coverages. In the upper right part of the STM image 2.13.a, DHTAP molecules do not diffuse on the surface and most part of the molecules show the orientation previously

observed, where the long molecular axis shows an angle of $\pm30\pm3^\circ$ with the $[1\bar{1}0]$ direction.

In this STM image we can also observe the formation of molecular dimers indicated by white circles. These two molecules are located in bridge positions between two atomic gold rows running in the $[1\bar{1}0]$ direction. The dimers show a particular orientation: an angle of $\pm50\pm5^\circ$ between the long molecular axis and the $[1\bar{1}0]$ direction has been determined.

Figure 2.13.b shows a histogram of the relative orientations of DHTAP molecules for a coverage of 0.24 ML. The distance between two molecules constituting the dimer, measured along the $[1\bar{1}0]$ direction, is 0.8 ± 0.1 nm (see histogram in figure 2.13.d) and the apparent height is slightly more important (110 ± 20 pm, profile shown in figure 2.13.f, corresponding to the red line in STM image 2.13.a.) with respect to molecules showing an angle of $\pm30\pm3^\circ$ between the $[1\bar{1}0]$ direction and their long molecular axes. These values remain in agreement with a flat lying configuration, but the intermolecular distance suggests that DHTAP molecules do not lie at equivalent positions on the gold substrate. From the intermolecular distance along the $[1\bar{1}0]$ direction and the angle of 50° between the long molecular axis and the $[1\bar{1}0]$ direction, it is possible to determine an intermolecular distance of 0.61 ± 0.1 nm along the direction perpendicular to the molecular axes.

This value is in agreement with the formation of hydrogen bonds between molecules constituting the dimer, assuming a head to tail configuration suggested by the simulation performed for DHTAP on Au(111). Interestingly these molecular dimers are stable and do not diffuse on the surface, contrary to the DHTAP adsorbed with an angle of $\pm30\pm3^\circ$ between the long molecular axis and the $[1\bar{1}0]$ direction.

A third orientation is also observed where molecules lie with their long axis parallel to the $[1\bar{1}0]$ direction. Statistical analysis shows for a coverage of 0.37 ML that 78% of the molecules adopt the configuration with an angle of $\pm30\pm3^\circ$ with respect to the $[1\bar{1}0]$ direction, 13% show the configuration with an angle of $\pm50\pm5^\circ$ with respect to the $[1\bar{1}0]$ direction and 9% are oriented with the long molecular axis parallel to the $[1\bar{1}0]$ direction.

Figure 2.13.c has been recorded at a coverage of 0.37 ML. In this case, DHTAP molecules adopt the previously mentioned orientations. However, the ratio between the different configurations evolve: 59% of the molecules adopt the configuration with an angle of $\pm30\pm3^\circ$ with respect to the $[1\bar{1}0]$ direction, 26% show the configuration with an angle of $\pm50\pm5^\circ$ with respect to the $[1\bar{1}0]$ direction and 15% are oriented with the long molecular axis parallel to the $[1\bar{1}0]$ direction.

The following STM image (2.13.e) has been recorded for a coverage of 0.89 ML. We observe clearly that at this coverage most of DHTAP molecules (68%) lie on the surface with the long molecular axis parallel to the $[1\bar{1}0]$ direction and only 7% are observed with an angle of $\pm30\pm3^\circ$ with respect to the $[1\bar{1}0]$ direction. Interestingly, the other DHTAP molecules (25%) do not adopt a well identified

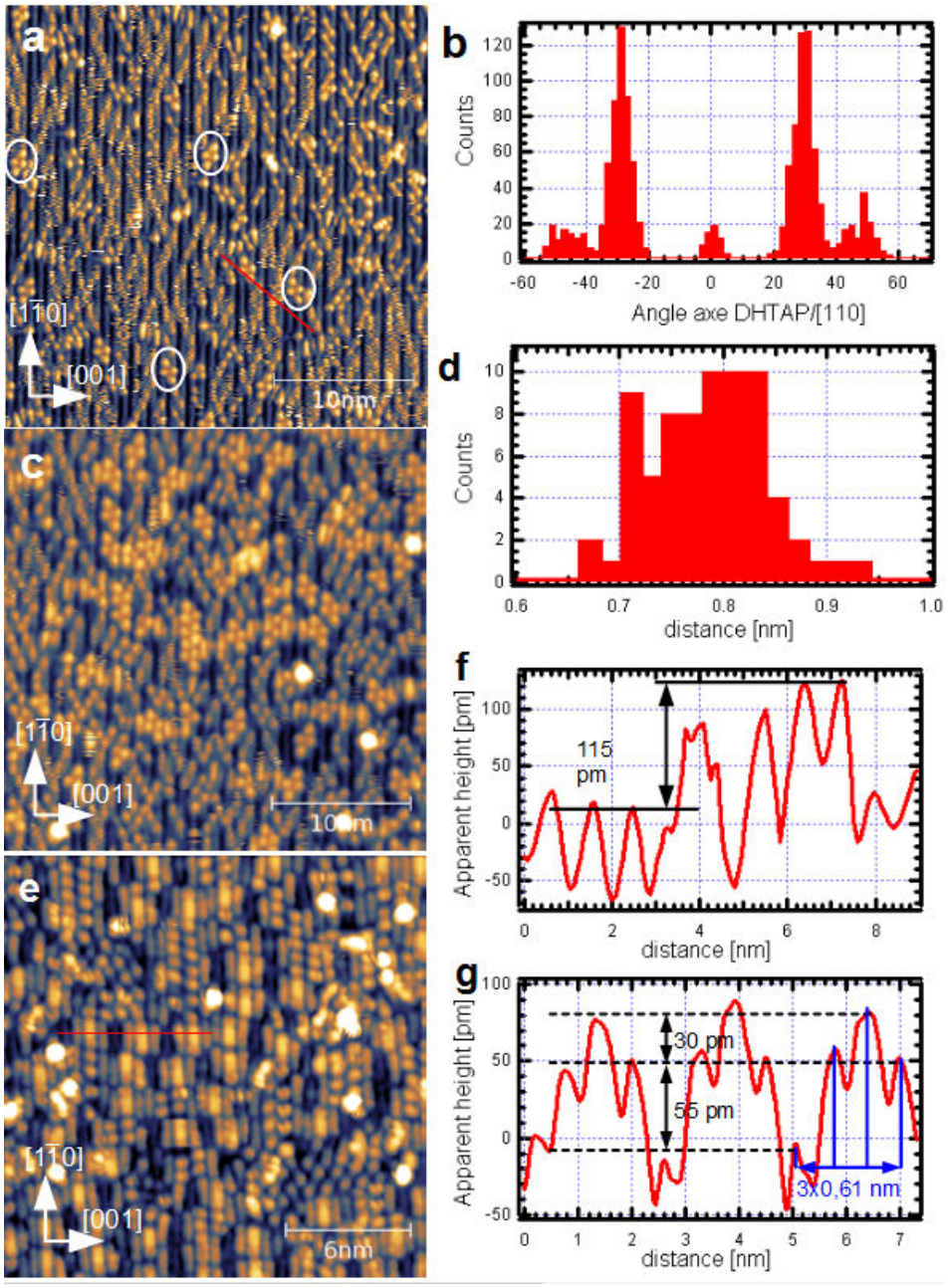

Figure 2.13.: STM images of DHTAP deposited on Au(110) at 210 K for three different coverages in the submonolayer range. a) 0.24 ML; 30 nm x 30 nm; U_b=0.8 V; I_t=100 pA. Some molecular dimers are surrounded by white circles. b) Molecular orientations observed in the coverage range 0.10-0.24 ML. c) 0.37 ML; 30 nm x 30 nm; U_b=0.7 V; I_t=60 pA. d) Intermolecular distance measured along the $[1\bar{1}0]$ direction. e) 0.89 ML; 20 nm x 20 nm; U_b=1.32 V; I_t=50 pA. f) STM profile corresponding to the red line in image a). g) STM profile corresponding to the red line in image e).

configuration, and we observe that the angle between the long molecular axis and the $[1\bar{1}0]$ direction can vary from $\pm 50°$ to $\pm 80°$. For these molecules, a slight decrease of the intermolecular distance, measured along the $[1\bar{1}0]$, is observed referring to the 0.8±0.1 nm observed in the case of the dimer configuration. The values concerning the relative orientation of DHTAP as a function of the coverage are summarized in the table 2.1.

-	30°	50°	0°	other
0.24 ML	78%	13%	9%	-
0.37 ML	59%	26%	15%	-
0.89 ML	7%	-	68%	25%

Table 2.1.: Relative orientations between the DHTAP molecules and the Au(110) surface as a function of the coverage.

Concerning DHTAP molecules lying with their long molecular axis parallel to the $[1\bar{1}0]$ direction, three different apparent heights are observed, and the intermolecular distance measured along the $[001]$ direction is around 0.61±0.05 nm (see STM profile in figure 2.13.g). An ordering can be observed for molecules in this configuration in the $[001]$ direction. It appears that the distance between two equivalent molecules (with the more important apparent height) is 2.4±0.08 nm, which is very close to three times the atomic parameter of the (1x2) reconstruction of the Au(110) along the $[001]$ direction. The structure of this first monolayer will be detailed in the section 2.3.2.

Very interesting observations have been made concerning the influence of the substrate temperature during the growth process of DHTAP/Au(110) at these coverages. In figure 2.14 STM images of DHTAP deposited on Au(110) at a substrate temperature of 210 K obtained before and after annealing the sample at RT are displayed. Image 2.14.a shows a large monoatomic terrace (more than 200 nm x 200 nm) and an atomic step in the upper left part.

The profile (grey line in the STM image) depicted in figure 2.14.d indicates an apparent height of 130±20 pm in good agreement with the height of a monoatomic step found in the literature.[4,92] A this large scale, individual DHTAP molecule cannot be resolved, but a STM image obtained at lower scale for the same coverage is depicted in figure 2.13.c. The high resolution allows us to distinguish gold atomic rows running in the $[1\bar{1}0]$ direction separated by a distance of 0.82±0.05 nm, characteristic of the (1x2) reconstruction.

After storing the sample for one night at RT under UHV conditions, STM images have been recorded, which are shown in figure 2.14.b and 2.14.c. We can observe on the large scale image the formation of unidimensional structures running in the $[1\bar{1}0]$ direction on the terraces. The apparent heights of these wires are 130±20 pm (see profile in figure 2.14.e), identical to the apparent height of

monoatomic gold steps. It seems that annealing the substrate at RT leads to the formation of gold wires growing along the $[1\bar{1}0]$ direction.

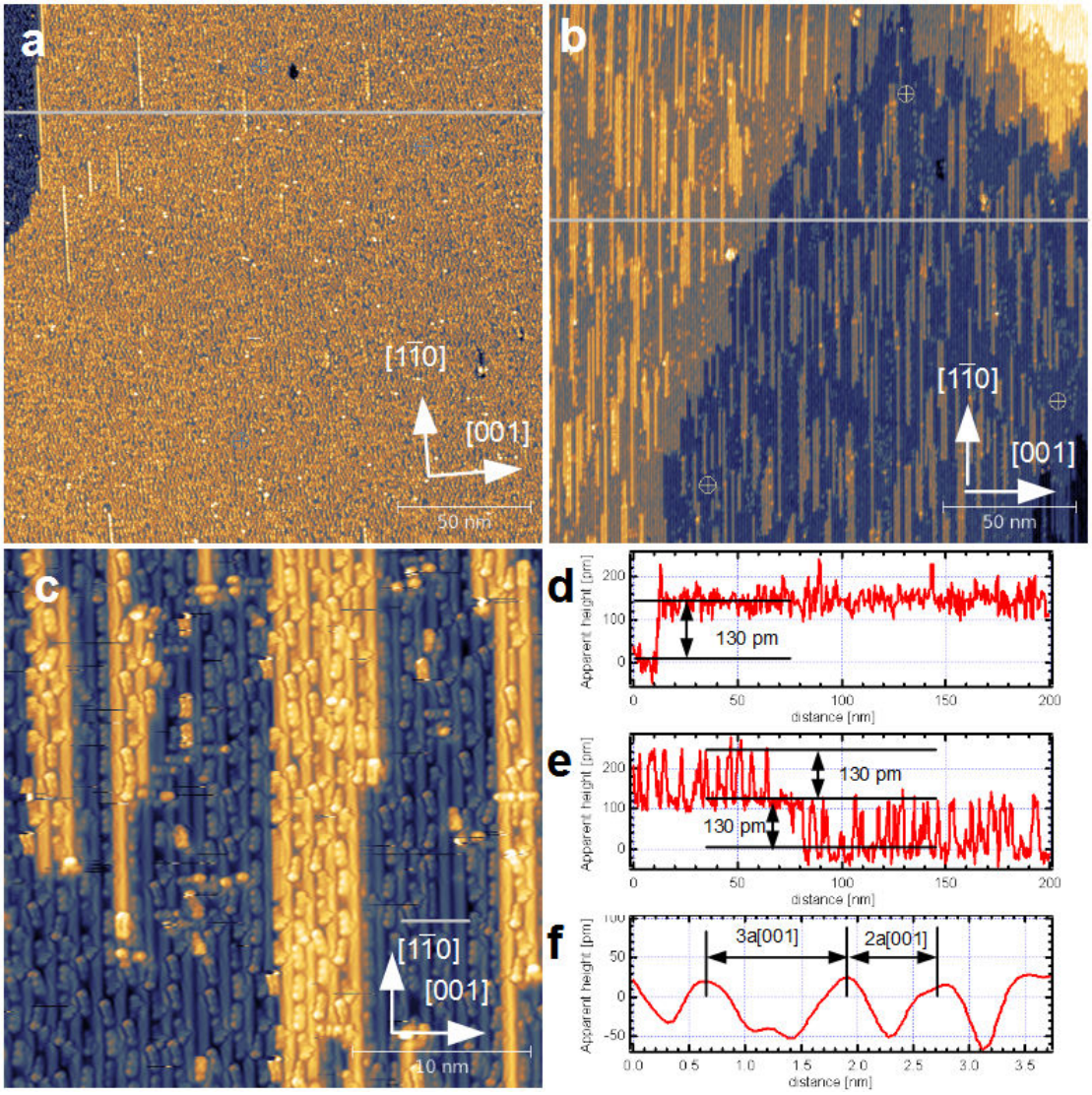

Figure 2.14.: STM image of DHTAP on Au(110) at T=210 K. a) 0.37 ML; 200 nm x 200 nm; U_b=0.9 V; I_t=30 pA. b) Same sample after annealing one night at RT under UHV conditions: 200 nm x 200 nm; U_b=1.04 V; I_t=90 pA. c) 30 nm x 30 nm; U_b=0.5 V; I_t=90 pA. d) STM profile measured before annealing the sample (grey line in a)). e) STM profile measured after annealing the sample (grey line in b)). f) STM profile measured in c) (grey line).

A STM image at smaller scale is presented in figure 2.14.c. The higher resolution of this STM image allows us to distinguish molecules lying in different orientations and gold rows running in the $[1\bar{1}0]$ close packed direction. Apparent

height measurements have been performed (see figure 2.14.f, corresponding to the grey line in figure 2.14.c). Inter-row distance measurements are clearly in very good agreement with the inter-row distance of the (1x3) structure along the $[001]$ direction. Due to these observations we can conclude that during annealing at room temperature, DHTAP molecules induce a reconstruction from the (1x2) to the (1x3) structure of the Au(110) surface. The formation of the (1x3) from the (1x2) structure causes the release of gold atoms. These released atoms diffuse on the surface and lead to the formation of the observed atomic gold wires running in the $[1\bar{1}0]$ direction. All these new wires show the (1x3) structure.

Various experiments have been performed to determine at which temperature the reconstruction takes place, in order to avoid this reconstruction and obtain a well-ordered film. A closer look in the upper part of the STM picture 2.14.a allows us to distinguish six bright stripes aligned with the $[1\bar{1}0]$ direction which can now be identified as gold atomic rows. This deposition has been performed at 210 K and the reconstruction of the surface already takes place during the deposition process, but it stops after the transfer of the sample inside the LT chamber, where it is cooled to LN_2 temperature. Other depositions performed at 200 K did not lead to the appearance of these atomic rows, consequently we decided to keep the substrate temperature below 200 K during further depositions of DHTAP to avoid this reconstruction. The temperature should however not be too low in order to avoid trapping of the molecules in a diffusion limited state.

2.2.3. DHATP/Ag(110)

STM images of the evolution of the growth process of DHTAP on Ag(110) at submonolayer coverage as a function of the temperature are depicted in figure 2.15.

For a coverage of 0.42 ML deposited at 180 K, a new structure appears as shown in figure 2.15.a. DHTAP molecules self-organize in molecular wires running in a particular direction: $\pm 39 \pm 5^\circ$ with respect to the $[1\bar{1}0]$ direction (see histogram in figure 2.15.b). Apparent height and intermolecular distance measurements have been carried out on these wires and and the ones running in the $[001]$ direction are displayed in 2.15.c and 2.15.d.

The molecular wires running along the $[001]$ direction show an intermolecular distance of 0.82 ± 0.02 nm equal to twice the interatomic Ag distance along the $[001]$ direction. The apparent height is 108 ± 15 pm, in agreement with a flat lying configuration as mentioned previously. Concerning the other kind of molecular wire, showing an angle of $\pm 39 \pm 5^\circ$ with respect to the $[1\bar{1}0]$ direction, the intermolecular distance (along the wire axis) is 0.67 ± 0.05 nm and the apparent height is 145 ± 20 pm. An angle close to 10° has been determined between the long molecular axis and the normal of the wire axis, leading to an intermolecular distance of 0.66 ± 0.05 nm. These values remain in agreement with a flat lying absorption but these wires are not commensurate with the Ag(110) substrate,

unlike wires running in the $[001]$ direction.

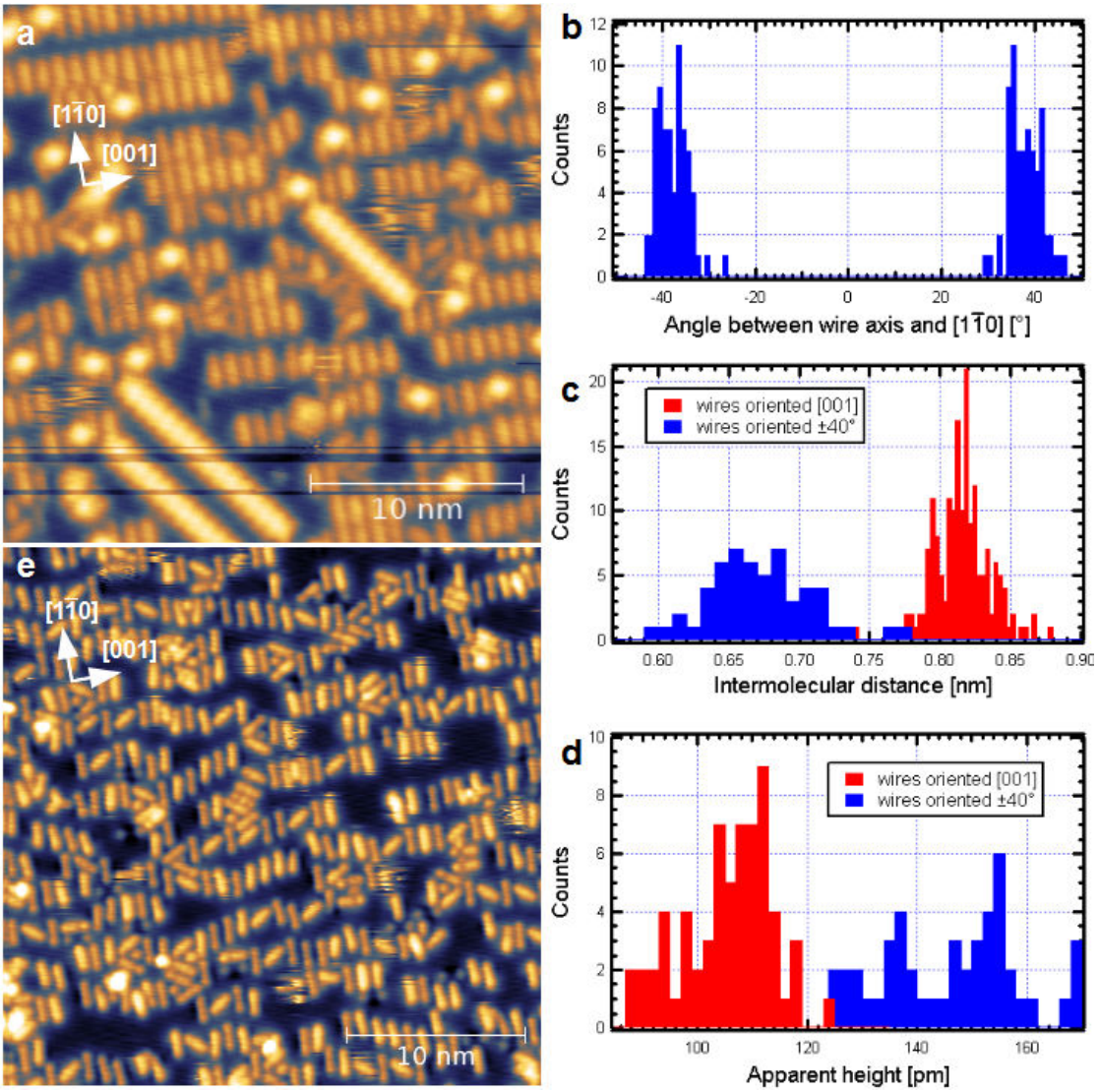

Figure 2.15.: a) STM picture of 0.42 ML of DHAP/Ag(110) deposited at 180 K (25 nm x 25 nm; U_b=0.9 V; I_t=100 pA). b) Angle between the $[1\bar{1}0]$ direction and the long axis of the new observed molecular wires. c) Intermolecular distance measured for both kinds of wires observed at LT. d) Apparent height of both kinds of wires. e) STM picture of 0.39 ML of DHAP/Ag(110) deposited at RT (30 nm x 30 nm; U_b=0.5 V; I_t=40 pA).

Interestingly, for DHTAP deposition of 0.39 ML performed at RT, we observe in the STM image displayed in figure 2.15.e that molecules adsorb preferentially with the long molecular axis parallel within $\pm 5^\circ$ to the $[1\bar{1}0]$ direction (70%) or with an angle of $\pm 56 \pm 6^\circ$ with respect to the $[1\bar{1}0]$ direction (30%). However, as

in the case observed at lower coverage, the formation of well-ordered molecular wires does not take place at RT.

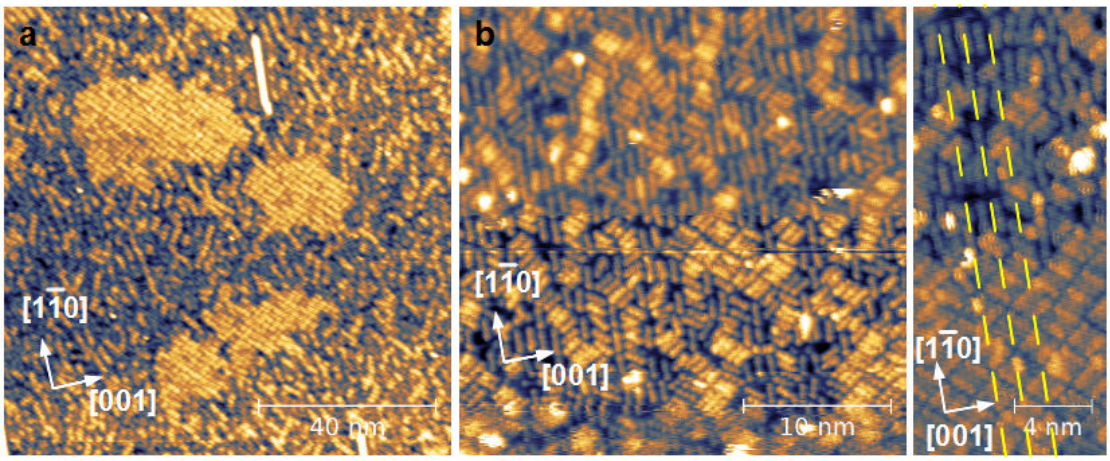

Figure 2.16.: a) STM image of 0.67 ML of DHTAP deposited at RT on Ag(110) (100 nm x 100 nm; U_b=0.5 V; I_t=40 pA). b) STM image performed on the same sample at smaller scale (30 nm x 30 nm; U_b=0.2 V; I_t=1.5 nA). c) STM image (10 nm x 22.5 nm) allowing the determination of the position of the center of a molecular trimer.

The next coverage investigated was 0.67 ML. A typical STM picture at large scale is shown in figure 2.16.a. We can see that the formation of 2D molecular island is taking place randomly on large mono-atomic terraces. However, individual molecules cannot be resolved at this scale.

A second STM image (2.16.b), obtained at smaller size allowed us to identify the origin of this 2D molecular structure. We can see that bright squares observed on the large scale STM image are constituted of three molecules aligned side by side. Interestingly its appears that two adjacent trimers have opposed molecular orientations.

The detailed structure of the film will be treated in section 2.3.3, however, an important information concerning the relative position of these trimers and the substrate can be obtain and is underlined in the figure 2.16.c. Indeed, we know from the section 2.1.3 that DHTAP molecules adsorbing on Ag(110) with their long molecular axes aligned with (or close to) the $[1\bar{1}0]$ direction have their central phenyl ring on top of a silver atom of the second atomic Ag layer. If we look carefully at the alignment of the center of trimers (equivalent to the center of the molecule in the middle of the trimer), as indicated by dashed yellow lines in the STM picture, we can see that the center of trimers are in the alignment with the long molecular axis of molecules localized on the upper part of the picture, or at half distance between two molecules. This clearly indicates that the center of a DHTAP trimer is localized between two silver atomic rows running

in the $[1\bar{1}0]$ direction.

On the STM pictures obtained for coverages of 0.67 ML, we can also observe that 40% of DHTAP molecules adsorb with their long molecular axis close to the $[1\bar{1}0]$ direction and 60% adsorb with an angle of $\pm 51 \pm 5°$. These differences compared to observations done at 0.42 ML is another nice example of the relative interplay between intermolecular interactions and molecule-substrate interactions.

2.2.4. Discussion

The growth process of DHTAP at submonolayer coverages deposited on different metal substrates is strongly influenced by the temperature of the substrate as underlined in the first section. On Au(111), at 250 K, and at low submonolayer coverage, the growth process is mainly influenced by the molecule-substrate interactions leading to the formation of molecular wires which start to grow on fcc domains up to the completion of these regions then on hcp domains. DHTAP forms molecular wires which clearly indicate an influence of the intermolecular interactions. At coverages around 0.75 ML intermolecular interactions becom more important due to the increase of the molecular density. Molecular wires do not follow the herringbone structure of the surface anymore, but start to form 2D molecular domains with particular orientations still reflecting the influence of the substrate. Monte Carlos simulations are in very good agreement with the observations made by STM: preferential growth on fcc domains at low coverages, formation of molecular wires, increase (resp. decrease) of the influence of the intermolecular (resp. molecule-substrate) interactions with the coverage. Moreover, they suggest a head to tail configuration of molecules constituting wires.

Another very interesting phenomenon concerning the temperature effect has been observed for DHTAP deposited on Au(110): the surface reconstruction from the (1x2) to the (1x3) structure. Above 200 K DHTAP molecules deposited on a freshly prepared (1x2) reconstructed surface induce a (1x3) reconstruction of the surface. This phenomenon has already been observed by STM in the case of pentacene[93] deposited at RT on Au(110). Other surface reconstructions ((1x5), (1x6), stepped (1x2)) have been observed for C_{60}[94] deposited at RT on Au(110). Unfortunately no information concerning the temperature dependence of the molecular induced reconstruction could be found. The reconstruction of Au(110) (1x2) to (1x3) structure is well-known from investigations by the means of HAS (helium atom scattering), LEED, and GIXD (grazing incidence X-ray diffraction) for copper-phtalocyanine deposited at RT.[95]

In the case of DHTAP on Au(110) deposited at a temperature around 200 K the appearance of different molecular structures is dependent on the molecular density. During the early first steps of growth DHTAP molecules adsorb on the surface with a particular orientation ($\pm 30 \pm 3°$) imposed by the substrate. At more

important molecular density, a new structure is observed, where molecules self-assemble in dimers in a bridge position between two gold rows running along the $[1\bar{1}0]$ direction. The intermolecular distance is in agreement with a possible establishment of hydrogen bonds stabilizing the dimers, assuming a head to tail configuration. In this case the angle between the long molecular axis and the $[1\bar{1}0]$ direction is $\pm 50 \pm 3°$. DHTAP molecules are also observed to adopt a configuration with their long molecular axis parallel to the $[1\bar{1}0]$ direction. We observe that the relative proportion of DHTAP lying in these different configurations is dependent with the coverage. Finally, at coverages close to the monolayer, most of the molecules are observed with their long molecular axis aligned with the $[1\bar{1}0]$ direction.

On Ag(110) the observations concerning the temperature dependence done in the first section are still valid. Low temperature depositions first lead to the formation of molecular wires, which are commensurate along the $[001]$ direction. At coverages of 0.42 ML, the formation of a new kind of wire, not commensurate, is observed. From STM observations, it seems that the formation of wires, running along the $[001]$ are mainly influenced by molecule-substrate interactions (commensuration). On the other hand, the formation of wires running in a direction tilted from $\pm 39°$, seems to be mainly influenced by intermolecular interactions (appearance at higher molecular denity and decrease of the intermolecular distance). In the case of deposition performed at RT the growth of these commensurate wires along the $[001]$ direction does not take place, even if most of the molecules are close to an alignment of their long molecular axis with the $[1\bar{1}0]$ direction. Increasing the coverage leads to the appearance of a new orientation for the DHTAP molecule deposited at RT. Finally at 0.67 ML the influence of the intermolecular interactions becomes stronger than the molecule-substrate interactions which leads to a phase transition and to the formation of a highly-ordered islands constituted by DHTAP trimers lying in two different orientations. Moreover, it turns out that the center of these trimers are localized in a bridge position between two rows of silver atoms running in the $[1\bar{1}0]$ direction.

The growth process of DHTAP at submonolayer coverage is strongly influenced by the temperature, which can leads to the formation of kinetically limited structures, and depends on the balance between intermolecular interactions and molecule-substrate interactions which leads to the formation of different structures depending on the substrate symmetry.

2.3. DHTAP on noble metal surfaces: above the monolayer

2.3.1. DHATP/Au(111)

In order to conclude the study of the structure of the first monolayer, we decided to perform a deposition slightly above the monolayer density to ensure that the most compact monolayer structure is established. The STM images in figure 2.17 have been recorded for a coverage of 1.07 ML of DHTAP deposited at 250 K on Au(111).

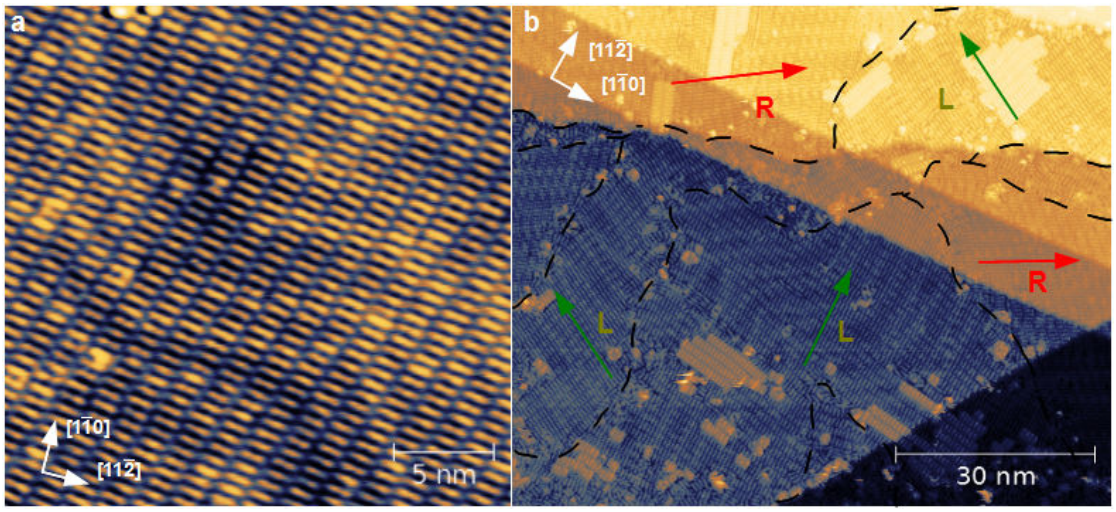

Figure 2.17.: a) STM image (30 nm x 30 nm) of a well-ordered domain of DHTAP deposited on Au(111) at 250 K. b) STM image (90 nm x 75 nm; U_b=1.21 V; I_t=200 pA) of 1.07 ML of DHTAP/Au(111). Black dotted lines underline domain boundaries and coloured arrows the orientation of the domains.

The image 2.17.a displays a large well-ordered domain (30 nm x 30 nm) of self-assembled DHTAP. The second STM image, shown in 2.17.b, has been recorded at larger scale. Some molecular islands corresponding to the formation of the second monolayer are observed. We will return to this later. A closer inspection of this image reveals that a great number of domains are present, which are indicated by the black dotted lines. These domains possess a particular orientation with respect to the $[1\bar{1}0]$ crystallographic direction of the surface, e.g. the densely packed rows of gold atoms. This direction can be determined unambiguously in the STM picture 2.17.b by the presence of the straight monoatomic steps which run into the $[1\bar{1}0]$ direction. Two mirrored domains have been identified, and we have observed six different orientations for each domain, which are rotated by 60° with respect to each other. Four of these orientations are indi-

cated by red (R) and green (L) arrows in the STM picture. Thus the orientation of the domains perfectly reflects the symmetry of the Au(111) substrate. It turns out that the R domain is rotated by 32° and the L domain is rotated by 28° with respect to the $[1\bar{1}0]$ direction of the Au(111) surface.

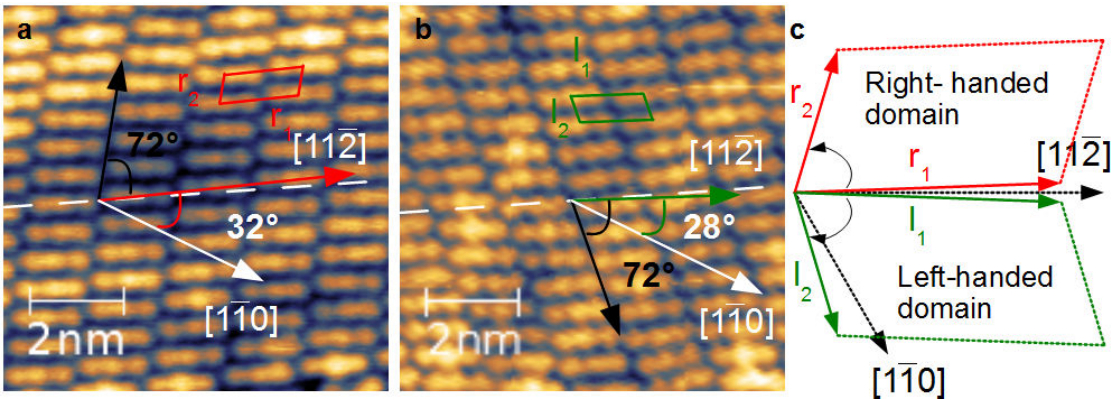

Figure 2.18.: a) STM image of the R-domain, white arrow indicates the Au(111) close packed direction. U_b=1 V; I_t=80 pA. b) STM image of the L-domain. U_b=1 V; I_t=80 pA. c) Schematic representation of both domains mirrored by horizontal reflection (along $[11\bar{2}]$).

Both R- and L-domain have a unit cell angle of 72±3° and are shown in figure 2.18.a and 2.18.b respectively. The experimentally measured unit cell distances between two neighbouring DHTAP molecules (measured center to center) in the long molecular axis direction are $\mathbf{r}_1$=$\mathbf{l}_1$=1.56±0.08 nm and the second unit cell vectors have a length of $\mathbf{r}_2$=$\mathbf{l}_2$=0.61±0.03 nm leading to an estimated molecular density of 1.11x10^{14} molecules per cm^2. The figure 2.18.c displays a schematic representation of both R- and L-domains and underlines the above-mentioned mirrored symmetry with respect to the $[11\bar{2}]$ direction.

These results are confirmed by the LEED pattern shown in figure 2.19. The first image shown in figure 2.19.a allows us to determine the orientation of the gold surface, relative to the diffraction pattern of the molecular film in the center, which is not well resolved. A lowering of the electron energy results in the well resolved pattern shown in figure 2.18.b. A first feature that can be observed is the six fold symmetry of the LEED pattern and the two symmetry axes, perpendicular to each other. A close analysis of these LEED patterns and the combination of the available information allowed us to deduce the schematic representation displayed in figure 2.19.c.

The software package LEEDpat[96] has been used to identify the different spots of the diffraction pattern using the unit cell parameters and the relative orientation between the film and the surface determined by STM. In the figure 2.19.c the unit cell vectors in the reciprocal lattice ($\mathbf{r}_1^*$, $\mathbf{r}_2^*$, $\mathbf{l}_1^*$, and $\mathbf{l}_2^*$) are shown which

are related to the unit cell vectors determined by STM in the direct lattice. A schematic view of the surface and the corresponding unit cell of a R-domain are shown in figure 2.19.d.

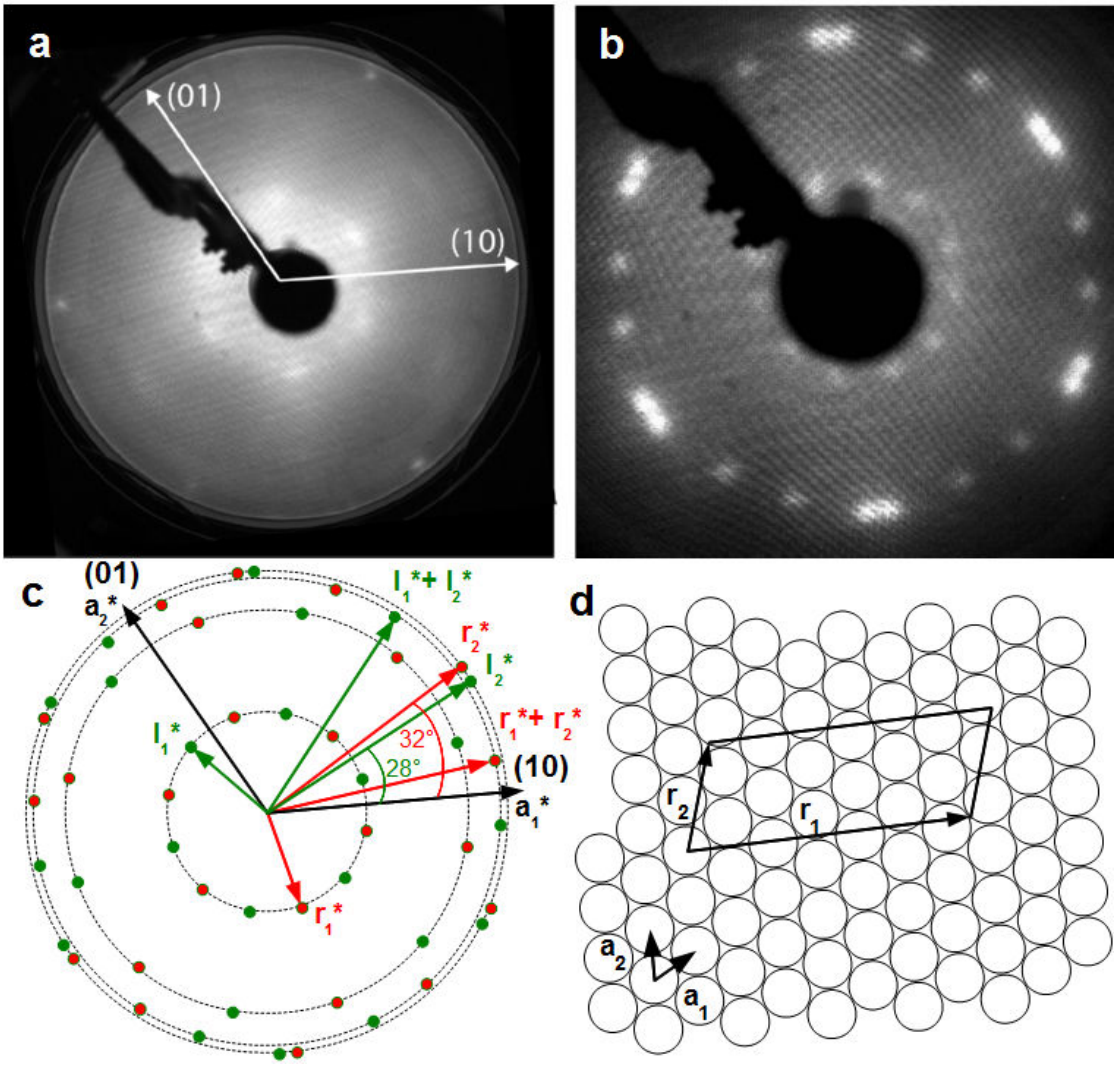

Figure 2.19.: a) LEED diffraction pattern of 1.07 ML of DHTAP/Au(111) at an energy of 43.6 eV revealing the orientation of the close pack $[1\bar{1}0]$ direction in the reciprocal lattice. b) LEED pattern of the same system at an energy of 17.6 eV. c) Schematic representation of the LEED pattern combining the orientation of the close packed direction and the information concerning the DHTAP layer. d) Schematic view of the surface and the unit cell of the R-domain.

In the figure 2.19.c the green and red spots (indicated by coloured vectors noted $\mathbf{l}_2^*$ and $\mathbf{r}_2^*$) correspond to first order diffraction spots which are related to

the $\mathbf{r}_1$ and $\mathbf{l}_1$ unit cell vectors, respectively. We find six spots corresponding to the R-domain likewise we find six spots for the L-domains due to the symmetry of the surface. These diffraction spots clearly possess the rotation angle found in STM images, 28° and 32° with respect to the $[1\bar{1}0]$ closed-packed direction of the Au(111) surface. This indicates that the long molecular axis is oriented by $\pm 2°$ with respect to the $[11\bar{2}]$ direction of the Au(111) surface. Second order diffraction spots can also be observed in these directions, however the intensity of these spots is very low in the LEED pattern. The remaining spots, indicated again in red and green, correspond to first order diffraction spots attributed to the linear combination, $\mathbf{r}_1^*$ + $\mathbf{r}_2^*$ and $\mathbf{l}_1^*$ + $\mathbf{l}_2^*$, respectively. Furthermore, the ratio of the norm of the vectors $\mathbf{r}_2^*$ and $\mathbf{r}_1^*$ is very similar to the ratio of the norm of the vectors $\mathbf{r}_1$ and $\mathbf{r}_2$, which indicates that both STM and LEED experiments are in good agreement.

Superstructures formed by adsorbates or rearrangements of the surface atoms can lead to a periodicity of the surface lattice greater than that of the bulk-truncated single crystal. In these cases, the lattice vectors for the superstructure, $\mathbf{b}_1^*$ and $\mathbf{b}_2^*$, can be related to the lattice vectors of the bulk-truncated surface, $\mathbf{a}_1^*$ and $\mathbf{a}_2^*$, through:

$$\mathbf{b}_1 = m_{11}\mathbf{a}_1 + m_{12}\mathbf{a}_2$$

$$\mathbf{b}_2 = m_{21}\mathbf{a}_1 + m_{22}\mathbf{a}_2$$

The numbers m_{ij} are the coefficients of the superstructure matrix:

$$M = \begin{pmatrix} m_{11} & m_{12} \\ m_{21} & m_{22} \end{pmatrix}$$

which is a straightforward way of characterising any superstructure.

The unit cell matrix (irrational due to the non-commensuration between the film unit cell and the substrate lattice) can also be simply obtained using the software utility LEEDpat and the results of STM measurement:

$$M = \begin{pmatrix} 6.25 & -2.94 \\ 0.67 & 1.70 \end{pmatrix}$$

The results presented so far have revealed the overall structure and the orientation of the DHTAP films, but the internal structure of the molecular rows has not been elucidated. The results suggest, however, that an interaction between rows stabilizes the DHTAP layers. We have thus explored the details of the internal structure of the layers. The DHTAP molecules, as opposed to pentacene, do not have a symmetry plane perpendicular to the long molecular axis, as mentioned before. It should thus be possible to identify the molecular orientation from STM images. Unfortunately, STM images of the first monolayer have not revealed this asymmetry independently of the applied bias voltage, probably due to screening effects by the metallic substrate. We have thus turned our attention

to the investigation of the second layer, in which the molecules should be better decoupled from the substrate.

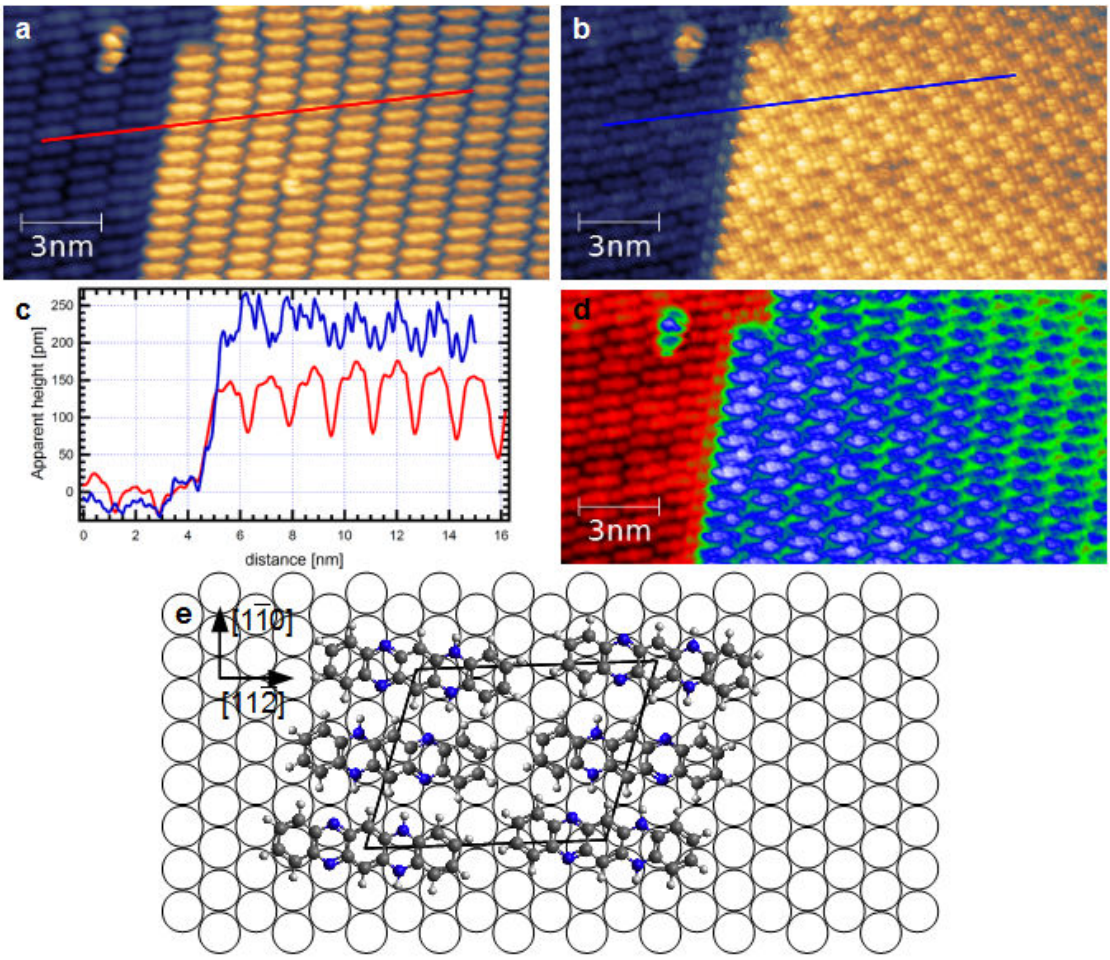

Figure 2.20.: a) STM image of the first and the second layer of DHTAP deposited on Au(111) (at 250 K) acquired in forward direction. U_b=1 V; I_t=30 pA. b) STM image of the same area of panel a) acquired in backward scan direction. U_b=-1 V; I_t=30 pA. c) STM profile performed on both STM images (a: red; b: blue). d) Superposition of images a) and b). e) Corresponding ball and stick model.

Figure 2.20.a shows a STM image of 1.6 ML of DHTAP deposited at 250 K and obtained at a bias voltage of $U_b = +1$ V. The apparent height of the second layer is 160$\pm$20 pm (see profiles in 2.20.c (red curve) and 2.21.c), again indicating flat-lying molecules. It can furthermore easily be seen that the second layer grows in epitaxy with the first layer.

Concurrently with the forward scan, we have imaged the layer with a sample bias of U_b=-1 V on the backward motion of the scan for each scan line. The

resulting image is shown in figure 2.20.b. The two images thus correspond to exactly the same position on the sample. In figure 2.20.b, an important alteration of the molecular contrast can be seen as compared to figure 2.20.a, clearly indicating the above-mentioned asymmetry of the molecules.

An increase of the apparent height, from 160±20 pm to 250±20 pm is observed and shown in figure 2.20.c. This suggests that we are tunnelling into the molecular orbitals of the compound at the bias voltage U_b=-1 V. However, the identification of the individual DHTAP molecules becomes more difficult in this case. We have thus superposed the two images, which resulted in the image displayed in figure 2.20.d. Here the individual DHTAP molecules can easily be identified in the second layer, and, moreover, the above-mentioned asymmetry is clearly visible.

A bright lobe can be identified for each DHTAP molecule, which is either on the right-hand side or the left-hand side of the molecule. We can, therefore, confirm a head-to-tail arrangement of the DHTAP molecules in adjacent lines, which gives rise to N-H$\cdots$N hydrogen bonding between adjacent molecules. Based on the unit cell parameters and orientations deduced above, we propose the model of the R-domain shown in figure 2.20.e. One should note that our measurements do not unequivocally allow assigning a specific adsorption site to the DHTAP molecules but rather show the orientation of the long molecular axis with respect to the substrate. From this model we can deduce the length of the N-H$\cdots$N hydrogen bonds, which corresponds to 3.3 Å. This bond length is well within the typical range for N-H$\cdots$N hydrogen bonds proposed by Steiner et al.[97] which is 2.5 Å to 3.4 Å.

Taking into account the head to tail arrangement of the DHTAP molecules along a molecular row allows us to determine a new unit cell for this system with the following parameters: $\mathbf{b}_1$=1.56±0.08, $\mathbf{b}_2$= 1.22±0.06 nm and θ=72±3°.

Due to the excellent order of the DHTAP thin film grown on Au(111), the growth properties have been studied up to the beginning of the formation of the fourth monolayer. The STM image displayed in figure 2.21.a illustrates the long range order of the film deposited at 250 K and confirms the observation made in the figure 2.10.f concerning the fact that boundaries of well-ordered domains follow the elbows of the underneath substrate (indicated by white dashed lines).

The STM image shown in figure 2.21.b illustrates the growth mode observed for DHTAP on Au(111) under these conditions: the Stranski-Krastanov mode. In this case the formation of 3D molecular islands takes place after the formation of two complete monolayer of DHTAP. This image has been recorded for a coverage of 2.6 ML. The layer in blue corresponds to the second monolayer, the yellow is the third monolayer and we can observe the beginning of the formation of the fourth monolayer, constituted of seven DHTAP molecules grown in epitaxy with the molecules of the underneath layers.

The apparent height of DHTAP in this case is 250±20 pm, for both third and fourth layers, as shown in the figure 2.21.d. Due to the epitaxial growth of

he layers the unit cell parameters remain unchanged compared to the unit cell parameters defined for both first and second layers. The increase of the apparent height is in fact due to the applied bias voltage (-1.4V) which allows to image molecular orbitals of DHTAP, as in the case of the STM image 2.20.b obtain a a bias voltage U_b=-1 V.

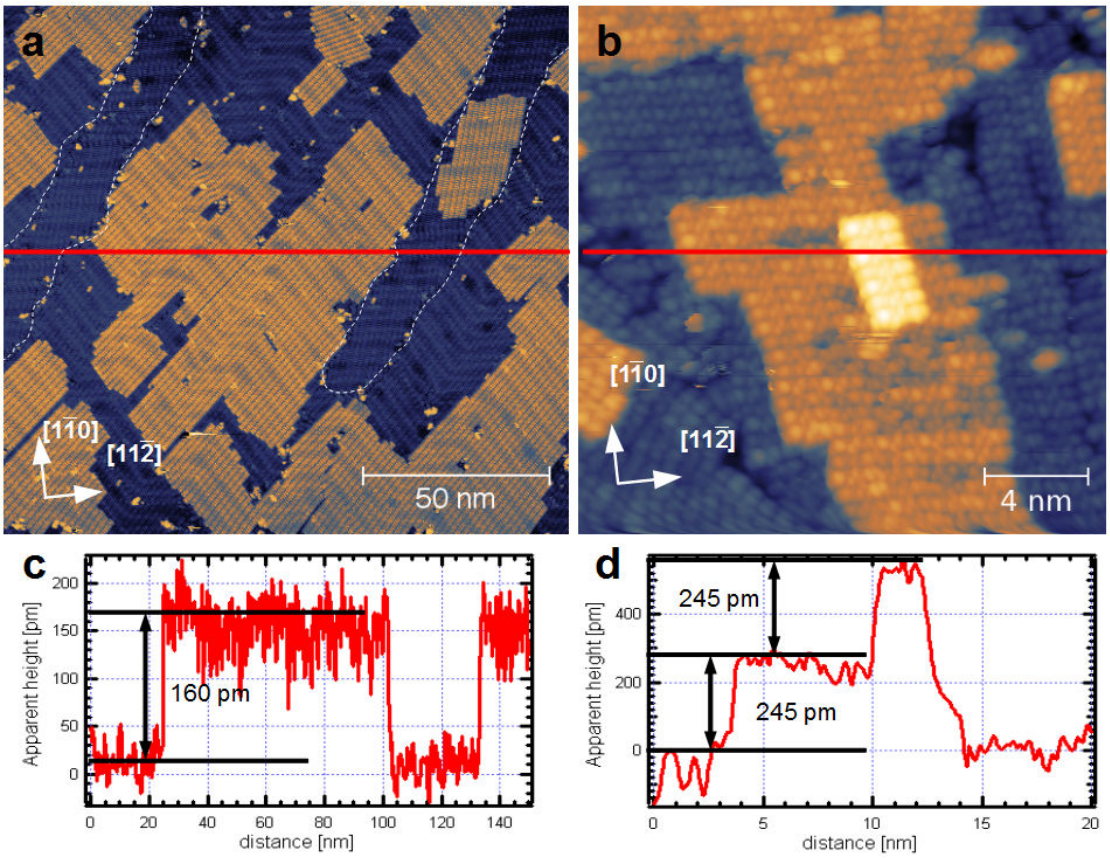

Figure 2.21.: a) STM image (150 nm x 150 nm) of 1.6 ML of DHTAP on Au(111) deposited at 250 K. U_b=1.6 V; I_t=50 pA. b) STM image (30 nm x 30 nm) of 2.6 ML of DHTAP on Au(111) deposited at 250 K. U_b=-1.4 V; I_t=20 pA. Note the appearance of DHTAP molecules of the fourth layer before the completion of the third, illustrating a Stranski-Krastanov growth mode. c) STM profile corresponding to the red line in a). d) STM profile corresponding to the red line in b).

2.3.2. DHATP/Au(110)

The STM images obtained for a coverage of 1.1 ML of DHTAP deposited on Au(110) are displayed in figure 2.22.

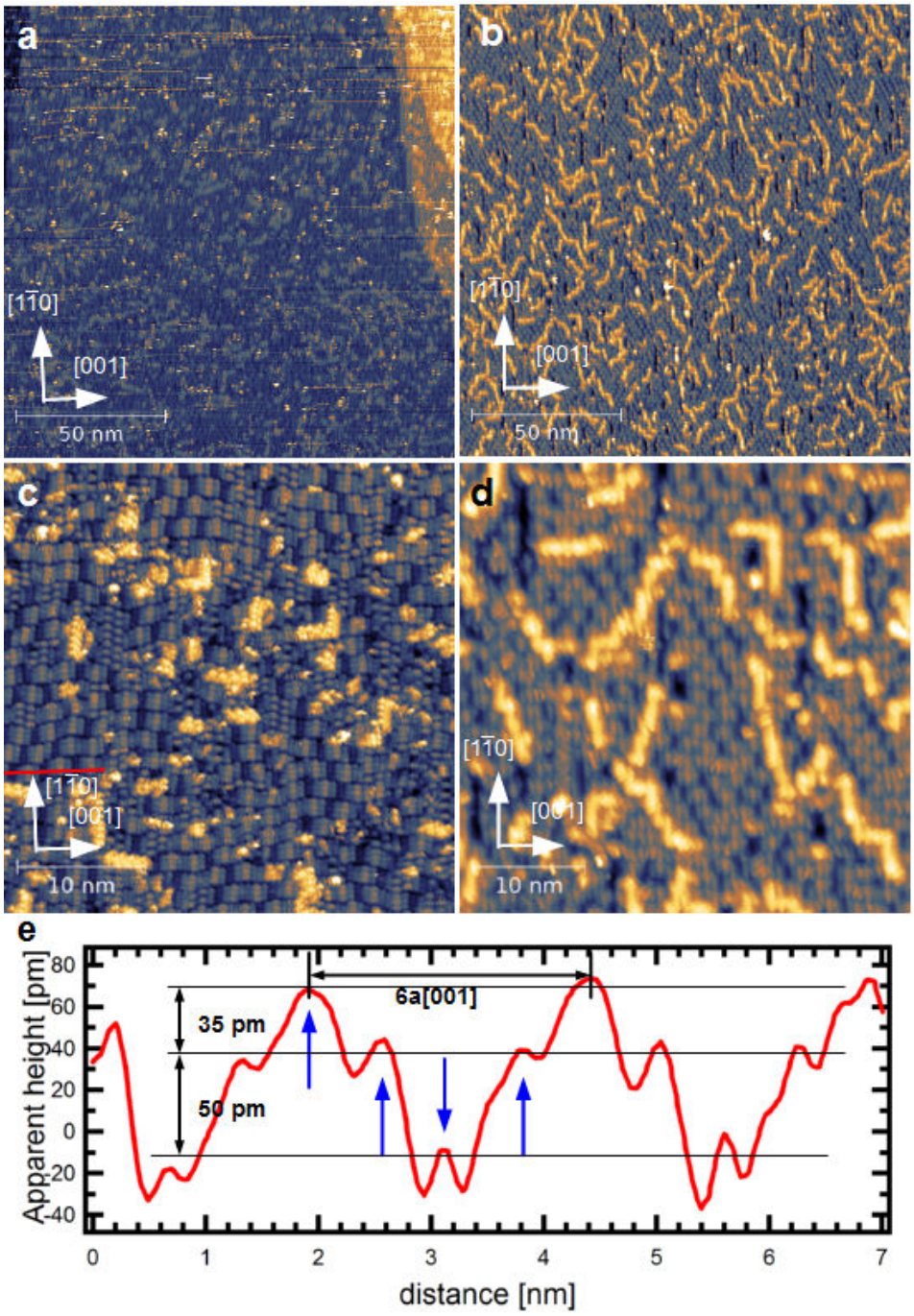

Figure 2.22.: STM image of 1.1 ML of DHTAP on Au(110) deposited at T=200 K. a) 150 nm x 150 nm; U_b=0.88 V; I_t=40 pA. b) After annealing one night at room temperature. 150 nm x 150 nm, U_b=1.1 V, I_t=30 pA. c) 35 nm x 35 nm; U_b=0.71 V; I_t=90 pA. d) Same sample after annealing; 35 nm x 35 nm, U_b=-1 V, I_t=50 pA. e) STM profile corresponding to the red line in c).

Image 2.22.a (150 nm x 150 nm) has been obtained after a deposition at 200 K. DHTAP molecules can be identified in the second layer, however no order at large scale can be observed. The limited diffusion of DHTAP at the temperature used during deposition can be the reason why no ordered structure is observed. The STM image 2.22.b has been recorded after annealing this sample for one night at RT under UHV conditions. We observe that the annealing leads to the formation of long molecular wires on the top of the first monolayer. This can be explained by a more important diffusion at RT of DHTAP molecules localized on top of the first monolayer. These wires observed in second monolayer show an apparent height of 140±20 pm, however, the resolution of STM images does not allow us to determine with accuracy the distance between two neighbouring molecules. The irregular form of these wires suggests that the molecule in the second layer are not in epitaxy with molecules of the first layer.

Images 2.22.c and 2.22.d correspond to a zoom of the previous images. At this scale it is possible to resolve individual molecules constituting the first monolayer and we can observe that most of molecules adopt an orientation with the long molecular axis in alignment with the $[1\bar{1}0]$ direction. This is in agreement with the trend observed in the previous section, where the DHTAP orientation evolves with the molecular density to finally lie mostly with the long molecular axis parallel to the $[1\bar{1}0]$ direction.

After deposition at 200 K (figure 2.22.c), only a few molecules are oriented with an angle of $\pm 70 \pm 10^{\circ}$ and the distance between molecules with these orientations constituting structures along the $[1\bar{1}0]$ direction is 0.66±0.05 nm. These measurements are not in agreement with a commensuration between the substrate and molecules showing these orientations. The orientation of this structure, and the previous observations suggest that this structure arises from a reorganization of the previously observed structure displaying an orientation of $\pm 50 \pm 3^{\circ}$. It seems that this reorganization leads to the formation of a kinetically limited structure, due to the combination of an increase in the molecular density and the limited diffusion of the molecules, due to the low temperature of the substrate during deposition.

Another interesting point concerning the structure of the first monolayer is related to molecules oriented with the long molecular axis along the $[1\bar{1}0]$ direction. It clearly appears that molecules in this configuration also tend to be aligned side-by-side along the $[001]$ direction. A profile along this direction (shown in figure 2.22.e, corresponding to the red line in the STM image 2.22.c) clearly shows three different apparent heights for the DHTAP molecules, and a commensuration of this structure constituted by four molecules (indicated by blue arrows) and the underneath substrate. The intermolecular distance between these molecules with different apparent height is 0.61±0.05 nm. This periodic structure has been already observed at a coverage of 0.89 ML (see subsection 2.2.2, figure 2.13.e and 2.13.f). A model for this structure will be introduced later.

After the annealing of this sample for one night at RT, interesting changes are observed: on the large scale image (2.22.b) we clearly observe that molecules constituting the second layer self-assemble to form longer wires. In the STM image in figure 2.22.d we can see that molecules constituting the first monolayer are now all aligned in the $[1\bar{1}0]$ direction. No molecules are observed with a tilted geometry anymore. This indicates that performing an annealing at RT of a complete monolayer leads to the reorganization of some of the molecules constituting the first layer, but without the reconstruction of the substrate (from the (1x2) to (1x3) structure) that has been observed for annealing of submonolayer coverages performed at RT.

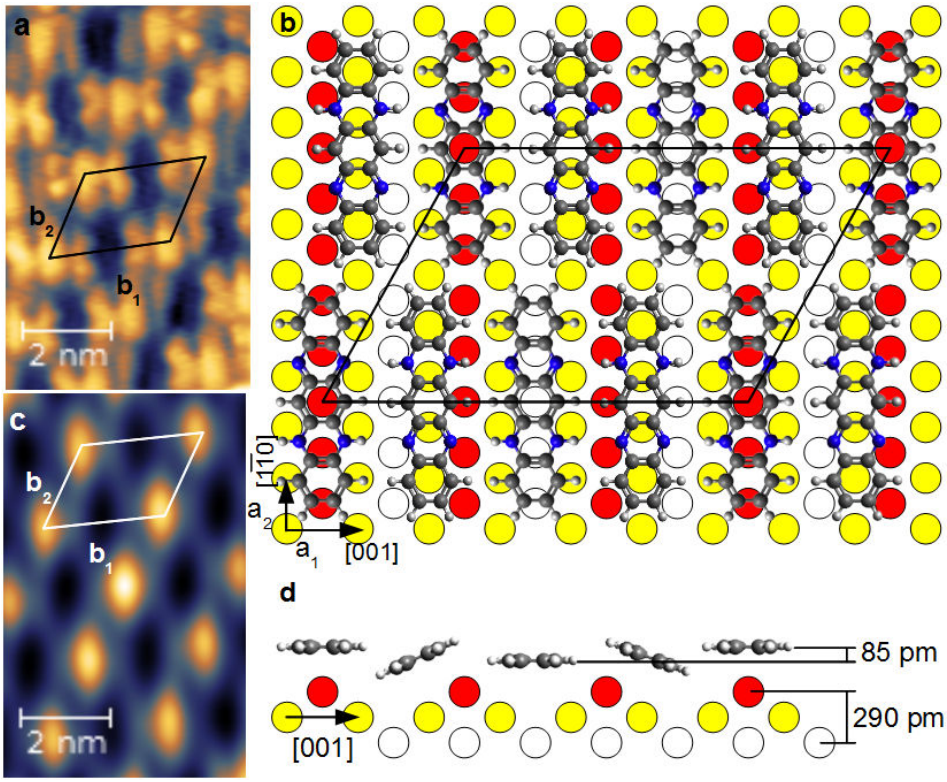

Figure 2.23.: a) STM image of the ordered first monolayer after annealing a RT (5.4 nm x 8.5 nm, U_b=0.88 V, I_t=50 pA). b) Corresponding ball and stick model (top view). c) 2D-autocorrelation of the STM picture in a), allowing a precise determination of the periodicity. d) Side view of the ball and stick model.

As discussed before, the complete monolayer shows an ordered structure, especially after annealing at RT, where all molecules are oriented with the long molecular axis parallel to the $[1\bar{1}0]$ direction. The first monolayer of DHTAP shows domains with particular high symmetry as depicted in the figure 2.23.a.

Figure 2.23.c is a 2D-autocorrelation of this STM image which underlines the periodicity of this structure and allows a precise determination of the unit cell parameters: $\mathbf{b}_1$=2.47±0.1 nm; $\mathbf{b}_2$=1.72±0.1 nm, θ=58±5°. The unit cell contains four DHTAP molecules. From these measurements we can estimate a molecular density of 1.11x10^{14} molecules per cm^2.

Apparent heights of these molecules are different, as underlined before, and allow a classification in three types: darkest molecules in a lower position, intermediate molecules (x2) with an apparent height around 50 pm above darkest molecules and finally, brighter molecules, on top, with an apparent height larger by 85 pm, still referring to the darkest molecule (see figure 2.22.e).

Moreover, the length and the orientation of the unit cell vector $\mathbf{b}_1$ is in good agreement with a commensuration between the molecular structure and the substrate: in the case of the (1x2) reconstruction, the distance between gold rows along the $[001]$ direction is 0.816 nm. The distance between two molecules showing the highest apparent height is equal to three times this value (2.47±0.1 nm). The distance between the darkest and the brightest molecule along the $[001]$ direction is 1.23±0.05 nm. This can explain differences observed in apparent heights: assuming brighter molecules are localized on top of a gold row, the closest darkest molecule in the $[001]$ direction is consequently localized between two gold rows. Consequently, the two other molecules, with intermediate apparent height are localized at intermediate positions. Interestingly, the intermolecular distances between these molecules with different apparent heights is constant along the $[001]$ direction (0.61±0.05 nm; see STM profile in 2.24.b).

Considering all these observations and assuming the brightest molecules are localized on top of the gold row running on the $[1\bar{1}0]$ direction, we propose the commensurate model depicted in figure 2.23.c (a side view of the ball and stick model is shown in figure 2.23.d).

Red circles correspond to Au surface layer. Yellow circles are gold atoms in the second layer and white circles are Au atoms located in the third layer. Note that the position of the DHTAP molecule along the $[1\bar{1}0]$ direction relative to the substrate (central benzene ring on top of a gold atom) is arbitrary. We assume that DHTAP molecules with highest and lowest apparent height adsorb with their molecular plane parallel to the surface. Molecule showing intermediate apparent heights are assumed to adsorb on the substrate with their small molecular axes tilted with respect to the surface plane due to two considerations: In the first place, the width of these molecules appears reduced in STM image 2.23.a and 2.24.a. The second reason is related to the underneath substrate: if DHTAP molecules with highest and lowest apparent heights are effectively localized on top and between two rows of gold respectively, the molecule with intermediate apparent height will be localized on top a (111) micro-facet. This suggests that the molecules observed at these positions will adsorb with a titled angle. DHTAP molecules are represented in a head to tail configuration in agreement with the observation done for DHTAP/Au(111). Unit cell parameters of this com-

mensurate model, $\mathbf{b}_{1c}$=24.47 Å, $\mathbf{b}_{2c}$=16.57 Å, θ_c=60.5 ° and the corresponding molecular density (1.13 x 10^{14} cm^{-2}) are in very good agreement with the STM measurements. The corresponding matrix of this structure, with respect to the unreconstructed Au(110) surface, is:

$$M_c = \begin{pmatrix} 6 & 0 \\ 2 & 5 \end{pmatrix}$$

Despite the very high organization of molecular structure observed in this case, different kinds of defects can be observed in the first monolayer, which prevent the formation of larger domains, as in the case of DHTAP deposited on Au(111). Indeed, this well-ordered structure is not observed at very large scale, the periodicity is rarely observed on domains larger than 10 x 10 nm^2. This can be explained by several reasons.

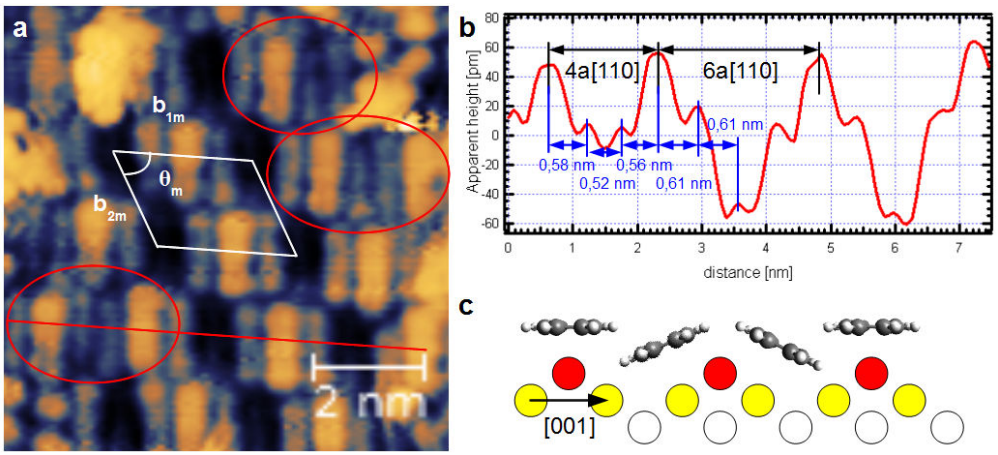

Figure 2.24.: a) STM image of 1.1 ML of DHTAP deposited at 210 K showing a mirrored domain. (7.8 nm x 7.8 nm, U_b=1.13 V, I_t=40 pA). b) STM profile corresponding to the red line in a). c) Ball and stick model corresponding to the structure underlined by red circles, side view.

In the first place, due to symmetry considerations, mirrored domains can be observed. In this case, $\mathbf{b}_{1m}$, $\mathbf{b}_{2m}$ and θ_m, unit cell parameters of the mirrored unit cell, are identical to the unit cell parameters $\mathbf{b}_1$, $\mathbf{b}_2$ and θ respectively. The unit cell vectors $\mathbf{b}_1$ remains aligned with the $[001]$ direction. A STM image of this mirrored domain is depicted in figure 2.24.a.

Another kind of defect can be observed in this STM picture and is underlined by red circles. In this case only two molecules, with similar apparent heights, are observed between two brighter DHTAP molecules (see STM profile in 2.24.b). The distance between these two brighter molecules, from center to center along the $[001]$ direction, is 1.6±0.1 nm. This distance is in very good agreement with

a commensuration between this molecular structure and the Au(110) substrate. A decrease in intermolecular distances is clearly observed and underlined in the STM profile. Moreover, the intermolecular distance between molecules involved in these defect is not constant: a smaller distance between the molecules with the lower apparent height is observed compared to the distance between these molecules and the closest DHTAP with higher apparent height. On the same STM profile, we can observed that the distance between molecules constituting the ordered structure depicted in figure 2.23 is more important and constant. These observations suggests that the molecules involved in the defect have their small molecular axes tilted with respect to the surface plane, as underlined in figure 2.24.c. This leads to the formation of a more compact molecular structure compared to the above-mentioned domain.

Furthermore, we observed in STM images obtained after annealing (2.22.b and 2.22.d) "black" stripes along the $[1\bar{1}0]$ direction. In the STM image depicted in figure 2.25.a and the STM profile in figure 2.25.b we can see that two molecules are present in this depression and show apparent heights lower than all the other DHTAP molecules (see arrows in the STM profile).

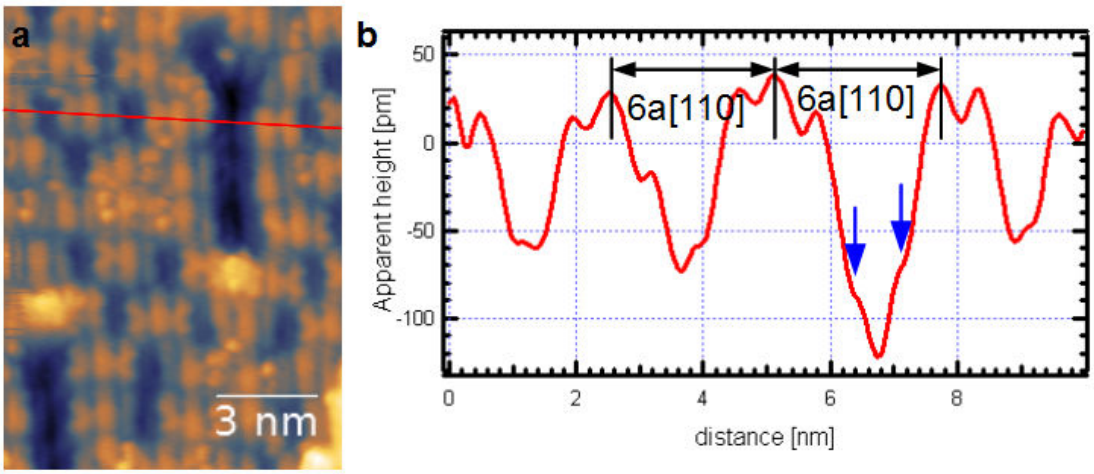

Figure 2.25.: a) STM image of 1.1 ML of DHTAP after annealing at RT showing defects (9.9 nm x 13.5 nm, U_b=1.13 V, I_t=40 pA). b) STM profile corresponding to the red line in a).

The fact that after annealing no molecules are observed with a tilted angle suggests that they reorganize during this process, to lie with their long molecular axis parallel to the $[1\bar{1}0]$ direction. But this implies that the (1x2) reconstructed surface can be exposed during this molecular reorganization and we know that for temperature above 200 K a reconstruction of the surface can take place. In this case, these black stripes could be due to a release of one part of gold atomic rows. This is a hypothesis which can explain these kinds of defects observed only

after annealing the sample at RT.

Even if the growth of well-ordered structure is feasible at very small scale under particular conditions of temperature, the great number of defects (mirrored domains, different molecular structures, reconstruction of the surface above a certain temperature) prevents us to grow larger ordered domains of DHTAP on Au(110).

2.3.3. DHATP/Ag(110)

The STM image depicted in figure 2.26.a has been recorded after the deposition of DHTAP on Ag(110) at 180 K. Molecules constituting the first monolayer show the orientations observed previously for depositions performed at low temperature and submonolayer coverages. Most of them show their long molecular axis aligned with the $[1\bar{1}0]$ direction, or show an angle of $\pm 39 \pm 5^{\circ}$ with respect to this direction. Other molecules, on the upper right part of the STM picture, are observed to adsorb on top of the first monolayer. The intermolecular distances of 0.58 ± 0.05 nm and apparent heights of 190 ± 10 pm suggest that DHTAP molecules adsorb with their short molecular axis slightly tilted from the surface plane in the second layer.

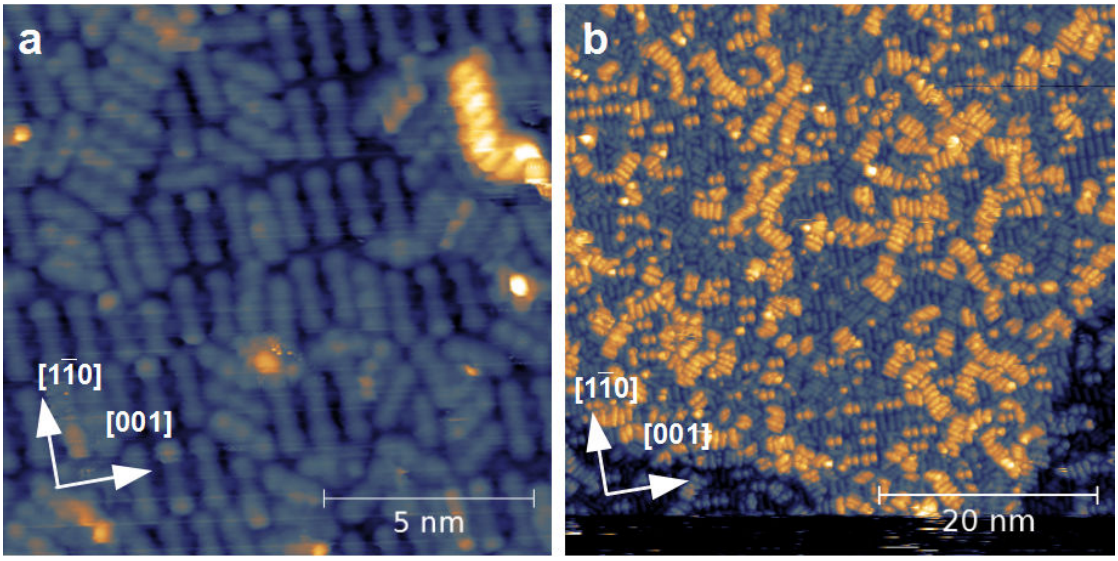

Figure 2.26.: a) STM image of an equivalent of 0.74 ML of DHTAP on Ag(110) deposited at 180 K (13 nm x 13 nm; U_b=0.7 V; I_t=40 pA. Molecules are localized on top of the first monolayer. b) STM image obtained after a deposition of 1.1ML (50 nm x 50 nm; U_b=0.4 V; I_t=200 pA). Molecules of the second monolayer do not show any particular long range order.

The molecular density, calculated using several STM images of this deposition,

is 8.32x10^{13} cm^{-2} which is equivalent to 0.74 ML compared to the density of the highly-ordered structure observed in first monolayer which will be describe in detail just below. Increasing the coverage at LT leads to the growth of a rather disordered second monolayer as observed in figure 2.26.b. Intermolecular distances and apparent height measurements are similar to those observed in image 2.26.a, which again suggests that the short molecular axis of DHTAP molecules adsorbed on top of the first monolayer is tilted from the surface plane and confirms the fact that no well-ordered growth is observed for deposition performed at low temperature.

In these cases, the temperature of the substrate during the deposition is too low and leads to the formation of molecular structures trapped in a kinetically limited state in the first monolayer. The commensuration between the substrate and molecular structure composed of DHTAP oriented with the long molecular axis parallel to the $[1\bar{1}0]$ direction underline the fact that, at low temperature, molecule-substrate interactions are favoured at the expense of the intermolecular interactions. This phenomenon is similar to the one observed in for DHTAP deposited at low coverage on Au(111) at 170 K.

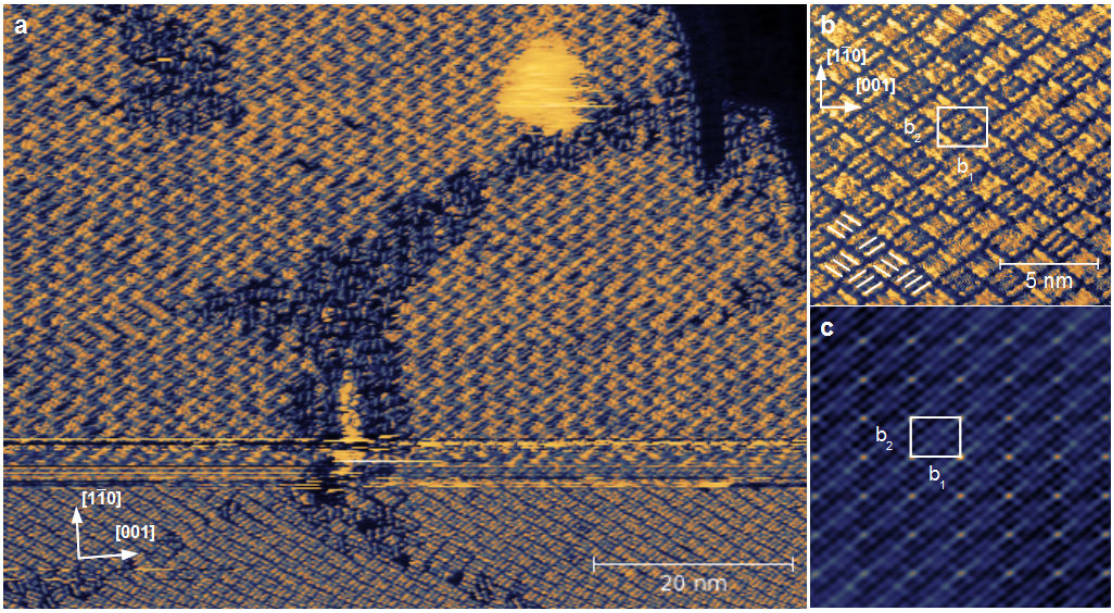

Figure 2.27.: a) STM image of DHTAP on Ag(110) deposited at RT (80 nm x 60 nm; U_b=0.5 V; I_t=50 pA). b) STM image of the highly-ordered first layer (15 nm x 15 nm; U_b=0.61 V; I_t=50 pA). c) 2D-autocorrelation of the STM picture b).

A STM image, which was recorded after annealing this sample for one night at RT is shown in figure 2.27.a. We observe the formation of well-ordered 2D domains and practically no molecules are on top of this layer except maybe for

a single island showing an apparent height of 0.8 nm. Molecules which are not involved in 2D molecular assembly can also be observed in the center of the STM picture and close to the step edge in the upper right corner. The resolution of the STM image combined with the large scale prevent from clearly distinguishing DHTAP molecules in these domains.

The STM image in figure 2.27.b is a zoom of the ordered domain, where the resolution allows us to distinguish individual DHTAP molecules and determine precisely the structure of the film. Molecules (the long molecular axis has been indicated white stripes in the lower left part of the image) self-assemble in aggregates of three molecules with two orientations, mirrored along the high symmetry direction of the Ag(110) substrate. An intermolecular distance of 0.60±0.03 nm has been determined between these three DHTAP molecules. A 2D-autocorrelation picture of the STM image 2.27.b is depicted in 2.27.c and reveals clearly the periodicity of the 2D structure, represented by the white rectangle. The determination of the unit cell parameters from 2D-autocorrelation images leads to the following unit cell parameters: $\mathbf{b}_1 = 2.47 \pm 0.1$ nm; $\mathbf{b}_2 = 2.15 \pm 0.1$ nm; $\theta = 90 \pm 3°$; angle between $\mathbf{b}_2$ and $[1\bar{1}0]$: $0 \pm 2°$.

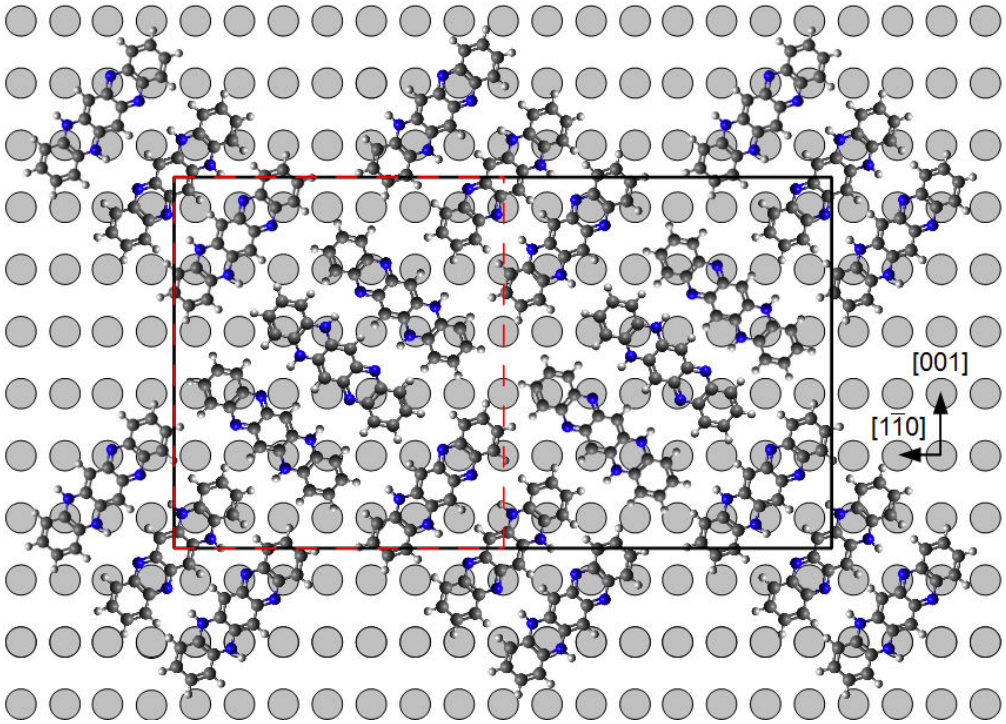

Figure 2.28.: Ball and stick model for DHTAP/Ag(110) corresponding to our observations. Red dashed lines represent the primitive unit cell determined by STM and the black lines represent the unit cell of the commensurate model.

Combined with apparent height measurements, it appears that DHTAP mole-

cules involved in this structure adsorb on the surface with their molecular planes parallel to the surface plane. Moreover, an angle of $\pm 51 \pm 5^{\circ}$ is measured between the long molecular axis and the $[1\bar{1}0]$ direction. It appears that two adjacent rows of trimers (along both $[1\bar{1}0]$ and $[001]$ directions) have opposed orientations. From the unit cell parameters and the fact that the unit cell contains six molecules, the molecular density of the first monolayer can be calculated: 1.13x10^{14} molecules per cm^2. The unit cell parameters strongly suggest a commensuration between the film and the substrate, especially in the $[001]$ direction ($\mathbf{b}_1$=6 x a$[001]$). Along the $[1\bar{1}0]$ direction, we observe $\mathbf{b}_2 \sim$7.5 x a$[1\bar{1}0]$, suggesting that the commensuration between the substrate and the film involves two molecular unit cells along the $[1\bar{1}0]$ direction. Moreover, we determine in the section 2.2.3 that the center of molecular trimer is localized between two rows of silver running in the $[1\bar{1}0]$ direction. From all these observations we propose the model shown in figure 2.28.

The corresponding matrix of this model is:

$$M_c = \begin{pmatrix} 6 & 0 \\ 0 & 15 \end{pmatrix}$$

Unfortunately we didn't have access to the Ag(110) sample long enough to investigate a complete monolayer of DHTAP deposited at RT and the formation of the corresponding overlayers. However, our investigations show that the formation of a highly-ordered first monolayer can be achieved if depositions are performed at RT, or after annealing a sample prepared at low temperature. Furthermore the high degree of organization shown in the first layer would provide an interesting template for the growth of subsequent layers.

2.3.4. Discussion

STM results and model parameters proposed for the observed well-ordered structures of DHTAP on Au(111), Au(110) and Ag(110) are summarized in the table 2.2.

We observe on all substrates that the formation of a well-ordered first monolayer is possible, which depends strongly of the temperature as illustrated in this case for DHTAP deposited on Au(110) and Ag(110) surfaces.

It has been shown that DHTAP grown on Au(111) at 250 K neighbouring molecules are in a head to tail configuration. We can note that the LEED diffraction pattern is not sensitive to this head to tail configuration, but is in very good agreement with STM measurements. The intermolecular distance, measured normal to the long molecular axis, is close to 0.58 nm (see table 2.2). This value and the head to tail configuration are in very good agreement with the establishment of hydrogen bonds between neighbouring molecules. We therefore suggest that this head to tail configuration is also adopted in the case of the first layer of DHTAP grown on Ag(110) at RT and Au(110) at temperatures below 200 K. On

Ag(110), the formation of molecular trimers showing intermolecular distances of 0.6 nm is in agreement with a formation of hydrogen bonds between neighbouring molecules. On Au(110) we observe variations of the apparent heights of the molecules constituting the ordered domains in the first monolayer (figure 2.23 and 2.24). These variations of apparent height are attributed to different adsorption sites on the reconstructed (1x2) Au(110) surface.

Surface		Au(111)	Au(110)	Ag(110)
T deposition		250 K	200 K	RT
STM	Unit cell parameters	$\mathbf{b}_1$=1.56±0.08nm $\mathbf{b}_2$=1.22±0.06nm θ=72±3°	$\mathbf{b}_1$=2.47±0.1nm $\mathbf{b}_2$=1.72±0.1nm θ=58±5°	$\mathbf{b}_1$=2.47±0.1nm $\mathbf{b}_2$=2.15±0.1nm θ=90±5°
	Molecular density	1.11x10^{14}cm^{-2}	1.11x10^{14}cm^{-2}	1.13x10^{14}cm^{-2}
Model	Unit cell parameters	/	$\mathbf{b}_{1c}$=2.45nm $\mathbf{b}_{2c}$=1.66nm θ_c=60.5°	$\mathbf{b}_{1c}$=2.45nm $\mathbf{b}_{2c}$=4.33nm θ_c=90°
	Molecular density	/	1.13x10^{14}cm^{-2}	1.13x10^{14}cm^{-2}
Intermolecular distance		0.58±0.03nm	0.61±0.05nm	0.60±0.03nm

Table 2.2.: Summary of the parameters of the different well-ordered structures of DHTAP deposited on noble metal surfaces.

The growth of well-ordered domains of DHTAP/Au(110) has been achieved using low temperatures in order to avoid the reconstruction of the substrate to the (1x3) structure. The commensuration between the unit cell and the atomic lattice suggests relatively strong interactions between the substrate and the DHTAP molecules. The growth of the second layer of DHTAP on Au(110) is different compared to Au(111). DHTAP molecules localized on top of the first monolayer do not show an epitaxial growth and the formation of small molecular wires is

observed, instead of the formation of 2D molecular islands. Annealing this sample leads to the formation of longer wires, due to an increase of the molecular diffusion. However, even after this annealing process, the second monolayer is not in epitaxy with the first layer. An interesting point is that the reconstruction of gold substrate observed for submonolayer deposition performed at RT, or after annealing a submonolayer film deposited at LT, does not happen after the deposition of a complete layer of DHTAP at LT. To be more precise, it seems that a partial reconstruction (release of gold atoms) only takes place when DHTAP molecules which are not aligned with the $[1\bar{1}0]$ direction, are present before the annealing step.

In the case of Ag(110) the conditions for the formation of well-ordered first layer are different, and molecular self-assembly is observed only in the case of deposition at RT, or after annealing a sample deposited at low temperature. In this case, the self-assembling process leads to the formation of large domains with a single orientation. It has been shown that the molecular structure is commensurate with the substrate, and moreover, the unit cell vectors are aligned with the high symmetry directions of the substrate. The investigation of bilayers grown at LT suggests that molecules constituting the first layer are trapped in kinetically limited state, and the limited potential energy does not allow any reorganization of the molecules with the coverage, as observed on Au(111) at 250 K. Moreover, as in the case of DHTAP on Au(110), the second monolayer of DHTAP deposited at low temperature on Ag(110) does not grow in epitaxy with the underneath layer.

Three models have been proposed to describe theses ordered 2D structures observed for DHTAP deposited on Au(111), Au(110) and Ag(110) based on our STM investigations. In the case of DHTAP deposited on (110) metals a commensuration between the molecular structure and the substrate is established, suggesting relatively stronger interactions between DHTAP and (110) surfaces. This is not the case for the model proposed for DHTAP on Au(111), but in this model we do not take into account the 23x$\sqrt{3}$ reconstruction of the first atomic layer, but we consider a surface atomically flat, with the interatomic distance of the bulk structure. All the proposed models are in very good agreement with STM measurements. Interestingly the molecular densities of these structures are very similar (1.11-1.13x10^{14} cm^{-2}) despite the fact that their structures and the substrate structures are completely different. The molecular density of the monolayer is thus determined by the size of DHTAP molecules.

2.4. Conclusion of the DHTAP growth

The growth of DHTAP has been investigated on Au(111), Au(110) and Ag(110). The influence of two important factors has been studied: the temperature and the coverage. The temperature plays a very important role through the molecular diffusion on surfaces and also concerning the kinetics of growth processes, which can lead to the formation of metastable structures. The coverage plays an important role in the balance between molecule-substrate and intermolecular interactions.

On Au(111), it turns out that the adequate substrate temperature for the formation of highly-ordered domains is 250 K. Indeed, the DHTAP growth at low coverage performed at 170 K leads to the formation of a kinetically limited structure and at RT, to the formation of amorphous molecular aggregates. The growth has been consequently studied for depositions performed at 250 K, from the nucleation up to the beginning of the formation of the fourth monolayer. It turns out that the nucleation of DHTAP takes place preferentially at the elbows of the fcc domains of reconstructed surface. The preferential growth of molecular wires continue up to the completion of the fcc domains, then the formation of molecular wires is observed on hcp domains. These observations are in very good agreement with simulations of the growth of DHTAP on Au(111).

After the completion of both fcc and hcp domains, a molecular reorganization takes places, due to the increased influence of the intermolecular interactions with the molecular density. This leads to the formation of highly-ordered domains after the completion of the first monolayer. Interestingly, the intermolecular distances remain similar during the complete growth process, before and after the molecular reorganization. The unit cell parameters and the relative orientation between the molecular film and the substrate have been determined by STM. LEED experiments performed on this system are in very good agreement with STM results, and confirm the relative orientation between the film and the substrate.

The investigation of the second layer of DHTAP reveals that the formation of molecular islands takes place in epitaxy with the first layer, and that molecules embedded in this well-ordered second layer are in a head to tail configuration along the unit cell vector $\mathbf{b}_2$. From these observations, we assume that DHTAP embedded in the first monolayer are also in a head to tail configuration and a non-commensurate model has been proposed. This head to tail configuration allows for the establishment of hydrogen bonds between molecules of neighbouring molecular rows. The growth has been studied up to the beginning of the formation of the fourth monolayer. It turns out that molecules remain in epitaxy with the underneath layer, and a Stransky-Krastanov growth mode is observed.

On Au(110), the most striking influence of the temperature has been observed: depositions performed above 200 K lead to the reconstruction of the gold sub-

strate from the (1x2) to the (1x3) structure. In this case it became impossible to grow highly-ordered films on this substrate. However, depositions performed below 200 K do not lead to this reconstruction and the growth has been studied to coverages up to slightly above the completion of the first layer. It tuns out that DHTAP molecules deposited on Au(110) adsorb on the substrate with different geometries depending on the molecular density. At low coverages, isolated molecules are observed which diffuse strongly on the surface, until they reach a stable position. At slightly higher coverages, stable molecular dimers are formed which show different orientations as compared to the isolated molecules. At coverages close to the monolayer, most of the molecules are aligned with the $[1\bar{1}0]$ direction. This evolution of the molecular orientation clearly indicates an increased influence of the intermolecular interactions at the expense of the molecule-substrate interactions.

The formation of ordered domains of DHTAP on Au(110) has been observed. However, the low temperature conditions required to avoid the reconstruction of the substrate prevents us to grow large well-ordered domains. From our STM measurements it turns out that DHTAP molecules adsorb in different positions on the reconstructed substrate, leading to the different apparent heights observed for these molecules. Assuming the head to tail configuration observed in the case of DHTAP /Au(111), a commensurate model has been proposed for this structure, in very good agreement with STM experiment.

The beginning of the growth of the second layer has been studied but it appears that the formation of a well-ordered second layer does not takes place at 200 K: molecules localized on top of the first layer are trapped in a diffusion limited state due to the low temperature during deposition. Annealing such a sample at RT leads to the formation of molecular wires in the second monolayer. The fact that no epitaxial growth is observed in this case can be related to the complex structure observed in the first layer which seems to strongly depend on the substrate structure and on molecule-substrate interactions.

On Ag(110), the growth has been studied at 180 K and RT. It turns out that at low temperature molecule are trapped in kinetically limited structure. At very low coverage, the formation of commensurate molecular wires is observed, followed by the formation of a second kind of wire at higher molecular density. Finally, increasing the coverage at this temperature leads to the adsorption of DHTAP molecules on top of these molecular wires, without any molecular reorganisation. When the growth is performed at RT (or after annealing at RT) an evolution of the molecular orientation is observed with the coverage. At very low coverage, DHTAP molecules adsorb on the substrate with their long molecular axes parallel (or very close) to the $[1\bar{1}0]$. It has also been unambiguously determined that the central carbon ring of this molecule is a top of a silver atoms of the second atomic layer. Increasing the molecular density leads to a progressive reorganization of the molecules in the first layer to finally form molecular trimers constituting the first monolayer. In the complete layer two adjacent rows

of trimers have opposed molecular orientations. These informations, combined with the unit cell parameters and considering that the molecules involved in trimers are in a head to tail configuration allowed us to propose a commensurate model for this system.

It is interesting to compare these different systems. It turns out that growth mode observed for DHTAP could be either a Stransky-Krastanov (established on Au(111)) or a Franck van der Merve growth mode, due to the fact that the completion of the first layer arises in each cases before the beginning of the formation of the second layer. It also turns out that the intermolecular distance is in all case very similar, and suggest the establishment of hydrogen bonds, especially for Au(111) and Ag(110). However, in the case of Au(110), the different apparent heights and the tilted configuration of some of the molecules constituting the first layer supposed by our model will have an influence on the establishment of such bonds between the neighbouring molecules. The molecular densities, determined by STM or from the commensurate models, are also very similar for each system. This suggests the molecular density of the monolayer deposited on metallic substrate is determined by the size of DHTAP molecules. It would be interesting to study the growth process and the formation of ordered DHTAP films on other noble metal substrates to confirm this suggestion. It would also been interesting to perform density functional theory (DFT) calculations, taking into account the surfaces and the surrounding molecules for these different systems in order to confirm the validity of our models.

3. Characterisation of bis-pyrene

In this chapter we will present results concerning the bis-pyrene growth (the chemical structure has been depicted in figure 1.19) on the Au(111) surface by the means of LT-STM and its optical properties on a BK7 amorphous glass substrate by the means of s-CRDS. Investigations on the growth and optical properties as a function of the coverage will be presented and the influence of the substrate temperature will be discussed.

3.1. Growth of bis-pyrene on Au(111)

3.1.1. Overall growth behaviour

In this section will be presented the overall growth behaviour of bis-pyrene on Au(111) from the innitial stages up to coverages close to 1.5 ML as well as the effect of the temperature on the molecular self-assembly. Performing several depositions of different durations at an evaporation temperature of 530 K allowed us to determine a stable deposition rate of 0.016 ML min^{-1} using the same calibration procedure as for DHTAP (see section 2.1.1). Directly after deposition the sample is transferred to the analysis chamber and cooled down to LN_2 temperature.

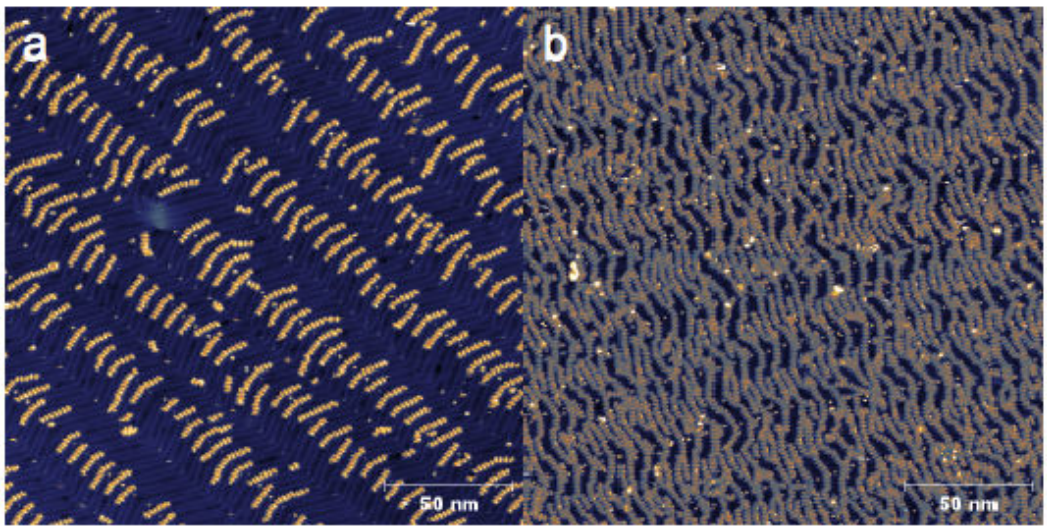

Figure 3.1.: Large scale STM images of bis-pyrene deposited at RT on Au(111). a) at 0.18 ML coverage imaged with a bias voltage of U_b=1 V and a tunnelling current of I_t=40 pA. b) at 0.45 ML coverage at U_b=-2 V, I_t=50 pA.

As it can be seen in figure 3.1.a, the initial growth pattern of bis-pyrene is controlled by the herringbone reconstruction of the Au(111) substrate. After deposition of 0.18 ML at RT a template-controlled growth pattern can be observed, which consists of molecular wires attached to the elbows of the herringbone reconstruction. This leads to a 2D patterning of the surface along the herringbone reconstruction. We can also observe that the growth at this coverage takes place exclusively on the fcc domains of the herringbone reconstruction. This behaviour has previously been observed for various molecules[85,87,88] and also for DHTAP deposited on Au(111) and suggests that the adsorption energy of the bis-pyrene is higher on the fcc domains than on the hcp domains. Increasing the coverage to 0.45 ML leads to the completion of the fcc domains and the formation of molecular wires on hcp domains as shown in figure 3.1.b. This observation confirms that the initial growth of bis-pyrene is controlled by the herringbone reconstruction and intermolecular interactions, through the formation of molecular wires. Interestingly the beginning of the growth process is independent of the substrate temperature in the range investigated (210 K to RT). The apparent height of these wires is 160$\pm$10 pm (see STM profile in 3.4.c).

If the coverage is further increased, this template-controlled mechanism is replaced by self-organization in the now denser molecular layers. Figures 3.2.a, 3.2.b, 3.2.c and 3.2.d show four STM images in which four different ordered structures can be observed. These will be in the following noted as α, β, γ, and δ structure, respectively.

We observe that disorder persists at the domain boundaries and that some molecular wires are still present. Two different orientations can be distinguished for the α structure (localized at the upper and right part in the figure 3.2.a), which are rotated by 60° with respect to each other, reflecting the symmetry of the gold surface. Furthermore, we observe the formation of a mirrored domain (lower left part of the figure 3.2.a) with respect to the high symmetry directions of the substrate. We can thus conclude that even though the structure of the domains is due to self-organization, the interaction with the Au(111) still plays an important role for the overall orientation of the domains.

Molecular structures β,γ and δ, respectively shown in figure 3.2.b, 3.2.c and 3.2.d, appear for coverage (0.7 ML) slightly above the coverage required to observe the α structure (0.5 ML). After the completion of the monolayer, the α structure is not observed anymore.

Furthermore, the formation of the structures γ and δ is temperature dependent. For films grown at RT, we observed essentially the β structure shown in figure 3.2.b and in rare cases the structure γ, displayed in figure 3.2.c. The γ structure, as the α structure, shows mirror domains with respect to the high symmetry directions of the crystalline surface. In the case of the β structure, unit cell vectors are aligned with these high symmetry directions. Theses structures are also observed with different orientations, rotated by 60° with respect to each other, reflecting once again the symmetry of the Au(111) surface.

Decreasing the substrate temperature during deposition leads to the appearance of the δ structure depicted in figure 3.2.d and a decrease of the domains sizes for the β structure is observed. For deposition performed below RT the γ structure has never been observed.

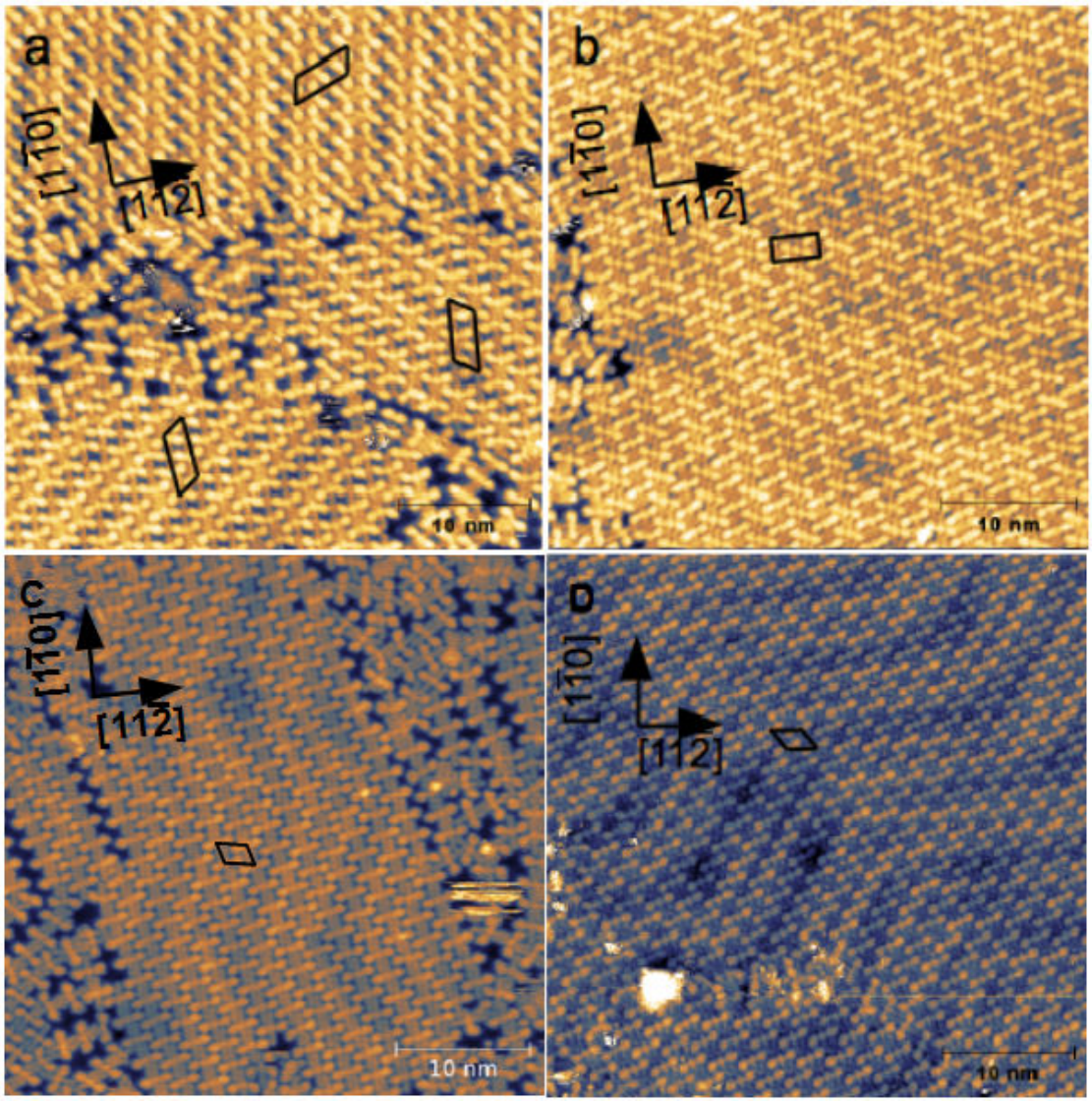

Figure 3.2.: STM images (40 nm x 40 nm) of bis-pyrene on Au(111) showing the four highly-ordered domains observed in the first monolayer. Unit cells are underlined in black. a) α domains; U_b=1 V; I_t=100 pA. Deposition temperature: RT. b) β domain ; U_b=1 V; I_t=100 pA. Deposition temperature: RT. c) γ domain ; U_b=1 V I_t=1 nA. Deposition temperature: RT. d) δ domain; U_b=0.5 V I_t=70 pA. Deposition temperature: 250 K.

Apparent heights of all these molecular structures are similar to that observed

in the case of molecular wires of bis-pyrene at low coverage: 160±10 pm. A closer look at the images in figure 3.2 reveals that in certain cases an important conformal modification of the molecule takes place. Whereas the molecules in the α structure appear to be "banana-shaped", the molecules in the denser structure (β, γ and δ) seem to be straight. We will come back to this observation later.

For coverages above the monolayer deposited at RT we observe that the first monolayer is well-ordered and shows large domains sizes consisting mainly of the above-mentioned β structure, as displayed in the figure 3.3.a. In this case, 1.1 ML of bis-pyrene was deposited on Au(111) and the second monolayer appears to grow in a disordered fashion. However, it seems that molecules deposited on top of the first monolayer are able to diffuse in order to form amorphous islands. This observation is confirmed by the figure 3.3.b, where 1.5 ML of bis-pyrene was deposited. Again, the first bis-pyrene monolayer is highly-ordered, no ordered growth in the second layer can be observed. The apparent height of these amorphous structures is in the range 200-250 pm, which suggests that molecules have different orientations than in the first layer, where an apparent height of 160±10 pm has been determined.

For deposition above the monolayer performed at temperatures below RT, both structures (β and δ) shown in figure 3.2.b and 3.2.d are observed in the first monolayer. The relative amount of the δ structure increases with decreasing temperature. Deposited at 180 K, the first monolayer possesses a lot of defects: we can observe the formation of an amorphous structure in the first monolayer, in figure 3.3.c, on the terrace localized on the upper part of the STM picture and on the left-hand side of the image. The formation of the β structure is also clearly observed in the center and on the left-hand side of the STM picture. On top of this first layer small aggregates are observed which are randomly distributed. The resolution does not however allow us to distinguish individual bis-pyrene molecules. A STM image at smaller scale is shown in figure 3.3.d. Apparent height measurements carried ou on structures observed on top of the first monolayer are in the range 200-250 pm and 350-400 pm. According to the previous measurements, this can be explained by the adsorption of molecules not lying strictly flat and the formation of an additional double layer.

Annealing the sample at room temperature for 150 min leads to the reorganization of the molecular film. Amorphous structures are not observed anymore in the first monolayer, and only the two above-mentioned structures (β and δ) are observed. Moreover, the formation of a new organized structure in the second monolayer can be observed, as shown in figure 3.3.c and 3.3.d. The apparent height of this structure is 250 pm and the unit cell parameters are **a**=2.7±0.2 nm; **b**=2.9±0.2 nm and θ=114±2°. Unfortunately the resolution is not sufficient to discern individual bis-pyrene molecules constituting this structure. For the same reason it is not possible to determine the molecular density of this structure. However, it clearly shows that an ordered growth takes place in the

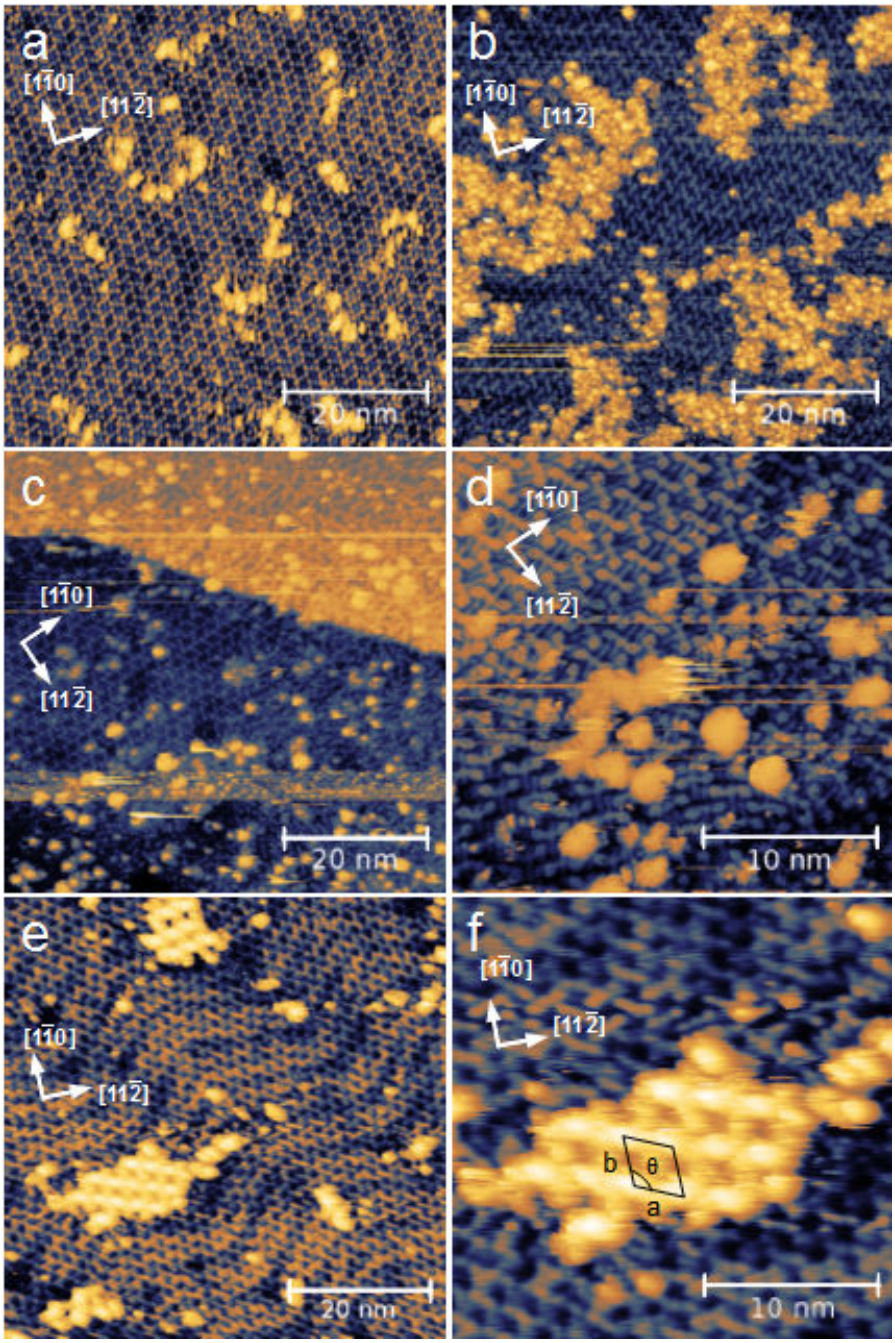

Figure 3.3.: STM image of bis-pyrene on Au(111) deposited at different temperatures and for coverages above the ML. a) 1.1 ML at RT, 60 nm x 60 nm, U_b=1 V, I_t=40 pA. b) 1.5 ML at RT, 60 nm x 60 nm, U_b=-1 V, I_t=50 pA. c) (60 nm x 60 nm) and d) (25 nm x 25 nm) 1.1 ML at 180 K, U_b=0.9V, I_t=50 pA. e) (60 nm x 60 nm) and f) (25 nm x 25 nm), same sample after annealing 150 min at RT under UHV conditions. U_b=-0.5 V, I_t=70 pA.

second monolayer.

Interestingly this structure has not been observed in the case of RT deposition. This implies that diffusion in the second monolayer is slow so that a certain time is needed for self-organization. For deposition temperatures close to RT presented in figure 3.3.a and 3.3.b the self-organization has not been observed because of a rapid sample transfer into the STM where the surface was quenched to liquid nitrogen temperature. The disorder in the second layer can thus be explained by the kinetics of diffusion at room temperature.

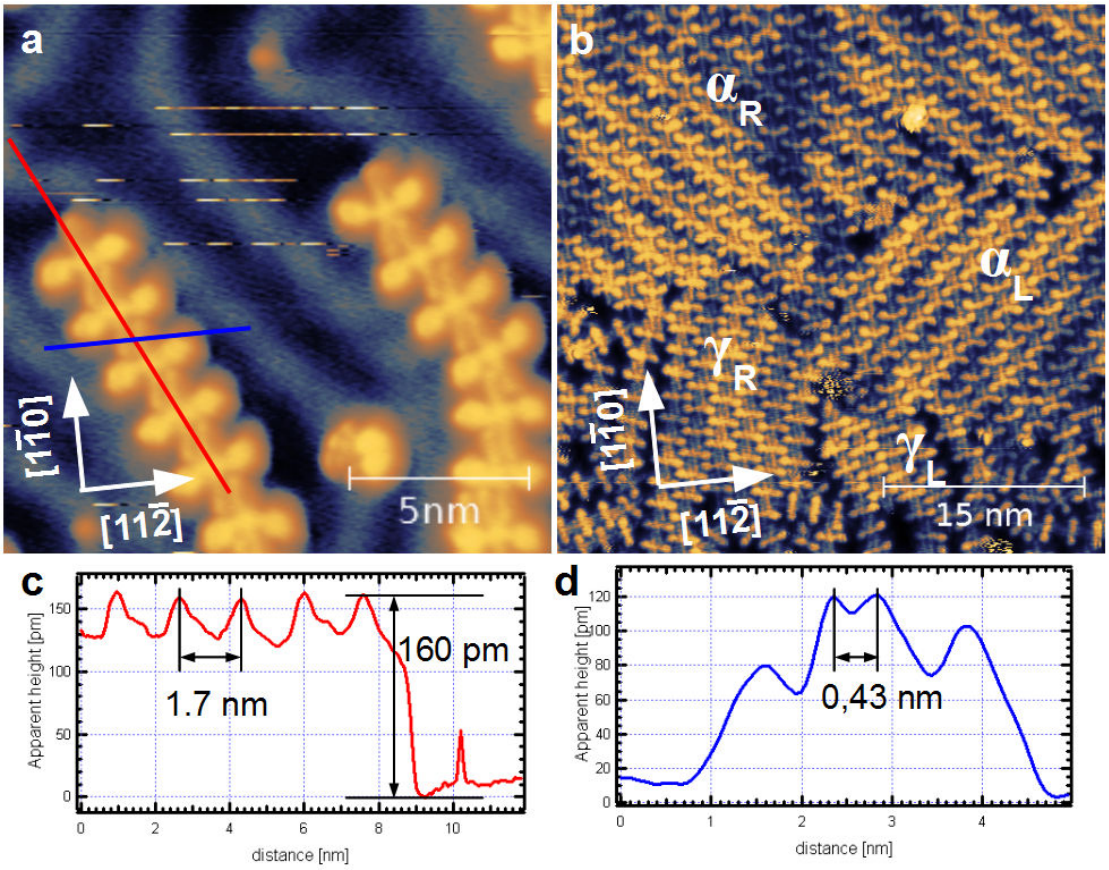

Figure 3.4.: a) STM image (15 nm x 15 nm; U_b=0.2 V; I_t=10 pA) of 0.18 ML of bis-pyrene deposited on Au(111) at RT. The resolution allows us to distinguish the pyrene moieties, the central phenyl ring and the interdigitated alkyl chains. b) STM image (40 nm x 40 nm; U_b=1 V; I_t= 300 pA) of 0.8 ML of bis-pyrene deposited on Au(111) at RT showing a transition from α to γ structure. c) STM profile corresponding to the red line in a). d) STM profile corresponding to the blue line in a).

After having discussed the overall growth behaviour we now turn to the details of the intermolecular and molecule-surface interactions, which lead to the for-

mation of the different structures that have been observed in the first monolayer. Figure 3.4.a shows a detailed STM image of 0.18 ML of bis-pyrene, which allows us to clearly identify the origin of the observed pattern. Again the importance of the Au(111) herringbone structure, which serves as a template, has to be pointed out. It is obvious that at this coverage, fcc domains are more favourable for the absorption of the bis-pyrene molecules than the hcp domains.

Furthermore we can clearly distinguish two types of conformers, previously referred to as "banana-shaped" and straight, which differ in the configuration of the conjugated molecular backbone. In the case of the "banana-shaped" configuration, pyrene moieties are in cis-configuration with respect to the oligophenylene vinylene bridge, whereas in straight configuration, pyrene groups are in trans-configuration. Note that the trans-configuration is more abundant in molecular wires. Another important point is that we can clearly distinguish the alkyl chains of the molecules in figure 3.4.a, which are oriented perpendicularly to the molecular backbone. This particular orientation allows for alkyl-alkyl interactions, which assure the linking between the molecules in the molecular wires. This is not very surprising since this type of van der Waals interaction mediated linking of molecules via alkyl chains is a well-known phenomenon.[98]

A closer statistical analysis of these STM images gives us some interesting information. The intermolecular distance, measured from center to center, is 1.7±0.1 nm and the apparent height is 160±10 pm, as shown in STM profile in figure 3.4.c. The inter-alkyl distance, d_{C8}, measured perpendicularly between two interdigitated alkyl chains, is 0.43±0.05 nm (see STM profile in 3.4.d). This value is in very good agreement with the value measured for interdigitated alkanes chains of different lengths grown on Au(111) in liquid phase.[99] The interdigitation length of two alkyl chain is 0.9±0.2 nm. The former value can be compared to the length of an octyl chain of about 1.05 nm. This measurement strongly suggests that the interdigitation takes place along almost the complete length of the alkyl chain.

STM image 3.4.b has been recorded for a coverage of 0.8 ML. Several interesting informations can be extracted. First, we observe two α domains (denoted α_R and α_L which are mirrored along the direction $[1\bar{1}0]$), two (smaller) γ domains (noted γ_R and γ_L, also mirrored) and molecular wires without particular orientation surrounding these domains. The most interesting information is related to the alkyl chain orientation: the molecular alkyl chains of the molecules in self-assembled domains (α, γ and mirrored domains) are oriented with the same orientation along the $[1\bar{1}0]$ direction. Moreover, a closer look at this STM image, especially at the boundaries between α and γ structure, allows us to conclude that in order to form the γ structure the molecules forming the α structure have to switch from cis to trans-configuration in the denser layer. Alkyl interactions are also involved in the formation of this γ structure where both alkyl chains of molecules are now interdigitated.

3.1.2. Structure of the ordered bis-pyrene domains

Due to the important number of ordered structures and the fact that three of them (α, γ and δ) show mirrored symmetry, we decided to use the following rules to determine the unit cells parameters:

- the unit cell vector $\mathbf{b}_2$ is defined as the vector between two molecular centers showing the smallest angle with the alkyl chain.
- the symmetry (right handed or left handed domains) is defined as a function of the geometry of the interdigitated alkyl with respect to the $\mathbf{b}_2$ direction: if the alkyl chain of the second molecule (after a translation along $\mathbf{b}_2$) is interdigitated on the right-hand (left-hand) side of the first molecule, the domain is considered as right-handed (left-handed).
- the unit cell vector $\mathbf{b}_1$ is defined as a function of the symmetry of the domain and the closest equivalent molecules.

These rules allow us to characterise mirrored domains using the same unit cell parameters.

We now come back to the structure of the ordered layer observed at a coverage above 0.4 ML, i.e. the α structure. The resolution of the STM image in figure 3.5.a allows us to distinguish the unit cell of the structure, which contains two molecules in cis-configuration.

In order to determinate the lattice parameters of this structure we have used the 2D-autocorrelation image in figure 3.5.b, which clearly shows a trapezoidal unit cell with the following parameters $\mathbf{b}_1$=1.85±0.2 nm, $\mathbf{b}_2$=4.3±0.3 nm and θ=120±3°. The molecular density calculated from the unit cell parameter is 2.90 x 10^{13} cm^{-2}.

Statistical studies of the relative orientation between the unit cell and the gold substrate suggest an angle of 10±5° between $\mathbf{b}_1$ and the $[1\bar{1}0]$ direction. Furthermore, an angle of 10±5 ° has been determined between alkyl chains and $\mathbf{b}_2$, in very good agreement with the above-mentioned alignment between alkyl chains and $[1\bar{1}0]$ direction.

The fact that this structure exists in six domains with rotation angles reflecting the symmetry of the Au(111) surface and the formation of mirrored domains (as shown in figures 3.2.a and 3.4.c) suggests that it should be commensurate. Thus, we tentatively ascribe the structure to a commensurate overlayer that can be represented by the following matrix.

$$M_\alpha = \begin{pmatrix} 7 & 6 \\ -14 & 2 \end{pmatrix}$$

The unit cell parameters, calculated from the proposed model are $\mathbf{b}_{1M}$=1.89 nm, $\mathbf{b}_{2M}$=4.35 nm, θ_M=121° and the molecular density calculated from these

parameters is 2.84 x 10^{13} cm^{-2}. These parameters are in very good agreement with unit cell parameters and molecular density of the α structure determined from STM measurements.

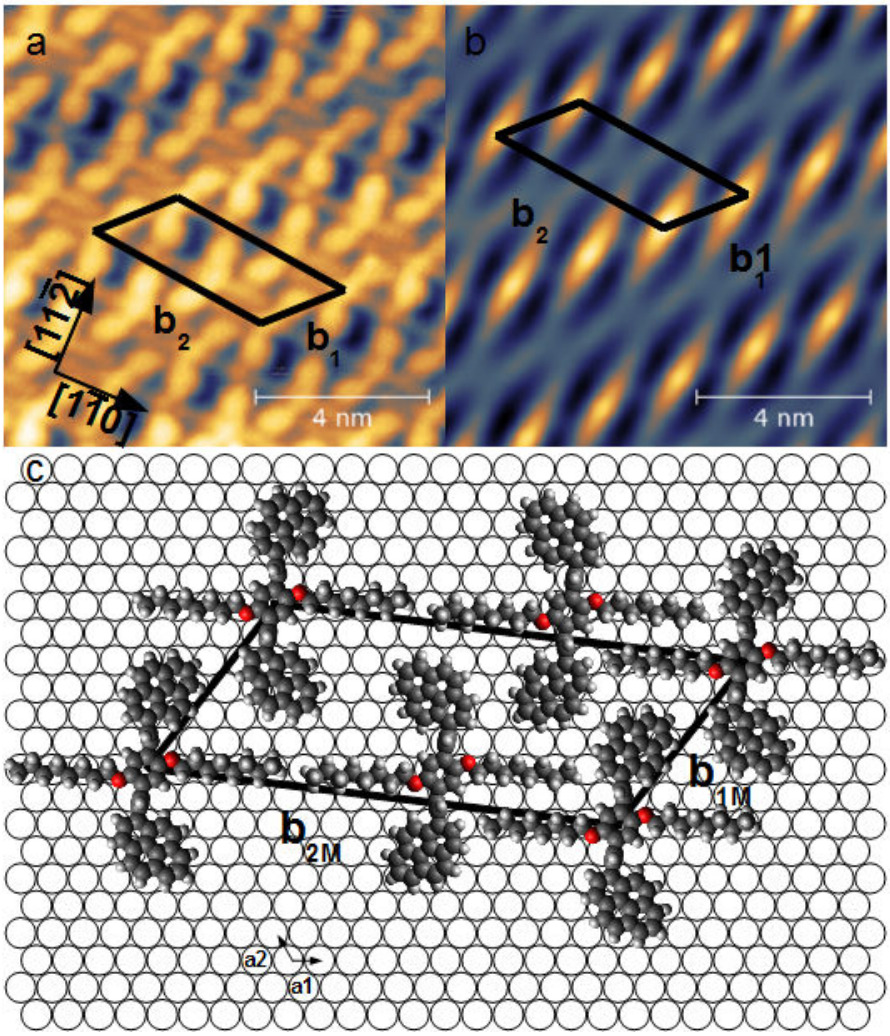

Figure 3.5.: a) STM image (10 nm x 10 nm, U_b=0.56 V, I_t=200 pA) of α domain of bis-pyrene/Au(111). Deposition temperature: RT. b) 2D-autocorrelation of a). c) Ball and stick model corresponding to the proposed matrix for this structure.

Moreover, the STM image in figure 3.5.a reveals further details concerning the internal structure of the film. First we can see that molecules adopt the cis-configuration, which is quite a significant change compared to the trans-configuration in the crystalline solid (see 1.19) and in denser structures observed by STM above 0.7 ML. Furthermore, we see that for each molecule only one of the two octyloxy chains is used for linking with neighbouring molecules due to

the steric hindering imposed by the cis-configuration.

This α structure is the only self-assembled structure observed for coverages below 0.7 ML. A closer inspection of the images allows us to determine the distance between the interacting alkyls to be d_{C8}=0.41±0.05 nm. The interdigitation length of the two interdigitated alkyl chains is 1.0±0.1 nm and is very similar to the length observed in the case of the molecular wire, suggesting a similar interaction. In figure 3.5.c a schematic representation of the structure is shown, based on STM measurements and calculated matrix, which indicates also the particular orientation of the layer with respect to the Au(111) lattice. However, our measurements do not allow us to determine the exact lateral position of the molecules with respect to the gold atoms. For simplicity we have thus chosen arbitrarily to place the central phenyl ring of the bis-pyrene molecule atop a gold atom.

If the coverage is increased above 0.7 ML a second ordered structure can be observed, which is presented in the figure 3.6.a. From the 2D-autocorrelation of STM images (an example is shown in figure 3.6.b) we can deduce a rectangular unit cell with the following parameters: $\mathbf{b}_1$=3.3±0.2 nm, $\mathbf{b}_2$=1.95±0.2 nm and θ=90±3°. From the unit cell parameters we can conclude a molecular density of 3.11 x 10^{13} cm^{-2}.

Statistical studies concerning the unit cell orientation show that the vectors $\mathbf{b}_1$ and $\mathbf{b}_2$ are oriented along the $[11\bar{2}]$ and the $[1\bar{1}0]$ directions of the Au(111) lattice, respectively. The fact that $\mathbf{b}_1$ and $\mathbf{b}_2$ are aligned with high symmetry directions of the substrate suggests again that the structure is commensurate.

The resolution achieved in the STM picture gives us several information concerning the film structure: molecules adopt the trans-configuration and two distinct orientations with respect to the Au(111) surface are observed. These orientations are symmetric with respect to both $[1\bar{1}0]$ and $[11\bar{2}]$ directions, the alkyl chains are rotated by ±15±4° with respect to the $[1\bar{1}0]$ direction. An angle close to 90° is observed between alkyl chains and the Pyr-OPV-Pyr π-conjugated system. Both alkyls chains of each molecule are linked to neighbouring molecules. These modifications with respect to the α structure lead to the formation of a denser layer, which is in agreement with the fact that this structure appears for coverage slightly higher than those for which the α structure has been observed.

We note also that the angle between the alkyl chains and the unit cell vector $\mathbf{b}_2$ is ±15°, and the distance between the interacting alkyl chains corresponds to d_{C8}=0.47±0.07 nm. This value is more important than the value measured in the case of the α structure, the molecular wire and the value calculated for the optimal interaction of two alkyl. The length of the interdigitated part of the alkyl chains is 0.75±0.1 nm. This is a considerable decrease in the interacting length as compared to the α structure and the molecular wires. These previous observations suggest a decrease in the interactions between interdigitated alkyl chains in the β structure which could in part be compensated by the fact that now both alkyl chains of each molecule interact.

From our measurements we tentatively ascribe the structure to a commensurate overlayer, however, it appears that the only matrix describing a commensuration between the molecular structure and the substrate contains two molecular unit cells along the $\mathbf{b}_1$ vector:

$$M_\beta = \begin{pmatrix} 26 & 13 \\ 0 & 7 \end{pmatrix}$$

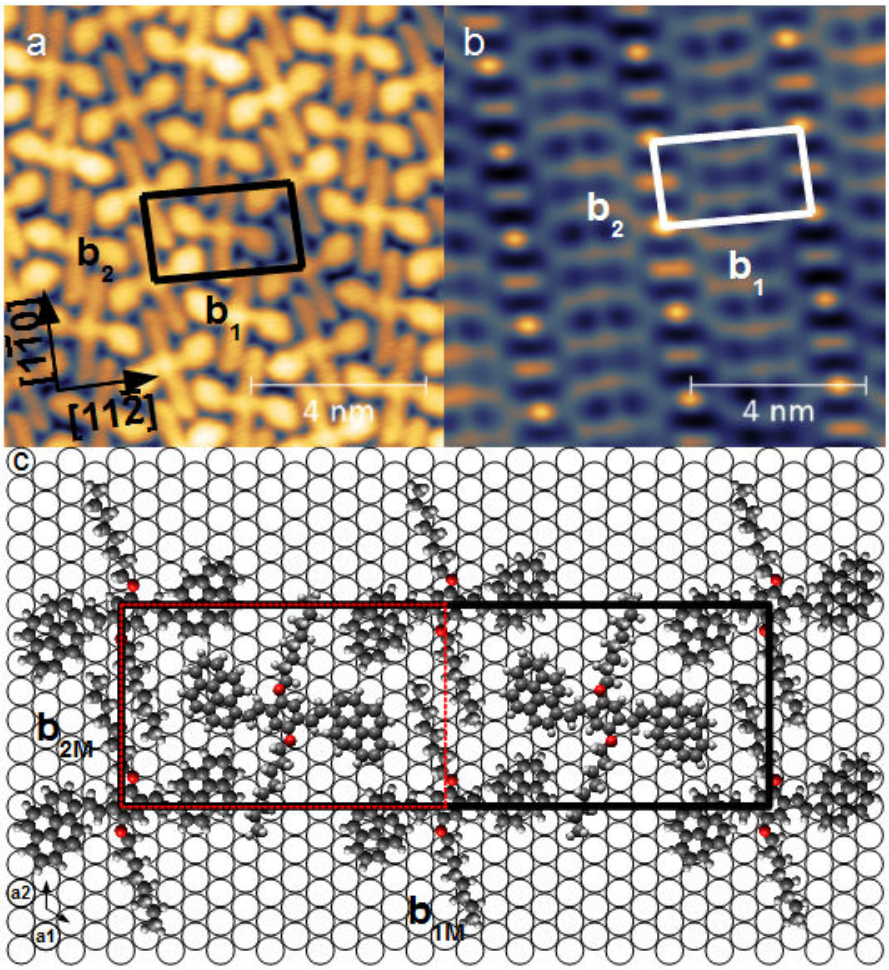

Figure 3.6.: a) STM image (10 nm x 10 nm; U_b=1.5 V; I_t=60 pA) of β structure. Deposition temperature: RT. b) 2D-autocorrelation of a. c) Ball and stick model corresponding to the proposed matrix for this structure. The primitive unit cell determined by STM is indicated by red dashed lines. The unit cell corresponding to the model is indicated by black lines and contains two primitive unit cells (red dotted rectangle) along the $[11\overline{2}]$ direction.

The unit cell parameters of the proposed model are $\mathbf{b}_{1M}$=6.49 nm (~2$\mathbf{b}_1$), $\mathbf{b}_{2M}$=2.02 nm, θ_M=90° and the molecular density calculated from these parameters is 3.05 x 10^{13} cm^{-2} which is in very good agreement with unit cell parameters and molecular density of the β structure determined from STM measurements. A schematic representation of the β structure, based on STM measurements and calculated matrix, is shown in figure 3.6.c. Again we have placed for simplicity the central phenyl ring of the bis-pyrene molecule atop a gold atom.

A second structure has been observed for bis-pyrene deposited on Au(111) at coverages above 0.7 ML which is shown in figure 3.7.a.

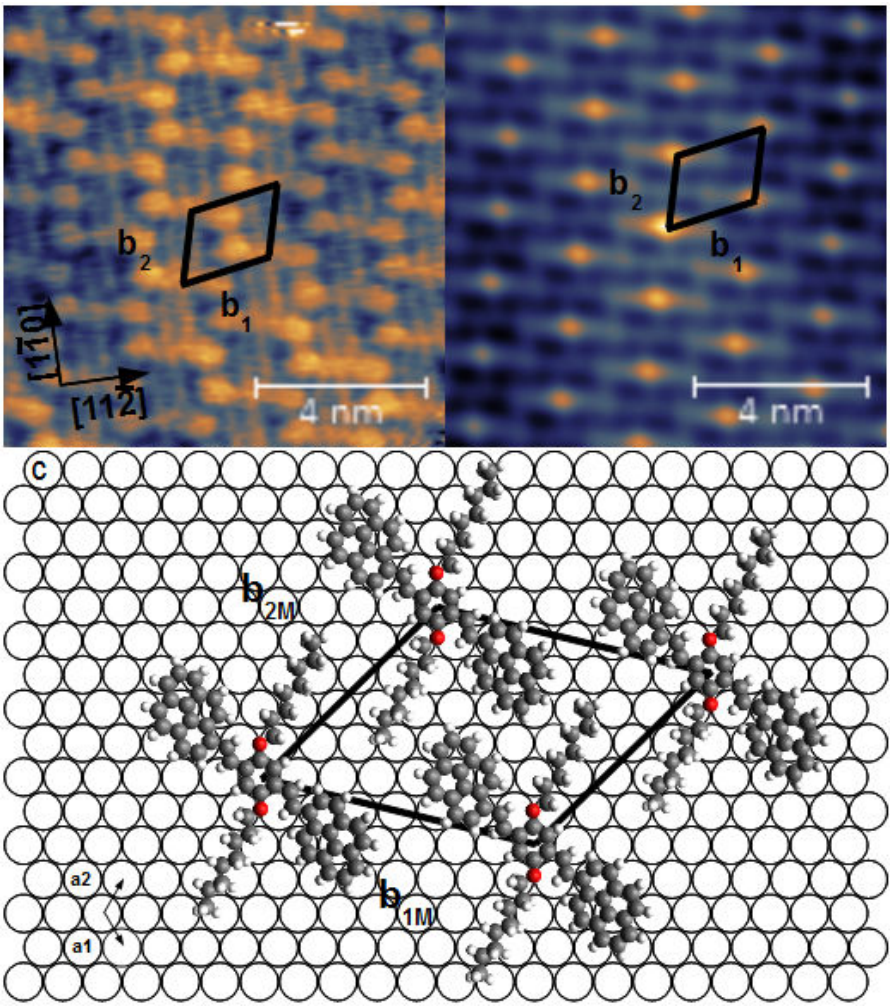

Figure 3.7.: a) STM image (10 nm x 10 nm; U_b=1 V; I_t=300 pA) of γ structure. Deposition temperature: RT. b) 2D-autocorrelation of a. c) Ball and stick model corresponding to the proposed matrix for this structure.

This structure has been observed only occasionally for depositions performed at room temperature. We can see in the STM picture that all molecules adopt the trans-configuration and show the same orientation on the surface, contrary to the α and β structures. Both alkyl chains of each molecule are interdigitated with the alkyl chains of the neighbouring molecules. From 2D-autocorrelation (figure 3.7.b) of the STM images we can deduce a trapezoidal unit cell with the following parameters for the γ structure: $\mathbf{b}_1$=2.15±0.15 nm, $\mathbf{b}_2$=1.70±0.1 nm and θ=61±4°. The molecular density calculated from unit cell parameters is 3.13 x 10^{13} cm^{-2}.

Due to the fact that the alkyl chains are aligned with the $[1\bar{1}0]$ direction, we can determine an angle of 15±5° between $\mathbf{b}_2$ and the $[1\bar{1}0]$ direction. Moreover, we note that an angle of 75° is observed between alkyl chains and the Pyr-OPV-Pyr conjugated system of each molecule. The interdigitation length is 0.80±0.1 nm and the distance between interdigitated alkyl chains (d_{C8}), measured perpendicularly to the alkyl direction is 0.45±0.05 nm. These measurements corroborate the fact that the molecular density is slightly more important than in the case of the β structure. From these measurements, we tentatively ascribe the structure to a commensurate overlayer, which can be represented by the following matrix:

$$M_\gamma = \begin{pmatrix} 8 & 6 \\ 2 & 7 \end{pmatrix}$$

Unit cell parameters of the proposed model are $\mathbf{b}_{1M}$=2.08 nm, $\mathbf{b}_{2M}$=1.80 nm, θ_M=57.8° and the molecular density calculated from these parameters is 3.16 x 10^{13} cm^{-2} which is in good agreement with unit cell parameters and molecular density of the β structure determined from STM measurements. A schematic representation of the structure is shown in figure 3.7.c. The central phenyl ring of the bis-pyrene molecule has been placed atop a gold atom for simplicity because our STM measurements do not allow us to determine the precise position of adsorption.

The last highly-ordered structure observed for bis-pyrene grown on Au(111) and observed above a coverage of 0.7 ML is the δ structure (see figure 3.8.a). As mentioned above, this structure has been observed only for depositions performed below RT, and is in competition with the formation of the β structure from the α structure: we observe that the ratio of the δ with respect to the β structure increases with decreasing deposition temperature. In the STM image, we can easily see that in this case molecules are all oriented in the same direction and adopt the trans-configuration. Both alkyl chains are interdigitated and the unit cell is again trapezoidal.

The unit cell parameters of this structure, determined from 2D-autocorrelation of STM pictures (see figure 3.8.b) are: $\mathbf{b}_1$=2.15±0.2 nm, $\mathbf{b}_2$=1.8±0.2 nm and θ=54±3°. The molecular density calculated from the unit cell parameters is 3.19 x 10^{13} cm^{-2}, which is slightly higher than in the case of the β and γ structures.

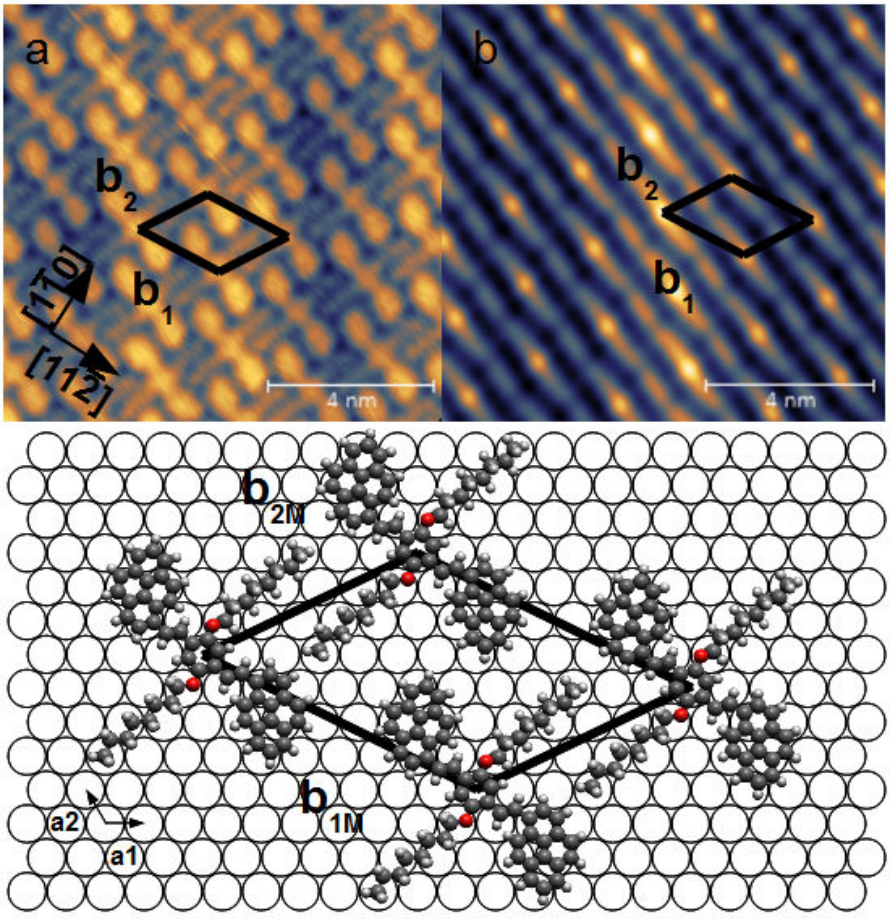

Figure 3.8.: a) STM image (10 nm x 10 nm, U_b=0.9 V, I_t=30 pA) of δ domain of bis-pyrene /Au(111). Deposition temperature: 250 K. b) 2D-autocorrelation of a). c) Ball and stick model corresponding to the proposed matrix for this structure.

The high resolution achieved in this image gives us interesting information: an angle close to 90° is observed between alkyl chains and the Pyr-OPV-Pyr complex, as in the case of the β structure. Statistical studies concerning the relative orientation between the unit cell and the substrate lead to the conclusion that the unit cell vector b_2 is close ($\pm 5°$) to the $[11\bar{2}]$ direction and show mirror domains as in the case of the α structure. Moreover, an angle of 15$\pm$4° is measured between the direction of alkyl chains and the unit cell vector $\mathbf{b}_2$. The measured distance between two interdigitated alkyl chains is d_{C8}=0.45$\pm$0.05 nm and the interdigitation length is 0.85$\pm$0.07 nm. We can again ascribed this structure to

a commensurate overlayer, which is described by the following matrix:

$$M_\delta = \begin{pmatrix} 5 & -4 \\ 7 & 3 \end{pmatrix}$$

Figure 3.8.c shows the schematic model corresponding to the proposed matrix. Again we have placed the central phenyl ring of the bis-pyrene molecule atop a gold atom. The unit cell parameters of the commensurate model are $\mathbf{b}_{1M}$=1.75 nm, $\mathbf{b}_{2M}$=2.25 nm and θ=51.6 °. The molecular density calculated from this matrix corresponds to 3.24 x 10^{13} cm^{-2}, which is in agreement with the value determined by STM. The length variation of approximately 0.15 nm observed for unit cell vector b_2 for the β and the δ structures can be explained by two different geometries of alkyls interdigitation, as shown in schematic models presented for both structure (figure 3.6.c and 3.8.c). These variations lead to the formation of a more compact layer compared to the other self-assembled structures.

Even though we have tentatively assigned the four different ordered structures to commensurate overlayers, we do not have a formal prove of that assumption. Moreover, the 23x$\sqrt{3}$ reconstruction of the Au(111) surface hasn't been taking into account in the proposed models, where interatomic distances of the first atomic layer of the substrate are considered equal to the interatomic distances of the bulk structure. We have undertaken LEED measurements of the overlayers but these have proven to be unsuccessful due to the electron beam damage encountered in conventional LEED. No conclusive results have thus been obtained.

3.1.3. Discussion

We compare the properties of the four distinct ordered layers and molecular wire in table 3.1.

Structure	W	α	β	γ	δ
ML density $[10^{13}cm^{-2}]$ STM/model	- / -	2.90/2.96	3.11/3.05	3.13/3.16	3.19/3.24
inter-alkyl distance (d_{C8}) [nm]	0.43±0.05	0.41±0.05	0.47±0.07	0.45±0.05	0.45±0.05
Interdigtation length [nm]	0.9±0.2	1.0±0.1	0.75±0.1	0.80±0.1	0.85±0.07
Conformation	Trans (maj.)/Cis	Cis	Trans	Trans	Trans

Table 3.1.: Comparison of the properties of the ordered layers and molecular wire.

From this, we can draw some important conclusions concerning the formation of the structures. First in the low coverage regime, the growth is template-

assisted and the linking between the molecules in molecular wires is assured by alkyl-alkyl interactions. At coverages around 0.39 ML the formation of a first self-organized two-dimensional structure takes place, the α structure, where only one alkyl chain of each molecule is interdigitated. The molecular backbone shows a cis-configuration with respect to the orientation of the pyrene moieties. The formation of the α structure takes place for molecular densities which are lower than in the case of the β, γ and δ structure. The relative coverage of the α structure compared to the β structure corresponds to 0.93 ML. However, since this structure is already found at 0.4 ML consequently some disorder must exist outside the ordered domains. This is corroborated by the STM image in figure 3.2.a.

Another very important point is the temperature dependence of the formation of these structures: the γ structure has never been observed for deposition performed below RT, whereas both β and δ were observed. The δ structure has never been observed for deposition performed at RT, whereas both β and γ (rarely) were observed. The main difference between δ and γ structure, besides the relative orientation with respect to the Au(111) substrate, is the angle between alkyl chains and the pi-conjugated molecular backbone, which are close to 90° and 75°, respectively. This difference can be explained by a different molecular configuration.

Most interestingly, the inter-alkyl distance (d_{C8}) shows slight variations depending on the molecular structures. Alkyl chains are closer in the case of molecular wires and the α structure. In the case of the denser structures this inter-alkyl distance is increasing. Furthermore we also observe that the interdigitation lengths are more important for the α structure and molecular wires and are decreasing for δ, γ and β domains. The most important interdigitation length (1.0$\pm$0.1 nm) in the case of the α structure can be attributed to a more favourable steric environment due to the cis-configuration of pyrene moieties. On the other hand, the smallest interdigitation length observed in the case of the β structure (0.75$\pm$0.1 nm) can be attributed to the trans-configuration of the pi-conjugated backbone, and the orientation of the pyrene group observed in the alignment of the alkyl. This last point can also explain the intermediate interdigitation length observed in the case of the γ and δ structure.

To explain this difference we need to consider that pyrene moieties and vinylene-pyrene moieties of the bis-pyrene compound can rotate at different position. For better clarity different configurations (this list is not exhaustive) of the bis-pyrene molecule are schematically shown in figure 3.9. Blue arrows in figure 3.9.a indicate positions where the rotation of the pyrene moieties can take place, and red arrows indicate positions where the vinylene-pyrene moieties can rotate. In figures 3.9.a, 3.9.b and 3.9.c three possible configurations for the cis-configuration are depicted. Figures 3.9.d, 3.9.e and 3.9.f show two different trans-configurations (3.9.d and 3.9.f are identical but are attributed respectively to β and δ domains as underlined by STM pictures).

The first step is to attribute a molecular conformation for the bis-pyrene molecule involved in the α structure. As we can see in the previous high resolution STM images, it appears that the pi-conjugated backbone shows a dissymmetry with respect to the alkyl chain direction, which can be attributed to the conformation depicted in figure 3.9.c.

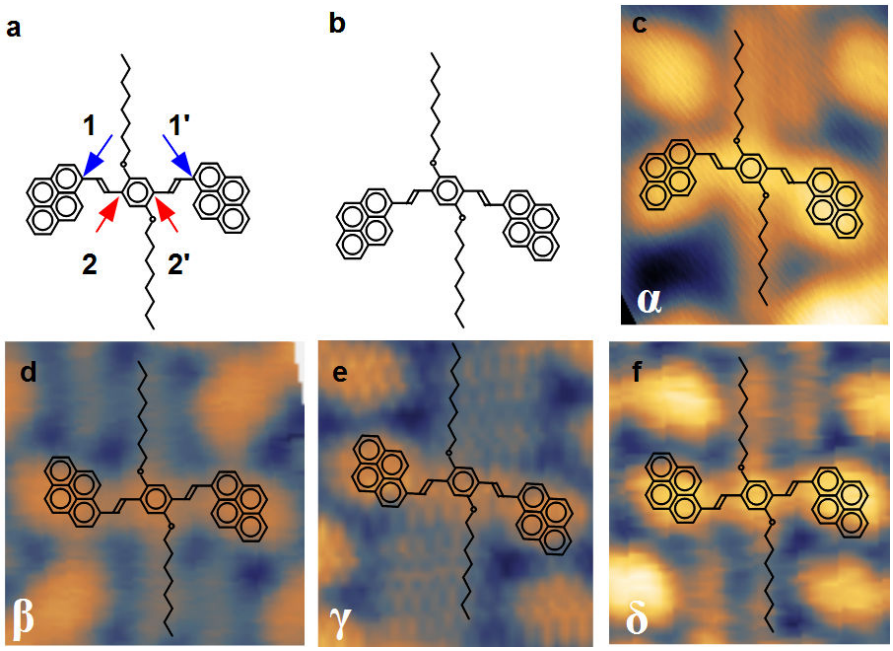

Figure 3.9.: Different Lewis representations of the bis-pyrene molecule. a),b) and c) Cis-configuration. d), e) and f): trans-configuration. Coloured arrows indicate where the rotation can take place. c), d), e) and f) show STM images of the bis-pyrene observed in the four different structures characterised.

Our STM experiments show that the β, γ and δ structures arise from a reorganization of the previously formed α structure which can be explained by different rotations of the molecular backbone moieties. The difference observed in the molecular configuration between δ and γ structure can be explained by different rotation processes, which lead to a trans-configuration with respect to the pyrene moieties, but differ from the orientation of the vinylene-phenylene bridge.

Another interesting point is related to bis-pyrene constituting β and δ domains which show the same molecular configuration but a difference in the interdigitated length. This can be explained with respect to the steric hindering imposed by the configuration of pyrene moieties in the case of the β structure. In the case of the δ, the configuration of the pyrene with respect to the interdigitated alkyl chain of the neighbouring molecule allows for a more important interdigitation length. This relative configuration of vinylene-pyrene moieties can also explain

the interdigitation length close to 1 nm observed in the case of the α structure.

From these observations we can conclude to a decrease of the influence of the alkyl chains interactions, responsible for the formation and the stability of molecular wires and α structures, with the molecular density.

This comparison between simple lewis model of the molecule and high resolution STM image allows us to explain the different features observed. However, density functional theory (DFT) calculations have to be performed to be sure of the molecular configuration, taking into account the surface and the surrounding molecules.

3.2. Optical properties of bis-pyrene

The investigation of the optical properties of bis-pyrene molecules will be presented in this section. Results for conventional UV-Vis measurements performed in solution and for thick films evaporated under vacuum conditions will be first discussed. However, conventional UV-Vis measurements do not allow the investigation of the optical properties at very low coverage due to the low sensitivity of the technique. Surface cavity ring-down spectroscopy is a powerful spectroscopic technique, which allows the investigation of the optical properties of surface adsorbates at very low coverages (few percent of a monolayer). The theory, the data treatment and the experimental setup are described in the subsection 1.2. Here, the investigation of the optical properties of bis-pyrene, using the s-CRDS technique will be presented. The bis-pyrene films were deposited in the coverage from 0.25 to 4 ML on a BK7 amorphous glass substrate. The influence of the coverage and the temperature will be discussed.

3.2.1. UV-Vis measurements of bis-pyrene

UV-Vis measurements have been performed under ambient conditions for bis-pyrene in tetrahydrofurane (THF) solution (blue curve) and for a thick film evaporated under high vacuum conditions (red curve). The normalized spectra are displayed in figure 3.10.

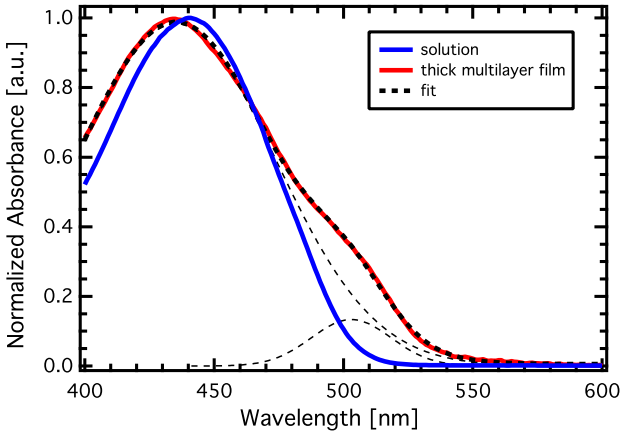

Figure 3.10.: UV-Vis spectroscopy of bis-pyrene. Blue spectrum recorded in THF solution. Red spectrum recorded for a thick film evaporated on BK7. Red spectrum can be fitted by two Gaussian curves.

We note that in the case of bis-pyrene in THF solution the compound is transparent above 520 nm and shows a single absorption band with a maximum

at 441 nm. In pyrene-containing compounds this low-energy band can be attributed to the long-axis polarized transition ^1L_a.[56,63,100] In solution, it appears that bis-pyrene exhibits a weak positive solvatochromism effect. The absorption spectrum of the thick film on BK7 is composed of an intense transition band (with a maximum at 434 nm, again attributed to the long-axis polarized transition ^1L_a), and a shoulder at higher wavelength. The compound is transparent above 550 nm. This spectrum can be fitted by two Gaussian curves, as shown in figure 3.10, which allows us to determine the position of the second peak: 505 nm. Interestingly, this shoulder has not been observed neither in THF solution, nor in other solvents. This suggests that this shoulder arises from an interaction of the transition dipole moment of neighbouring molecules. This phenomenon is well-known as Davydov splitting[101] in the case of organic crystals.

In order to elucidate the origin of this additional absorption band, the coverage-dependent optical properties of bis-pyrene deposited on BK7 substrate have been investigated by s-CRD spectroscopy, which allows to cover the very low coverage regime inaccessible by conventional UV-Vis spectroscopy. The influence of the substrate temperature (RT or 120 K) has also been investigated.

3.2.2. S-CRDS of bis-pyrene deposited at LT

In figure 3.11.a, four s-CRD spectra recorded in the wavelength range from 420 to 680 nm are displayed. These spectra have been recorded for molecular densities from 1.6 to 6.6 x 10^{13} cm^{-2} (equivalent to 0.5-2.1 ML considering the molecular densities of the compact structures observed on Au(111), see table 3.1) deposited on a cold substrate (120 K). Depending on the molecular density, s-CRD spectra show distinct features.

The spectra recorded for the two lowest coverages show an intense transition band at 434 nm. At coverages of 4.6 x 10^{13} cm^{-2} and above, spectra show the same features as the UV-Vis spectra recorded for thick films deposited on a BK7 glass substrate: an intense transition band at 434 nm, a shoulder around 505 nm, and the compound is transparent above 550 nm. At the lowest coverage investigated (1.6 x 10^{13} cm^{-2}) the s-CRD spectrum does not show this shoulder at 505 nm. In all spectra, the maximum of the absorption band is localized at 434 nm and its position is independent of the coverage. The loss per pass at this wavelength is linearly proportional to the molecular density, as expected (see figure 3.12).

In order to visualize the intensity changes at 505 nm, the normalized raw spectra in the range 480 to 540 nm, a region that corresponds to a single set of highly reflective mirrors, are depicted in figure 3.11.b for molecular densities ranging from 1.6 x 10^{13} cm^{-2} to 1.2 x 10^{14} cm^{-2} (0.5-3.9 ML). We can clearly observe an increase in the relative absorption intensity around 505 nm as a function of the coverage up to a coverage of 6.6 x 10^{13} cm^{-2}. For higher film thicknesses, the normalized intensity of this shoulder remains constant despite the intensity

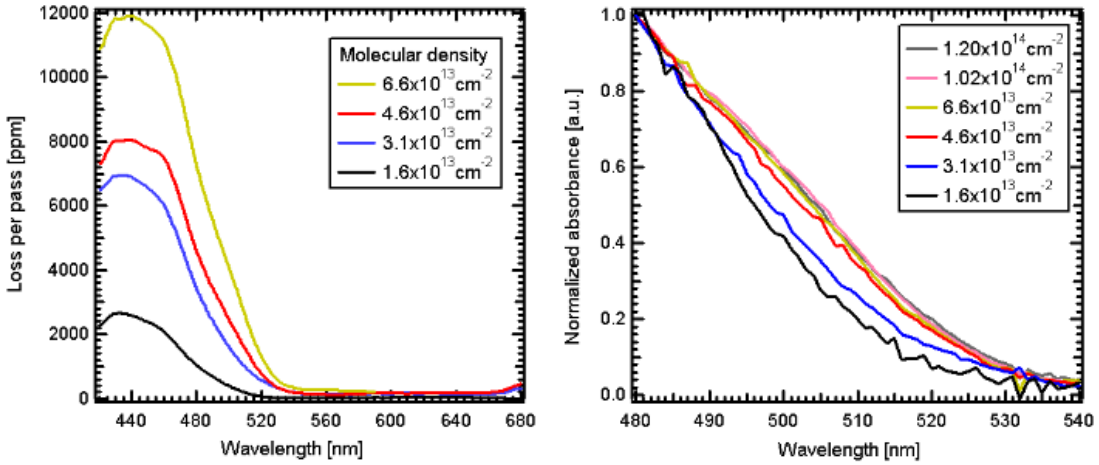

Figure 3.11.: S-CRDS spectra of bis-pyrene deposited on BK7 substrate at T=120 K. a) full range spectra (420-680 nm) recorded for four different coverages. b) Raw data recorded in the range 480-540 nm (single set of mirrors) normalized at 480 nm recorded for six different coverages.

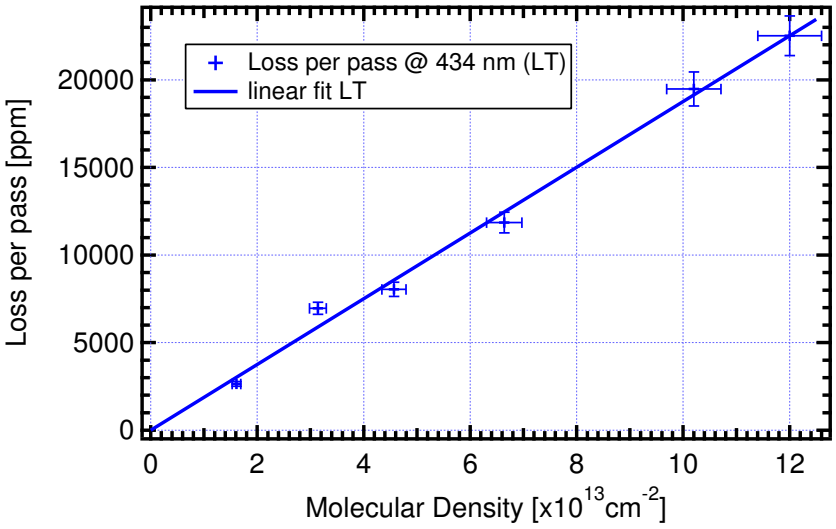

Figure 3.12.: Loss per pass measured at 434 nm as function of the molecular density.

increase of the peak at 434 nm. It is known that we can observe the appearance of spectral components at lower and higher energy in the absorption spectrum of chromophores coupled in different geometries.[102] This effect is well-known in the case of molecular crystals[101] and has been observed in the case of the formation of amorphous films with local crystalline order.[103,104] The shoulder is already visible at a coverage of 3.1 x 10^{13} cm^{-2}, which corresponds approximately to the completion of the first monolayer as determined by STM measurements (see table 3.1). We attribute the development of this shoulder to a particular molecular stacking allowing the interaction of transition dipole moments of the first and the second layer. The fact that this shoulder appears for coverages below the monolayer suggests the formation of molecular islands. At higher coverages we observe that the intensity of this shoulder saturates for molecular density above 4.6 x 10^{13} cm^{-2}. This suggests that above this coverage, the interfacial region between the first layer and the second layer does not increase any more. The shoulder can thus unequivocally be attributed to the interface of the first and the second molecular layer.

3.2.3. S-CRDS of bis-pyrene deposited at RT

A second series of experiments has been performed for bis-pyrene deposited on BK7 at room temperature. Full s-CRD spectra recorded in the wavelength range from 420 to 680 nm are shown in figure 3.13.a. Three different coverages are displayed, from 7.2 x 10^{12} cm^{-2} (0.25 ML) to 4.2 x 10^{13} cm^{-2} (1.35 ML). Here again, only the molecular transition at 434 nm is observed for coverages up to 2.3 x 10^{13} cm^{-2}, and the shoulder appears at coverages of 4.2 x 10^{13} cm^{-2}.

The normalized absorbances obtained at different molecular densities and in the range 480–530 nm are shown in figure 3.13.b. As in the case of the deposition at LT, an increase of the intensity of the shoulder at 505 nm is observed between 7.2 x 10^{12} cm^{-2} and 2.3 x 10^{13} cm^{-2}, indicating that the interaction of molecules in the first and the second layer already takes place at this low coverage. A saturation of the normalized absorption is observed above 4.2 x 10^{13} cm^{-2}, which can again be explained by an interaction of the transition dipole moments of of the molecules at the interface between the first and the second layer. Note that the saturation of the shoulder takes place at a lower molecular density in this case compared to a deposition performed at LT, which will be discussed below.

3.2.4. Discussion

In order to get a better understanding of the changes observed by the means of s-CRD spectroscopy, we compare these results with the results obtained by STM for bis-pyrene deposited on Au(111). It is known that the Au(111) surface interacts weakly with organic adsorbates[105] which gives us the possibility to study the

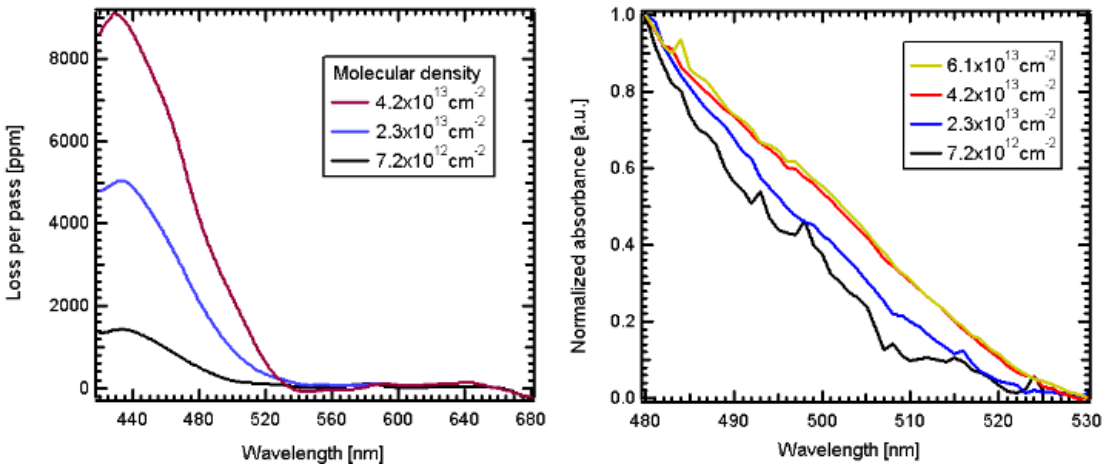

Figure 3.13.: S-CRDS spectra of bis-pyrene deposited on BK7 substrate at RT. a) Full range spectra (420-680 nm) recorded for 3 different coverages. b) Raw data recorded in the range 480-530 nm (single set of mirrors) normalized at 480 nm for four different coverages.

physisorbed bis-pyrene molecules in a weakly perturbed state that should be similar to the state on BK7 substrate used for the optical measurements.

The informations obtained in the STM studies allow us to discuss with more details the s-CRD results. First, we know from our STM measurements that the molecular density of the first monolayer is close to 3.1 x 10^{13} cm^{-2}, a value in the range of molecular densities investigated by s-CRDS measurement. Secondly, we know that the temperature plays an important role at different stages of the growth process. The size of the domains observed in the first monolayer is affected: the lower the temperature, the smaller the domain size. Furthermore, the temperature also plays a role in the formation of the second monolayer. Whereas a self-assembled growth takes place at RT (see figure 3.3.e and .f) at low temperature (180 K) the limited molecular diffusion leads to the formation of amorphous structures randomly distributed after the formation of the first monolayer (see figure 3.3.c and .d).

In the case of s-CRD measurements we observe that the interaction of the molecular transition dipole moments, which is attributed to the formation of the second layer, already starts below the molecular density expected for a complete monolayer. This strongly suggests the formation of molecular multi-layers allowing these kind of interactions before a completion of the first monolayer. The saturation of the signal for molecular density of 4.2 x 10^{13} cm^{-2}, in the case of the deposition performed at RT, corresponds approximately to a coverage of 1.35 ML observed in STM. This saturation of the signal can only be explained when considering different growth modes on Au(111) and BK7.

On Au(111), we observed a growth mode with a completion of the first mono-

layer before the second layer starts to grow, independently of the temperature. Since higher coverages have not been investigated this could either be a Frank–van der Merwe or Stranski–Krastanov growth mode for the RT deposition. At LT, the mode can clearly be identified as being of Stranski–Krastanov type, which is indicated by the presence of structures in the STM images showing an apparent height of two times the apparent height measured for the second monolayer. On BK7, the appearance of the signal at coverages below the monolayer and the saturation of the signal at coverages below an equivalent of two monolayers suggests strongly a Volmer–Weber growth mode. This is an important difference compared to the growth mode observed on Au(111). On BK7 no complete wetting takes place in the coverage range investigated. As underlined before, the saturation of the signal takes place at lower coverages in the case of deposition performed at RT.

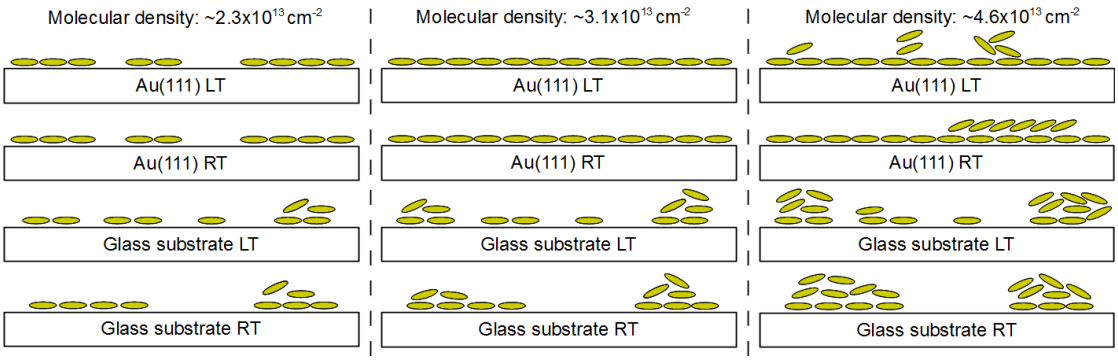

Figure 3.14.: Schematic growth of bis-pyrene on Au(111) and on BK7 substrate at different coverages and temperatures.

Figure 3.14 displays schematically the growth modes proposed for bis-pyrene on Au(111) and on BK7 at low and room temperature. It is well-known[106] that in the case of thin film growth, the number of molecular islands strongly depends on the substrate temperature. Increasing the temperature leads to an enhanced diffusion, which favours the growth of larger molecular islands. This temperature effect leads also to a decrease in the density of islands at higher temperature. The distinct evolution of the shoulder at 505 nm in s-CRD measurements in the submonolayer regime can thus be explained by the different growth kinetics at LT and RT, i.e. the formation of fewer molecular islands at RT. This leads to a saturation of the signal taking place at molecular density lower than in the case of the LT deposition. The growth mode corresponds however, to a Volmer–Weber type at the two temperatures as shown in figure 3.14.

The electronic states of the adsorbed bis-pyrene on Au(111) were also investigated by scanning tunnelling spectroscopy. Local I(V) measurements were performed on top of the pyrene groups and averaged (black line in figure 3.15) in

order to reduce the noise of the spectra. The differential conductivity dI/dV, which corresponds to the local density of states (LDOS) of the sample, has then been calculated from the averaged I(V) curve by numerical differentiation (red curve). The spectrum clearly shows a bandgap with a residual differential conductivity in the gap, which is due to the Au(111) substrate. From the dI/dV curve a HOMO-LUMO gap of 2.85 eV can be derived, which is indicated by the increase of the LDOS below -1.2 eV (HOMO) and above 1.65 eV (LUMO). This HOMO-LUMO gap of 2.85 eV derived by STS is in excellent agreement with the optical gap, which corresponds to the transition at 434 nm (2.86 eV). This suggests that the interaction of the bis-pyrene with the Au(111) surface is indeed weak and thus very similar to the adsorption on the BK7 substrate used for the s-CRD measurements. The small peaks, which are observed in the region -1 eV to -0.5 eV, can be attributed to the Shockley surface band of the Au(111) surface, which is located at -0.5 eV[107] on the clean surface. It has been reported that this surface state is shifted by the presence of various adsorbates,[105,108] which seems also to be the case here.

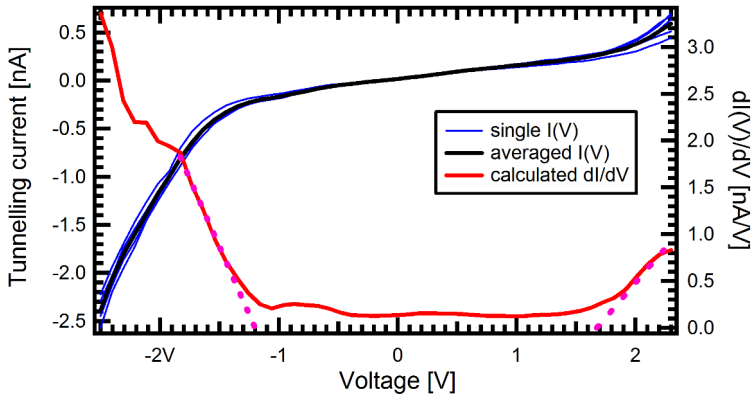

Figure 3.15.: Scanning tunnelling spectroscopy of bis-pyrene on Au(111). The blue curve results from an average of several I(V) measurements. The red curve has been calculated. A HOMO-LUMO gap of 2.85 eV can be determined from the calculated dI/dV.

3.3. Conclusion and outlook

In this chapter the characterisation of the growth process, the electronic and optical properties of bis-pyrene molecules deposited on Au(111) and an amorphous BK7 glass substrate have been presented.

STM experiments show that the growth process and particularly the formation of the different ordered structures strongly depends on the substrate temperature

and on the molecular density. The growth process is guided by an interplay of intermolecular interactions of van der Waals type, due to the interdigitation of alkyl chains, and molecule-substrate interactions, as for example in the case of the preferential growth of molecular wires on fcc domains of the Au(111) reconstructed surface.

The fact that we observe four different ordered structure can be related to the rather flexible molecular backbone where rotations of pyrene and/or vinylene-pyrene moieties can take place at different locations. This allows bis-pyrene molecules to have different geometries leading to the formation of the distinct structures. For these self-assembled domains commensurate models have been proposed which are in very good agreement with the STM results.

It appears from our observations that the β structure is the kinetically most stable structure when films are grown at RT: single highly-ordered domains can be observed covering entire atomic terraces larger than several hundreds of nanometres. The γ structure is rarely observed when bis-pyrene is deposited at RT and never when depositions are performed at LT. The δ structure has only been observed when molecules are deposited at low LT, despite the fact that this structure is the most dense that has been observed on Au(111).

We observe that the formation of a second well-ordered layer takes place under particular conditions: deposition has to be performed at RT, and the quenching to LN_2 temperature necessary for imaging has to be done after only a few tens of minutes to allow the self-organization of the molecules. If these conditions are not respected, the formation of an amorphous second layer takes place. However, annealing a sample at RT after deposition leads to the formation of an ordered structure in the second layer.

Due to the fact that the kinetics of the growth process depends on the molecular flux and the temperature, it should be possible to grow this ordered structure by increasing slightly the temperature of deposition or reducing the molecular flux. Unfortunately, we were not able from our STM experiments to determine precisely the structure and the organization of bis-pyrene molecules involved in these well-ordered structures observed in the second layer.

An interesting modification of the optical properties as a function of the coverage has been observed in s-CRD spectroscopy. The appearance, followed by a saturation, of a shoulder around 505 nm in the optical spectra is observed as a function of the molecular density. Combining observations from these measurements of the optical properties obtained by s-CRDS with conventional UV-Vis measurement and STM experiments performed on Au(111) allow us to assign this modification to an interaction of the transition dipole moments of molecules of the first and the second layer.

Furthermore, these experiments reveal also that the molecular growth process on the BK7 glass substrate is a Volmer-Weber growth mode, which is different from the growth mode observed for bis-pyrene on Au(111). We also observe that the substrate temperature has a strong influence on the molecular diffusion and

the formation of molecular structure: higher temperature enhances the molecular diffusion, leading to the formation of multi-layers islands at lower molecular density compared to deposition performed at lower temperature.

An interesting experiment that could be done to confirm these observations is to deposit bis-pyrene molecules on thin oxide films, such as Al_2O_3/Ni_3Al (111), and investigate the growth process as function of temperature by the means of STM.

4. DHTAP/Au(111): chemical modifications induced by STM

During the STM investigations of DHTAP on Au(111), we observed intriguing modifications of DHTAP molecules embedded in the first and the second monolayer after recording STM images at higher bias voltage. We decided to investigate the electronic properties of these species by STS and compare their properties to those of the 5,14-DHTAP molecules. During these investigations we observed that we can in fact use the STS technique to induce chemical modifications of a selected molecule, and not only randomly over an area scanned at high bias voltage. After these observations, we also investigated the possibility of inducing these modifications by applying a pulse voltage and monitoring the tunnelling current. The following chapter will focus in the first part on the modifications observed for molecules embedded in the first monolayer, the second part will focus on modifications observed in the second monolayer, where more complex modifications are observed.

4.1. Modifications induced in the first monolayer

4.1.1. STM/STS results

The STM image depicted in figure 4.1.a shows DHTAP molecules in the first monolayer. This image captured our attention due to the presence of molecules displaying a different shape. Most molecules in the image appear to have the well-known structure of DHTAP, but 5 molecules show particular features: the molecular orbitals of these compounds seem to be imaged.

A particularly interesting detail is the fact that these molecular orbitals show two symmetry axes, along the long and the short molecular axis of the molecule. Apparent height measurements reveal a difference of 25 pm between DHTAP and this different type of molecules. Due to the asymmetry of the DHTAP (presence of H atoms in position 5 and 14) this can only be explained by a chemical modification of the DHTAP molecule. We thus decided to perform STS measurements to investigate the electronic properties of these two different kinds of molecules. The corresponding STS spectra are depicted in figure 4.1.b and 4.1.c. Each STS measurement has been reproduced several times to ensure the reproducibility of the results.

In the first case (4.1.b), STS measurements have been performed on a 5,14-DHTAP molecule, at the position 1 in the STM picture. The spectra obtained show a metallic behaviour characterised by a non-zero density of states at low voltages. However, dI/dV curves clearly show a HOMO-LUMO gap of 2.2 eV,

which is indicated by the steep increase in the LDOS below -0.7 V (attributed to the HOMO, with a maximum at -1.0 V) and above 1.5 V (attributed to the LUMO).

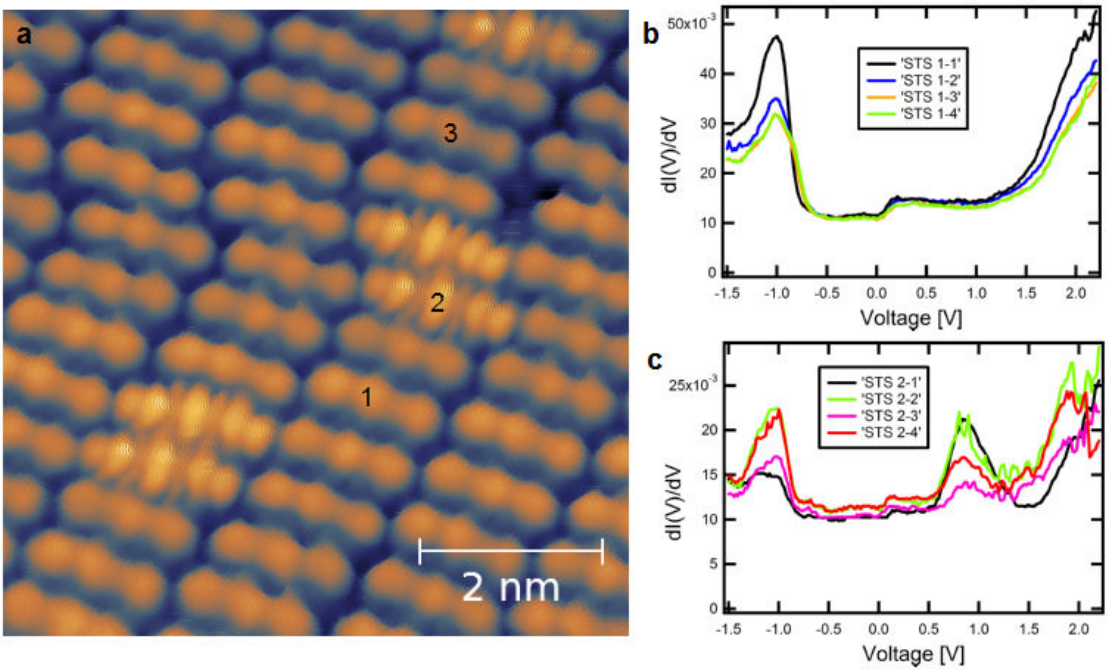

Figure 4.1.: a) STM image (7 nm x 7 nm) of the first monolayer of DHTAP deposited on Au(111) at 250 K. U_b=0.9 V; I_t=70 pA. b) STS spectra performed at the position 1: four spectra were recorded to ensure reproducibility. c) STS spectra performed at the position 2: four spectra were recorded to ensure reproducibility.

In the second case (4.1.c), STS measurements have been performed on a modified molecule at position 2 in the STM image. As in the previous case a metallic behaviour is observed, characterised by a non-zero density of state in the observed band gap. In this case the HOMO-LUMO gap, indicated by the increase in the LDOS below -0.7 V (HOMO, with a maximum at -1.05 V) and above 0.6 V (LUMO, with a maximum at 0.85 V), is consequently reduced to 1.3 eV. Moreover, a second increase in the LDOS is observed above 1.5 V and can be tentatively attributed to the LUMO+1.

It is obvious from these measurements that the electronic properties of both types of molecules are different. Moreover, the STM image 4.1.a has been acquired at a bias voltage of 0.9 V, very close to the peak maximum (LUMO) observed in the STS measurements of the modified molecules. The molecular orbitals imaged for the new compound can thus unambiguously be attributed to the LUMO of this molecule.

In order to confirm these observations we conducted further STS on the 5,14-DHTAP molecule at position 3 in figure 4.1.a. The corresponding STS spectra are displayed in figure 4.2.a.

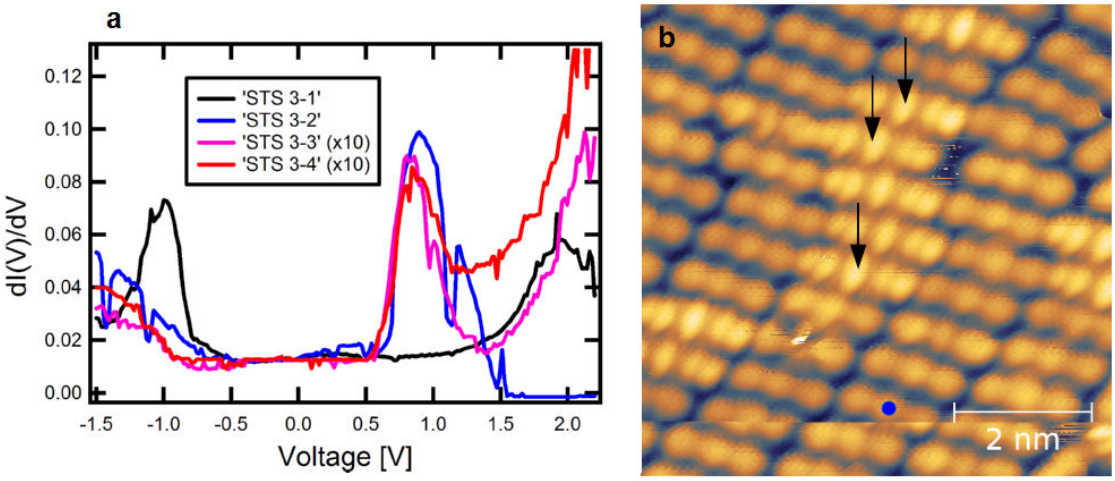

Figure 4.2.: a) STS spectra performed at the position 3 of figure 4.1.a: four spectra are recorded but are not reproducible. b) STM image recorded after the STS measurements: U_b=0.9 V; I_t=70 pA.

In this case, STS spectra are not reproducible. For a better clarity, STS spectra 3-3 and 3-4 have been rescaled. The first spectrum (STS 3-1) shows the typical features of DHTAP as depicted in figure 4.1.b. An increase in the LDOS localized below -0.7 V, associated with the HOMO, and an increase in the LDOS above 1.5 V, associated with the LUMO, are observed. The second spectrum, 3-2, does not show this behaviour. An increase in the LDOS is observed below -0.7 V, without resolving a peak maximum and which can be associated to a HOMO. Another increase in the LDOS is observed above 0.6 V, with a peak maximum resolved at 0.85 V. The LDOS decreases then to zero, which differs from the spectrum 3-3, where an increase of the LDOS at higher bias voltage is observed. Note that changes in STS spectra 3-1, 3-2 and 3-3 suggest that chemical modification of the molecule occurs during spectroscopy and that the final spectrum, 3-4, is similar with STS spectra depicted in 4.1.c, which suggests the formation of the new compound.

The STM image shown in figure 4.2.b has been recorded after the acquisition of these STS spectra. First, we can observe an alteration of the resolution, suggesting a modification of the tip characteristics (shape, adsorbate at the apex, ...) which can lead to a modification of the tip states and thus to instabilities in the STS measurements. However, the high resolution of the LUMO on the new molecular compound is preserved. Secondly, in addition to the five previously observed modified molecules, three newly modified molecules are observed, in-

dicated by black arrows. These observations suggest that we are able to induce a modification of the original 5,14-DHTAP molecules by STS, leading to the formation of the new compound.

To be sure about the reproducibility of these observations, we decided to perform further STS measurement on DHTAP molecules. Successive STM images recorded after each STS measurement (at positions indicated by blue dots) are displayed in figure 4.3.

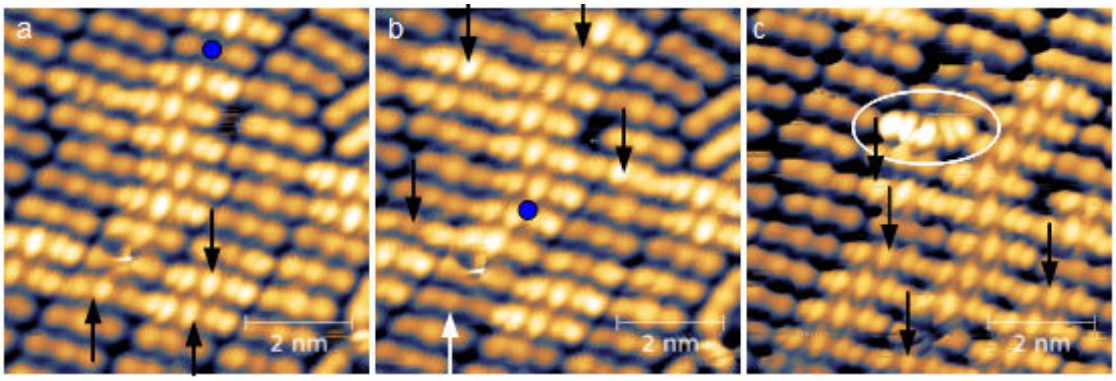

Figure 4.3.: a) & b) STM image performed after other STS measurements performed on DHTAP molecules: the process is reproducible. c) After several STS performed on a compound with symmetric orbitals, a new structure with asymmetric orbitals is observed. STM parameters: U_b=0.9 V; I_t=70 pA.

The first STM image has been recorded after one STS measurement performed in the lower part of the image, at the position indicated by a blue circle in the figure 4.2.b. We can confirm that we induced again modifications in the 5,14-DHTAP molecules localized under the tip during the STS measurement, leading to the formation of three new compounds, indicated by black arrows, which have molecular orbitals with two symmetry axes.

The second STM picture (4.3.b) has been recorded after another STS measurement at the position indicated by the blue circle in the previous STM image. This STS measurement leads to the formation of four other symmetrical compounds indicated by black arrows. We also observe that a compound imaged previously with symmetrical molecular orbitals is now imaged as a 5,14-DHTAP molecule (white arrow) suggesting that the modification process could be reversible.

After another STS measurement, indicated by the blue dot in the STM image 4.3.b, the STM image in figure 4.3.c has been recorded. We can again denote a clear change in the resolution between figure 4.3.b and 4.3.c which can be attributed to a modification of the tip states as mentioned above. We observe the formation of four additional compounds with symmetrical orbitals, indicated by black arrows. In addition to that we observe the formation of a molecule imaged with different molecular orbitals (shape of a “croissant”, surrounded by

a white circle). The apparent height of this "croissant" is 80 pm higher than DHTAP molecules (55 pm higher than the compound showing highly symmetric molecular orbitals) suggesting that the molecular compound is not perfectly embedded in the first monolayer anymore. It has to be pointed out that this compound with these asymmetric orbitals has been observed only once for STM/STS experiments performed in the first monolayer. We will return to this point latter.

From these observations, we can conclude that it is possible to induce chemical modifications of 5-14,DHTAP molecules embedded in well-ordered self-assembled first monolayer using the tunnelling current. Our observations suggest that the modification leads to the formation of a compound showing molecular orbitals with particular symmetry with respect to the long and short molecular axes.

4.1.2. Discussion

It has been shown recently that it is possible to induce a dehydrogenation using the inelastic electron tunnelling for various isolated compounds as methylaminocarbyne,[109] tetrahydroxybenzene,[25] Co-N,N'-ethylenebis (salicydeneiminato) complexes,[24] tetraphenyl-porphyrin[22] or phtalocyanine.[110] This dehydrogenation has also been (rarely) observed for molecules embedded in well-ordered monolayers.[26] The reversibility of the process has been demonstrated for some of these systems.[26,109,110]

As mentioned above, our attention was captured by the symmetry of the molecular orbitals along the long and short molecular axes. In our case, the two most promising candidates for the formation of a symmetric compound from 5,14-DHTAP are 5,7,12,14-dihydro-5,7,12,14-tetraazapentacene (THTAP) and the 5,7,12,14-tetraazapentacene (TAP) because these are the only two molecules derived from 5,14-DHTAP showing a symmetry along the long and short molecular axes. Consequently, their respective molecular orbitals should show symmetry along the long and short molecular axes.

The formation of a symmetric compound from 5,14-DHTAP can be conceived in two different ways: a double dehydrogenation of nitrogen atoms in position 5 and 14, leading to the formation of TAP, or a double hydrogenation of nitrogen atoms in position 7 and 12 resulting in the formation of THTAP. We decided to perform DFT calculations[111] for these compounds and compare the shape of the molecular orbitals with our STM results. The calculations were done using GAMESS for single molecules using the B3LYP functional.[112] The chemical structure and shape of HOMO and LUMO resulting from the DFT calculations are summarized in figure 4.4 for 5,14-DHTAP, THTAP and TAP.

As expected, the molecular orbitals symmetry reflects the symmetry of the molecular backbone. Only the symmetry, with respect to the long molecular axis, is observed in the case of the 5,14-DHTAP. Both TAP and THTAP HOMO's and LUMO's show two symmetry axes, along the short and long molecular axes.

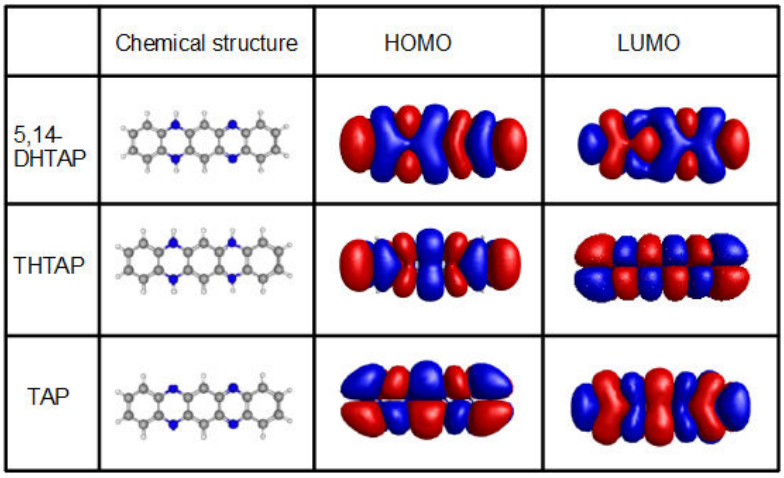

Figure 4.4.: DFT calculation performed for isolated DHTAP, THTAP and TAP molecules.[111] The shape of the calculated HOMO and LUMO is shown.

As already mentioned, the STS measurement performed on the compound showing symmetrical axes combined with the bias voltage used to record the STM image allow us to unambiguously attribute the molecular orbitals to the LUMO of the compound. A comparison between molecular orbitals observed by STM and the shape of the LUMO calculated for TAP strongly suggests that the modification induced in the 5,14-DHTAP is a double dehydrogenation taking place at the position 5 and 14. Indeed, the high resolution of the STM images (4.1.a 4.2.b and 4.3) allows us to unambiguously determine seven lobes constituting the molecular orbitals, which are aligned along the long molecular axis, in very good agreement with DFT calculations performed for the LUMO of the isolated TAP molecule.

It also seems possible that a reversible process occurs, as underlined previously, where a TAP molecule observed in the lower part of figure 4.3.a is imaged as a 5,14-DHTAP molecule in the following image (white arrow in 4.3.b) and then again as a TAP molecule (figure 4.3.c) after another STS measurement. However, the formation of DHTAP from TAP would require two hydrogen atoms which have to be incorporated in the TAP molecule. The origin of these hydrogens remains uncertain, however, it is possible that these atoms came from 5,14-DHTAP molecules dehydrogenated during the STS measurement. Another possibility, proposed by Smykalla et al.[26] in the case of the reversible dehydrogenation of tetra(p-hydroxyphenyl)porphyrin molecules, is that hydrogen atoms released during a previous dehydrogenation of DHTAP adsorb on the tip apex and are incorporated in the TAP molecule during a following STS measurement.

The TAP molecule has been the subject of a number of publications until Dutt[113] claimed in 1926 that TAP can be obtained by the condensation of 2,3-diaminophenazine with 1,2-benzoquinone. However, Badger et al.[114] disputed

Dutt's claim in 1951 to have prepared TAP molecules. Numerous attempts have been made to repeat Dutt's preparation of TAP, but without success. Many attempts to oxidize the 5,12-DHTAP molecule to the TAP structure were made, but all proved unsuccessful. The synthesis of TAP molecule by oxidation of 5,14-DHTAP has also been studied without success by Miao et al.[115] To our knowledge, it is not possible to synthesize this molecule by conventional chemical ways. However, we are able to produce, in a controllable manner, TAP from the dehydrogenation of nitrogen atoms localized in position 5 and 14 in the 5,14-DHTAP molecule embedded in the ordered first monolayer using the tunnelling current of a STM. This process is very reproducible and leads to the formation of TAP.

4.2. Modifications induced in the second monolayer

After having observed that we are able to induce the dehydrogenation of DHTAP molecules embedded in the first monolayer, we decided to investigate the possibility of inducing these modifications in molecules embedded in the second monolayer. Up to now, all STM and STS measurement presented were performed at liquid nitrogen temperature. In the following part, some STM images and STS measurements have also been obtained at liquid helium (LHe) temperature.

4.2.1. STM observations

In figure 4.5 successive STM images recorded at coverages of approximately 1.5 ML of DHTAP on Au(111) are displayed. In the first STM image (4.5.a), we can clearly observe the presence of different molecules in the second monolayer, which are imaged with resolution on molecular orbitals of various shapes.

Two of these molecular orbitals (indicated by black arrows) show a symmetry along the long and short molecular axes and can thus be identified as TAP, as it has been observed in the case of modifications induced in the first monolayer. Four new compounds (indicated by white arrows) show an asymmetric shape, looking like a "croissant", which was observed only once during an experiment performed in the first monolayer (see fig. 4.3.c). Two other molecules, indicated by yellow and blue arrows also show an asymmetric shape completely different from the "croissant" shape, suggesting the formation of a further molecular compound derived from DHTAP. STS spectra have been recorded at positions indicated by blue circles in figure 4.5.a. Unfortunately, these STS spectra were not reproducible, probably due to the complex tunnelling gap involving two molecular layers. However, the STM image in figure 4.5.b which has been recorded after the STS measurement clearly indicates that, again, modifications have been induced in several molecules.

The modified molecules are indicated by arrows of different colours. Note that the molecule previously indicated by the yellow arrow in STS image 4.5.a appears now as a 5,14-DHTAP molecule (red arrow). This observation suggests, as in the case observed in the first monolayer, that the reformation of 5,14-DHTAP is feasible.

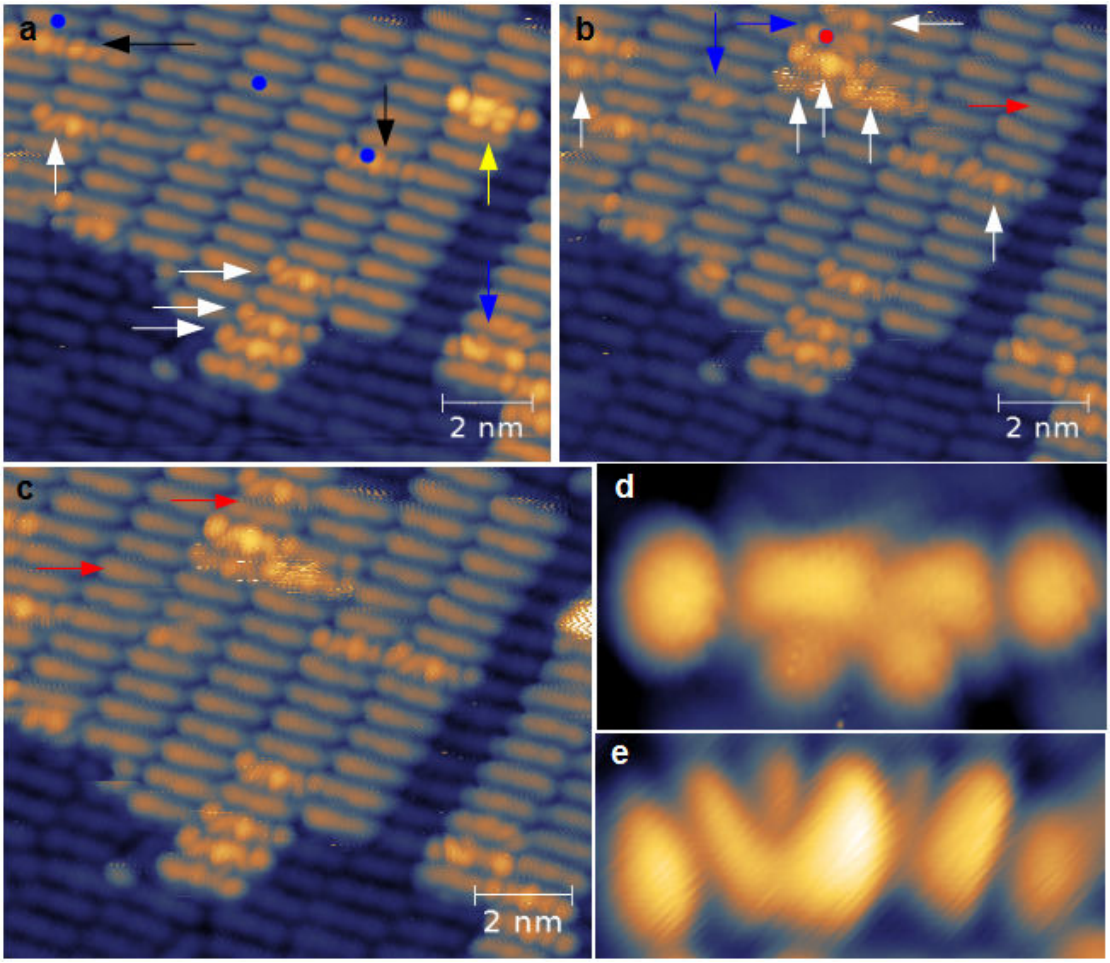

Figure 4.5.: STM image of 1.5ML of DHTAP deposited on Au(111) at 250 K. U_b= 1.36 V, I_t= 70 pA. a) Several molecules embedded in the second layer show particular molecular orbitals (coloured arrows). b) STM image recorded after several STS measurements. Modified molecules are indicated by arrows. c) STM image recorded after a pulse voltage (-1.6 V, 300 ms) at the position indicated by a red circle in image b. Two molecules, indicated by red arrows are now imaged as 5,14-DHTAP. d) Zoom on the structure indicated by the yellow arrow in image a. e) Zoom on the "croissant" structure (image obtained at LHe temperature, U_b=1.0 V, I_t=30 pA).

Image 4.5.c has been recorded after a voltage pulse (-1.6 V, 300 ms) performed

at the position indicated by a red circle in the STM image 4.5.b. We can observed that two molecules indicated by red arrows which were previously imaged with a resolution on molecular orbitals are now imaged as 5,14-DHTAP. The STM image shown in figure 4.5.d is a zoom performed on the molecule indicated by a yellow arrow in STM image 4.2.a. We can clearly observe the above-mentioned asymmetry of the molecular orbitals. The STM image depicted in figure 4.5.e is another zoom, carried out on one molecule with molecular orbitals looking like a "croissant", which underlines clearly the asymmetry of this structure.

4.2.2. DFT calculations and discussion

In order to identify these structures observed in the second monolayer, we decided to perform other DFT calculations[111] for asymmetric molecules derived from 5,14-DHTAP. The most promising candidates identified due to the asymmetry of their molecular backbones are the 5-monohydro-5,7,12,14-tetraazapentacene (MHTAP) and the 5,7,12-trihydro-5,7,12,14-tetraazapentacene (TrHTAP), which are both radicals. We also perform calculation for the 5,12-dihydro-5,7,12,14-tetraazapentacene (5,12-DHTAP), even if this compound shows a central symmetry, because it corresponds to a molecular structure that can be obtained by tautomerisation of the 5,14-DHTAP. The shape of the molecular orbitals, HOMO and LUMO, has been determined for 5,14-DHTAP, TAP and 5,12-DHTAP and the SOMO (singly occupied molecular orbital, due to the radical nature of the compounds) has been determined for MHTAP and TrHTAP. All these results, the chemical structure of these compounds and results from STM experiments are summarized in the figure 4.6.

On the first line a STM image obtained at a bias voltage of -1.2 V for 5,14-DHTAP in the second monolayer is shown. The STM image and DFT calculation of the HOMO are in very good agreement. Similar features are observed: two pronounced lobes at the extremity of the molecule, a big lobe looking like a "butterfly" on the left-hand side of the molecules, where N-H groups are localized, and two other smaller lobes, which appear darker in the STM image. This allows us to confirm that our calculations performed for isolated molecules are in good agreement with the molecular orbitals of 5,14-DHTAP molecules embedded in self-assembled monolayer observed by STM.

As expected, the symmetry of the molecular orbitals reflects the symmetry of the molecular backbone, as it has already been mentioned for TAP. This is also the case for the 5,12-DHTAP, which possesses molecular orbitals with point symmetry (equivalent to rotational symmetry of order two). Molecular orbitals of MHTAP and TrHTAP, depicted in the second panel, do not show any symmetry. The similar features observed in the STM images depicted in figure 4.5.d and 4.5.e allow us to unambiguously attribute these structures to the SOMO of the MHTAP and TrHTAP respectively. The fact we are imaging the SOMO rather than the LUMO is due to the radical nature of these compounds possessing an

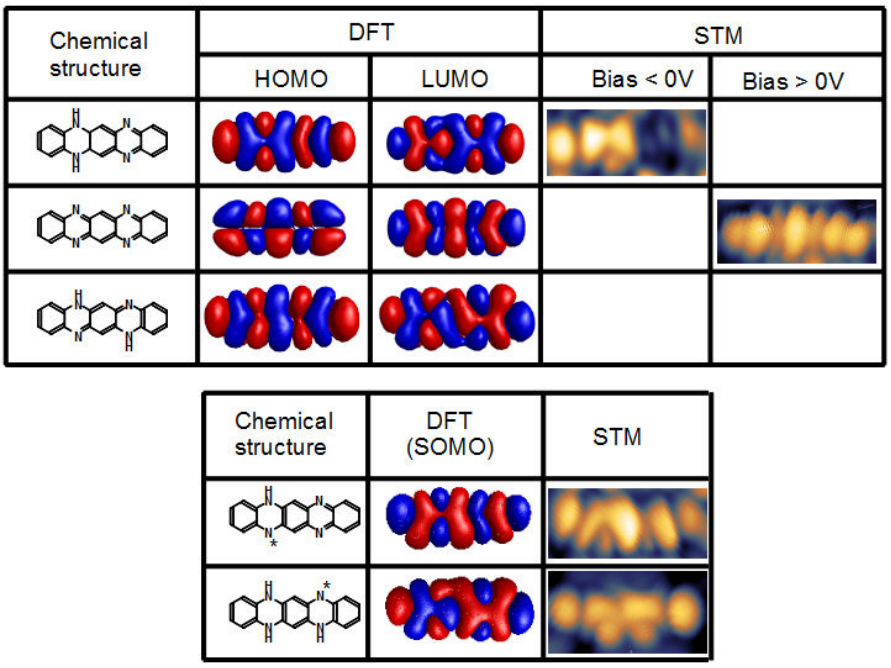

Figure 4.6.: Summary of the chemical structure, DFT calculation (HOMO,LUMO, SOMO) and STM image related to 5,14-DHTAP and other azapentacenes.[111]

unpaired electron. This suggests that 5,14-DHTAP can either be dehydrogenated or hydrogenated in the second layer, leading to the formation of these radicals observed only in the second monolayer.

Radicals are generally highly chemically reactive due to their unpaired electron, however, under the UHV conditions it is possible that these compounds are stable. Moreover, it is known that a coupling can take place between the molecules constituting the first layer and the surface, but it is also known that molecules localized in the second monolayer are generally better decoupled from the substrate. This can explain the fact that we observe the formation of MHTAP and TrHTAP only for the 5,14-DHTAP molecules which are located in the second monolayer: the radical compound would not be stable when it is in contact with the metallic substrate. However, in the second monolayer, the radical is stable due to the presence of the first monolayer. From this observation, a remark concerning the formation of the TAP in the first monolayer can be done: instead of a double dehydrogenation induced by the tunnelling current, it is possible that a single dehydrogenation takes place, as in the case observed in the second monolayer, but, due to the low stability of the compound and its coupling with the metallic substrate, a subsequent second dehydrogenation might take place, leading to the formation of a more stable compound: the TAP.

However, during the dehydrogenation experiments performed on the first monolayer, we observed the formation of a molecular compound showing molec-

ular orbitals now associated to SOMO of the MHTAP (see figure 4.3.c). But it was mentioned that the compound showed an apparent height more important than the other structure. This suggests in this case that this compound is not anymore embedded in the first monolayer and is consequently decoupled from the substrate, leading to a better stability of the radical compound formed by the hydrogenation of a TAP molecule.

Another remark concerning the TrHTAP is that we observe this structure only rarely during our STM experiments and it appears that this structure is not very stable: STS measurements performed on these structures always involve the reformation of DHTAP by dehydrogenation. Moreover, this structure appears tilted in several STM images, as shown in figure 4.7.

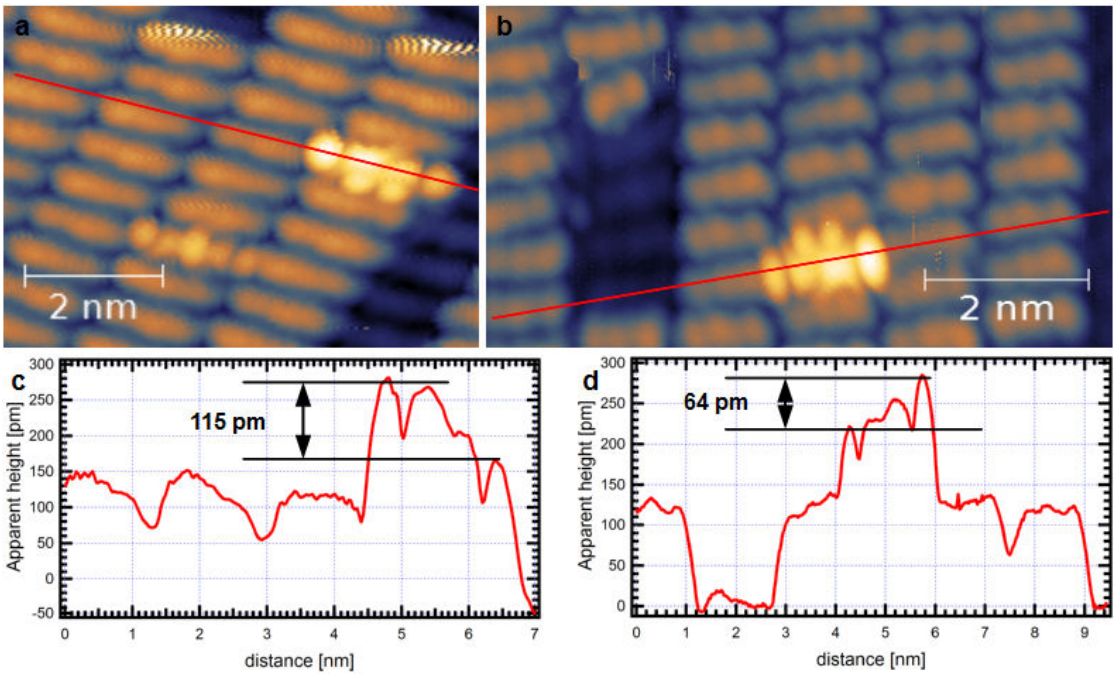

Figure 4.7.: STM images showing the tilted configuration of TrHTAP in second monolayer. a) STM parameters: U_b= 1.36 V; I_t= 70 pA. b) STM parameters: U_b= 1.2 V; I_t= 30 pA. c) STM profile corresponding to the red line in a). d) STM profile corresponding to the red line in b).

Apparent height measurements depicted in figure 4.7.c and 4.7.d clearly show that molecular orbital lobes localized at the extremity of the molecules show different apparent heights. This tilted configuration can be attributed to the fact that the hydrogenation of one nitrogen atom, at position 7 or 12, does not permit an establishment of the hydrogen bond with the molecule located on side where the hydrogenation takes place. Moreover, a steric repulsion due to the incorporation of this hydrogen atom could occur between TrHTAP and the neighbouring

DHTAP molecules. That can explain the fact that TrHTAP is observed with a tilted angle along the long molecular axis.

It has to be mentioned that small differences are observed between the calculated shape of the molecular orbitals and the STM images of molecular orbitals obtained in the second monolayer: one part of the features observed in calculation are not observed. These differences occurs at the positions indicated by the black dotted lines in the figure 4.8 for DHTAP, MHTAP and TrHTAP. One STM image is also displayed to support this observation.

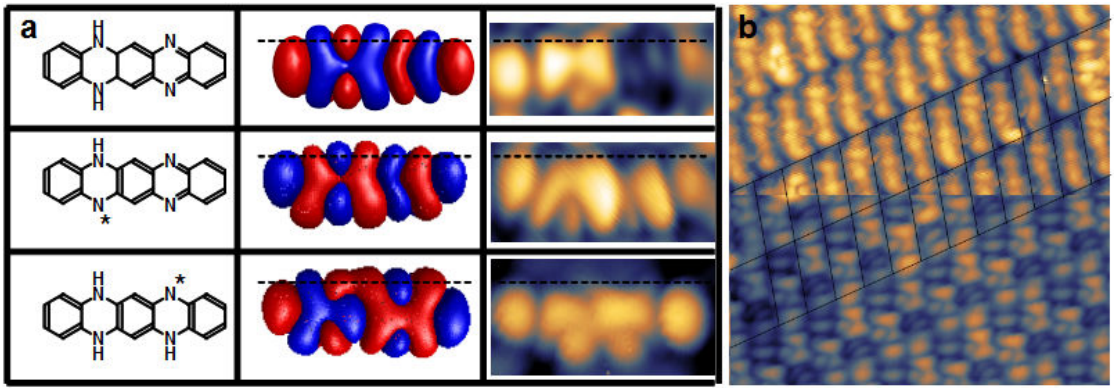

Figure 4.8.: a) Chemical structure of DHTAP, MHTAP and TrHTAP, DFT results (HOMO of the DHTAP, SOMO of the MHTAP and TrHTAP and corresponding STM images: slight differences between calculations and experiments suggest a slightly tilted configuration along the short molecular axis. b) STM image (8 nm x 8 nm, I_t=40 pA) of the second layer of DHTAP deposited at 250 K. Upper part: U_b=-0.5 V; lower part: U_b=-1.2 V

The STM image depicted in figure 4.8.b has been obtained at LHe temperature. The upper part of the image has been recorded at a bias voltage of -0.5 V, the lower part at a bias voltage of -1.2 V. A grid has been placed to visualize the limits between neighbouring molecules in the lower part of the STM image. In the lower part, the applied bias voltage (negative) indicates that electron tunnel from the sample to the tip, and more precisely from the HOMO of the 5,14-DHTAP to the STM tip. Indeed, the resolution allows us to observe with an extreme precision the shape of these molecular orbitals, which are in very good agreement with the calculation performed for the HOMO of the isolated 5,14-DHTAP molecule.

A small part of molecular orbitals calculated using DFT, the part localized above the black dotted line in 4.8.a, is not well-resolved. This lets us suppose that the DHTAP molecules of the second monolayer do not lie strictly flat, i.e. with their molecular planes parallel to the surface, but with a small angle along the short molecular axis. This can explain the fact that molecular orbitals imaged by STM for MHTAP and TrHTAP also show these differences compared to DFT

calculation: one part of the molecular orbitals are not imaged well because these are screened by the proximity of the neighbouring molecule.

This observation concerning the small tilt of the molecule along the short molecular axis suggests that one of the hydrogen atoms of the 5,14-DHTAP will be tilted out of the plane of the second layer more than the other, and intuitively we can imagine that this hydrogen atom will be dehydrogenated more easily than the other. This hypothesis is confirmed by the figure 4.9 which shows successive STM images, recorded after a voltage pulse measurement inducing chemical modification.

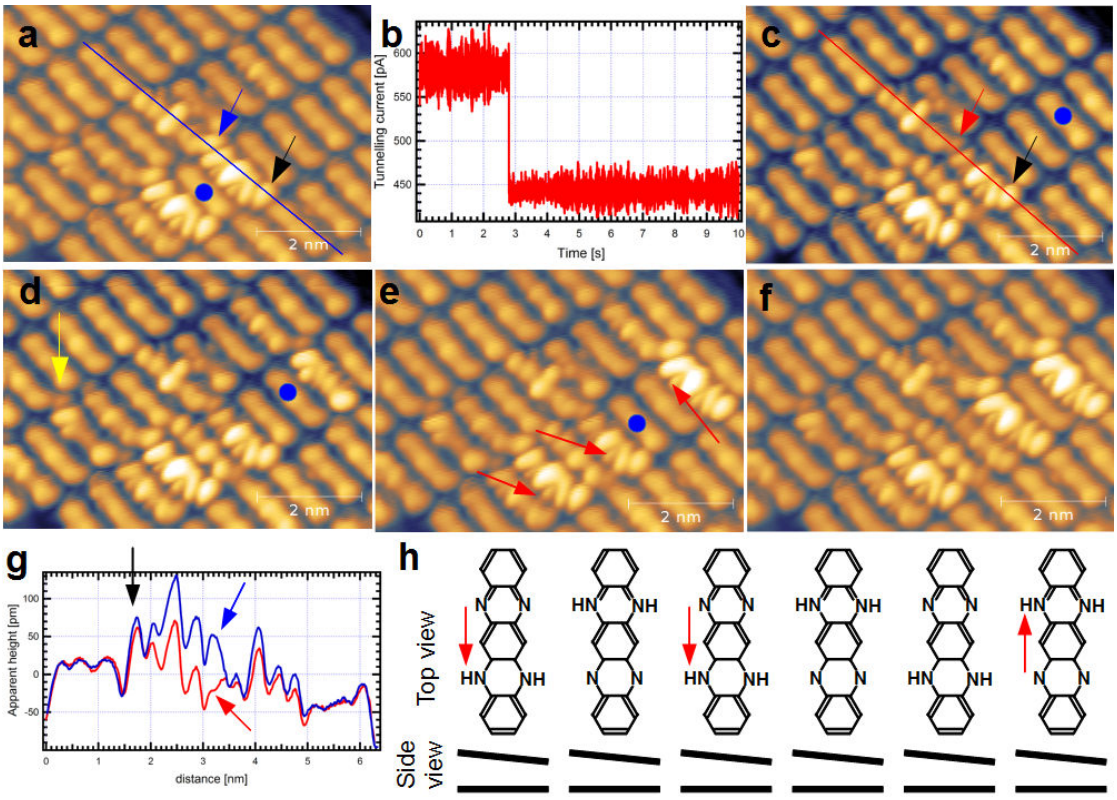

Figure 4.9.: a, c-f) Successive STM images recorded after voltage pulse measurements (position indicated by blue circles) at liquid helium temperature. STM parameters: U_b= 0.3 V and I_t= 70 pA. b) Typical voltage pulse measurement. The drop in the tunnelling current indicates the formation of a new compound. g) STM profiles corresponding to the blue and red line in a) and c) respectively. h) Schematic model underlining the head to tail and tilted configuration of 5,14-DHTAP constituting the second monolayer. Arrows indicate the dehydrogenated H atoms in the molecular row of e).

The figure 4.9.a displays a STM image of the second monolayer of DHTAP on Au(111). Two molecules, aligned in the same molecular row, show molecular

orbitals with asymmetric shapes which can now be unambiguously attributed to the MHTAP molecule. One molecule is imaged with symmetric molecular orbitals, which can be attributed to a TAP molecule. Finally, four other molecules are imaged with a resolution on asymmetric molecular orbitals, but their apparent heights are low compared to the above-mentioned TAP and MHTAP molecules. Most part of these molecules can in fact be identified as MHTAP molecules, we will return to this point latter. Concerning the MHTAP molecules with pronounced molecular orbitals, we can observed that the molecular orbitals show the same orientation (these can be superposed). Combined with the head to tail configuration of the DHATPs constituting the molecular rows and the fact that these molecules are separated by just one molecule, we conclude that the dehydrogenation took place at an identical position for both compounds. The dehydrogenated atoms of the 5,14-DHTAP are indicated by red arrows in the figure 4.9.h.

In figure 4.9.b a typical voltage pulse measurement is shown. In this case we measured the tunnelling current as a function of the time, applying a constant voltage bias of 2.25 V. The strong decrease in tunnelling current can be unambiguously attributed to fact that a chemical modification takes place in the original molecule. During this type of measurement it occasionally happen that an increase instead of a decrease in the tunnelling current is observed which led, however, to the same modification. Figure 4.9.c and 4.9.d show two other STM images recorded after voltage pulse measurements performed at the position indicated by blue circles, we will return in detail to these images latter.

The STM image displayed in figure 4.9.e shows another compound which can be unambiguously attributed to MHTAP molecules. Note that this time, the orientation of the molecular orbitals is different from the orientation observed in the STM image 4.9.a: it shows a mirror symmetry with respect to the short molecular axis. This is in very good agreement with the fact that DHTAP molecules self-assemble in head to tail fashion: these molecules are separated by an odd number (3 or 5) of molecules. This means that the dehydrogenation always takes place on the left-hand side of the molecules, independently of the head to tail configuration (see figure 4.9.h, the dehydrogenated atom is indicated by a black arrow). This tends to confirm that one of the hydrogen atoms in position 5 or 14 is more reactive than the other, certainly due to a slightly tilted configuration of the molecule of the second layer, as indicated in the side view of the schematic representation in figure 4.9.h.

These observations are confirmed by the following STM image, shown in 4.9.f, which was obtained after another voltage pulse measurement. One more DHTAP molecule is dehydrogenated to a MHTAP molecule which shows the same orientation of the molecular orbitals than the MHTAP molecule observed after the pulse voltage measurement performed in 4.9.d.

Another interesting information can be extracted from these successive STM images. The image 4.9.b has been recorded after a voltage pulse measurement

performed at the location indicated by a blue dot in the image 4.9.a. It appears that this measurement leads to the formation of a compound showing symmetrical orbitals that can be identified as a TAP molecule. This proves also that the chemical state change of a single molecule embedded in a well-ordered molecular layer by a voltage pulse is possible with molecular resolution.

Furthermore, another modification is observed: the decrease of the apparent height of one of the molecules previously identified as MHTAP. This decrease is underlined by STM profile recorded on both STM image 4.9.a and 4.9.c, and shown in figure 4.9.g. We can see in this profile a clear decrease (70 pm) of the apparent height of one side of the molecule, indicated by the blue and the red arrows, while on the other side, the apparent height remains similar in both STM images (black arrows). This can be explained by the fact that in the case of the STM image 4.9.a, the MHTAP molecule was not perfectly embedded in the second monolayer and its position changes during the voltage pulse measurement.

The same process seems to take place during the voltage pulse measurement performed at the position shown in STM image 4.9.d, where the molecule localized on the right with respect to the position where the measurement is done, appears with pronounced molecular orbitals in the STM image 4.9.e. Note that the shape of this molecule in image 4.9.d is very similar to the shape of the molecular orbitals of the molecule indicated by a yellow arrow in the same image, suggesting once again different adsorption configurations.

4.2.3. Electronic properties of azapentacenes in the second monolayer

Due to the fact that these molecules (5,14-DHTAP, TAP and MHTAP) are different, they should exhibit distinct electronic properties as a function of the bias voltage during STM imaging. Successive STM pictures that have been obtained at different bias voltage are depicted in figure 4.10 and illustrate these different electronic properties.

The STM image depicted in figure 4.10.a shows a second monolayer of DHTAP that has been recorded at a bias voltage of -0.8 V. Several defects (molecules missing in the second monolayer) allows us to determine the relative position of each molecules constituting this second monolayer. We can observe the abovementioned asymmetry of the molecular orbitals and the head to tail configuration of the DHTAP molecules.

The second STM image, displayed in 4.10.b has been recorded at a bias voltage of 0.4 V and consequently in the band gap. At this bias voltage, all molecules constituting the second layer are imaged similarly, and the asymmetry of the molecular orbitals is not observed. Increasing the bias voltage to 0.8 V leads to the appearance of several compounds showing molecular orbitals associated to the SOMO of the MHTAP molecule.

Interestingly, a closer look at the STM image depicted in 4.10.a allows us to distinguish these molecules which show molecular orbitals with slightly different shape and are brighter compared to those of other molecules.

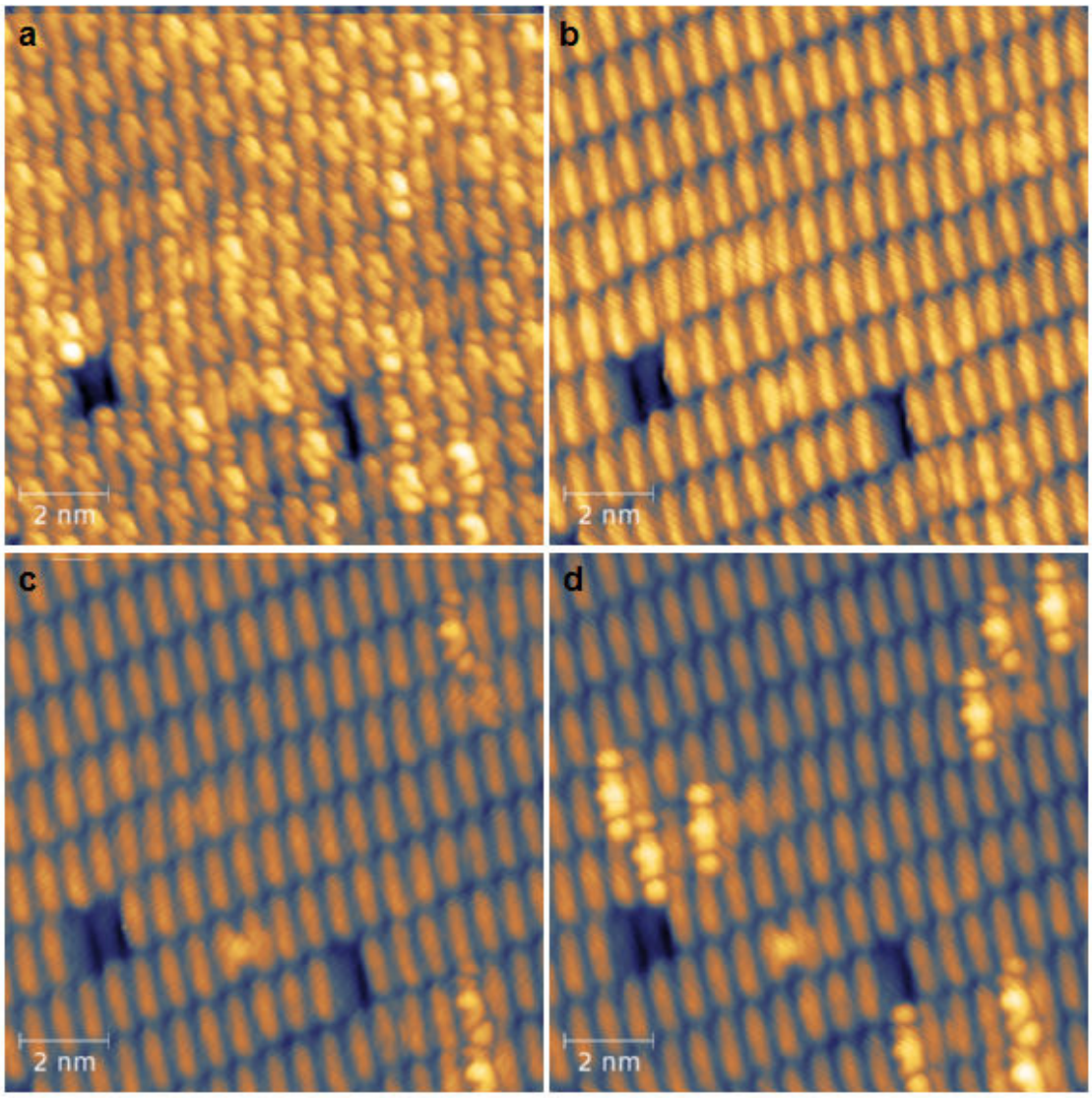

Figure 4.10.: Successive STM images recorded at different bias voltages and at liquid helium temperature for 1.6 ML of DHTAP deposited on Au(111) at 250 K. STM parameters: a) U_b= -0.8 V and I_t= 20 pA. b) U_b= 0.4 V and I_t= 20 pA. c) U_b= 0.8 V and I_t= 20 pA. d) U_b= 1.3 V and I_t= 20 pA.

Finally, another increase in the bias voltage to 1.3 V leads to the appearance of other compounds, which show two symmetry axes and which can be unambiguously identified as the TAP molecule.

From these observations, we can suppose that these different molecules will

exhibit different electronic properties, as in the case observed for 5,14-DHTAP and TAP in the first monolayer. Particularly, the MHTAP compound should show an increase in the LDOS around -0.8 V and 0.8 V, the 5,14-DHTAP around -0.8 V, and the TAP around 1.3 V. STS spectra recorded for these three compounds are shown in figure 4.11.

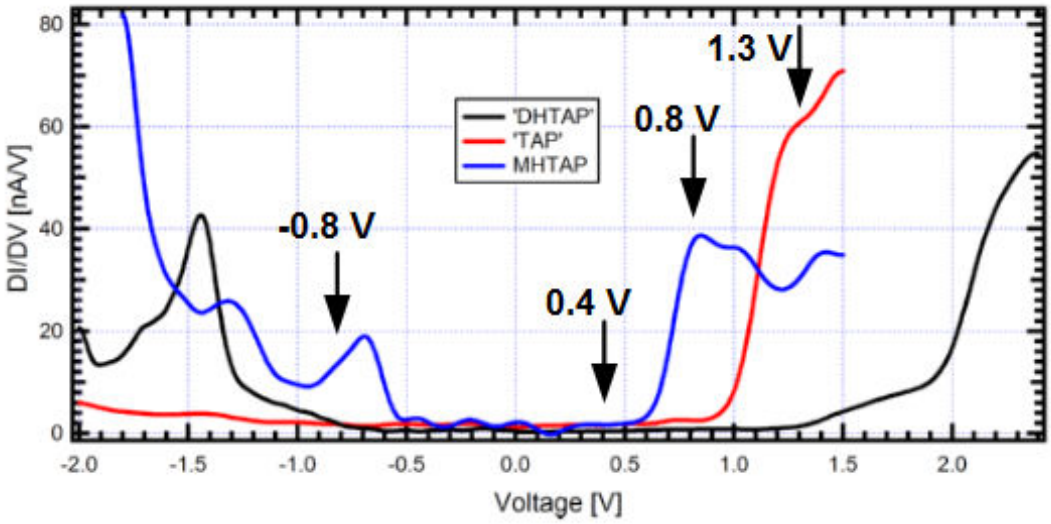

Figure 4.11.: STS measurements performed on top of DHTAP (black line), MHTAP (blue line) and TAP (red line) molecules.

In both cases we can see that the LDOS is zero at low positive and negative bias voltage. This means that the metallic behaviour observed in the case of STS measurements performed in the first monolayer (see figure 4.1.b, 4.1.c and 4.2.a) is not observed anymore, suggesting that the second monolayer is completely decoupled from the metallic substrate. This corroborates our previous observations concerning different possible coupling between the molecules constituting the first or the second layers and the metallic substrate, and the influence of this coupling on the formation of preferential structures: TAP in the first monolayer or TAP, MHTAP and TrHTAP in second monolayer.

In the case of DHTAP, an increase in the LDOS at voltages below -0.7 V is in agreement with the appearance of the molecular orbitals of DHTAP in the STM image 4.10.a obtained at a bias of -0.8 V. A peak maximum is observed at -1.4 V. Another increase in the LDOS is observed above 1.3 V, without resolving a peak maximum. These steep increases in the LDOS allow us to determine a HOMO LUMO gap of 2.0 eV. The STS spectrum obtained for the TAP compound (red line) shows an increase in the LDOS above 1 V, which is also in good agreement with the STM image obtained at 1.3 V and depicted in figure 4.10.d. Below 1 V and down to -1.2 V, the differential conductivity remains zero, suggesting a

bandgap of 2.2 eV. A slight increase LDOS is observed below -1.2 V and a small peak is resolved around -1.4 V. Finally, the STS spectrum obtained for MHTAP (blue line) displays clearly two peaks at -0.7 V and 0.8 V, again in very good agreement with STM images depicted in figure 4.10.a and 4.10.c. The bandgap, estimated from the steep increase in the LDOS below -0.5 V and above 0.6 V, is 1.1 eV. These STS spectra are in very good agreement with the observations of the bias dependence of the STM image.

4.3. Conclusions and outlook

In this chapter we have investigated the possibility of inducing chemical modifications of the 5,14-DHTAP molecule embedded in well-ordered self-assembled monolayer using the tunnelling current of the STM. The formation of different compounds has been observed and these products have been identified by comparison with DFT calculation.

Interestingly, in the first monolayer only one compound has been observed. It has been identified as a TAP molecule by comparison between the imaged molecular orbitals, attributed to the LUMO according to the STS spectra, and the shape of the LUMO determined by DFT calculation for the isolated compound. The TAP molecule presents interesting properties, due to the fully π-conjugated backbone, and the presence of nitrogen atoms in this backbone which should provide a good stability under ambient conditions. This TAP molecule cannot be synthesized by common chemical way, however we showed in this chapter that this compound can be obtained by a double dehydrogenation of the 5,14-DHTAP molecule embedded in a first monolayer.

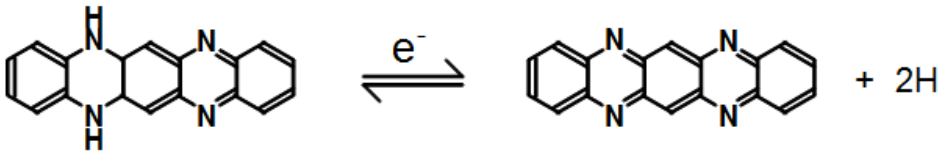

Figure 4.12.: Synthesis of TAP from DHTAP by STM

In the case of modifications induced in the second layer, we observed the formation of three different species: the above-mentioned TAP, and two compounds identified as radicals. The identification of these radicals has been done by comparison between the molecular orbitals imaged with STM and the shape of the SOMO for both isolated compounds, obtained from DFT calculations. This allows us to identified these compounds as MHTAP and TrHTAP. MHTAP is obtained by a single dehydrogenation of the 5,14-DHTAP. TrHTAP is obtained after the hydrogenation of the 5,14-DHTAP molecule, but this radical has been observed only rarely during all the STM experiments.

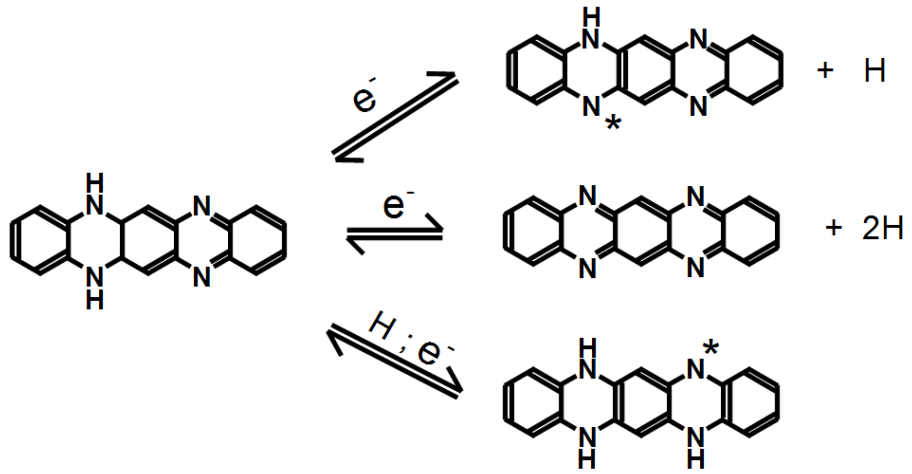

Figure 4.13.: Synthesis of TAP, MHTAP and TrHTAP from DHTAP

We suggest that radical compounds are observed only in the second monolayer because molecules are better decoupled from the substrate which leads to a better stability of the radicals. The mechanism for the formation of MHTAP in the second monolayer is a single dehydrogenation. It seems that the single dehydrogenation allowing the formation of MHTAP takes place preferentially on one side of molecules constituting a molecular row, which lets us think that these molecules adsorb with their small molecular axes slightly tilted from the surface plane. This can also explain the fact that a small part of the molecular orbitals imaged by STM for all these compounds is less visible when compared to the DFT calculations.

We have also investigated the electronic properties of these different compounds. In the first monolayer, the DHTAP molecule show a HOMO-LUMO gap of 2.2 eV. The value of this gap is reduced to 1.3 eV in the case of the TAP molecule. In the second layer, STS measurements show HOMO-LUMO gap of 2.0 eV for DHTAP. The bandgap determined for the MHTAP is 1.1 eV.

The following step which has to be undertaken would be to determine the quantum efficiency of this reaction as function of the bias voltage in order to confirm that the process involved is due to inelastic electron tunnelling

It would also be interesting to see if the DHTAP layer could be dehydrogenated by the use of low energy electrons from an electron gun. This would allow for the fabrication of TAP layers in devices.

5. Conclusion

The study of the formation of well-ordered thin films is of prime interest for developments in the field of organic electronics. The formation of these thin films strongly depends on the formation of an ordered first monolayer, which may serve as a template for further growth. The self-assembling process involved in the formation of the first monolayer strongly depends on the balance between two kinds of interactions: intermolecular interactions and molecule-substrate interactions. These intermolecular interactions (π-π interactions, van der Waals, hydrogen bonding, ...) can be tuned by the incorporation of functional groups with tailored properties in the molecular backbone.

In this thesis we investigated the growth properties of two organic compounds, the 5,14-dihydro-5,7,12,14-tetraazapentacene (DHTAP) and the 1,4-Di-n-octyl-oxy-2.5-bis(pyren-1-ylethenyl)benzene (bis-pyrene), which were synthesized in the CINaM laboratory, by the means of scanning tunnelling microscopy at low temperature under UHV conditions. These compounds present tailored properties, which play an important role during the self-assembling process: the presence of donor and acceptor of hydrogen bonds in the case of DHTAP, and the presence of alkyl chains for bis-pyrene.

The growth process at submonolayer coverage has been studied, and it appears that the substrate, which has the role of a template for the first monolayer, plays a very important role and leads to the formation of different structures. However, independently of the molecules and the surfaces, a similar behaviour during the growth process is observed in all cases:

- In the beginning, the growth process is mainly guided by molecule-substrate interactions, which lead to a preferential growth on fcc then on hcp domains of the reconstructed Au(111) surface for example. However the influence of the intermolecular interactions can be observed through the formation of molecular wires stabilized by intermolecular hydrogen bonds in the case of DHTAP or van der Waals interactions of the interdigitated alkyl chains in the case of bis-pyrene.

- Above a certain coverage, a reorganization of the molecular layer takes place, which leads to the formation of well-ordered 2D domains. This reorganization can be explained by an increase in the influence of the intermolecular interaction due to the increasing molecular density, and above a certain density, the influence of the intermolecular interactions became more important than molecule-substrate interactions. This leads to the above-mentioned reorganization of the molecular layer.

- The formation of ordered domains is observed and the first layer is completed before the growth of the second layer. Consequently, either a Frank-

van der Merwe or a Stranski-Krastanov growth mode is involved for the growth of DHTAP and bis-pyrene molecules on these surfaces.

The growth of DHTAP has been investigated on different noble metal substrates: Au(111), Au(110) and Ag(110). The influence of the substrate temperature during deposition has been investigated and it turns out that it is a critical parameter for the formation of well-ordered structures. The most striking influence of the temperature has been observed for DHTAP deposited on Au(110) where a reconstruction of the surface (from the (1x2) to the (1x3) structure) takes place for deposition performed above 200 K or after an annealing of submonolayer coverages deposited below 200 K. The influence of the temperature in the case of Au(111) and Ag(110) is less pronounced, however, a variety of structures, for example the formation of commensurate molecular wires at low temperature has been observed. A decrease of the domain size is also observed for deposition performed at low temperature. This influence of the temperature can also explain the small size of the domains observed for DHTAP on Au(110). A last example concerning the influence of the temperature on the growth of DHTAP has been observed on Ag(110), where the reorganization of the molecules constituting the first monolayer does not take place at low temperature, leading to the formation of a disordered second layer. At higher temperature, however, the formation of large and well-ordered molecular domains takes place.

In all cases, using the appropriate temperature during deposition, the formation of ordered domains has been observed. Our STM experiments demonstrate unambiguously that DHTAP molecules embedded in highly-ordered layers on Au(111) are arranged in a head to tail fashion along a molecular row. This head to tail configuration allows for the establishment of hydrogen bonds between neighbouring molecules constituting molecular rows. Due to these observations and the similar intermolecular distances between DHTAP molecules observed on the other surfaces investigated, the head to tail configuration is assumed for molecules constituting the ordered domains on Au(110) and Ag(110).

On Au(111), a non commensurate model has been proposed for the first monolayer where DHTAP molecules arranged in a head to tail configuration lie with their molecular plane parallel to the surface. Two mirrored domains, with respect to the crystallographic direction of the substrate, have been observed by STM. Six different orientations are observed for each domain, reflecting the symmetry of the Au(111) substrate. These observations are in very good agreement with the LEED experiments.

The preferential side of the dehydrogenation observed in the second monolayer of DHTAP deposited on Au(111) combined with the slight difference observed between molecular orbitals imaged by STM and the results of DFT results concerning the shape of these orbitals strongly suggest that the DHTAP molecules constituting the second monolayer adsorb with their small molecular axis slightly tilted from the surface plane. However, the unit cell parameters remain identical to those of the first monolayer due to the epitaxial growth.

For a complete monolayer of DHTAP deposited on noble metal (110) surfaces, the models presented to describe the ordered domains also show a commensuration between the molecular film and the substrate. In the case of DHTAP/Au(110), mirrored domains are observed, with only one orientation, reflecting the symmetry of the surface. Deposited on Ag(110), monocrystalline domains of DHTAP show only one orientation and no mirrored domains because unit cell vectors are aligned with the high symmetry crystallographic directions.

In the case of bis-pyrene on Au(111), the temperature does not seem to play an important role during the first steps of the growth process, however, at higher coverages, the formation of different structure has been observed. Two of these structures (α and β) are always observed independently of the temperature, the γ structure is observed (rarely) only when the film is grown at room temperature and the δ structure is observed only when bis-pyrene molecules are deposited at low temperature. The size of these different molecular domains also depends on the temperature. The formation of an ordered second monolayer takes place at RT only.

The growth of the bis-pyrene molecules initially leads to the formation of molecular wires on the fcc domains of the Au(111) surface. The intermolecular interactions are in this case of van der Waals type and mediated by the interdigitation of the alkyl chains. Increasing the molecular density leads to a molecular reorganization and to the formation of the 2D molecular structure referred as α structure. This is followed by a second molecular reorganization at higher coverage. This second reorganization leads to the formation of three more compact domains, β, γ, δ, depending on the temperature of the substrate during the growth process. Models proposed for these four different structures are all commensurate with the Au(111) surface. Three of them (α, γ, δ) show mirror domains, the fourth (β) shows an alignment between their unit cell vectors and the substrate lattice. These four domains show six different orientations, reflecting the symmetry of the Au(111) substrate.

The optical properties of bis-pyrene have also been investigated by the means of surface cavity ring-down spectroscopy under UHV conditions at the Technische Universität München. We have been able to observe an evolution of the optical properties of bis-pyrene evaporated on borosilicate glass substrate as a function of the coverage. This modification, the appearance of a shoulder in the optical spectra at a wavelength of about 505 nm, is due to the coupling between the transition dipole moment of molecules in adjacent layers, and can be attributed to Davydov splitting. Above a certain coverage the relative intensity of this transition does not increase anymore with respect to the intensity of the main transition (434 nm). Combining this information concerning the evolution of the optical properties with the molecular density and the information obtained by STM, we are able to conclude that:

- The appearance of the shoulder is due to an interfacial effect attributed to the beginning of the formation of the second layer.

- The saturation of the signal is attributed to the fact that the interfacial region between the first and the second layer does not increase anymore.
- The growth mode for bis-pyrene on borosilicate glass substrate is a Volmer-Weber growth mode.

The influence on the temperature has also been investigated, and it appears that the saturation of the shoulder in the optical spectrum is found at lower coverages in the case of deposition performed at higher temperature. This can be explained by different growth kinetics at LT and at RT, i.e. the formation of fewer molecular island at RT.

Finally, we showed that it is possible to use the tunnelling current of the STM to induce chemical modifications in single 5,14-DHTAP molecules embedded in the self-assembled monolayer. Due to the different electronic properties of the resulting compounds, we were able to distinguish them from 5,14-DHTAP by STS and by imaging their molecular orbitals. The resolution of the orbitals in the STM images combined with DFT calculations performed for various compounds derived from 5,14-DHTAP allowed us to identify the chemical structure of the modified DHTAP.

Modifications performed on molecules embedded in the first monolayer lead exclusively to the formation of 5,7,12,14-tetraazapentacene (TAP) which implies a double dehydrogenation of the 5,14-DHTAP. This TAP molecule, which possesses interesting electronic properties similar to pentacene cannot be synthesized by standard chemical methods. However we showed that it is possible to synthesize this molecule using the tunnelling current of a scanning tunnelling microscope.

In the second layer, the formation of three different compounds has been observed. These compounds have been identified as TAP, monohydro-5,7,12,14-tetraazapentacene (MHTAP) and 5,7,14-trihydro-5,7,12,14-tetraazapentacene (TrHTAP). MHTAP and TrHTAP are both radicals. The fact that we observed these radical compounds exclusively in the second monolayer is ascribed to different coupling between the molecules of the first and the second layer. It appears that the strong coupling of the molecules to the metal in the first layer prohibits the formation of these radicals.

Bibliography

[1] G. Binnig, H. Rohrer, Ch. Gerber, et al. “Surface Studies by Scanning Tunneling Microscopy”. en. In: *Physical Review Letters* 49.1 (July 1982), pp. 57–61. ISSN: 0031-9007. DOI: 10.1103/PhysRevLett.49.57 (cit. on pp. 22, 25, 35).

[2] Russell Young, John Ward, and Frederic Scire. “The Topografiner: An Instrument for Measuring Surface Microtopography”. en. In: *Review of Scientific Instruments* 43.7 (1972), p. 999. ISSN: 00346748. DOI: 10.1063/1.1685846 (cit. on p. 25).

[3] G. Binnig. “Tunneling through a controllable vacuum gap”. en. In: *Applied Physics Letters* 40.2 (1982), p. 178. ISSN: 00036951. DOI: 10.1063/1.92999 (cit. on p. 25).

[4] G. Binnig, H. Rohrer, Ch. Gerber, et al. “(111) facets as the origin of reconstructed Au(110) surfaces”. In: *Surface Science* 131.1 (Aug. 1983), pp. L379–L384. ISSN: 0039-6028. DOI: 10.1016/0039-6028(83)90112-7 (cit. on pp. 25, 86).

[5] G. Binnig and H. Rohrer. “Scanning tunneling microscopy”. en. In: *Surface Science* 126.1-3 (Mar. 1983), pp. 236–244. ISSN: 00396028. DOI: 10.1016/0039-6028(83)90716-1 (cit. on pp. 25, 35).

[6] G. Binnig, H. Rohrer, Ch. Gerber, et al. “7 × 7 Reconstruction on Si(111) Resolved in Real Space”. en. In: *Physical Review Letters* 50.2 (Jan. 1983), pp. 120–123. ISSN: 0031-9007. DOI: 10.1103/PhysRevLett.50.120 (cit. on p. 25).

[7] Gerd Binnig and Heinrich Rohrer. “Scanning tunneling microscopy—from birth to adolescence”. en. In: *Reviews of Modern Physics* 59.3 (July 1987), pp. 615–625. ISSN: 0034-6861. DOI: 10.1103/RevModPhys.59.615 (cit. on p. 25).

[8] J. Tersoff and D. R. Hamann. “Theory and Application for the Scanning Tunneling Microscope”. en. In: *Physical Review Letters* 50.25 (June 1983), pp. 1998–2001. ISSN: 0031-9007. DOI: 10.1103/PhysRevLett.50.1998 (cit. on pp. 25, 33, 35).

[9] J. Tersoff and D. R. Hamann. “Theory of the scanning tunneling microscope”. en. In: *Physical Review B* 31.2 (Jan. 1985), pp. 805–813. ISSN: 0163-1829. DOI: 10.1103/PhysRevB.31.805 (cit. on pp. 25, 35).

[10] W.J. Kaiser and R.C. Jaklevic. “Direct observation of an ordered step surface reconstruction on Au(111) by scanning tunneling microscopy”. en. In: *Surface Science* 182.3 (Apr. 1987), pp. L227–L233. ISSN: 00396028. DOI: 10.1016/0039-6028(87)90001-X (cit. on p. 25).

[11] V. M. Hallmark, S. Chiang, J. F. Rabolt, et al. “Observation of Atomic Corrugation on Au(111) by Scanning Tunneling Microscopy”. en. In: *Physical Review Letters* 59.25 (Dec. 1987), pp. 2879–2882. ISSN: 0031-9007. DOI: 10.1103/PhysRevLett.59.2879 (cit. on p. 25).

[12] Ch. Wöll, S. Chiang, R. J. Wilson, et al. “Determination of atom positions at stacking-fault dislocations on Au(111) by scanning tunneling microscopy”. en. In: *Physical Review B* 39.11 (Apr. 1989), pp. 7988–7991. ISSN: 0163-1829. DOI: 10.1103/PhysRevB.39.7988 (cit. on p. 25).

[13] J. V. Barth, H. Brune, G. Ertl, et al. “Scanning tunneling microscopy observations on the reconstructed Au(111) surface: Atomic structure, long-range superstructure, rotational domains, and surface defects”. In: *Physical Review B* 42.15 (Nov. 1990), pp. 9307–9318. DOI: 10.1103/PhysRevB.42.9307 (cit. on p. 25).

[14] R. M. Feenstra, Joseph A. Stroscio, J. Tersoff, et al. “Atom-selective imaging of the GaAs(110) surface”. en. In: *Physical Review Letters* 58.12 (Mar. 1987), pp. 1192–1195. ISSN: 0031-9007. DOI: 10.1103/PhysRevLett.58.1192 (cit. on pp. 25, 35).

[15] H Neddermeyer. “Scanning tunnelling microscopy of semiconductor surfaces”. In: *Reports on Progress in Physics* 59.6 (June 1996), pp. 701–769. ISSN: 0034-4885, 1361-6633. DOI: 10.1088/0034-4885/59/6/001 (cit. on p. 25).

[16] Hans-Joachim Freund and Gianfranco Pacchioni. “Oxide ultra-thin films on metals: new materials for the design of supported metal catalysts”. en. In: *Chemical Society Reviews* 37.10 (2008), p. 2224. ISSN: 0306-0012, 1460-4744. DOI: 10.1039/b718768h (cit. on p. 25).

[17] C Becker, A Rosenhahn, A Wiltner, et al. “Al $_2$ O $_3$ -films on Ni $_3$ Al(111): a template for nanostructured cluster growth”. In: *New Journal of Physics* 4 (Oct. 2002), pp. 75–75. ISSN: 1367-2630. DOI: 10.1088/1367-2630/4/1/375 (cit. on p. 26).

[18] M. Moors, A. Krupski, S. Degen, et al. “Scanning tunneling microscopy and spectroscopy investigations of copper phthalocyanine adsorbed on Al2O3/Ni3Al(111)”. en. In: *Applied Surface Science* 254.14 (May 2008), pp. 4251–4257. ISSN: 01694332. DOI: 10.1016/j.apsusc.2008.01.029 (cit. on p. 26).

[19] B.R. Conrad, W.G. Cullen, B.C. Riddick, et al. “Pentacene islands grown on ultra-thin SiO2”. en. In: *Surface Science* 603.3 (Feb. 2009), pp. L27–L30. ISSN: 00396028. DOI: 10.1016/j.susc.2008.12.020 (cit. on p. 26).

[20] D. M. Eigler and E. K. Schweizer. “Positioning single atoms with a scanning tunnelling microscope”. In: *Nature* 344.6266 (Apr. 1990), pp. 524–526. ISSN: 0028-0836. DOI: 10.1038/344524a0 (cit. on p. 26).

[21] G. Meyer, B. Neu, and K. -H. Rieder. “Controlled lateral manipulation of single molecules with the scanning tunneling microscope”. en. In: *Applied Physics A Materials Science & Processing* 60.3 (Mar. 1995), pp. 343–345. ISSN: 0947-8396, 1432-0630. DOI: 10.1007/BF01538415 (cit. on p. 26).

[22] Willi Auwärter, Knud Seufert, Felix Bischoff, et al. “A surface-anchored molecular four-level conductance switch based on single proton transfer”. In: *Nature Nanotechnology* 7.1 (Dec. 2011), pp. 41–46. ISSN: 1748-3387, 1748-3395. DOI: 10.1038/nnano.2011.211 (cit. on pp. 26, 147).

[23] Takashi Kumagai, Felix Hanke, Sylwester Gawinkowski, et al. “Thermally and Vibrationally Induced Tautomerization of Single Porphycene Molecules on a Cu(110) Surface”. en. In: *Physical Review Letters* 111.24 (Dec. 2013). ISSN: 0031-9007, 1079-7114. DOI: 10.1103/PhysRevLett.111.246101 (cit. on p. 26).

[24] Nadjib Baadji, Stefan Kuck, Jens Brede, et al. “Controlled sequential dehydrogenation of single molecules by scanning tunneling microscopy”. en. In: *Physical Review B* 82.11 (Sept. 2010). ISSN: 1098-0121, 1550-235X. DOI: 10.1103/PhysRevB.82.115447 (cit. on pp. 26, 147).

[25] Fabian Bebensee, Katrine Svane, Christian Bombis, et al. “Adsorption and dehydrogenation of tetrahydroxybenzene on Cu(111)”. en. In: *Chemical Communications* 49.81 (2013), p. 9308. ISSN: 1359-7345, 1364-548X. DOI: 10.1039/c3cc45052j (cit. on pp. 26, 147).

[26] Lars Smykalla, Pavel Shukrynau, Carola Mende, et al. “Manipulation of the electronic structure by reversible dehydrogenation of tetra(p-hydroxyphenyl)porphyrin molecules”. en. In: *Surface Science* 628 (Oct. 2014), pp. 92–97. ISSN: 00396028. DOI: 10.1016/j.susc.2014.05.015 (cit. on pp. 26, 147, 148).

[27] J. Bardeen. “Tunnelling from a Many-Particle Point of View”. en. In: *Physical Review Letters* 6.2 (Jan. 1961), pp. 57–59. ISSN: 0031-9007. DOI: 10.1103/PhysRevLett.6.57 (cit. on p. 34).

[28] J. P. Ibe. “On the electrochemical etching of tips for scanning tunneling microscopy”. In: *Journal of Vacuum Science & Technology A: Vacuum, Surfaces, and Films* 8.4 (July 1990), p. 3570. ISSN: 07342101. DOI: 10.1116/1.576509 (cit. on p. 40).

[29] Inger Ekvall, Erik Wahlström, Dan Claesson, et al. “Preparation and characterization of electrochemically etched W tips for STM”. In: *Measurement Science and Technology* 10.1 (Jan. 1999), pp. 11–18. ISSN: 0957-0233, 1361-6501. DOI: 10.1088/0957-0233/10/1/006 (cit. on p. 40).

[30] Giel Berden, Rudy Peeters, and Gerard Meijer. “Cavity ring-down spectroscopy: Experimental schemes and applications”. en. In: *International Reviews in Physical Chemistry* 19.4 (Oct. 2000), pp. 565–607. ISSN: 0144-235X, 1366-591X. DOI: 10.1080/014423500750040627 (cit. on p. 44).

[31] Anthony O’Keefe and David A. G. Deacon. “Cavity ring-down optical spectrometer for absorption measurements using pulsed laser sources”. en. In: *Review of Scientific Instruments* 59.12 (1988), p. 2544. ISSN: 0034-6748. DOI: 10.1063/1.1139895 (cit. on p. 44).

[32] J. J. Scherer, J. B. Paul, A. O’Keefe, et al. “Cavity Ringdown Laser Absorption Spectroscopy: History, Development, and Application to Pulsed Molecular Beams”. en. In: *Chemical Reviews* 97.1 (Feb. 1997), pp. 25–52. ISSN: 0009-2665, 1520-6890. DOI: 10.1021/cr930048d (cit. on p. 44).

[33] Martyn D. Wheeler, Stuart M. Newman, Andrew J. Orr-Ewing, et al. “Cavity ring-down spectroscopy”. In: *Journal of the Chemical Society, Faraday Transactions* 94.3 (1998), pp. 337–351. ISSN: 09565000, 13645455. DOI: 10.1039/a707686j (cit. on p. 44).

[34] Shucheng Xu, Guohe Sha, and Jinchun Xie. “Cavity ring-down spectroscopy in the liquid phase”. en. In: *Review of Scientific Instruments* 73.2 (2002), p. 255. ISSN: 00346748. DOI: 10.1063/1.1430729 (cit. on p. 44).

[35] Alexander J. Hallock, Elena S. F. Berman, and Richard N. Zare. “Ultratrace Kinetic Measurements of the Reduction of Methylene Blue”. en. In: *Journal of the American Chemical Society* 125.5 (Feb. 2003), pp. 1158–1159. ISSN: 0002-7863, 1520-5126. DOI: 10.1021/ja028129r (cit. on p. 44).

[36] A. J. Hallock, E. S. F. Berman, and R. N. Zare. “Use of Broadband, Continuous-Wave Diode Lasers in Cavity Ring-Down Spectroscopy for Liquid Samples”. en. In: *Applied Spectroscopy* 57.5 (May 2003), pp. 571–573. ISSN: 00037028, 00037028. DOI: 10.1366/000370203321666614 (cit. on p. 44).

[37] Richard Engeln, Gert von Helden, André J. A. van Roij, et al. “Cavity ring down spectroscopy on solid C[sub 60]”. en. In: *The Journal of Chemical Physics* 110.5 (1999), p. 2732. ISSN: 00219606. DOI: 10.1063/1.477997 (cit. on p. 44).

[38] Rachel N. Muir and Andrew J. Alexander. “Structure of monolayer dye films studied by Brewster angle cavity ringdown spectroscopy”. In: *Physical Chemistry Chemical Physics* 5.6 (Feb. 2003), pp. 1279–1283. ISSN: 14639076, 14639084. DOI: 10.1039/b212790c (cit. on p. 44).

[39] Andrew C. R. Pipino, Johan P. M. Hoefnagels, and Noboru Watanabe. “Absolute surface coverage measurement using a vibrational overtone”. en. In: *The Journal of Chemical Physics* 120.6 (2004), p. 2879. ISSN: 00219606. DOI: 10.1063/1.1637338 (cit. on p. 44).

[40] Martin Thämer, Aras Kartouzian, Philipp Heister, et al. “Linear and Nonlinear Laser Spectroscopy of Surface Adsorbates with Sub-Monolayer Sensitivity”. en. In: *The Journal of Physical Chemistry C* 116.15 (Apr. 2012), pp. 8642–8648. ISSN: 1932-7447, 1932-7455. DOI: 10.1021/jp300292e (cit. on p. 44).

[41] Jean-Marie Antonietti, Marcin Michalski, Ulrich Heiz, et al. “Optical Absorption Spectrum of Gold Atoms Deposited on SiO 2 from Cavity Ring-down Spectroscopy”. en. In: *Physical Review Letters* 94.21 (June 2005). ISSN: 0031-9007, 1079-7114. DOI: 10.1103/PhysRevLett.94.213402 (cit. on p. 44).

[42] S. Gilb, K. Hartl, A. Kartouzian, et al. “Cavity ring-down spectroscopy of metallic gold nanoparticles”. en. In: *The European Physical Journal D* 45.3 (Dec. 2007), pp. 501–506. ISSN: 1434-6060, 1434-6079. DOI: 10.1140/epjd/e2007-00211-9 (cit. on p. 44).

[43] Martin Thämer, Aras Kartouzian, Philipp Heister, et al. “Small Supported Plasmonic Silver Clusters”. en. In: *Small* 10.12 (June 2014), pp. 2340–2344. ISSN: 16136810. DOI: 10.1002/smll.201303158 (cit. on p. 44).

[44] A. Kartouzian, M. Thämer, T. Soini, et al. “Cavity ring-down spectrometer for measuring the optical response of supported size-selected clusters and surface defects in ultrahigh vacuum”. en. In: *Journal of Applied Physics* 104.12 (2008), p. 124313. ISSN: 00218979. DOI: 10.1063/1.3053179 (cit. on p. 50).

[45] Aras Kartouzian. “Optical properties of size-selected supported metal clusters measured by cavity ring-down spectroscopy”. PhD thesis. TECHNISCHE UNIVERSITÄT MÜNCHEN, Lehrstuhl für Physikalische Chemie, Lichtenbergstraße 4, 85748 Garching, 2010 (cit. on p. 50).

[46] Claire Seillan, Hugues Brisset, and Olivier Siri. “Efficient Synthesis of Substituted Dihydrotetraazapentacenes”. en. In: *Organic Letters* 10.18 (Sept. 2008), pp. 4013–4016. ISSN: 1523-7060, 1523-7052. DOI: 10.1021/ol801509v (cit. on pp. 54, 55).

[47] Tony Lelaidier, Thomas Leoni, Pandurangan Arumugam, et al. “Highly Ordered Molecular Films on Au(111): The N-Heteroacene Approach”. en. In: *Langmuir* 30.20 (May 2014), pp. 5700–5704. ISSN: 0743-7463, 1520-5827. DOI: 10.1021/la404214u (cit. on pp. 54, 55, 181).

[48] Qian Miao. “N-Heteropentacenes and N-Heteropentacenequinones: From Molecules to Semiconductors”. en. In: *Synlett* 23.03 (Feb. 2012), pp. 326–336. ISSN: 0936-5214, 1437-2096. DOI: 10.1055/s-0031-1290323 (cit. on p. 54).

[49] Qin Tang, Jing Liu, Hoi Shan Chan, et al. “Benzenoid and Quinonoid Nitrogen-Containing Heteropentacenes”. en. In: *Chemistry - A European Journal* 15.16 (Apr. 2009), pp. 3965–3969. ISSN: 09476539, 15213765. DOI: 10.1002/chem.200900160 (cit. on pp. 54, 55).

[50] Yongqiang Ma, Yanming Sun, Yunqi Liu, et al. “Organic thin film transistors based on stable amorphous ladder tetraazapentacenes semiconductors”. en. In: *Journal of Materials Chemistry* 15.46 (2005), p. 4894. ISSN: 0959-9428, 1364-5501. DOI: 10.1039/b508594b (cit. on pp. 54, 55).

[51] M.B. Casu, P. Imperia, S. Schrader, et al. “Ultraviolet photoelectron spectroscopy on new heterocyclic materials for multilayer organic light emitting diodes”. en. In: *Synthetic Metals* 124.1 (Oct. 2001), pp. 79–81. ISSN: 03796779. DOI: 10.1016/S0379-6779(01)00427-1 (cit. on p. 54).

[52] Baoxiang Gao, Ming Wang, Yanxiang Cheng, et al. “Pyrazine-Containing Acene-Type Molecular Ribbons with up to 16 Rectilinearly Arranged Fused Aromatic Rings”. en. In: *Journal of the American Chemical Society* 130.26 (July 2008), pp. 8297–8306. ISSN: 0002-7863, 1520-5126. DOI: 10.1021/ja800311a (cit. on p. 54).

[53] Uwe H. F. Bunz, Jens U. Engelhart, Benjamin D. Lindner, et al. “Large N-Heteroacenes: New Tricks for Very Old Dogs?” en. In: *Angewandte Chemie International Edition* 52.14 (Apr. 2013), pp. 3810–3821. ISSN: 14337851. DOI: 10.1002/anie.201209479 (cit. on p. 54).

[54] Chong-an Di, Jing Li, Gui Yu, et al. “Trifluoromethyltriphenodioxazine: Air-Stable and High-Performance n-Type Semiconductor”. en. In: *Organic Letters* 10.14 (July 2008), pp. 3025–3028. ISSN: 1523-7060, 1523-7052. DOI: 10.1021/ol8008667 (cit. on p. 55).

[55] Claire Seillan, Pierre Braunstein, and Olivier Siri. “Selective Reduction of Carbonyl Amides: Toward the First Unsymmetrical Bischelating N-Substituted 1,2-Diamino-4,5-di-amidobenzene”. en. In: *European Journal of Organic Chemistry* 2008.18 (June 2008), pp. 3113–3117. ISSN: 1434193X, 10990690. DOI: 10.1002/ejoc.200800087 (cit. on p. 55).

[56] Stéphanie Leroy-Lhez, Adam Parker, Paulette Lapouyade, et al. “Tunable fluorescence emission in pyrene?(2,2?-bipyridine) dyads containing phenylene?ethynylene bridges”. en. In: *Photochemical & Photobiological Sciences* 3.10 (2004), p. 949. ISSN: 1474-905X, 1474-9092. DOI: 10.1039/b409250c (cit. on pp. 56, 57, 134).

[57] Stéphanie Leroy-Lhez and Frédéric Fages. “Synthesis and Photophysical Properties of a Highly Fluorescent Ditopic Ligand Based on 1,6-Bis(ethynyl)pyrene as Central Aromatic Core”. en. In: *European Journal of Organic Chemistry* 2005.13 (July 2005), pp. 2684–2688. ISSN: 1434-193X, 1099-0690. DOI: 10.1002/ejoc.200500059 (cit. on p. 56).

[58] Francoise M. Winnik. “Photophysics of preassociated pyrenes in aqueous polymer solutions and in other organized media”. en. In: *Chemical Reviews* 93.2 (Mar. 1993), pp. 587–614. ISSN: 0009-2665, 1520-6890. DOI: 10.1021/cr00018a001 (cit. on p. 56).

[59] T. C. Chiang. “Electrolytic Preparation and EPR Study of Crystalline Pyrene, Perylene, and Azulene Perchlorates”. en. In: *The Journal of Chemical Physics* 54.5 (1971), p. 2051. ISSN: 00219606. DOI: 10.1063/1.1675135 (cit. on p. 56).

[60] Fabrice Moggia, Christine Videlot-Ackermann, Jörg Ackermann, et al. “Synthesis and thin film electronic properties of two pyrene-substituted oligothiophene derivatives”. en. In: *Journal of Materials Chemistry* 16.24 (2006), p. 2380. ISSN: 0959-9428, 1364-5501. DOI: 10.1039/b601870j (cit. on p. 56).

[61] Christine Videlot-Ackermann, Jörg Ackermann, Hugues Brisset, et al. “α,ω-Distyryl Oligothiophenes: High Mobility Semiconductors for Environmentally Stable Organic Thin Film Transistors”. en. In: *Journal of the American Chemical Society* 127.47 (Nov. 2005), pp. 16346–16347. ISSN: 0002-7863, 1520-5126. DOI: 10.1021/ja054358c (cit. on p. 56).

[62] Ugo. Mazzucato and Fabio. Momicchioli. “Rotational isomerism in trans-1,2-diarylethylenes”. en. In: *Chemical Reviews* 91.8 (Dec. 1991), pp. 1679–1719. ISSN: 0009-2665, 1520-6890. DOI: 10.1021/cr00008a002 (cit. on p. 56).

[63] St?phanie Leroy-Lhez, Magali Allain, Jean Oberl?, et al. “Synthesis and zinc(ii) complexation modulated fluorescence emission properties of two pyrene-oligo(phenylene vinylene)-2,2?-bipyridine conjugated molecular rods”. en. In: *New Journal of Chemistry* 31.6 (2007), p. 1013. ISSN: 1144-0546, 1369-9261. DOI: 10.1039/b617497c (cit. on pp. 57, 134).

[64] Uwe H. F. Bunz. “Poly(aryleneethynylene)s: Syntheses, Properties, Structures, and Applications”. en. In: *Chemical Reviews* 100.4 (Apr. 2000), pp. 1605–1644. ISSN: 0009-2665, 1520-6890. DOI: 10.1021/cr990257j (cit. on p. 57).

[65] Naomi Sakai, Nirmalya Majumdar, and Stefan Matile. “Self-Assembled Rigid-Rod Ionophores”. en. In: *Journal of the American Chemical Society* 121.17 (May 1999), pp. 4294–4295. ISSN: 0002-7863, 1520-5126. DOI: 10.1021/ja983893s (cit. on p. 57).

[66] I. K. Robinson. “Direct Determination of the Au(110) Reconstructed Surface by X-Ray Diffraction”. en. In: *Physical Review Letters* 50.15 (Apr. 1983), pp. 1145–1148. ISSN: 0031-9007. DOI: 10.1103/PhysRevLett.50.1145 (cit. on p. 59).

[67] W. Moritz and D. Wolf. “Structure determination of the reconstructed Au(110) surface”. en. In: *Surface Science* 88.2-3 (Oct. 1979), pp. L29–L34. ISSN: 00396028. DOI: 10.1016/0039-6028(79)90093-1 (cit. on p. 59).

[68] C. Seidel, C. Awater, X.D. Liu, et al. “A combined STM, LEED and molecular modelling study of PTCDA grown on Ag(110)”. en. In: *Surface Science* 371.1 (Jan. 1997), pp. 123–130. ISSN: 00396028. DOI: 10.1016/S0039-6028(96)00981-8 (cit. on p. 61).

[69] Aras Kartouzian, Martin Thämer, and Ulrich Heiz. “Characterisation and cleaning of oxide support materials for cavity ring-down spectroscopy”. en. In: *physica status solidi (b)* (Jan. 2010), n/a–n/a. ISSN: 03701972, 15213951. DOI: 10.1002/pssb.200945482 (cit. on pp. 61, 62).

[70] Martin Thämer. “Linear and Nonlinear Surface Spectroscopy of Supported Size Selected Metal Clusters and Organic Adsorbates”. PhD thesis. TECHNISCHE UNIVERSITÄT MÜNCHEN, Lehrstuhl für Physikalische Chemie, Lichtenbergstraße 4, 85748 Garching, 2012 (cit. on p. 62).

[71] L. Martinez. “Thermally stable ultra thin metal transparent electrodes”. In: Eindhoven, Netherlands, 2008, pp. 363–365 (cit. on p. 62).

[72] Angelika Kühnle. “Self-assembly of organic molecules at metal surfaces”. en. In: *Current Opinion in Colloid & Interface Science* 14.2 (Apr. 2009), pp. 157–168. ISSN: 13590294. DOI: 10.1016/j.cocis.2008.01.001 (cit. on p. 63).

[73] J. H. Kang and X.-Y. Zhu. “Layer-by-Layer Growth of Incommensurate, Polycrystalline, Lying-Down Pentacene Thin Films on Au(111)”. en. In: *Chemistry of Materials* 18.5 (Mar. 2006), pp. 1318–1323. ISSN: 0897-4756, 1520-5002. DOI: 10.1021/cm051990w (cit. on p. 64).

[74] W.-H. Soe, C. Manzano, A. De Sarkar, et al. “Direct Observation of Molecular Orbitals of Pentacene Physisorbed on Au(111) by Scanning Tunneling Microscope”. en. In: *Physical Review Letters* 102.17 (May 2009). ISSN: 0031-9007, 1079-7114. DOI: 10.1103/PhysRevLett.102.176102 (cit. on p. 64).

[75] S. Lukas, S. Vollmer, G. Witte, et al. “Adsorption of acenes on flat and vicinal Cu(111) surfaces: Step induced formation of lateral order”. en. In: *The Journal of Chemical Physics* 114.22 (2001), p. 10123. ISSN: 00219606. DOI: 10.1063/1.1370936 (cit. on p. 64).

[76] P. G. Schroeder, C. B. France, J. B. Park, et al. “Energy level alignment and two-dimensional structure of pentacene on Au(111) surfaces”. en. In: *Journal of Applied Physics* 91.5 (2002), p. 3010. ISSN: 00218979. DOI: 10.1063/1.1445286 (cit. on p. 64).

[77] A. Kraft, R. Temirov, S. K. M. Henze, et al. “Lateral adsorption geometry and site-specific electronic structure of a large organic chemisorbate on a metal surface”. en. In: *Physical Review B* 74.4 (July 2006). ISSN: 1098-0121, 1550-235X. DOI: 10.1103/PhysRevB.74.041402 (cit. on p. 64).

[78] Weidong Dou, Dandan Guan, Hongying Mao, et al. “Aggregation of organic molecules on silver surface with the balance between molecule–substrate interaction and intermolecular interaction”. en. In: *Chemical Physics Letters* 470.1-3 (Feb. 2009), pp. 126–130. ISSN: 00092614. DOI: 10.1016/j.cplett.2009.01.040 (cit. on p. 64).

[79] Joseph A. Stroscio. “Microscopic aspects of the initial growth of metastable fcc iron on Au(111)”. In: *Journal of Vacuum Science & Technology A: Vacuum, Surfaces, and Films* 10.4 (July 1992), p. 1981. ISSN: 07342101. DOI: 10.1116/1.578013 (cit. on p. 66).

[80] F. A. Möller, O. M. Magnussen, and R. J. Behm. “Overpotential-Controlled Nucleation of Ni Island Arrays on Reconstructed Au(111) Electrode Surfaces”. en. In: *Physical Review Letters* 77.26 (Dec. 1996), pp. 5249–5252. ISSN: 0031-9007, 1079-7114. DOI: 10.1103/PhysRevLett.77.5249 (cit. on p. 66).

[81] D. D. Chambliss, R. J. Wilson, and S. Chiang. “Nucleation of ordered Ni island arrays on Au(111) by surface-lattice dislocations”. en. In: *Physical Review Letters* 66.13 (Apr. 1991), pp. 1721–1724. ISSN: 0031-9007. DOI: 10.1103/PhysRevLett.66.1721 (cit. on p. 66).

[82] S. Helveg, J. V. Lauritsen, E. Lægsgaard, et al. “Atomic-Scale Structure of Single-Layer MoS 2 Nanoclusters”. en. In: *Physical Review Letters* 84.5 (Jan. 2000), pp. 951–954. ISSN: 0031-9007, 1079-7114. DOI: 10.1103/PhysRevLett.84.951 (cit. on p. 66).

[83] Xin Zhang, Lin Tang, and Quanmin Guo. “Low-Temperature Growth of C_{60} Monolayers on Au(111): Island Orientation Control with Site-Selective Nucleation”. en. In: *The Journal of Physical Chemistry C* 114.14 (Apr. 2010), pp. 6433–6439. ISSN: 1932-7447, 1932-7455. DOI: 10.1021/jp1006318 (cit. on p. 66).

[84] Matthias Böhringer, Karina Morgenstern, Wolf-Dieter Schneider, et al. “Two-Dimensional Self-Assembly of Supramolecular Clusters and Chains”. en. In: *Physical Review Letters* 83.2 (July 1999), pp. 324–327. ISSN: 0031-9007, 1079-7114. DOI: 10.1103/PhysRevLett.83.324 (cit. on p. 66).

[85] Z.H. Cheng, L. Gao, Z.T. Deng, et al. “Epitaxial Growth of Iron Phthalocyanine at the Initial Stage on Au(111) Surface”. en. In: *Journal of Physical Chemistry C* 111.6 (Feb. 2007), pp. 2656–2660. ISSN: 1932-7447. DOI: 10.1021/jp0660738 (cit. on pp. 66, 79, 116).

[86] Yu-Hang Jiang, Li-Wei Liu, Kai Yang, et al. “Self-assembly and growth of manganese phthalocyanine on an Au(111) surface”. In: *Chinese Physics B* 20.9 (Sept. 2011), p. 096401. ISSN: 1674-1056. DOI: 10.1088/1674-1056/20/9/096401 (cit. on p. 66).

[87] Z.H. Cheng, L. Gao, Z.T. Deng, et al. “Adsorption Behavior of Iron Phthalocyanine on Au(111) Surface at Submonolayer Coverage”. en. In: *Journal of Physical Chemistry C* 111.26 (July 2007), pp. 9240–9244. ISSN: 1932-7447. DOI: 10.1021/jp0703881 (cit. on pp. 66, 79, 116).

[88] L. Gao, J.T. Sun, Z.H. Cheng, et al. “Structural evolution at the initial growth stage of perylene on Au(111)”. en. In: *Surface Science* 601.15 (Aug. 2007), pp. 3179–3185. ISSN: 00396028. DOI: 10.1016/j.susc.2007.05.050 (cit. on pp. 66, 79, 116).

[89] Romain Bernard, Thomas Leoni, Axel Wilson, et al. “Growth of Si ultrathin films on silver surfaces: Evidence of an Ag(110) reconstruction induced by Si”. en. In: *Physical Review B* 88.12 (Sept. 2013). ISSN: 1098-0121, 1550-235X. DOI: 10.1103/PhysRevB.88.121411 (cit. on pp. 72, 181).

[90] Thomas Roussel. personal communication. May 7, 2013 (cit. on pp. 81, 83).

[91] Thomas J. Roussel and Lourdes F. Vega. “Modeling the Self-Assembly of Nano Objects: Applications to Supramolecular Organic Monolayers Adsorbed on Metal Surfaces”. en. In: *Journal of Chemical Theory and Computation* 9.5 (May 2013), pp. 2161–2169. ISSN: 1549-9618, 1549-9626. DOI: 10.1021/ct3011248 (cit. on p. 81).

[92] J. K. Gimzewski, R. Berndt, and R. R. Schlittler. “Scanning-tunneling-microscope study of antiphase domain boundaries, dislocations, and local mass transport on Au(110) surfaces”. en. In: *Physical Review B* 45.12 (Mar. 1992), pp. 6844–6857. ISSN: 0163-1829, 1095-3795. DOI: 10.1103/PhysRevB.45.6844 (cit. on p. 86).

[93] Ph. Guaino, D. Carty, G. Hughes, et al. “Long-range order in a multilayer organic film templated by a molecular-induced surface reconstruction: Pentacene on Au(110)”. en. In: *Applied Physics Letters* 85.14 (2004), p. 2777. ISSN: 00036951. DOI: 10.1063/1.1786655 (cit. on p. 91).

[94] S. Modesti, J.K. Gimzewski, and R.R. Schlittler. “Stable and metastable reconstructions at the C60/Au(110) interface”. en. In: *Surface Science* 331-333 (July 1995), pp. 1129–1135. ISSN: 00396028. DOI: 10.1016/0039-6028(95)00390-8 (cit. on p. 91).

[95] A. Cossaro, D. Cvetko, G. Bavdek, et al. “Copper-Phthalocyanine Induced Reconstruction of Au(110) †”. en. In: *The Journal of Physical Chemistry B* 108.38 (Sept. 2004), pp. 14671–14676. ISSN: 1520-6106, 1520-5207. DOI: 10.1021/jp049108h (cit. on p. 91).

[96] K.E. Hermann and M.A. Van Hove. *LEEDpat4, LEED symmetry pattern simulator*. URL: http://www.fhi-berlin.mpg.de/KHsoftware/LEEDpat/index.html (cit. on p. 94).

[97] Thomas Steiner. “Lengthening of the N?H bond in N?H ? N hydrogen bonds. Preliminary structural data and implications of the bond valence concept”. en. In: *Journal of the Chemical Society, Chemical Communications* 13 (1995), p. 1331. ISSN: 0022-4936. DOI: 10.1039/c39950001331 (cit. on p. 98).

[98] Ya.Yu. Lopatina, a.a. Marchenko, Senenko, A.I., et al. “Self-Organization of Long-Chain Aliphatic Molecules and Their Derivatives on Atomically Flat Surfaces”. In: *Ukrainian Journal of Physics* 60.2 (Feb. 2015), pp. 153–159. ISSN: 20710186, 20710194. DOI: 10.15407/ujpe60.02.0153 (cit. on p. 121).

[99] R. Yamada and K. Uosaki. “Two-Dimensional Crystals of Alkanes Formed on Au(111) Surface in Neat Liquid: Structural Investigation by Scanning Tunneling Microscopy”. en. In: *The Journal of Physical Chemistry B* 104.25 (June 2000), pp. 6021–6027. ISSN: 1520-6106, 1520-5207. DOI: 10.1021/jp994061z (cit. on p. 121).

[100] Hong Li, Douglas R. Powell, Randy K. Hayashi, et al. “Poly((2,5-dialkoxy-*p* -phenylene)ethynylene *-p* -phenyleneethynylene)s and Their Model Compounds”. en. In: *Macromolecules* 31.1 (Jan. 1998), pp. 52–58. ISSN: 0024-9297, 1520-5835. DOI: 10.1021/ma970899d (cit. on p. 134).

[101] Davydov A. S. “Theory of absorption spectra of molecular crystal”. en. In: *Ukrainian journal of physics* 53.1 (Jan. 2008), pp. 65–70. ISSN: 2017-0194 (cit. on pp. 134, 136).

[102] Michael Kasha. “Energy Transfer Mechanisms and the Molecular Exciton Model for Molecular Aggregates”. In: *Radiation Research* 20.1 (Sept. 1963), p. 55. ISSN: 00337587. DOI: 10.2307/3571331 (cit. on p. 136).

[103] Yusei Maruyama and Noriko Iwasaki. “Absorption spectra of amorphous organic films”. en. In: *Chemical Physics Letters* 24.1 (Jan. 1974), pp. 26–29. ISSN: 00092614. DOI: 10.1016/0009-2614(74)80205-8 (cit. on p. 136).

[104] R. Jankowiak, K. D. Rockwitz, and H. Baessler. “Adsorption spectroscopy of amorphous tetracene”. en. In: *The Journal of Physical Chemistry* 87.4 (Feb. 1983), pp. 552–557. ISSN: 0022-3654, 1541-5740. DOI: 10.1021/j100227a008 (cit. on p. 136).

[105] Nicoleta Nicoara, Elisa Román, José M. Gómez-Rodríguez, et al. “Scanning tunneling and photoemission spectroscopies at the PTCDA/Au(111) interface”. en. In: *Organic Electronics* 7.5 (Oct. 2006), pp. 287–294. ISSN: 15661199. DOI: 10.1016/j.orgel.2006.03.010 (cit. on pp. 136, 139).

[106] J A Venables, G D T Spiller, and M Hanbucken. “Nucleation and growth of thin films”. In: *Reports on Progress in Physics* 47.4 (Apr. 1984), pp. 399–459. ISSN: 0034-4885, 1361-6633. DOI: 10.1088/0034-4885/47/4/002 (cit. on p. 138).

[107] W. Chen, V. Madhavan, T. Jamneala, et al. “Scanning Tunneling Microscopy Observation of an Electronic Superlattice at the Surface of Clean Gold”. en. In: *Physical Review Letters* 80.7 (Feb. 1998), pp. 1469–1472. ISSN: 0031-9007, 1079-7114. DOI: 10.1103/PhysRevLett.80.1469 (cit. on p. 139).

[108] Thomas Andreev, Ingo Barke, and Heinz Hövel. “Adsorbed rare-gas layers on Au(111): Shift of the Shockley surface state studied with ultraviolet photoelectron spectroscopy and scanning tunneling spectroscopy”. en. In: *Physical Review B* 70.20 (Nov. 2004). ISSN: 1098-0121, 1550-235X. DOI: 10.1103/PhysRevB.70.205426 (cit. on p. 139).

[109] S. Katano, Y. Kim, M. Hori, et al. “Reversible Control of Hydrogenation of a Single Molecule”. en. In: *Science* 316.5833 (June 2007), pp. 1883–1886. ISSN: 0036-8075, 1095-9203. DOI: 10.1126/science.1141410 (cit. on p. 147).

[110] Kai Yang, Liwei Liu, Lizhi Zhang, et al. “Reversible Achiral-to-Chiral Switching of Single Mn–Phthalocyanine Molecules by Thermal Hydrogenation and Inelastic Electron Tunneling Dehydrogenation”. en. In: *ACS Nano* 8.3 (Mar. 2014), pp. 2246–2251. ISSN: 1936-0851, 1936-086X. DOI: 10.1021/nn405490h (cit. on p. 147).

[111] Conrad Becker. personal communication. Jan. 15, 2015 (cit. on pp. 147, 148, 151, 152).

[112] Michael W. Schmidt, Kim K. Baldridge, Jerry A. Boatz, et al. “General atomic and molecular electronic structure system”. en. In: *Journal of Computational Chemistry* 14.11 (Nov. 1993), pp. 1347–1363. ISSN: 0192-8651, 1096-987X. DOI: 10.1002/jcc.540141112 (cit. on p. 147).

[113] Sikhibhushan Dutt. “CL.?A theory of colour on the basis of molecular strain. The effect of chromophoric superposition”. en. In: *Journal of the Chemical Society (Resumed)* 129 (1926), p. 1171. ISSN: 0368-1769. DOI: 10.1039/jr9262901171 (cit. on p. 148).

[114] G. M. Badger and R. Pettit. “707. Polynuclear heterocyclic systems. Part IV. The linear pentacyclic compounds”. en. In: *Journal of the Chemical Society (Resumed)* (1951), p. 3211. ISSN: 0368-1769. DOI: 10.1039/jr9510003211 (cit. on p. 148).

[115] Shaobin Miao, Anthony L. Appleton, Nancy Berger, et al. “6,13-Diethynyl-5,7,12,14-tetraazapentacene”. en. In: *Chemistry - A European Journal* 15.20 (May 2009), pp. 4990–4993. ISSN: 09476539, 15213765. DOI: 10.1002/chem.200900324 (cit. on p. 149).

[116] Tony Lelaidier, Tobias Lünskens, Alexander von Weber, et al. “Optical and morphological properties of thin films of bis-pyrenyl π-conjugated molecules”. en. In: *Phys. Chem. Chem. Phys.* 18.7 (2016), pp. 5299–5305. ISSN: 1463-9076, 1463-9084. DOI: 10.1039/C5CP06011G (cit. on p. 181).

ANNEXES: List of publications

A. Article 1: Growth of Si ultrathin films on silver surfaces: Evidence of an Ag(110) reconstruction induced by Si.

Romain Bernard, Thomas Leoni, Axel Wilson, et al. “Growth of Si ultrathin films on silver surfaces: Evidence of an Ag(110) reconstruction induced by Si”. en. In: *Physical Review B* 88.12 (Sept. 2013). ISSN: 1098-0121, 1550-235X. DOI: 10.1103/PhysRevB.88.121411

B. Article 2: Highly Ordered Molecular Films on Au(111): The N-Heteroacene Approach.

Tony Lelaidier, Thomas Leoni, Pandurangan Arumugam, et al. “Highly Ordered Molecular Films on Au(111): The N-Heteroacene Approach”. en. In: *Langmuir* 30.20 (May 2014), pp. 5700–5704. ISSN: 0743-7463, 1520-5827. DOI: 10.1021/la404214u

C. Article 3: Optical and morphological properties of thin films of bis-pyrenyl π-conjugated molecules.

Tony Lelaidier, Tobias Lünskens, Alexander von Weber, et al. “Optical and morphological properties of thin films of bis-pyrenyl π-conjugated molecules”. en. In: *Phys. Chem. Chem. Phys.* 18.7 (2016), pp. 5299–5305. ISSN: 1463-9076, 1463-9084. DOI: 10.1039/C5CP06011G